The Analysis and Application of Dynamic MRI Contrasts to Grape Berry Biology

PhD Thesis

Ryan J. Dean

BSc (Advanced Science), Honours (1st Class)

School of Biomedical and Health Sciences

University of Western Sydney, Australia

Supervisors	William S. Price	University of Western Sydney, Australia
	Timothy Stait-Gardner	University of Western Sydney, Australia
	Simon J. Clarke	Charles Sturt University, Australia
	Suzy Y. Rogiers	New South Wales Department of Primary Industries, Australia

This thesis was submitted to the University of Western Sydney (UWS) in fulfilment of the requirements for the Doctorate of Philosophy in May, 2015

I (Ryan J. Dean) declare that this thesis contains no material that has been accepted for the award of any other degree or diploma and that, to the best of my knowledge and belief, this thesis contains no material previously published or written by another person, except when due reference has been made in the text of this thesis.

_____

Ryan J. Dean

/ /

Acknowledgements

Firstly I would like to thank my four supervisors, Prof. William S. Price, Dr Timothy Stait-Gardner, Dr Simon J. Clarke and Dr Suzy Y. Rogiers. The four of you have been excellent mentors throughout the duration of my PhD candidature, and I want to thank you all for your hard work and encouragement.

To all the members of the Nanoscale Dynamics group, past and present, I want to thank you for all your support. From amongst you there are a few I especially want to thank. I want to thank Dr Scott Willis for happily answering all those questions I've pestered you with over the years, from the operation and calibration of the NMR spectrometer to the presentation of this thesis. To Dr Bahman Ghadirian and Abhishek Gupta, I want to thank you both for patiently reading through all of those equations to ensure they were comprehensible. To Mikhai Zubkov, I want to thank you for help with the coding of some of my MATLAB scripts, those scripts were invaluable. I also want to thank Dr Allen Torres, for the training you have given me with the NMR spectrometer, and Robyn Grey, for your tireless efforts to ensure the smooth administration and operation of our research group. And I want to thank you Gabriele Bobek for all those hours you spent helping me acquire all those confocal micrographs!

To my all friends, especially Heidi Thomson, Samuel Kirk, Iain Russell, Josie Moroney and Stacey and John Pope, I want thank you all for helping to keep me sane. You guys whisked me out of the lab for a BBQ or a day at the beach when I needed it, and we had some awesome times together. May they continue into the future!

To Ben Moroney, I want to thank you for being such a great friend. We made it through our PhD candidatures! You have always been a brilliant sounding board for bouncing ideas off and I've learnt a lot from you over these past few years. And I'll always fondly remember your terrible puns.

To my parents, Philip and Assunta, I can't express how much I'd like to thank you for all your love and support. Thanks to you, I've made it through university, and through my PhD candidature. I want to especially thank you for the long nights you

spent together with me, reading through and correcting the drafts of my papers and of my thesis. You made some incredibly helpful suggestions to my papers, even though you both claimed you couldn't really understand the material!

To my wonderful fiancée Alicia, I want to thank you too. Your love and support has been overwhelming. You listened to every problem I had with my research projects, and you happily let me talk (and complain) about what must have sounded like nonsense until I managed to work out a solution. I cannot thank you enough for the faith you've had in my work, and in me.

In memory of my little sister, Amanda.

Abstract

Magnetic resonance imaging (MRI) is a powerful, non-invasive imaging tool. When MRI is employed in the study biological systems, the acquired images reflect different aspects of system morphology and/or physiology. This thesis explores the application of relaxation and diffusion MRI to the study of different biological aspects of the fruit of the common grape vine, *Vitis vinifera* L., a highly valued botanical species. The results of this investigation have put forth a number of contributions to this area of research.

The studies within this thesis began with a necessary validation for the application of diffusion MRI techniques to the grape berry using simulated cellular geometries to determine how broad plant cells could potentially influence the accurate reconstruction of the grape berry morphology. The result of this validation will also prove useful for other wide geometry applications wider than 10 µm.

Relaxation and diffusion MRI was also used to study changes to berry morphology resulting from berry development and ripening. This study provided a novel perspective on grape berry development and demonstrated that diffusion anisotropy patterns correlated with the microstructure of the major pericarp tissues of grape berries, including the exocarp, outer and inner mesocarp, seed interior, as well as microstructural variations across grape berry development. This study also provided further evidence that the inner mesocarp striation patterns observed in the spin-spin relaxation weighted images of previous studies arise due to variations in cell width across the striation bands.

Diffusion MRI was employed to investigate the morphological and physiological changes to occur within grape berries during fruit split, a costly source of fruit loss in vineyards. This study revealed water uptake through splits in the berry epidermis will result in the loss of parenchyma cell vitality about these wounds. The amount of water left standing on the surface of split grape berries may hence be an important determinant of the cellular response of the fruit to this trauma, and the subsequent establishment of adventitious fruit pathogens.

Additionally, paramagnetically enhanced spin-lattice relaxation MRI was used to undertake a novel examination of the diffusive transport of manganese across the berry pericarp. The results of this study shows that the transport of manganese is within the berry xylem influences manganese exiting of ‘downstream’ of the pedicel, and that cellular membranes affect the spatial distribution of manganese across the berry pericarp. Manganese proved to be an excellent tracer for these experiments, and future investigations making use of paramagnetically enhanced relaxation MRI, perhaps employing other paramagnetic materials such as iron or copper, could prove to be valuable in determining how botanical species transport and store these materials within sink organs.

List of abbreviations

ADC	Apparent diffusion coefficient
E	Attenuated signal intensity
b	b value
$\mathbf{b}$	b matrix
CPMG	Carr-Purcell-Meiboom-Gill
cv.	Cultivar
DAF	Days after flowering
D	Diffusion coefficient
$\mathbf{D}$	Diffusion tensor (second order)
DTI	Diffusion tensor imaging
DWI	Diffusion weighted imaging
$\mathbf{R}$	Displacement vector
TE	Echo time
λ	Eigenvalue
υ	Eigenvector
FOV	Field of view
FA	Fractional anisotropy
δ	Gradient pulse length
g	Gradient pulse strength (diffusion gradient)
G	Gradient pulse strength (imaging gradient)

γ	Gyromagnetic ratio
$\mathbf{k}$	**k**-space wave vector
x, y, z	Laboratory reference frame
ω_0	Larmor (precession) frequency
Δ	Length of diffusion measurement
T_1	Spin-lattice relaxation time
MRI	Magnetic resonance imaging
B_0	Magnetic strength (external field)
MTX	Matrix size
$\langle \mathbf{R}^2 \rangle$	Mean square displacement
MSME	Multi-slice multi-echo
NMR	Nuclear magnetic resonance
NA	Number of averages
$\mathbf{r}$	Position vector
PGSE	Pulse gradient spin echo
$\mathbf{q}$	**q**-space wave vector
rf	Radio-frequency
RA	Relative anisotropy
TR	Repetition time
$\langle \lVert \mathbf{R} \rVert \rangle$	Root mean square displacement
x', y', z'	Rotating reference frame
S_0	Signal intensity (diffusion-unweighted)

S	Signal intensity (diffusion-weighted)
SNR	Signal-to-noise ratio
THK	Slice thickness
ρ	Spin density
t	Time
Tr	Trace
T_2	Spin-spin relaxation time
VR	Volume ratio

Publications

The following publications were prepared, presented and accepted during the course of this thesis.

W. Srichamnong, W. S. Price, T. Stait-Gardner, R. J. Dean, E. Plougonven, A. Léonard and G. Srzednicki (2013). "Studies of microstructure of kernels of *macadamia integrifolia* and its hybrids through MRI, x-ray tomography and confocal microscopy." *Journal of Food Science and Engineering* **3**, 503-516.

R. J. Dean, T. Stait-Gardner, S. J. Clarke, S. Y. Rogiers, G. Bobek and W. S. Price (2014). "Use of diffusion magnetic resonance imaging to correlate the developmental changes in grape berry tissue structure with water diffusion patterns." *Plant Methods* **10**, 35.

R. J. Dean, T. Stait-Gardner, S. J. Clarke, S. Y. Rogiers, G. Bobek and W. S. Price (2015). “Time course study of grape berry split using diffusion MRI." Accepted for publishing in the *Australian Journal of Grape and Wine Research*.

The Analysis and Application of Dynamic MRI Contrasts to Viticulture

Table of contents

Preface

Research background and context

Viticulture is a highly valuable horticultural industry for Australia. In 2012-2013 Australia produced 1.23 billion litres of wine [1, 2]. Of this, 459 million litres of Australian wine were sold domestically while 698 million litres were exported to 123 countries, including the United Kingdom, the United States, Canada, China and New Zealand [1]. Consequently, Australia ranks as the fourth largest exporter of wine in the world. Table grapes also make a significant contribution to Australian horticulture. In 2012-2013 Australia exported 68 thousand tonnes of table grapes grown in Victoria, the state which accounts for the majority of Australia's table grape production [3]. Key export destinations of table grapes include Hong-Kong, Indonesia, Vietnam, Thailand and China. To ensure that Australia remains competitive relative to other high volume viticultural product exporters (e.g. New Zealand, France and Chile), continued investment and research is required to further improve grape production methods and fruit quality. This requires a continued improvement of our understanding of grape berry morphology and physiology.

Knowledge of grape berry morphology largely stems from previous investigations of grape berry tissues using optical or electron based microscopy [4, 5]. Many different aspects of grape berry physiology have also been studied, some of which include the vasculature transport of water mobile solutes [6-8], cell turgor pressure [9, 10], cell hydraulic connectivity [11, 12] and sugar uptake/distribution [13, 14]. These studies have provided a wealth of information regarding the structure and biochemistry of the grape berry at many different stages of development.

Many previous studies of grape berry morphology/physiology were highly invasive, requiring the dissection of the grape, the excision of tissues, the puncturing of cells or the introduction of non-physiological compounds to the berry (such as fluorescent dyes). However, the conduction of morphological/physiological investigations using intact grape berries is preferred. There are a number of non-invasive biomedical

imaging technologies available that could potentially be used for viticulture studies, including ultrasonography, x-ray computed tomography (CT), position emission tomography (PET) and magnetic resonance imaging (MRI). Of these choices, MRI is the stand out candidate. MRI offers superior soft-tissue characterisation to x-ray based imaging techniques, and is capable of resolving image objects on a near cellular scale. Additionally, rather than producing images where contrast is based on electron-density or gamma radiation intensity (i.e., x-ray CT and PET images, respectively), magnetic resonance (MR) images are weighted by the properties of the atomic nuclei within the sample under study [15-17]. These properties can include the density of atomic nuclei (spin-density MRI), the rate at which nuclei excited by radio-frequency magnetic fields relax (relaxation MRI) and the displacements of diffusing nuclei (diffusion MRI). MRI can hence provide extensive information regarding the physical and chemical composition of biological systems, as well as physiological functions such as solute transport.

Since the inception of MRI, the technology has been largely reserved for biomedical purposes. While some previous studies have involved the use of MRI to investigate different aspect of plant morphology/physiology [18-21], in many cases botanical specimens serve only as biological phantoms for zoological MRI studies [20, 22-25]. Consequently, the number of MRI studies that have been conducted to examine the morphology/physiology grape berries is limited [26, 27]. MRI provides an unrivalled opportunity to further explore and improve our understanding of grape berry biology. To this end, this thesis will examine how relaxation and diffusion MRI can be employed to provide novel information regarding the morphology/physiology of grape berries, and explore the practical implications of the findings.

The objectives of this research

This thesis has four primary objectives. The first objective is to determine the applicability of different diffusion MRI for the study and analysis of grape berry morphology. This validation was required to ensure the diffusion MRI techniques employed in this thesis would be able to accurately reconstruct the morphology of the grape berries. The second objective is to use relaxation and diffusion MRI to

study changes to berry morphology resulting from berry development and ripening. This study was included to provide a novel prospective on grape berry development while simultaneously establishing a library of relaxation and diffusion images/values for normal grape berries for comparisons with treated grape berries in subsequent studies. The third objective of the thesis is to use diffusion MRI to study the changes to berry morphology that arise from physical injury. This investigation was performed in order to study morphological and physiological changes to the grape berry due to the formation of splits in the berry epidermis, as well as to determine the practical implications this research could have on viticulture. The fourth and final objective is to investigate the transport and spatial diffusion of micronutrients across the berry pericarp using relaxation and diffusion MRI. This study was undertaken in order to explore the use of manganese as a tracer for vascular/extra-vascular ionic transport within the grape berry, potentially providing an alternative to studying solute transport without involving the use of much larger, non-physiological compounds.

Thesis organisation

This thesis has been divided into nine chapters, each with a distinct focus.

Chapter 1 provides an overview of grape berry morphology, focusing on the tissues that comprise the grape berry pericarp. A description of grape berry growth and development is also included.

In Chapter 2, an introduction to the fundamentals of magnetic resonance imaging is presented. The principles of nuclear magnetism and spin are discussed, as well as how the magnetic moments of atomic nuclei can be manipulated using magnetic fields. This chapter also includes an explanation of magnetic resonance image data processing, the different forms of relaxation, and relaxation MRI.

Chapter 3 provides a comprehensive review of the fundamentals of diffusion, including both mutual and translation self-diffusion, and how diffusion can be measured with MRI. Additionally, the characterisation of diffusing particle

distributions is discussed as well as the effect of motional restriction by microstructures.

Chapter 4 presents and discusses the principles underpinning two important diffusion MRI techniques; diffusion tensor imaging, a commonly employed method for the analysis of three-dimensional diffusion MRI data, and Bessel Fourier reconstruction imaging, a recently developed diffusion MRI technique.

In Chapter 5 the materials and methods for the investigations used in this thesis are presented. This chapter includes descriptions of the hardware and software employed, and descriptions of the growing conditions for specimens that were used.

Chapter 6 tested the suitability of Bessel Fourier orientation reconstruction imaging for morphological studies of botanical tissue structure. The results from this analysis indicated that diffusion tensor imaging is better suited to the analysis of the grape berry pericarp than this diffusion MRI.

Chapter 7 details an exploration of the application of diffusion MRI to viticulture and, by extension, other agricultural industries. Here the correlation between macroscopic diffusion patterns and well-defined stages of grape berry growth/development was investigated. This research also resolved several questions raised by the results of previous studies.

In Chapter 8 changes to grape berry morphology prior and post the formation of fruit splits *in vivo* are examined using diffusion MRI. This investigation revealed that external water can enter the grape pericarp through splits in the berry epidermis and trigger tissue ischemic cell death. It also highlights the potential importance of rainfall events post the incidence of fruit split.

In Chapter 9 the passive transport of metal ions into the grape were studied using paramagnetically enhanced spin-lattice relaxation MRI. This MRI technique was used to directly observe the unloading of manganese from the berry vasculature and its subsequent transport throughout the berry pericarp via diffusion mediated processes.

Chapter 10 is the concluding chapter of the thesis, in which the findings of this thesis are reviewed.

Chapter 1 - Grape berry morphology

To provide context for later discussions of the grape berry morphology in this thesis, this chapter provides an overview of the morphology of the tissues that constitute the grape berry as well as a description of grape berry growth and development.

1.1 The tissues of the grape berry pericarp

The grape berry is a relatively simple fruit (Figure 1). It consists of one to four viable seeds (or no viable seeds for seedless varieties) surrounded by the fleshy pericarp [4]. The berry pericarp is the part of the grape that is consumed and used in wine making. For the purposes of this thesis, the grape berry pericarp will be considered in terms of four constituent tissues; the exocarp, outer mesocarp, inner mesocarp and septum.

The grape exocarp is the component of the pericarp that separates and protects the berry from the environment. It comprises of the cuticle and the outer epidermal and hypodermal layers of the grape berry [4, 5]. The cuticle is a waxy layer several micrometres in thickness which assists in reducing the amount of water lost from the surface of the fruit via transpiration [28]. The outer epidermal and hypodermal tissues consist of 2 and 7 – 8 layers of cells, respectively. These cells are thick-walled relative to other cells of the pericarp [5], and are tangentially elongated. The grape mesocarp contains the bulk of the grape pericarp. It consists of 25 – 30 layers of radially elongated parenchyma cells [5]. Parenchyma cells are used for the storage of soluble solids, primarily glucose and fructose (the total soluble solids present in the juice of a grape is measured in terms of °Brix, i.e. 1 g of soluble solids per 100 g of solution). The mesocarp also contains vascular bundles, which comprise a network of xylem and phloem vessels, that supply water and nutrients to the berry [4]. The peripheral vasculature marks the boundary between the outer mesocarp and the inner mesocarp. The outer mesocarp is the tissue between the outer hypodermis and the tissue exterior to the peripheral vascular bundles, while the inner mesocarp is the tissue inwards from the peripheral vascular bundles. The septum is the region of

regular tissue found at the centre of the grape berry adjacent to the berry seed(s) and locule(s). The septum fills the void where one or more grape seeds have been aborted and consists of irregularly shaped and sized cells [4].

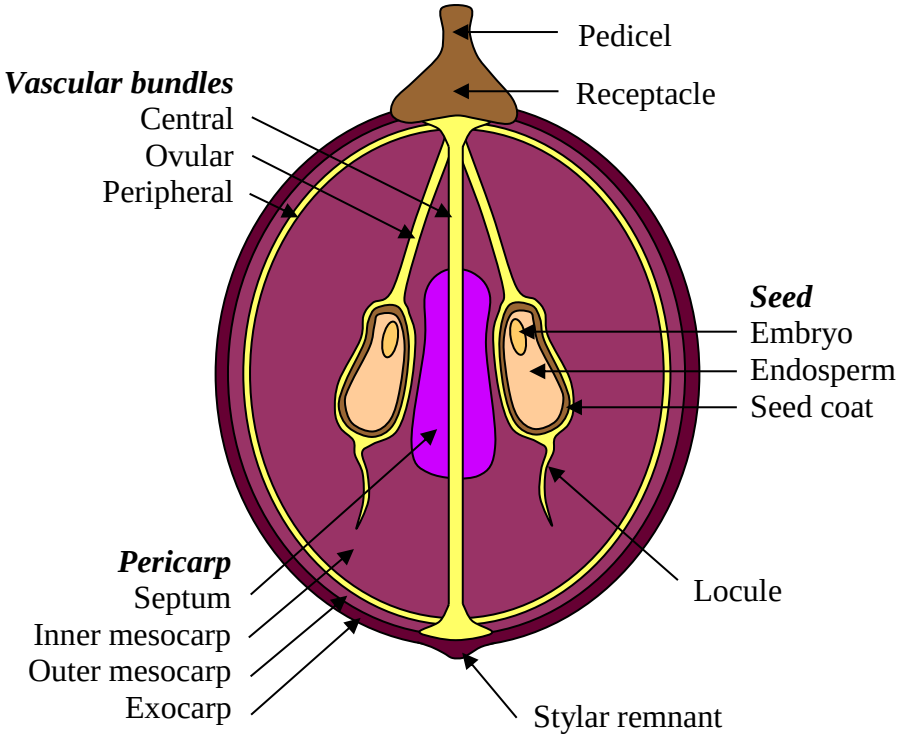

Figure 1: Schematic diagram of the grape berry and its constituent tissues.

One tissue of the pericarp that has not been included in this discussion is the endocarp, the component of the pericarp that directly encases the seeds. This is because the grape berry endocarp only consists of 2 – 3 layers of cells, which are highly compacted and difficult to discern [5]. Consequently, for the remainder of this thesis the endocarp will be considered as part of the inner mesocarp rather than a separate tissue.

The grape berry also possesses three noticeable external features. These are the pedicel, receptacle and the stylar remnant. The pedicel is the stem that connects the berry to the vine while the receptacle is the bulbous tissue that directly contacts the berry [4]. The stylar remnant, found on the end of the berry opposite the pedicel, is

the remains of the entrance to the ovary of the flower before the ovary developed to form the grape berry.

1.1.1 Cell sizes of the grape berry pericarp tissues

Pericarp cells are smaller towards the exterior of the berry and larger towards the interior. For example, a mature grape berry (126 days after flowering (DAF)), cv. Traminer, has a mean outer epidermis radial cell width of 6.5 ± 1.5 μm, a mean outer hypodermis radial cell width of 5.4 ± 0.6 μm and a mean mesocarp cell width of 68.0 ± 4.5 μm [5]. However, the size of pericarp cells will noticeably vary between grape berries of different cultivars [29], ages [4, 5] and those grown under different conditions (e.g., applications of plant growth hormones, such as gibberellic acid [30]).

1.2 Grape berry growth and development

As grape berries develop, they pass through two distinct phases of growth interspaced by a lag phase where little to no growth occurs (Figure 2) [4, 31, 32]. The initial growth phase of the grape berry is dedicated to cell and seed production. The grape berry produces all of the cells it will possess at maturity during this growth phase [4]. To discourage wildlife from eating the fruit before the seeds have had time to mature, the berry also accumulates sizable quantities of tartaric and malic acid during this period [33]. At the end of the lag phase, the grape berry begins to soften and change colouration. This period is termed véraison, and it marks the beginning of fruit ripening [4, 31, 32]. During the latter growth period the grape berry will approximately double in weight. It also accumulates large quantities of sugar during this time (Figure 2). Once the second growth phase is complete, the grapes are ready to be harvested. Harvest may be forced to occur earlier than this in order to avoid poor weather conditions. Heavy rain or hail can lead to the onset of fungal infections or cause physical damage to the crop [34]. If the weather remains fine, harvest may occur later than is necessary if desired. Leaving grapes on the vine longer than is

necessary helps concentrate the amount of sugar in the berries for the production of sweeter wines [35].

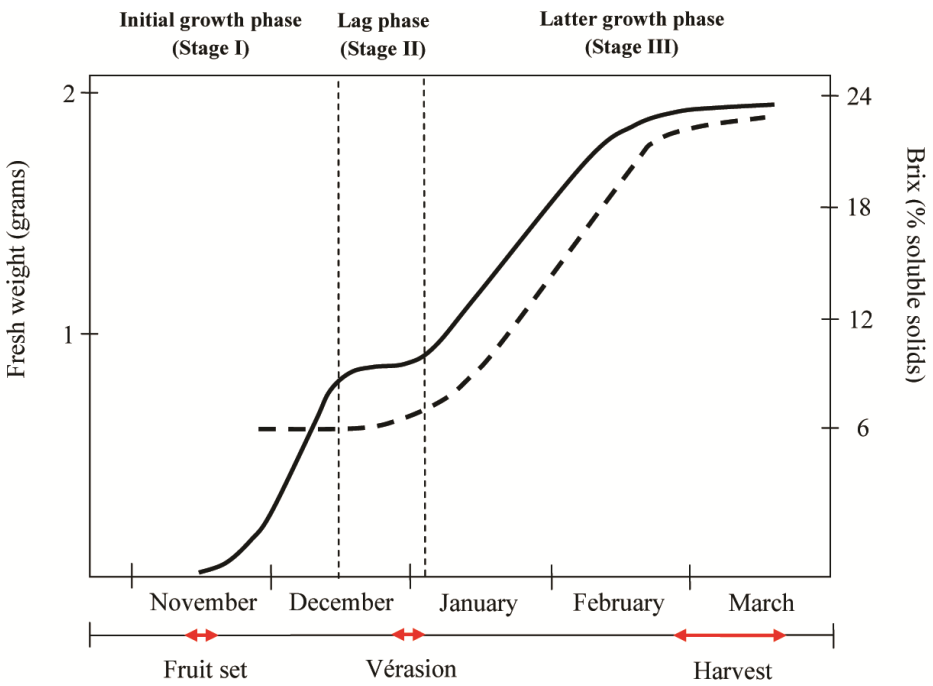

Figure 2: A representation of an approximation of the fresh weight of the berries (left axis, unbroken line) and the concentration of soluble solids (right axis, broken line) in relation to the three stages of grape growth (the initial growth phase, the lag phase and the latter growth phase, respectively). The bottom axis is an approximate timescale of berry development for grapes grown in Australia. The duration of each of these stages is dependent on the grape cultivar and climatic conditions in which they grow. Image adapted from previous studies [32, 36].

Chapter 2 - Magnetic resonance imaging

To provide a foundation for later discussions of MRI in this thesis, this chapter provides an overview of the fundamental principles of MRI and how MR images are acquired.

2.1 Atomic nuclei magnetism and spin

All atomic nuclei possess two intrinsic and closely linked properties; nuclear magnetism and nuclear spin [15, 16, 37]. Nuclear magnetism provides a nucleus with a magnetic dipole, allowing it to interact with other magnetic fields. Nuclear spin, on the other hand, provides the nucleus with angular momentum. The magnetic and spin angular moments which characterise these two properties can be represented using a pair of parallel, or anti-parallel, vectors (Figure 3). The magnitude of the spin angular moment, which can have either an integer or half-integer value, is termed the spin quantum number and characterises quantum mechanical interactions between subatomic particles [15, 16, 37]. Nuclei with an odd number of protons and/or neutrons have a non-zero spin quantum number (e.g., ^{1}H, ^{2}H, ^{13}C, ^{14}N, ^{15}N, ^{19}F and ^{23}Na) while nuclei with an even number of protons and neutrons have a spin quantum number of zero (e.g., ^{12}C and ^{16}O). Only nuclei with a non-zero spin quantum number are MR sensitive and can be detected with an NMR spectrometer.

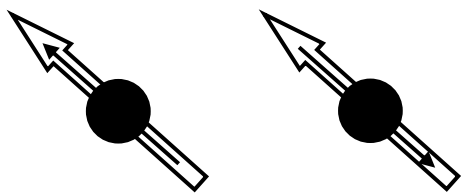

Figure 3: Two nuclei (•), the left with parallel magnetic (white arrow) and spin angular moments (black arrow) and the right with anti-parallel magnetic and spin angular moments.

When an MR sensitive atomic nucleus is placed in an external magnetic field, $\mathbf{B}_0$, the magnetic moment of the nucleus generates torque. This force is generated in order to align the magnetic moment of the nucleus with the orientation of the external magnetic field [15, 16]. For the purposes of this thesis, $\mathbf{B}_0$ will be considered to be aligned with the *z*-axis of the laboratory reference frame. However, the spin angular moment of the nucleus also generates torque, opposing any changes to its initial orientation. As a consequence, rather than aligning to the magnetic field, the magnetic and spin angular moments of the nucleus will rotate about the axis of the magnetic field (the nucleus itself does not physically spin or rotate); this motion is termed precession (Figure 4) [15, 16]. In an NMR (nuclear magnetic resonance) spectrometer, $\mathbf{B}_0$ is generated by liquid helium cooled superconducting magnetic coils. The magnitude of the external magnetic field, B_0, of the superconducting magnetic coils for current generation NMR spectrometers is typically upwards of 1.5 T. To provide a comparison, the magnetic field of the Earth is 25 – 65 μT [38], while the magnetic field strength of a magnetic crane used in car junk yards is ~1 T.

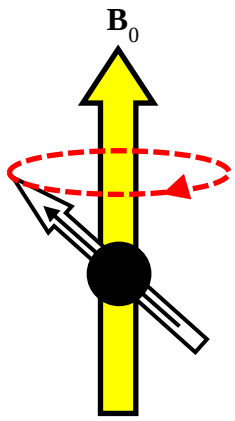

Figure 4: Precession of the magnetic (white arrow) and spin angular (black arrow) moments of a nucleus (•) about the axis of an external magnetic field ($\mathbf{B}_0$, yellow arrow). The torque generated by these moments result in their precession (red arrow) about the external magnetic field.

The frequency at which a spin angular moment, or 'spin', precesses about an external magnetic field is termed the Larmor (or resonance) frequency, ω [15, 16]. The Larmor frequency is calculated from the gyromagnetic ratio, γ, of the nucleus and the strength of the external magnetic field; i.e.,

$$\omega = -\gamma B_0 . \quad (1)$$

The gyromagnetic ratio is the ratio of the magnetic and the spin angular moments of the nucleus [15, 16]. For example, the gyromagnetic ratio of ^{1}H is 267.52×10^{6} rad s^{-1} T^{-1} while the gyromagnetic ratio of ^{15}N is -27.12×10^{6} rad s^{-1} T^{-1} [39]. The gyromagnetic ratio of ^{15}N is negative because the magnetic and the spin angular moments of this isotope are anti-parallel; a positive gyromagnetic ratio will result in clockwise spin precession about the external magnetic field, while a negative gyromagnetic ratio will result in anti-clockwise spin precession [15]. Within a 1.5 T external magnetic field, ^{1}H and ^{15}N will precess at 63.86 MHz and 6.47 MHz, respectively. The precession frequencies of other MR sensitive nuclei isotopes will likewise precess within the radio-frequency (rf) range.

The magnetic moment associated with a precessing spin is capable of inducing a small, oscillating electric current in an appropriate nearby conductor [15, 16]. In an NMR spectrometer, this signal is induced in the receiver coil. The coherent (i.e., in-phase) precession of many spins can produce a current strong enough for a sensitive detector to register. It is the electronic signal from this detector that is used to characterise and create images of a sample. The receiver coil is tuned to optimise the detection of the range of MR signals that can be generated by a particular isotope. Isotopes with a high gyromagnetic ratio will precess relatively quickly (see Eq. (1)) and hence induce a strong current in the receiver coil. ^{1}H has the highest gyromagnetic ratio and is also naturally abundant in biological systems (mostly as water, but also in the form of organic molecules); for these reasons, ^{1}H MRI is highly popular. In order to prevent small fluctuations in $\mathbf{B}_0$ inducing a current in the receiver coil, which would otherwise obscure the weaker currents induced by precessing spins, the receiver coil is typically situated so that it is perpendicular to $\mathbf{B}_0$ [15, 16]. In other words, only the *x*-*y* (i.e., transverse) component of precessing spins contributes to the current induced in the receiver coil (Figure 5). The induced current is thus maximised when spin precession occurs solely in the transverse plane; a system containing precessing spins can be moved towards this state by combining (the static) $\mathbf{B}_0$ with another, weaker, generally time-dependent external magnetic field, $\mathbf{B}_1$.

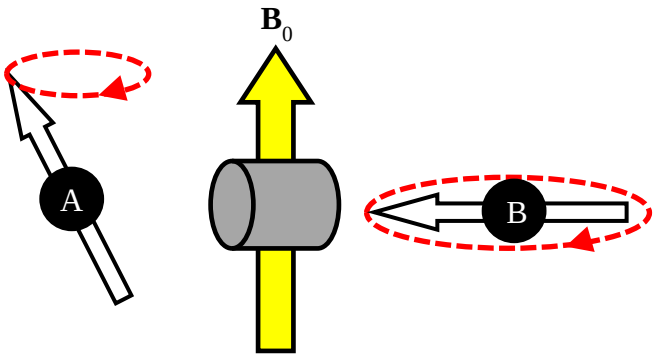

Figure 5: The magnetic moments (white arrows) associated with two nuclei (•) are precessing about the axis of an external magnetic field, $\mathbf{B}_0$ (yellow arrow), which is perpendicular to the receiver coil (grey cylinder). The transverse component of spin A is smaller than that of spin B. Hence the current induced by spin A is likewise smaller than that of spin B.

Ordinarily, a second external magnetic field several orders of magnitude weaker than $\mathbf{B}_0$ would have little to no effect on spin precession. However, if $\mathbf{B}_1$ oscillates at the Larmor frequency of a precessing spin, the effect of the smaller torque generated by $\mathbf{B}_1$ will accumulate with time; this effect is termed magnetic resonance [15, 16]. For example, consider a number of small pushes given over time to a child's swing; by matching the frequency of these pushes to the oscillation of the swing, the amplitude of the swing will increase. The effect of magnetic resonance can overcome the torque generated by $\mathbf{B}_0$, and cause spins to slowly rotate (relative to ω) about this weaker magnetic field [15, 16]. As discussed above, the Larmor frequency of precessing spins (and hence $\mathbf{B}_1$) is generally within the rf range; thus $\mathbf{B}_1$ is commonly referred to as an rf pulse [15]. In an NMR spectrometer, rf pulses are generated by a small electromagnetic transmitter coil (depending on the design of the NMR spectrometer the transmitter and receiver coils may in fact be the same coil). By carefully timing the strength and duration of the rf pulse, the magnetic moment of precessing spins can be rotated by a particular angle about an axis [15, 16]. For example, a $\pi/2_x$ rf pulse will rotate precessing spins 90° about the x-axis (as denoted by the x subscript) of the laboratory reference frame and into the transverse plane (Figure 6). The precessing nuclei frequency range that an rf pulse will excite, termed the effective spectral width, is inversely proportional to its duration [15, 16]. Hence short rf pulses will excite a wide range of spin precession frequencies, and vice versa.

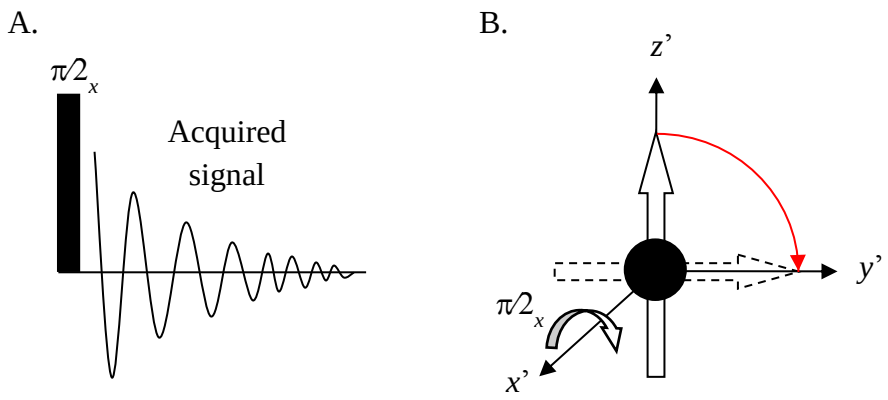

Figure 6: (A) Schematic diagram of a one-pulse MR pulse sequence. A magnetically resonant $\pi/2_x$ rf rotates the magnetic moments of precessing spins 90° into the transverse before the MR signal is acquired. (B) A potential pathway for the rotated magnetic moment (white arrow) of a precessing spin is outlined in red. Here the rotation of the magnetic moment is observed in the rotating reference frame, *x*', *y*', *z*' (i.e., the reference frame is rotating about the external magnetic field at the Larmor frequency of the precessing spin) in order to simplify the visualisation of the pathway (cf. Levitt 2001, Fig. 10.21).

Depending on the surrounding chemical environment, the precession frequency of a nucleus can vary tens of kilohertz from the natural precession frequency calculated via Eq. [15, 40]. Hence the effective spectral width excited by an MRI rf pulse is generally large enough to encompass the possible frequencies at which nuclei of a particular isotope (e.g., ^{1}H) may precess (i.e., a non-selective rf pulse). However, as nuclei in particular chemical environments will precess at specific frequencies, this property is can be useful for selecting particular molecules of interest [15, 40]. For example, the effective spectral range can be tailored to excite only hydrogen nuclei in water molecules and not hydrogen nuclei in fat (i.e., a selective rf pulse). As will be discussed later, the effective spectral width of an rf pulse is also important in determining the volume of the specimen that will be imaged (see Section 2.4.1 Image slice selection).

2.2 Magnetic resonance images

Before explaining how a two-dimensional MR image is produced, it would be helpful to discuss imaging terminology. The physical area of the MR image, termed the field of view (FOV), is divided into a matrix (MTX) of constituent elements. As will be discussed later (see Section 2.4.1 Image slice selection), MR data is acquired from a volume of the sample [15, 41, 42]. Consequently, the elements that constitute the MR image are three-dimensional, and are termed voxels (volumetric picture elements).

The physical dimensions of voxels are determined by the size of MTX in relation to the FOV, as well as the thickness, THK, of the image slice. For example, an MR image with a 20 mm × 30 mm FOV, a 1 mm THK and a 128 × 128 MTX will consist of voxels with dimensions 156 μm × 234 μm × 1000 μm. The resolution of an MR image can be improved by decreasing voxel sizes. However, smaller individual voxels will have a lower spin density (i.e., they contain fewer precessing spins). As a consequence, the MR signals generated by these voxels will be weaker and are more likely to be obscured by MR signal noise. Fortunately the MR signal-to-noise ratio (SNR) can be improved by averaging the MR signal over multiple acquisitions. The SNR will improve by a factor equal to the square root of the number of times the MR signal is averaged (NA) [43]. For example, if the MR signal is averaged over sixteen acquisitions, the SNR will improve by a factor of four.

The magnetic moments of the spins contained with the bounds of a voxel contribute to its net magnetisation and in turn the acquired MR signal. Hence the acquired MR signal is in fact the superimposed MR signals generated by each voxel [15, 16]. If the components of the acquired MR signal have some form of spatial label, it becomes possible to determine from which voxel each component of the MR signal originated, allowing the reconstruction of an MR image [15, 17]. In current generation MRI, the spatial labelling of the superimposed MR signals is achieved through magnetic field gradients.

2.3 Magnetic field gradients

A magnetic field gradient, **G**, is a magnetic field that varies in strength along its axis [15, 44, 45]. When **G** combines with $\mathbf{B}_0$, the effective external magnetic field experienced by MR sensitive nuclei linearly varies with respect to position [15], i.e.,

$$\mathbf{B}_{eff}\left(\mathbf{r}\right) = \left(B_0 + \mathbf{G}\cdot\mathbf{r}\right)\hat{\mathbf{k}} \tag{2}$$

where **r** is the position of the MR sensitive nuclei within the eternal magnetic field and $\hat{\mathbf{k}}$ is the *z*-axis unit vector of the laboratory reference frame. Consequently, nuclei will precess at different frequencies depending upon their position with respect to the orientation of the magnetic field gradient [15], i.e.,

$$\omega\left(\mathbf{r}\right) = \gamma\left(B_0 + \mathbf{G}\cdot\mathbf{r}\right). \tag{3}$$

This is known as frequency spatial encoding. If the magnetic field gradient is turned off, all MR sensitive nuclei experience the same external magnetic field and hence will precess with the same frequency. However, the difference in spin precession frequency along **G** prior to its deactivation results in the spins precessing at different phase angles along this axis. This is known as phase spatial encoding. Both frequency and phase spatial encoding are used to label the positions of precessing spins in MRI [15, 17]. Magnetic field gradient can also be used to measure the displacement of mobile spins, as will be discussed later (see Section 3.3 Measuring diffusion using magnetic field gradients). Henceforth, **G** will be used to describe magnetic field gradients employed to spatially label spins imaging while **g** will be used to describe magnetic field gradients employed to measure spin displacement.

2.4 Magnetic resonance image pulse sequences

An MRI pulse sequence is a specific series of rf pulses and magnetic field gradients which can induce a detectable MR signal. MRI pulse sequences are designed to measure specific characteristics of MR sensitive nuclei [39], such as spin density (Figure 7).

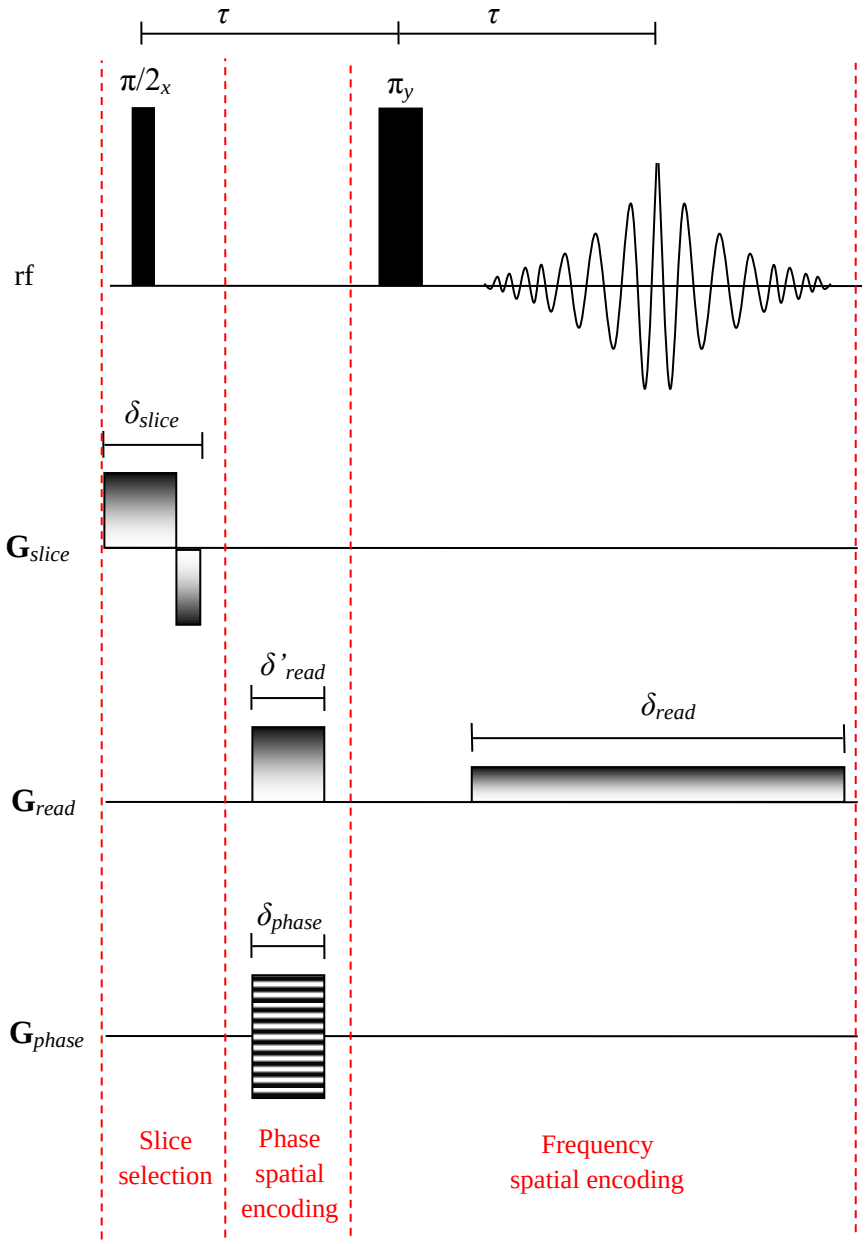

Figure 7: A simplified pulse sequence for two-dimensional spin-density-weighted MR imaging. The pulse sequence can be divided into three components: image selection, phase spatial encoding, frequency spatial encoding/MR signal acquisition. The strength and duration of the rf pulses and magnetic field gradients in this figure are not to scale; image magnetic field gradients are typically microseconds in length while τ is usually measured in milliseconds. All three magnetic field gradients are orthogonal to one another.

An MRI pulse sequence which measures spin density primarily consists of three components; image slice selection, phase spatial encoding and frequency spatial encoding/MR signal acquisition. All three steps are required to spatially label the voxels of the MR image. Each of these three steps is described in detail below.

2.4.1 Image slice selection

The objective of image slice selection is to excite only spins in the volume of interest (i.e., the image slice) with an rf pulse and to rotate these spins towards the transverse plane [15, 41]. To accomplish this, a magnetic field gradient, $\mathbf{G}_{slice}$, is used to vary the frequency of spin precession along an axis of the volume (e.g., the *z*-axis). By employing an rf pulse with an effective spectral range that encompasses the precession frequencies of spins within the volume of interest, only these spins will rotate towards the transverse plane (Figure 8 and Figure 9A).

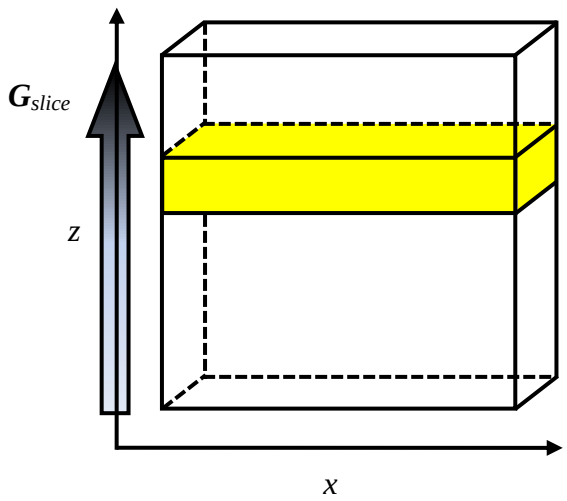

Figure 8: Image slice selection. By applying a magnetic field gradient along the *z*-axis ($\mathbf{G}_{slice}$), spins within the sample will precess at different frequencies. An rf pulse with a particular effective spectral width can then be used to excite only precessing spins within this range (e.g., yellow rectangle).

2.4.2 Phase spatial encoding

Once the image slice has been selected, image spatial encoding can begin. The first stage of image spatial encoding involves the application of phase encoding magnetic field gradients, $\mathbf{G}_{phase}$, along one of the axes of the image (i.e., the read axis) before MR signal acquisition commences for a period of δ_{phase}. The net magnetisations of voxels along $\mathbf{G}_{phase}$ will be therefore encoded with a particular phase (Figure 9B and C) when the MR signal is acquired [15, 17]. The MR pulse sequence is then repeated after MR signal acquisition with a different phase encoding magnetic field gradient strength. This process continues until a separate MR signal has been acquired for each row of voxels along the phase encoding axis. This does not include multiple MR signal acquisitions for MR signal averaging. As the MR pulse sequence must be repeated for each phase encoding step, the number of voxels along the phase axis will affect the length of the total MR image acquisition time.

2.4.3 Frequency spatial encoding/MR signal processing

During MR signal acquisition, a frequency encoding magnetic field gradient, $\mathbf{G}_{read}$, is applied along an axis perpendicular to the phase axis of the image slice (i.e., the read axis) [15, 17] for a period of δ_{read}. Consequently, each row of voxels along $\mathbf{G}_{read}$ will be associated with a unique net magnetisation precession frequency during MR signal acquisition (Figure 9D).

A π_y rf pulse is included before MR signal acquisition in order to refocus precessing spins [15, 46]. This is necessary because over time the system of excited spins slowly returns to thermal equilibrium and the amplitude of the acquired MR signal exponentially decays towards zero [15, 16]. The processes involved in this return to thermal equilibrium will be later discussed in detail (see Section 2.6 Nuclear spin relaxation).

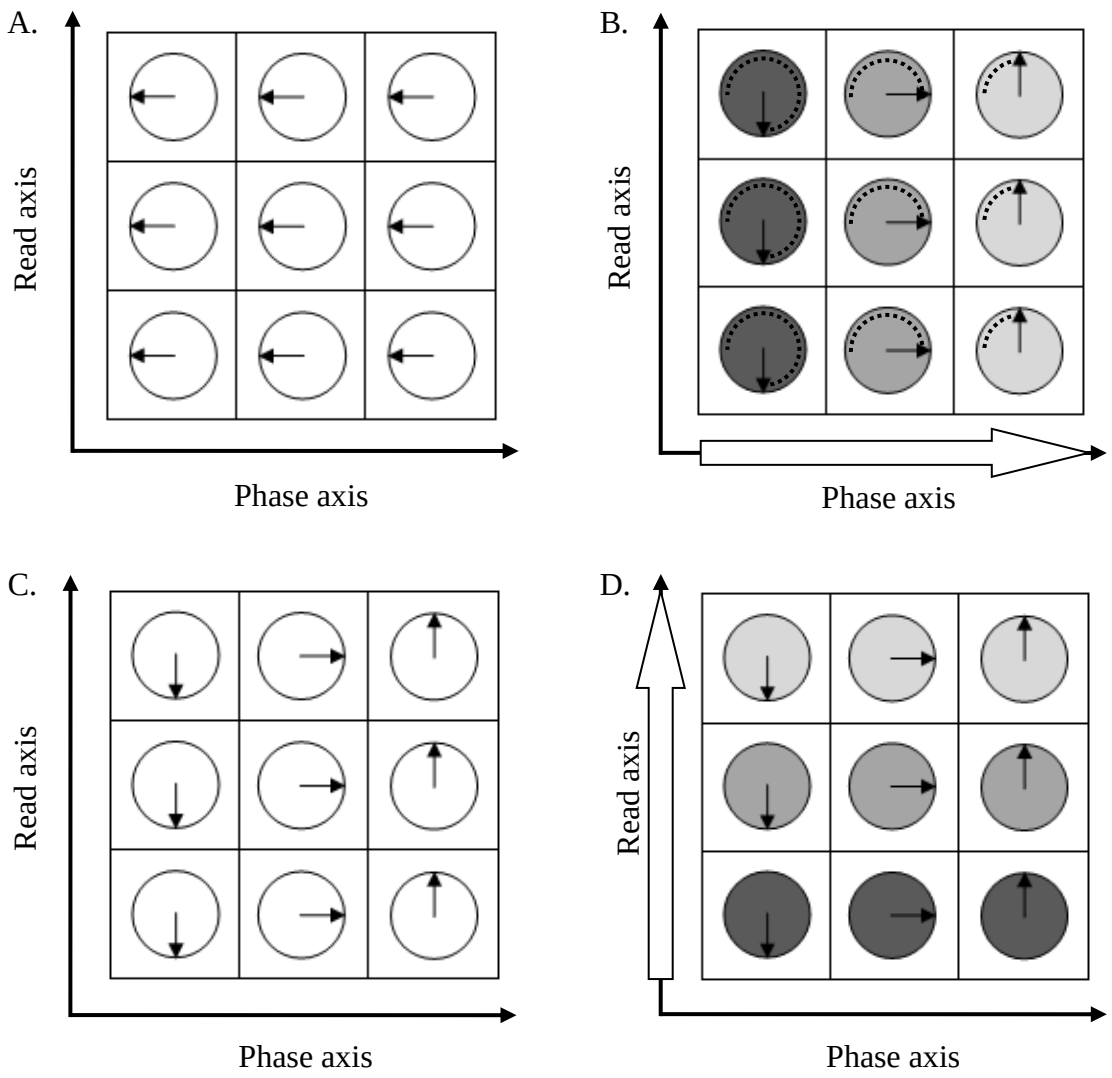

Figure 9: A schematic representation of the effect of phase and frequency spatial encoding on the precession of the net magnetisation vectors associated with each voxel of a 3 × 3 MR image. (A) After image slice selection the net magnetisation vectors (the black arrows) are in-phase and precess at the same frequency. (B) While the phase encoding gradient is active (white arrow), the net magnetisation vectors precess faster where the field is stronger (as indicated by darker spin shading). (C) When the phase encoding gradient is turned off, the net magnetisation vectors again precess at the same frequency. However, the phase of the net magnetisations vectors differs with respect to column position. (D) The frequency encoding gradient (white arrow) is applied while MR signal acquisition simultaneously occurs; each voxel is hence both frequency and phase spatially encoded.

2.5 *k*-space imaging

During the acquisition of the MR signal, the raw MR signal data is temporarily stored in a mathematical space known as *k*-space [47]. Once the MR signal acquisition is complete, the spatially encrypted MR data can be processed to yield an image. This data processing makes use of a mathematical operation known as the Fourier transform [48-50].

Fourier transforms convert signal data between mathematical domains/spaces, such as between the time domain and its inverse, the frequency domain (Figure 10). In MRI, Fourier transforms are used to transform the spatially encoded MR signals, S, into a map of position dependent spin density, ρ [15, 17]. Here it will be assumed that the read axis coincides with the y-axis of the MR image and that the MR signal was sampled with an even number of time points during the MR signal acquisition period, T. It will also be assumed the phase axis coincides with the x-axis of the MR image and that the MR signal was sampled with an even number of the phase encoding gradients. Each phase gradient used is assumed to have the same duration, but a different magnitude.

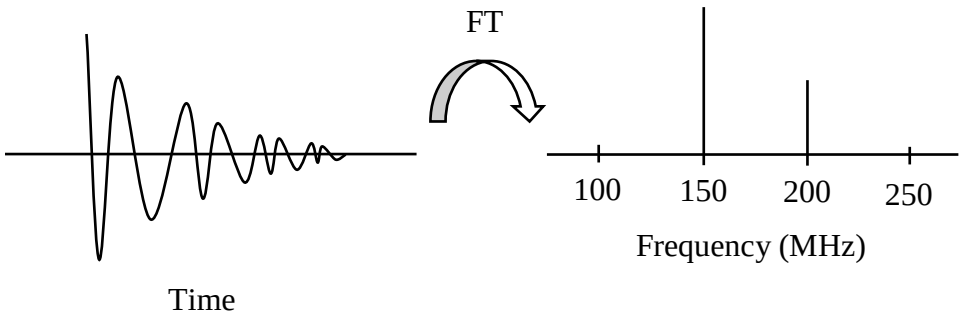

Figure 10: An illustration of an acquired MR signal consisting of two component MR signals, one oscillating at 150 MHz and the other at 200 MHz. Using a Fourier transform (FT), the MR signal is converted from the time domain to the frequency domain. The resultant MR spectrum features two peaks, one at 150 MHz and the other at 200 MHz. The difference in peak heights is related to the relative difference in the amplitude of the components of the acquired MR signal.

Hence the relationship between the raw MR data in k -space and the MR image is given by the two-dimensional Fourier transform [17, 48]

$$S(k_x, k_y) = \int_{-k_x/2}^{k_x/2} \int_{-k_y/2}^{k_y/2} \rho(x, y) \exp\left(-2\pi i \left(k_x x + k_y y\right)\right) dy\, dx\,, \tag{4}$$

where $k_x = (1/2\pi)\gamma G_{phase}\delta_{phase})$, $k_y = (1/2\pi)\gamma G_{read}\delta_{read})$ and i is the square root of negative one. Eq. (4) can therefore be solved for $\rho(x, y)$ using the inverse Fourier transformation, i.e., [17, 48]

$$\rho(x, y) = \int_{-k_x/2}^{k_x/2} \int_{-k_y/2}^{k_y/2} S(k_x, k_y) \exp\left(2\pi i \left(k_x x + k_y y\right)\right) dy\, dx\,. \tag{5}$$

By performing the inverse Fourier transform for each pair of voxel coordinates, the two-dimensional MR image can be reconstructed. While $\rho(x, y)$ is not a quantitative measure of the number of precessing spins in each voxel, it does indicate the relative concentration of precessing spins [15, 17]. As will be discussed later, by suitably modifying the two-dimensional MRI pulse sequence presented earlier (Figure 7), $\rho(x, y)$ can be weighted by different nuclear properties of spins to create other sources of MR contrast (see Section 2.6 Nuclear spin relaxation and Section 3.3 Measuring diffusion using magnetic field gradients).

2.6 Nuclear spin relaxation

This chapter concludes with a discussion of nuclear spin relaxation. When rf pulses disturb a system of precessing spins, the system moves away from thermal equilibrium. Over time the system will move back towards equilibrium, destroying the order imposed on the system by the rf pulses [16]. This return to thermal equilibrium is termed nuclear spin relaxation (henceforth referred to as relaxation). As the relaxation rate of a spin depends on its local magnetic environment, differences in relaxation rates can be used to create contrast between tissue types which differ in structure or chemical composition (see Chapter 7 - Diffusion MRI of grapes at different stages of development) [15, 51, 52]. Relaxation can also be used to study vascular/extra-vascular metal ion transport (see Chapter 9 - The diffusive

transport of manganese in the grape berry). Hence relaxation MRI will be an important tool for studying and characterising the morphology and physiology of grape berries.

There are two pathways by which nuclear spins can relax; spin-spin (i.e., transverse) and spin-lattice (i.e., longitudinal) relaxation. The effect of relaxation on the net spin magnetic moment, **M**, is described by the Bloch equation [16],

$$\frac{\partial \mathbf{M}}{\partial t} = \gamma \mathbf{M} \times \mathbf{B} - \frac{M_x \hat{\mathbf{i}} + M_y \hat{\mathbf{j}}}{T_2} - \frac{\left(M_z - M_0\right)\hat{\mathbf{k}}}{T_1} \tag{6}$$

where M_0 is the net spin magnetisation at thermal equilibrium, M_x, M_y and M_z are the orthogonal components of **M**, **B** is the total magnetic field, and $\hat{\mathbf{i}}$ and $\hat{\mathbf{j}}$ are the unit vectors of the x, y axes, respectively. T_1 and T_2 are the spin-spin and spin-lattice relaxation values of the spins, respectively.

Spin-spin relaxation relates to the rate at which the transverse component of **M** vanishes after the system has been excited by the application of rf pulses [15, 46, 53]. This is caused by a loss of phase coherence between the magnetic moments of precessing spins over time due to minor variations in the external magnetic field causing localised differences in spin precession rates (Figure 11). The spin-spin relaxation rate, $1/T_2$, is principally related to the reorientational motions of the spins. Slowly tumbling spins (i.e., spins which are part of a solid, or are in a viscous environment) relax at a faster rate than spins which are quickly tumbling [53]. By rewriting Eq. (6) in terms of transverse magnetisation (i.e., $m_{xy} = M_x + iM_y$), it can be shown that the relationship between the acquired MR signal intensity and T_2 is given by [46]

$$S(t) = S(0)\exp\left(-\frac{t}{T_2}\right). \tag{7}$$

where $S(t)$ is the measured, time dependent MR signal intensity and $S(0)$ is the MR signal intensity at time zero.

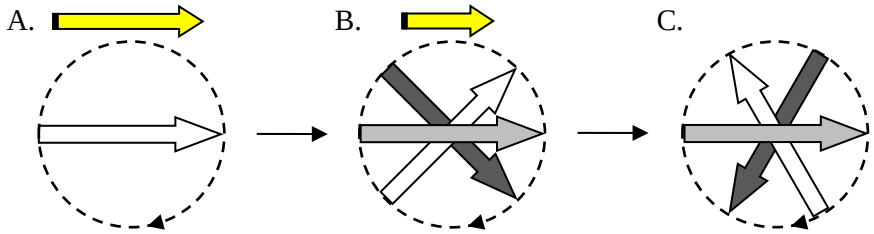

Figure 11: Schematic diagram of spin-spin relaxation. (A) A system of spins (white arrow) coherently precessing in the clockwise direction; the net (i.e., vector sum) magnetisation of the system is maximised (yellow arrow). (B) Minor differences in spin precession rates (the darkest arrows precess fastest) result in the magnetic moments of the spins dephasing, reducing the magnitude of the net magnetisation. (C) Phase coherence is completely lost and the magnitude of the net magnetisation is zero – even though the spins are not returned to thermal equilibrium.

Spin-spin relaxation weighted images are commonly acquired using a Carr-Purcell-Meiboom-Gill (CPMG) MRI pulse sequence (Figure 12) [52, 54, 55]. The CPMG MRI pulse sequence is an example of a spin-echo pulse sequence. Spin-echo pulse sequences features one or more π_y rf pulses to refocus the transverse component of the magnetic moments of precessing spins (Figure 13) [15, 46]. This refocusing results in the amplitude of the acquired MR signal increasing to a local maximum before decaying once more, creating an 'echo' of the MR signal. Increasing the length of the echo train will strengthen the spin-spin weighting of MR images reconstructed from the acquire MRI data [52, 54, 55]. The MR signal echo is maximised at intervals of 2τ (i.e., twice the period between the $\pi/2_x$ and π_y rf pulses) [15, 46]; consequently, the 2τ period is referred to as the echo time (TE). As the transverse component of the MR signal intensity is dependent on TE, t in Eq. (7) is replaced with TE. In order to determine the T_2 associated with spins, several spin-spin weighted MR images are acquired which are weighted by different TE values. Eq. (7) can then be fitted to the acquired MR signal intensity data (Figure 14) to calculate the T_2 of each voxel and thus create a map of spatially varying T_2 (i.e., a T_2 image).

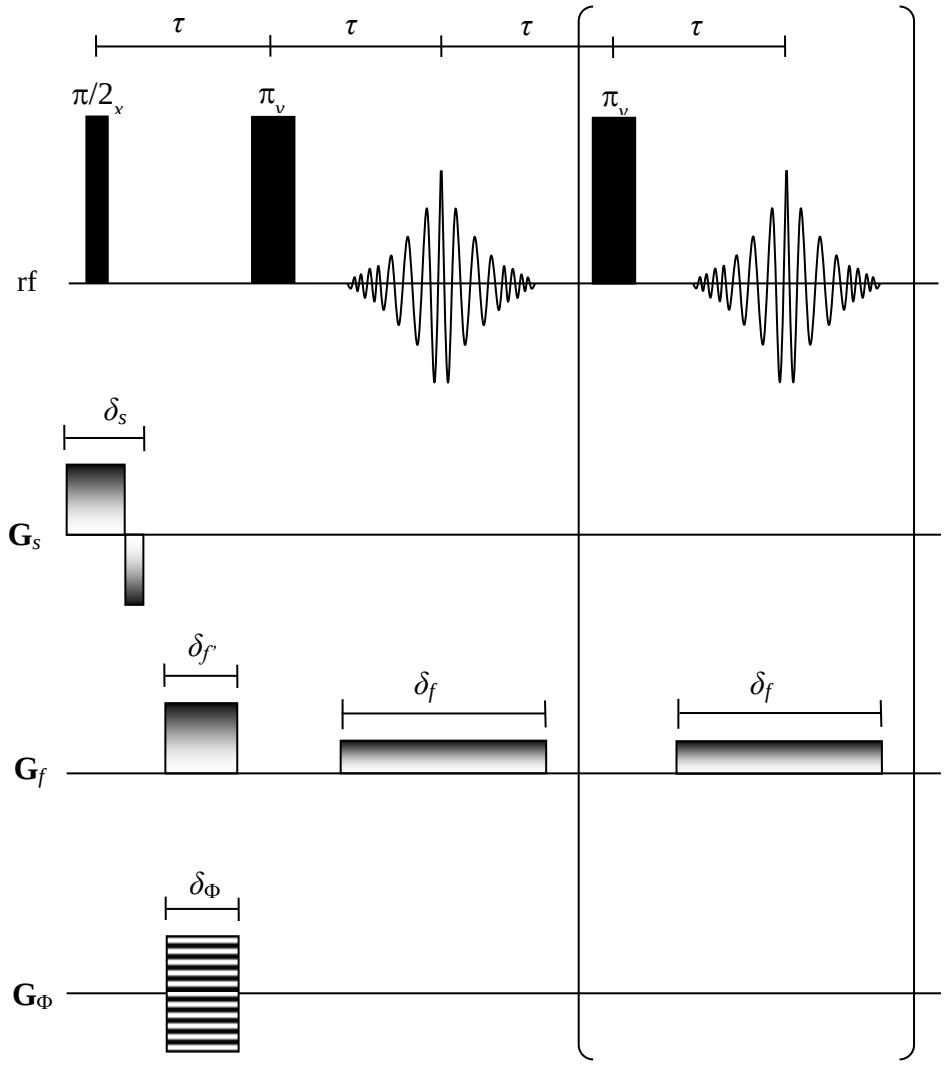

Figure 12: A simplified pulse sequence for two-dimensional CPMG MRI. This pulse sequence is similar to the spin-density MRI pulse sequence presented earlier (Figure 7) except that it includes a train of π_y pulses that continually refocus the transverse component of MR signal (i.e., the region of the MRI pulse sequence in brackets is repeated *n* times, where *n* is the number of echoes desired). The 2τ period is referred to as the echo time (TE), and its length influences spin-spin relaxation weighting of the MR image. The period between the first rf pulse of the MR pulse sequence and the first rf pulse of a following MR pulse sequence, on the other hand, is termed the repetition time (TR). The length of the TR influences the spin-lattice relaxation weighting of the MR image.

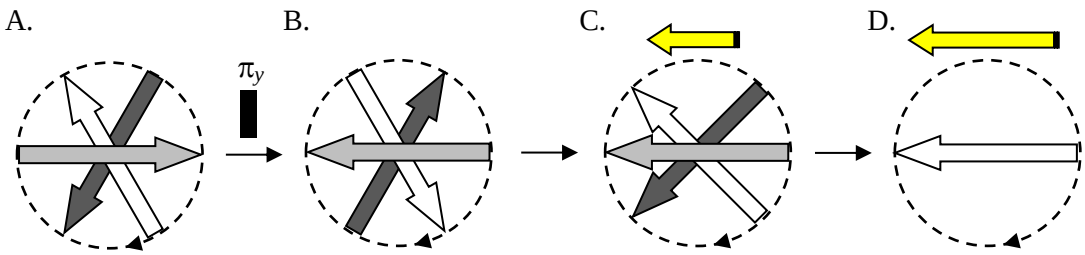

Figure 13: Schematic diagram of spin refocusing. (A) A system of spins (greyscale arrows; darker arrows precess faster than lighter arrows) incoherently precessing in the clockwise direction. (B) After applying a π_y rf pulse, the orientations of the magnetic moments are inverted. (C) The coherency of the magnetic moments increase with time, increasing the magnitude of the net magnetisation. (D) The magnetic moments of the spins are once again in-phase and system net magnetisation is maximised. After this the magnetic moments of the spins in the system will begin to lose precession coherency.

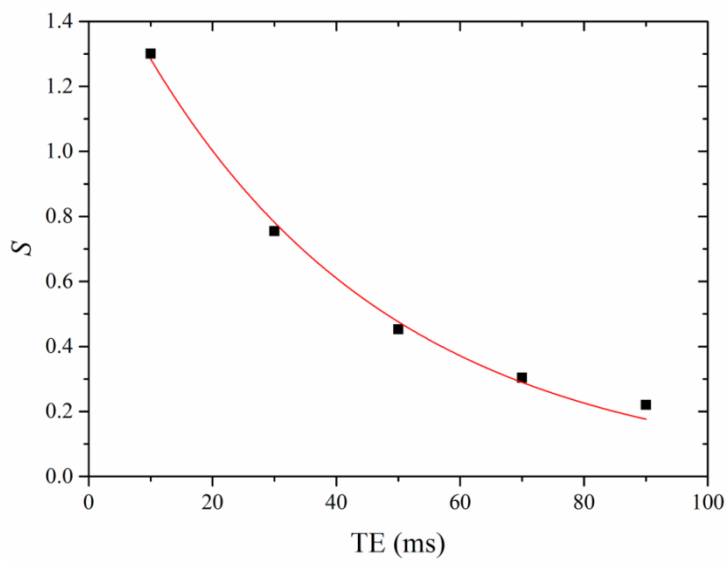

Figure 14: The attenuation of the MRI signal intensity values (■) of a single voxel with increasing TE due to spin-spin relaxation during the MRI pulse sequence. Upon fitting Eq. (7) to the data points (red curve), the T_2 associated with this voxel was determined to be 40 ms.

Spin-lattice relaxation, on the other hand, relates to the rate at which the longitudinal component of **M** returns to thermal equilibrium after the system has been excited by the application of rf pulses [15, 53]. In the absence of rf pulses, the rf energy used to disturb nuclear spin magnetisation from equilibrium slowly returns to the surrounding system (i.e., the lattice) and the precessing spins re-establish their initial orientation distribution about $\mathbf{B}_0$ [15, 16]. Assuming that spins were rotated in the

transverse plane using a $\pi/2$ rf pulse, Eq. (6) can be rewritten in terms of longitudinal magnetisation to show that the relationship between the MR signal intensity and T_1 is given by [56]

$$S(t) = S(0)\left(1 - \exp\left(-\frac{t}{T_1}\right)\right). \tag{8}$$

As spin-lattice relaxation is linked to the recovery of the longitudinal component of **M**, T_1 is related to the repetition time (TR) of the MR pulse sequence, where the TR is the period between the first rf pulse of a MRI pulse sequence and the first rf pulse of a following MRI pulse sequence. $S(t)$ will hence be only maximised if TR is sufficiently long to ensure the MR signal fully relaxes before the following MRI pulse sequence begins; consequently, Eq. (8) is often rewritten in terms of TR, instead of t. Spin-lattice relaxation weighted images can be acquired using a CPMG MRI pulse sequence (Figure 12) if the TR is varied between acquired images instead of TE [56]. By acquiring several spin-lattice weighted MR images at different TR, the MR signal intensity data can be fit to Eq. (8) to calculate the T1 per voxel (Figure 15) and in turn create a map of spatially varying T_1 (i.e., a T_1 image).

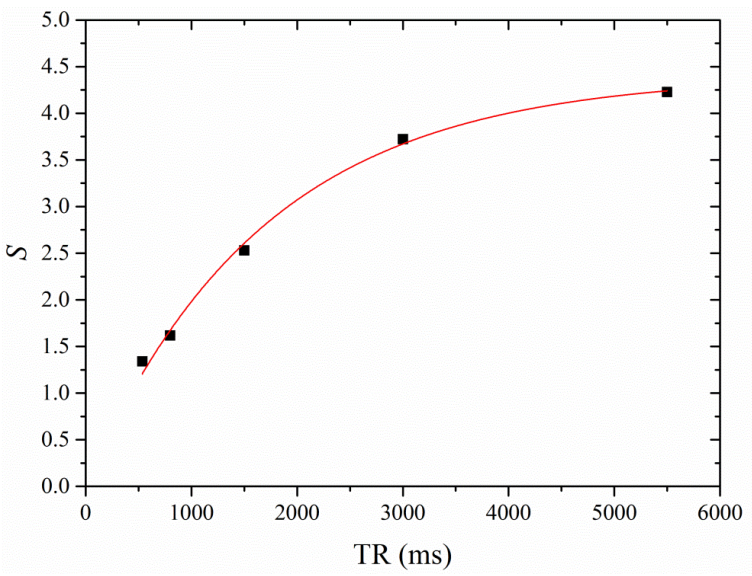

Figure 15: The increase of the MRI signal intensity values (■) of a single voxel with increasing TR due to spin-lattice relaxation during the MRI pulse sequence. Upon fitting Eq. (8) to the data points (red curve), the T_1 associated with this voxel was determined to be 1675 ms.

2.6.1 Paramagnetic relaxation contrast agents

Introducing a paramagnetic relaxation contrasts agent to a system is a common method for increasing relaxation contrast between different regions of an MR image [16, 57, 58]. Paramagnetic relaxation contrasts agents are ions or compounds which possess one or more unpaired electrons. As unpaired electrons possess a strong magnetic moment, the presence of paramagnetic relaxation contrasts agents result in greater variations in the local magnetic field, causing nearby spins to relaxing more rapidly [15, 59]; even when these contrast agents are present in micromolar quantities, they can noticeably increase the relaxation rates of a sizeable quantity of mobile spins.

Paramagnetic relaxation contrast agents affect both spin-spin and spin-lattice relaxation, although the extent each relaxation pathways is affected depends upon the magnetic and motional properties of the constant agent in question. This often dictates the use of the contrast agent. For example, iron oxide crystals are commonly used to increase the spin-spin relaxation rates of surrounding spins, while manganese and gadolinium are used to increase spin-lattice relaxation rates [16, 57, 58]. Paramagnetic relaxation contrast agents have employed in previous biomedical studies in order to examine traumatic brain injury [60, 61], perform auditory brain mapping [62, 63] and to enhance the contrast between healthy and cancerous tissues [64, 65]. The use of relaxation contrast agents in grape berries will be explored later (see Chapter 9 - The diffusive transport of manganese in the grape berry). In addition to spin-density and relaxation, MR images can also be weighted by the displacement of spins via translational self-diffusion. As will be discussed in the following, diffusion-weighted MR images are an excellent source of information regarding the morphology and physiology of biological systems.

Chapter 3 - The fundamentals of diffusion MRI

A number of the studies within this thesis involve the analysis of diffusion-weighted MR images in order to characterise the morphology of botanical specimens. To aid in later discussion and the interpretation the diffusion-weighted MR data, this chapter contains a review of diffusion and its relationship to MRI.

3.1 Diffusion processes

Diffusion is one of several transport processes found in nature. It leads to the incoherent transport of mass and molecular mixing without bulk motion of liquids and gases, where examples of bulk motion include convection and flow [45, 66, 67]. There are two distinct types of diffusion that will be discussed in this work; mutual diffusion and translational self-diffusion. While the particular MRI techniques discussed in this thesis only measure translational self-diffusion, the mathematical formalism used to describe mutual diffusion forms the basis of the formalism used to characterise translational self-diffusion. It is therefore important to explore mutual diffusion further.

Mutual diffusion is the net transport of particles through a system due to the presence of a macroscopic chemical concentration gradient (i.e., a difference in chemical concentration with respect to position in the system. Figure 16A) [45, 66, 67]. Osmosis is a special case of mutual diffusion, which occurs due to a difference in chemical concentration across a semi-permeable membrane [68-70]. While MRI is primarily employed to study translational self-diffusion, mutual diffusion can be measured using MRI in certain cases [71, 72].

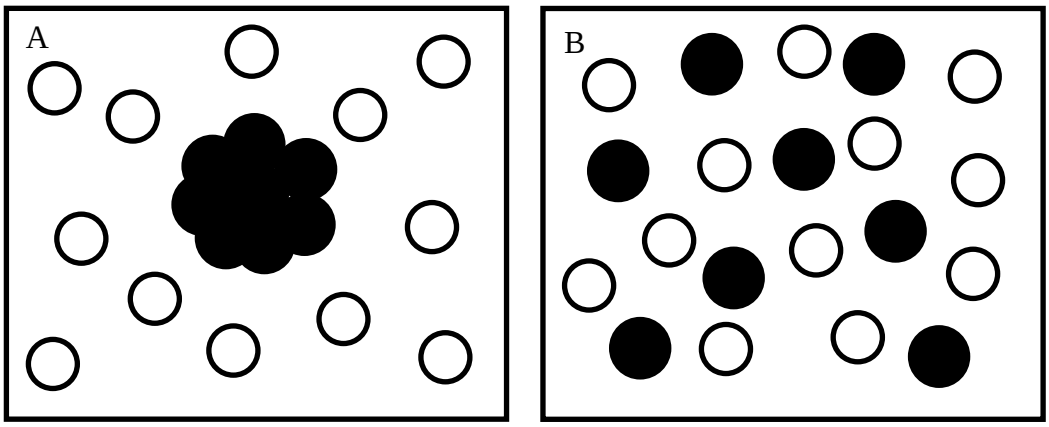

Figure 16: The mutual diffusion of a drop of ink particles (●) and water molecules (○). (A) The ink particles are initially concentrated at a single point. (B) The concentration gradient will drive the mutual diffusion of the ink. Over time, a homogenous solution of ink and water will form, reducing the chemical concentration gradient to zero and terminating the mutual diffusion process. Self-diffusion of both particles is however still operative.

The process of mutual diffusion can be described using the laws proposed by Adolph Fick. Fick's first law is expressed as [45, 66, 67]

$$\mathbf{J}(\mathbf{r},t) = -D_M \nabla C(\mathbf{r},t) \tag{9}$$

where **J** is the net flux of freely diffusing particles (a function of particle position, **r**, and time, t), ∇ is the del operator (defined in Cartesian coordinates by $\nabla = (\partial/\partial x, \partial/\partial y, \partial/\partial z)$, C is the particle concentration or density, and D_M is a constant of proportionality termed the mutual diffusion coefficient. D_M is a useful measure for making comparisons between different systems of two (or more) mutually diffusing chemical species. Systems with higher diffusion coefficients are more likely to have a greater degree of mixing than those with lower diffusion coefficients during the same period of diffusion. For example, at 30 °C the D_M of a trace amount of hydrogen gas carried by nitrogen gas is 0.82×10^{-4} m^2 s^{-1} [73] while the D_M of a 0.1 M aqueous solution of glucose is 0.74×10^{-9} m^2 s^{-1} [74]. As the particles within the system diffuse the concentration of particles at a given point inside the system will change with time. Since mass must be conserved, the continuity equation applies [45, 66, 67]. Thus

$$\frac{\partial C(\mathbf{r},t)}{\partial t} + \nabla \mathbf{J}(\mathbf{r},t) = 0 \,. \tag{10}$$

Substituting Eq. (9) into Eq. (10) results in Fick's second law [66, 67, 75],

$$\frac{\partial C(\mathbf{r},t)}{\partial t} = D_M \nabla^2 C(\mathbf{r},t) \tag{11}$$

where ∇^2 is the Laplace operator. The rate of change in concentration will hence slow as time progresses and the solution becomes increasingly homogeneous; as $t \to \infty$, the concentration of the diffusing substance will be equal throughout the system and the mutual diffusion process will end (Figure 16B) [66, 67].

Translational self-diffusion (henceforth simply referred to as diffusion) is particle motion arising from collisions between neighbouring, thermally agitated particles [76, 77]. The displacement of each particle in the ensemble is random (Figure 17), and unlike mutual diffusion it continues as $t \to \infty$.

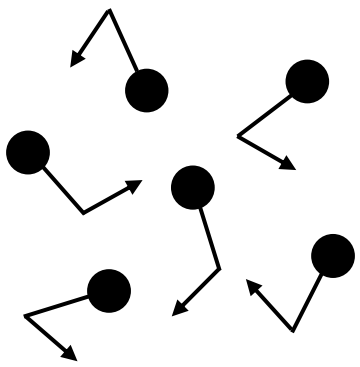

Figure 17: An ensemble of thermally agitated particles (●) undergoing translational self-diffusion. Although no chemical concentration gradients exist, the collisions between neighbouring particles cause incoherent movements (as indicated by the paths of the arrows).

Since the motion of the particles is undirected the net displacement of the ensemble will be zero. Therefore it is more useful to consider the statistical motion of the ensemble [45, 77]. A key concept required for this analysis is the conditional probability density function, $P(\mathbf{r}_0,\mathbf{r}_1,t)$. This function describes the probability of finding a particle at a final position $\mathbf{r}_1$, after diffusion time t, having started from an

initial position $\mathbf{r}_0$. For a large number of particles, the total probability of find one of these particles at $\mathbf{r}_1$ at time t is given by [45, 78, 79]

$$P(\mathbf{r}_1,t)=\int \rho(\mathbf{r}_0)P(\mathbf{r}_0,\mathbf{r}_1,t)\,d\mathbf{r}_0 \ . \tag{12}$$

where $\rho(\mathbf{r}_0)$ is the initial distribution of particles. In this context, $P(\mathbf{r}_0,\mathbf{r}_1,t)$ is also known as the diffusion propagator.

$P(\mathbf{r}_1,t)$ is a measure of the labelled particle density. Thus if it is assumed that $C(\mathbf{r}_1,t)$ represents the concentration of labelled particles, $P(\mathbf{r}_1,t)$ can be substituted for $C(\mathbf{r}_1,t)$ in Eqs. (9) and (11). Due to the relationship between $P(\mathbf{r}_1,t)$ and the diffusion propagator, it follows that Fick's laws can also be rewritten in terms of $P(\mathbf{r}_0,\mathbf{r}_1,t)$, providing that all diffusing particles are located at $\mathbf{r}_0$ when $t = 0$ (i.e., $P(\mathbf{r}_0,\mathbf{r}_1,0) = \delta(\mathbf{r}_1 - \mathbf{r}_0)$, where $\delta(\cdot)$ is the delta function) [45, 79]. Rewriting Eqs. (9) and (11) in terms of $P(\mathbf{r}_0,\mathbf{r}_1,t)$ respectively yields

$$\mathbf{J}(\mathbf{r}_0,\mathbf{r}_1,t)=-D\nabla P(\mathbf{r}_0,\mathbf{r}_1,t) \tag{13}$$

and [45, 80, 81]

$$\frac{\partial P(\mathbf{r}_0,\mathbf{r}_1,t)}{\partial t}=D\nabla^2 P(\mathbf{r}_0,\mathbf{r}_1,t). \tag{14}$$

where $\mathbf{J}(\mathbf{r}_0,\mathbf{r}_1,t)$ is the flux of the diffusion propagator and D is the diffusion coefficient. D is analogous to D_M. However, D characterises the diffusivity of only one diffusing chemical species. For example, water molecules in bulk solution at room temperature have a D of 2.3×10^{-9} m^2 s^{-1} [82]. The diffusion of sugar molecules in a 0.15 M aqueous glucose solution is 0.55×10^{-9} m^2 s^{-1}; the water of that same aqueous solution, on the other hand, will have a D of 1.81×10^{-9} m^2 s^{-1} [83].

Eq. (14) can then be solved to yield an analytical expression for $P(\mathbf{r}_0,\mathbf{r}_1,t)$. In the case of one-dimensional free diffusion, this solution will have the form of a Gaussian function [45, 80, 81], i.e.,

$$P(\mathbf{r}_0,\mathbf{r}_1,t)=\frac{1}{\sqrt{4\pi Dt}}\exp\left(-\frac{(\mathbf{r}_1-\mathbf{r}_0)^2}{4Dt}\right). \tag{15}$$

However this expression is the solution for free diffusion; it assumes that the diffusing particles encounter no physical obstacles, barriers or other microstructures which restricts their motion. The effect of diffusion restriction on particle displacement amounts to applying different boundary conditions to Eq. (14), as will be discussed further below (see Section 3.2 The effect of restriction on diffusion).

Although it is initially useful to describe particle motion as a displacement from $\mathbf{r}_0$ to $\mathbf{r}_1$ in time t, it is more convenient for future calculations to instead consider particle motion in terms of a certain displacement, $\mathbf{R}$, from $\mathbf{r}_0$ in time t (i.e., $\mathbf{r}_1 = \mathbf{r}_0 + \mathbf{R}$). Rewriting Eqs. (12) and (15) in this new formalism yields [45, 78, 79]

$$\bar{P}(\mathbf{R},t) = \int \rho(\mathbf{r}_0) P(\mathbf{r}_0, \mathbf{r}_0 + \mathbf{R}, t)\, d\mathbf{r}_0 \tag{16}$$

and [45, 80, 81]

$$\bar{P}(\mathbf{R},t) = \frac{1}{\sqrt{4\pi Dt}} \exp\left(-\frac{\mathbf{R}^2}{4Dt}\right) \tag{17}$$

where $\bar{P}(\mathbf{R})$ is the ensemble averaged propagator (EAP). Since the EAP is a probability function [45, 79],

$$\int \bar{P}(\mathbf{R},t)\, d\mathbf{R} = 1\,. \tag{18}$$

By including the squared displacements of the diffusing particles in this integration, the mean squared displacement (MSD) of the ensemble can be calculated [45, 79, 84],

$$\left\langle \mathbf{R}^2 \right\rangle = \int \mathbf{R}^2 \bar{P}(\mathbf{R},t)\, d\mathbf{R} \tag{19}$$

where $\langle . \rangle$ denotes the mean. Upon substituting Eq. (17) into Eq. (19), it can be readily calculated using the standard integral (e.g., 3.462.8 in [85]) that the MSD of an ensemble of particles freely diffusing along one dimension has the following linear relationship with time [45, 80, 81],

$$\left\langle \mathbf{R}^2 \right\rangle = 2Dt\,. \tag{20}$$

When Eq. (19) is solved for the n-dimensional free diffusion EAP, the linear relationship between the MSD and t will be maintained, i.e.,

$$\left\langle \mathbf{R}^2 \right\rangle = 2nDt\,. \tag{21}$$

Taking the square root of Eq. (21) yields the ensemble averaged particle displacement [45, 80, 81], also known as the root mean squared displacement (RMSD)

$$\left\langle \|\mathbf{R}\| \right\rangle = \sqrt{2nDt}\,, \tag{22}$$

where $\|.\|$ denotes the normal. For example, it can be calculated using Eq. (22) that water molecules in bulk solution at room temperature freely diffusing in three-dimensions over a period of 50 ms will have an RMSD of ~26 μm.

3.2 The effect of restriction on diffusion

Diffusion restricting microstructures hinder the movement of diffusing particles [45, 67]. For example, in a biological system these microstructures can include cellular membranes/structures [86, 87] and aggregated proteins [88, 89]. The presence of these obstructions will result in an overall reduction of particle displacement relative to their displacement in a bulk solution. This reduction will become more pronounced as t increases and the probability of particles encountering one for more restricting boundaries becomes higher [45, 67].

As the particles interact with restricting microstructures, the displacements of these particles are dependent on the local system structure (e.g., its shape and dimensions) in addition to t [45, 67]. It is this dependence that allows diffusion NMR and MRI to characterise the microstructure of diffusion restricting systems. As t approaches the long-time limit (i.e., $t \gg d^2/D$, where d is the average distance between restricting microstructures) the diffusing particles will have sufficient time to probe the entire volume of the structure that encloses them [45, 90, 91]. At this point the displacement of the particle ensemble becomes independent of t and solely reflects the structural features of the restricting system.

The local orientations of diffusion restricting microstructures can be determined from measurements of particle displacement. This can be achieved by comparing measurements of particle mobility along a large number of different directions.

When diffusion displacements are equal with respect to all directions, this is termed isotropic diffusion (Figure 18A). Diffusion isotropy is expected when tissue microstructures are not coherently organised within voxels, as is often observed in MR images of brain grey matter [86, 92].

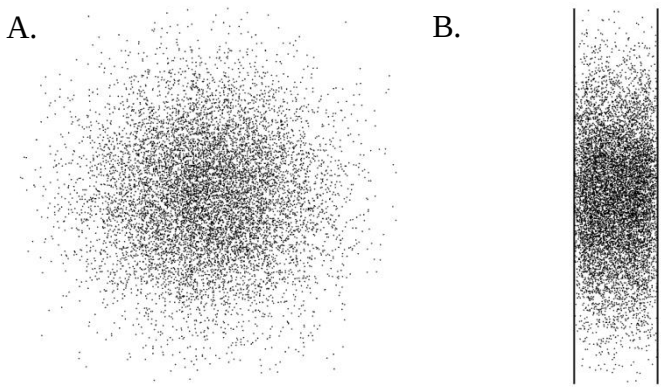

Figure 18: Two dimensional simulations of isotropic (A) and anisotropic (B) diffusion. (A) The distribution of particles (●) remains even with respect to direction. (B) The distribution of particles possesses a directional dependence due to the encapsulating parallel barriers. These figures were created by simulating the random walks of 10 000 particles, each undertaking 100 steps.

If measurements of particle displacement indicate that motion is not restricted equally with respect to direction, this is termed anisotropic diffusion (Figure 18B). Anisotropic diffusion signifies that the restricting microstructure is coherently organised on the length scale of the voxel. The direction(s) of least displacement restriction likely indicate direction(s) where the restricting microstructure is elongated. Thus knowledge of diffusion anisotropy in a diffusion restricting system can be used to determine the prevalent orientation of organised restricting microstructures [86, 93, 94]. For example, anisotropically restricted diffusion has been previously observed in brain white matter and skeletal tissue where the direction of least diffusion was parallel to the orientation of the tissue fibre [86, 87]. As diffusion anisotropy provides an insight the coherency and orientation of cellular and tissue microstructures, it will prove useful later when characterising the morphology of grape berries via MRI (see Chapter 7 - Diffusion MRI of grapes at different stages of development).

3.3 Measuring diffusion using magnetic field gradients

Diffusion MRI is typically conducted using the pulsed gradient spin-echo (PGSE) nuclear magnetic resonance sequence [45, 95], a modification of the Hahn spin-echo sequence (Figure 19).

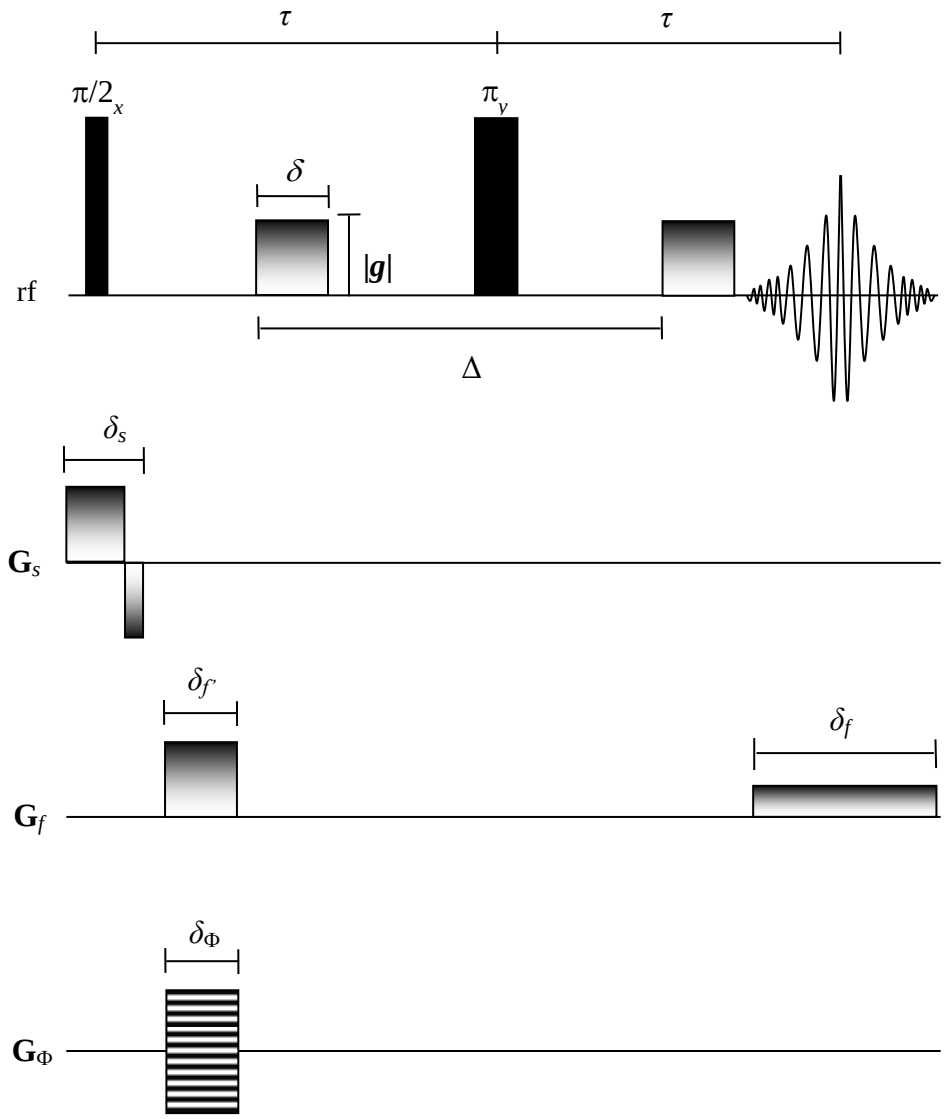

Figure 19: A simplified pulse sequence for pulsed gradient spin-echo (PGSE) MRI sequence. This pulse sequence is similar to the spin-density MRI pulse sequence presented earlier (Figure 7) except that it includes an identical pair of diffusion magnetic field gradients spaced about the π rf pulse in order to weight acquired MR images with diffusion. The duration of the diffusion magnetic gradients, δ, is typically milliseconds in length while the diffusion period, Δ, is tens to hundreds of milliseconds in length.

First, a π/2 rf pulse is used to establish a net spin polarisation perpendicular to the static magnetic field. Shortly thereafter, the diffusion encoding gradient is applied. The purpose of the diffusion encoding gradient is to spatially label the starting and final positions of an ensemble of spins along **g**, much like how they can be used to spatially encode MR images, in order to weight the MR image with the displacement of an ensemble of spins. The effect is particularly easy to visualise in the short gradient pulse (SGP) limit [96], when δ approaches an infinitely small length while the product of δ and $|\boldsymbol{g}|$ remains finite as motion during the diffusion gradient pulse can be ignored. While this is of course technically impossible, this condition can be reasonably approximated if $\delta \ll \Delta$ and $\delta \ll d^2/D$ [45, 95, 97]. Due to the applied gradient pulse, the phase of each spin, ϕ_0, becomes

$$\phi_0 = \gamma\delta B_0 + \gamma\int_0^{\delta} \mathbf{g}\cdot\mathbf{r}_0 \, dt = \gamma\delta B_0 + \gamma\delta\mathbf{g}\cdot\mathbf{r}_0 \,. \tag{23}$$

As a result, the spin magnetisation vectors are arrayed in the shape of a helix along the direction of **g** (Figure 20).

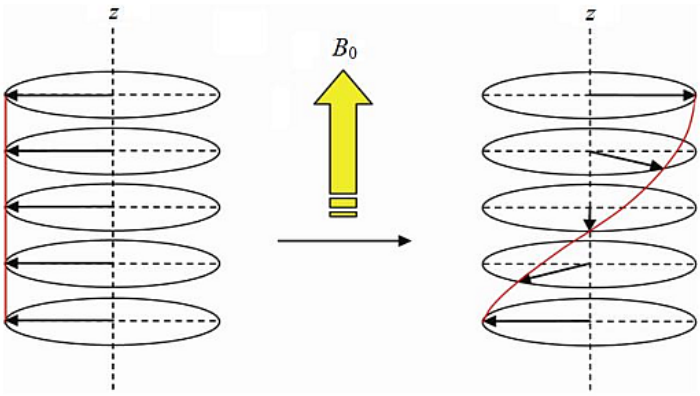

Figure 20: Effect of a gradient pulse on spin phase. Before the application of the gradient pulse, there is no difference in the phase between spins (left) and thus the magnitude of the transverse magnetisation (i.e., vector sum) is maximised. After the application of the magnetic gradient, **g** (represented by the yellow arrow), the phase of each spin in the ensemble changes due to the variation in the magnitude of the gradient pulse along the magnetic field axis. This causes the spin ensemble to adopt a helical shape (right) resulting in a loss of net magnetisation.

After a period of time, a second rf (π) pulse is used to reverse the phase of each spin in the ensemble. This results in a helix of spins which is a mirror image of the first,

although now attenuated as a result of the mixing of spins with different phases due to diffusive translational motion [45, 90, 96].

The diffusion encoding gradient is then applied, unwinding the helix and re-establishing a net transverse magnetisation and allowing the measurement of the attenuated, diffusion-weighted MR signal; the effect of the second diffusion gradient on the phase of each spin, ϕ_1, is given by [45, 96]

$$\phi_1 = \gamma B_0 \delta + \gamma \int_{\Delta}^{\Delta+\delta} \mathbf{g} \cdot \mathbf{r}_1 \, dt = \gamma B_0 + \gamma \delta \mathbf{g} \cdot \mathbf{r}_1 . \tag{24}$$

Therefore the net phase shift, $\Delta\phi$, for each spin is

$$\Delta\phi = \phi_1 - \phi_0 = \gamma \delta \mathbf{g} \cdot \left(\mathbf{r}_1 - \mathbf{r}_0 \right). \tag{25}$$

As spin displacement parallel to **g** is random, $\Delta\phi$ varies between spins. It is the averaging of $\Delta\phi$ over the spin ensemble that leads to an attenuation of the acquired MR signal [45, 55]. The attenuation of the measured MR signal will increase with increasing spin displacement and thus the length of the diffusion measurement (see Eq. (22)). The length of the diffusion measurement (or period), Δ, is defined as beginning at the leading edge of the first diffusion encoding gradient and ending at the leading edge of the second diffusion encoding gradient (Figure 19).

Increasing Δ will increase the length-scale probed by the diffusing spins [45, 90, 91]. Increasing the strength of the magnetic gradient, on the other hand, will improve the resolution of the diffusion measurements. This is because stronger diffusion encoding gradients will tighten the winding of the magnetisation helix. As a result even relatively small displacements can have a noticeable effect on the attenuation of the MR signal, allowing the restricting effect of smaller microstructures to contribute [45, 96]. Uniform flow will not affect the attenuation of the measured MR signal, even though it will result in a net shift of the spin phase of all spins in the sample. This is because this coherent form of particle motion will result in a net displacement of the spins [45, 90]. Making the reasonable assumption that the flow velocity, **v**, of a diffusing particle remains constant over the length of the displacement, the initial position of a spin is $\mathbf{r}_0 + \mathbf{v}t$ while its final position is $\mathbf{r}_1 + \mathbf{v}t$. Substituting these new positions into Eq. (25) results in the $\mathbf{v}t$ components cancelling; the magnetisation helix is simply translated along the direction of **v**.

One drawback of the design of the PGSE MRI sequence is that spin-spin relaxation will result in a continuous loss of signal during the τ periods, and that TE is longer than Δ [45, 90, 96]. Therefore increasing Δ to increase the length-scale probed by diffusing spins (see Eq. (22)) will require lengthening TE, resulting in further MR signal loss from spin-spin relaxation. If a suitable balance between MR signal intensity and the length-scale probed by diffusing spins becomes difficult to achieve, a pulsed-gradient stimulated (spin-) echo (PGSTE)-based sequence [45, 98] can be used instead (Figure 21).

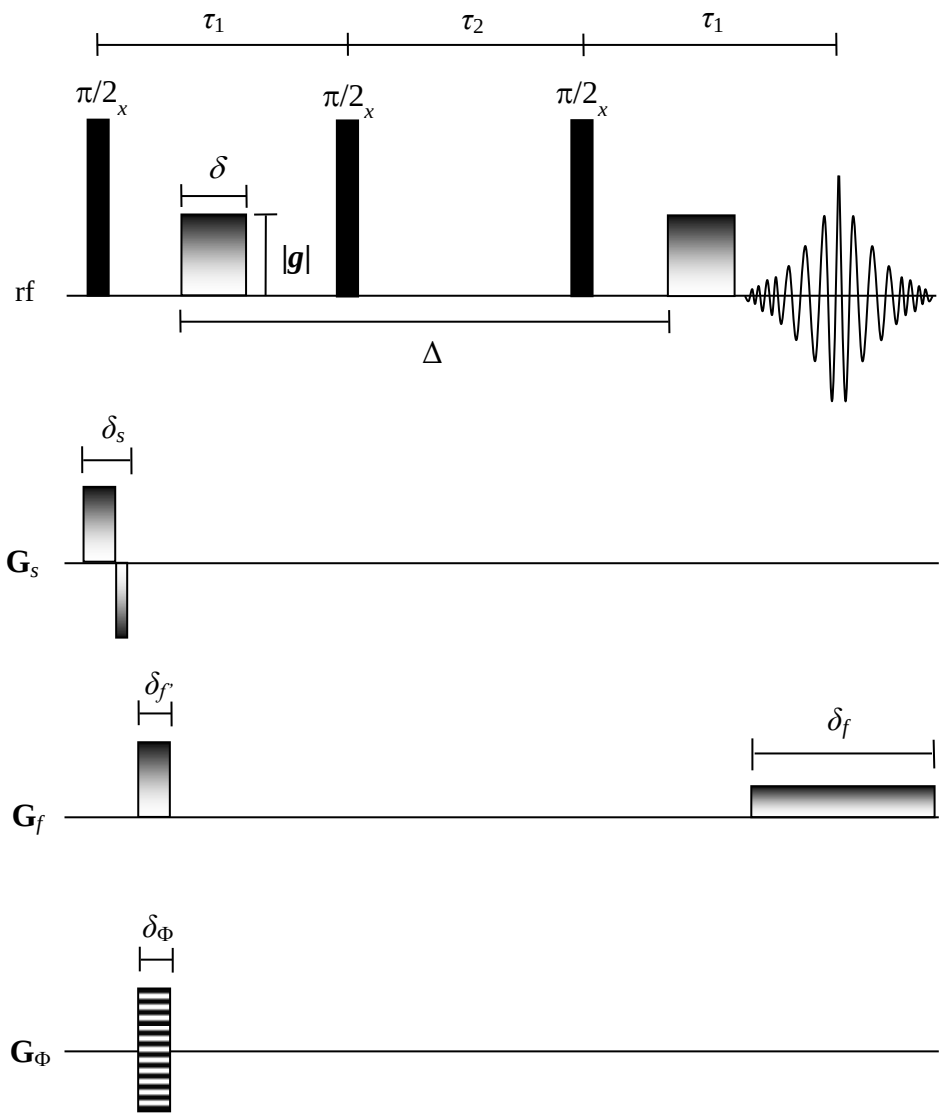

Figure 21: A simplified pulse sequence for pulsed gradient spin-echo (PGSE) MRI sequence. This pulse sequence is differs from the PSGE MRI pulse sequence presented earlier (Figure 19) except it replaces the π rf pulse with an identical pair $\pi/2$ rf pulses. Consequently the loss of MR signal during the diffusion period is largely due to spin-lattice, rather than spin-spin, relaxation.

PGSTE is a modification of the PGSE sequence in which the π pulse is replaced by $\pi/2–\tau_2–\pi/2$ (with τ being relabelled to τ_1) [45, 98]. After the first diffusion encoding gradient, a π/2 rf pulse is used to reorient the spatially labelled spin magnetisation vectors so that they lie parallel to the static magnetic field. As a result, the spin ensemble is largely subjected to spin-lattice relaxation during Δ rather than spin-spin relaxation. However, the PGSTE sequence only refocusses half of the available transverse magnetisation. Consequently, neglecting losses due to relaxation, the measured MR signal intensity will be only half that of a Hahn-echo sequence [45, 98]. Thus PGSTE is most useful for diffusion studies involving large/slowly reorientating molecules, such as studies of protein binding/aggregation [45, 99] or when $T_1 \gg T_2$ and Δ must be longer than T_2 to in order to probe diffusion restricting microstructures (see 7.4.2 Analysis of the mature olive MRI experimental results).

3.4 *q*-space imaging

During the acquisition of the MR signal, the raw MR diffusion data is temporarily stored in a mathematical space known as *q*-space. This mathematical space is analogous to *k*-space, however spin-displacement data is being stored instead of spin-density data. In *q*-space, the wave vector $\mathbf{q} = (1/2\pi)\gamma\delta\mathbf{g}$ relates the diffusion-weighted MR signal to the diffusion propagator via the following Fourier transform [45, 100],

$$E(\mathbf{q}) = \int \bar{P}(\mathbf{R}) \underbrace{\exp\left(2\pi i \mathbf{q}\cdot\mathbf{R}\right)}_{\mathfrak{W}} d\mathbf{R} \tag{26}$$

where E is the attenuated diffusion-weighted signal and $\mathfrak{W}$ is the plane wave of the Fourier transform. Depending on the magnitude and direction of **q**, different points of *q*-space will be sampled; the magnitude of **q** (i.e., *q*) determines the distance of the point sampled from the centre of *q*-space (located at **q** = 0) while the orientation of **q** indicates the direction of the sampled point relative to the centre of *q*-space.

It can be inferred from Eq. (26) that by sampling a sufficient number of unique points in *q*-space (i.e., $E(\mathbf{q})$ values), the EAP can be reconstructed via an inverse Fourier transform [45, 100]. However, the Fourier transform requires that *q*-space must be sampled at each point of a dense, three-dimensional Cartesian lattice (Figure

22A) [101]. Unfortunately, sampling *q*-space in this manner would require the acquisition of hundreds of diffusion-weighted MR images, resulting in prohibitively long image acquisition times. As a consequence, a number of three-dimensional diffusion MRI techniques estimate the EAP using a variation of Eq. (26) to process diffusion data acquired using a more time efficient sampling scheme. These techniques commonly sample *q*-space using high angular resolution diffusion imaging (HARDI) schemes involving one or more *q*-shells [102, 103]. A *q*-shell is a user-defined sphere in *q*-space with a radius of *q*. By sampling points on a number *q*-shells, the angular (i.e., the anisotropy) and radial (i.e., the shape) components of the EAP can be estimated using far fewer points than a three-dimensional Cartesian lattice.

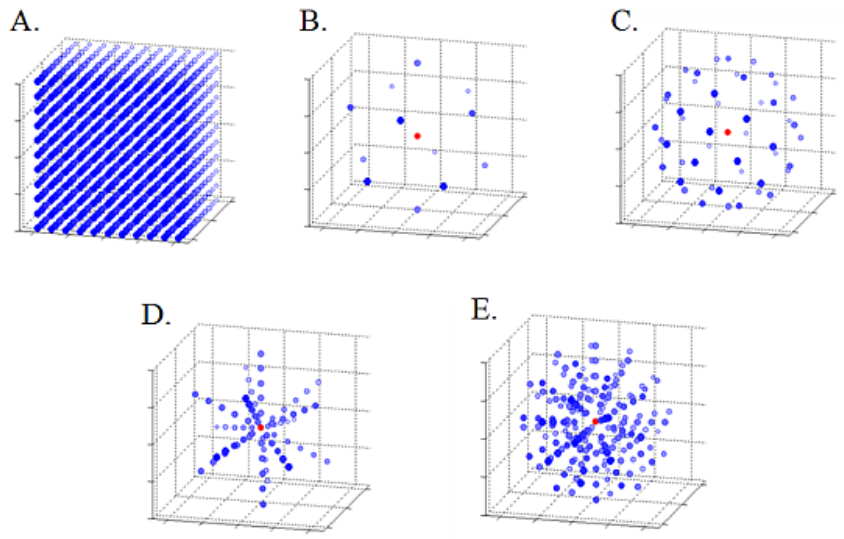

Figure 22: Examples of *q*-space sampling schemes. (A) Cartesian lattice sampling, (B) low angular resolution sampling on a single *q*-shell, (C) high angular resolution sampling on a single *q*-shell, (D) high radial/low angular resolution sampling on multiple *q*-shells, (E) high radial/high angular resolution sampling on multiple *q*-shells. The size and shade of the markers indicates their relative depth in the image. The origin of *q*-space is indicated by a red dot. The dimensional axes of *q*-space are measured in m^{-1}.

The accuracy of the estimation of the angular and radial component of the EAP depends on the number of points sampled on each *q*-shell and the total number of *q*-shells that are sampled. For exampling, increasing the density of points sampled on the *q*-shell will better recover the angular component of the EAP, improving the estimation of the orientation of the local diffusion restricting microstructure (Figure 22B and C). Increasing the number of *q*-shells sampled, on the other hand, will improve the recovery of the radial component of the EAP (Figure 22D and E).Since the diffusion-weighted MR signal profile is antipodally symmetric (i.e., $E(\mathbf{q}) = E(-\mathbf{q})$), acquiring antipodal points in *q*-space will not yield additional information regarding diffusion anisotropy. However, antipodal sampling will help reduce the effect of cross-term interactions between the diffusion gradients and the image gradients, therefore reducing an unwanted source of MR signal attenuation [22, 104].

3.5 Characterising probability distributions

This chapter concludes with a discussion on how the EAP, being a distribution of probability, can be characterised using a number of useful scalars known as cumulants. Cumulants are related to the moments of a distribution, and can be used to quantify the shape of a set of points; the EAP is related to the complex cumulant generating function via the relation [105]

$$\exp\left(\sum_{n=0}^{\infty}\kappa_n\frac{(2\pi iq)^n}{n!}\right)=\int\bar{P}(\mathbf{R})\exp\left(2\pi i\mathbf{q}\cdot\mathbf{R}\right)d\mathbf{R} \tag{27}$$

where κ_n is the *n*-th cumulant of the expansion. The first cumulant of the series, κ_1, is the mean of the distribution, and indicates the net displacement of the diffusing particle ensemble [106]. As previously explained, the net displacement of a diffusing particle ensemble will be zero. The second cumulant, κ_2, is the variance of the EAP, which is also the MSD of the particle ensemble [106, 107]. The third cumulant, κ_3, indicates the skewness of the EAP; an EAP that is skewed (i.e., $\kappa_3 \neq 0$) will be an asymmetric distribution [106, 107]. Skewness is difficult to accurately measure using diffusion MRI (see Appendix A - Generalised diffusion tensor imaging) and as a

result, the skewness of the diffusion propagator is typically assumed to be zero. The fourth cumulant, κ_4, reflects the kurtosis of the EAP and describes the 'peakedness' of the EAP [80, 106, 107]. When diffusion is restricted, kurtosis will be non-zero. As the density of microstructures within a restricted system increases, the distance between these structures decreases. As a result, smaller particle displacements become relatively more likely than larger displacements and the diffusion propagator will become narrower (i.e., the peak of the distribution becomes sharper) [108]. Examples of how the shape of the EAP are described using these four cumulants are presented below (Figure 23). While cumulants beyond these four exist, they do not have an intuitive physical meaning.

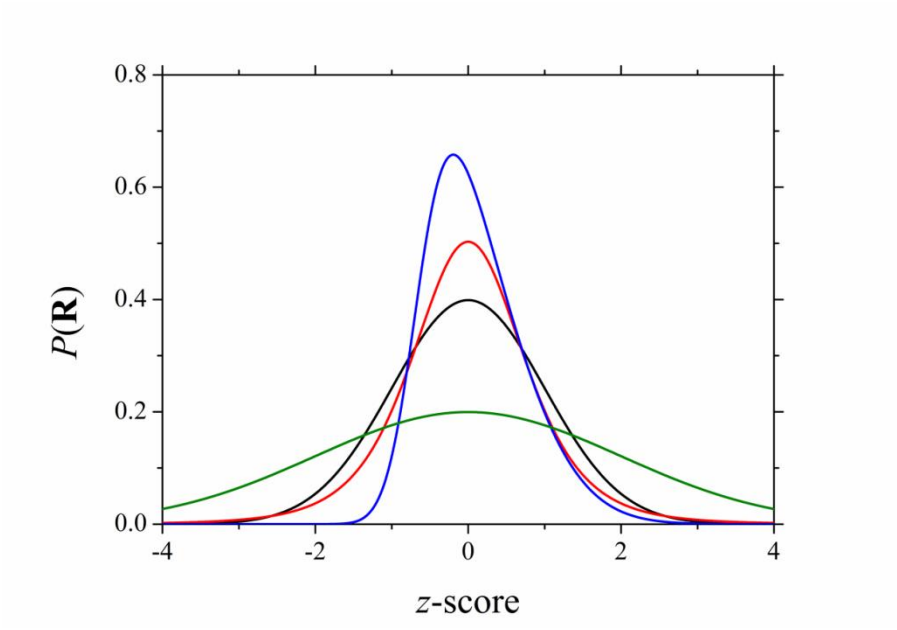

Figure 23: Describing the shape of the EAP using cumulants. Here several distributions have been provided which have a mean of zero (κ_1 = 0) and the same area under the curve. Both the green and black distributions are Gaussian (κ_3 = 0 and κ_4 = 0). However, the green distribution has a greater variance than the black distribution (κ_2 = 2 and κ_2 = 1, respectively). The blue distribution is asymmetrical and thus is skewed (κ_3 = 3). The red distribution, on the other hand, has a sharpened peak relative to the Gaussian distributions, and thus has higher kurtosis (κ_4 = 10).

Chapter 4 - Diffusion magnetic resonance imaging techniques

Having reviewed the fundamental principles of diffusion MRI, a method for processing the MR diffusion data must be selected which will be appropriate for the needs of the present work. There are a great many diffusion MRI techniques available. A generous selection of these are reviewed in the appendix (see Appendix A), detailing the core principles that underpin these methods, their minimum requirements, advantages, limitations, as well as how components of the diffusion data can be visualised. Each diffusion MRI technique has associated advantages and limitations, and is suited to different circumstances. A flowchart summarising the selection of an appropriate diffusion MRI technique for different criteria has been provided below (Figure 24).

For the studies within this thesis, the selection of a diffusion MRI technique to analyse the acquired diffusion MR data was based on its performance in three key areas; its accuracy in reconstructing cell/tissue orientation, its computational robustness and its ability to process noisy diffusion MR data. After considering the pool of diffusion MRI techniques available, two candidates were short listed; diffusion tensor imaging (DTI) and Bessel Fourier reconstruction (BFOR) imaging. DTI is a well-established and popular diffusion MRI technique; it solves the Bloch-Torrey equation to determine the effect of diffusion on the net spin magnetisation. BFOR imaging is a relatively recent diffusion MRI technique which solves Eq. (26) to determine the diffusion propagator from the diffusion-weighted MR signal. To aid later discussion and analysis of the diffusion MR data, the theory for both of these diffusion MRI techniques is presented in this chapter.

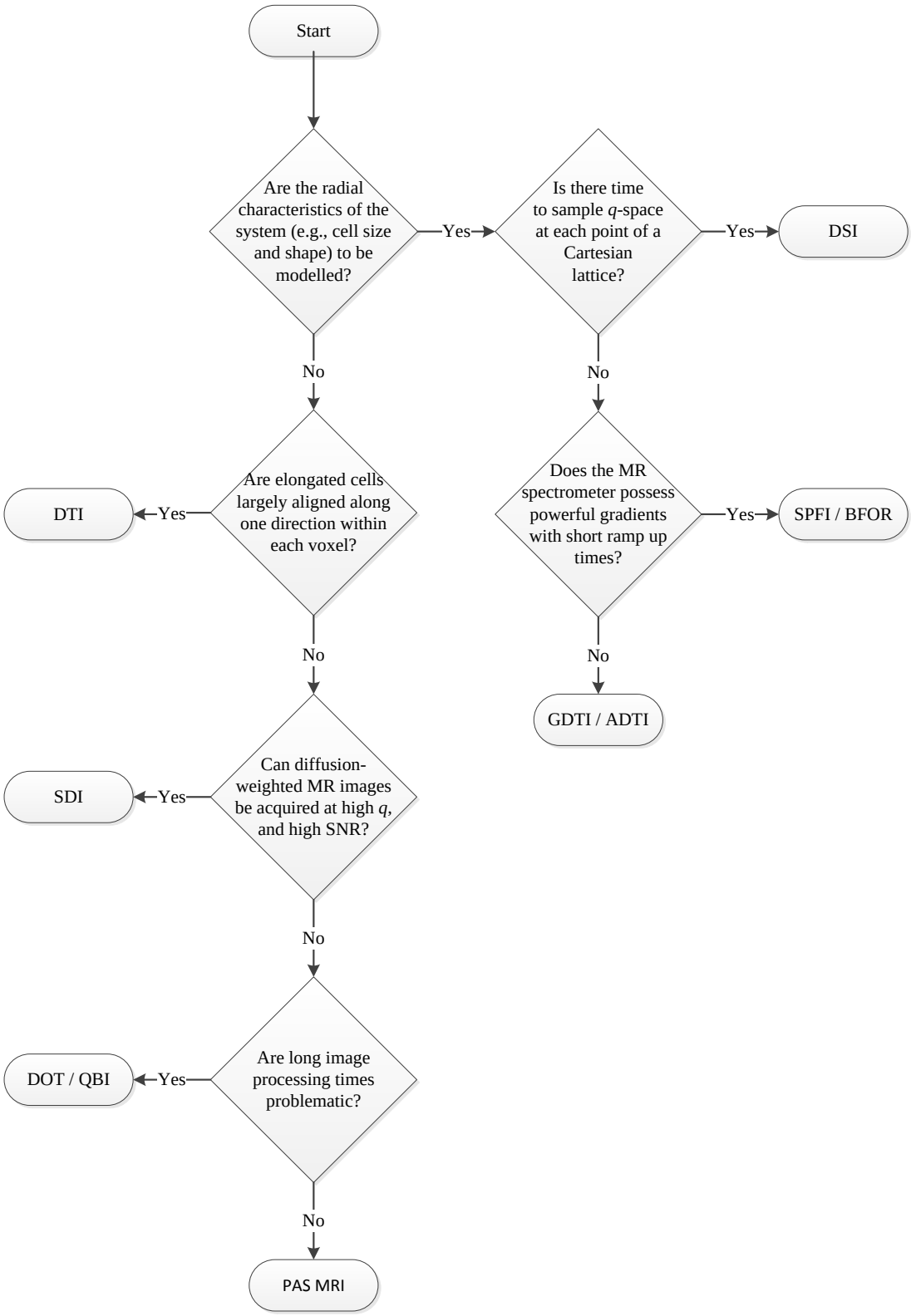

Figure 24: A flowchart showing the selection of an appropriate diffusion MRI technique for a given set of conditions. This chart includes diffusion tensor imaging (DTI), spherical deconvolution imaging (SDI), diffusion orientation transform (DOT), *q*-ball imaging (QBI), persistent angular structure (PAS) MRI, diffusion spectrum imaging (DSI), spherical polar Fourier imaging (SPFI), Bessel Fourier orientation reconstruction (BFOR) MRI, generalised DTI (GDTI), and anomalous DTI (ADTI).

4.1 The Bloch-Torrey equation

The Bloch-Torrey equation is a modification of the Bloch equation (cf. Eq. (6)) which includes terms to account for the effect of diffusion and flow on **M** [109],

$$\frac{\partial \mathbf{M}}{\partial t} = \gamma \mathbf{M} \times \mathbf{B} - \frac{M_x \hat{\mathbf{i}} + M_y \hat{\mathbf{j}}}{T_2} - \frac{\left(M_z - M_0\right)\hat{\mathbf{k}}}{T_1} + D\nabla^2 \mathbf{M} + \nabla \cdot \mathbf{v} \cdot \mathbf{M} . \tag{28}$$

Assuming that there is no flow (i.e., $\mathbf{v} = 0$) and that **B** is parallel to $\hat{\mathbf{k}}$ (i.e., $B_x = 0$, $B_y = 0$ and $B_z = B_0 + \mathbf{g}\cdot\mathbf{r}$), the transverse component of Eq. (28) can be rewritten in terms of $m_{xy} = M_x + iM_y$,

$$\frac{\partial m_{xy}}{\partial t} = -i\gamma B_0 m_{xy} - i\gamma\left(\mathbf{g} \cdot \mathbf{r}\right) m_{xy} - \frac{m_{xy}}{T_2} + D\nabla^2 m_{xy} . \tag{29}$$

m_{xy} relaxes exponentially with time, and Eq. (29) can be readily solved to determine the attenuation of the diffusion-weighted MR signal [45, 95],

$$E\left(g\right) = \frac{S\left(g\right)}{S_0} = \exp\left(-\gamma^2 \delta^2 g^2 \left(\Delta - \frac{\delta}{3}\right) D\right) , \tag{30}$$

where S is the measured diffusion-weighted MR signal intensity, S_0 (= $S(0)$) is the diffusion-unweighted MR signal intensity. The analysis of diffusion MRI data could be simplified by rewriting Eq. (30) as a linear relation, i.e.,

$$\ln E\left(b\right) = -bD . \tag{31}$$

However, due to the inclusion of the natural logarithm in Eq. (31), the effect of MR signal noise will appear more pronounced at high b than at low b. Thus if the $\ln E(b)$ values are not appropriately weighted, there could be significant error associated with the calculated value for D [45, 110]. Consequently, it is preferable to calculate D by fitting Eq. (30) to the diffusion data. Regardless, if Eq. (30) or (31) is used to analysis data from a diffusion restricted system, D will be dependent on δ and Δ in addition to the geometry of local restricting microstructure. In this context, D is an apparent diffusion coefficient (ADC), or more accurately, a time dependent diffusion coefficient [45, 111, 112].

To simplify future calculations, the effective diffusion weighting of the pulse sequence in Eq. (30) will be summarised as a single scalar factor, $b = \gamma^2 g^2 \delta^2 (\Delta - \delta/3)$. For clinical diffusion MRI, a maximum b-value of $1/D$ is typical; for example, when studying the human brain a maximum b-value of 1000-1500 × 10^6 s m^{-2} might be employed [113]. However, some diffusion MRI techniques may require the use of much higher b-values. This will be discussed further when these special cases arise.

4.2 Diffusion tensor imaging

As previously discussed (see Section 3.2 The effect of restriction on diffusion), anisotropic diffusion measurements are highly useful for determining the orientation of coherent restricting microstructures. However, D in Eq. (30) has no directional dependence, and hence does not provide any information regarding diffusion anisotropy. DTI replaces D with a mathematical object known as a tensor [114]. Tensors are special multi-dimensional arrays which are used to express a linear relationship between scalars, vectors or other tensors [115, 116]. Within this thesis the dimensionality of a tensor will be indicated by its order (e.g. a zeroth order tensor is a scalar, a first order tensor is a vector, a second order tensor is a matrix) while the lengths of the columns and/or rows of the tensor will be described by its rank. Unless explicitly stated otherwise, the components of these tensors are described in the laboratory reference frame using x, y and z, and will thus have a column and/or row rank of three.

Tensors are commonly used to establish a linear relation between two vector quantities which do not share the same orientation [115, 116]. For example, scalar D in Eq. (13) can only relate the flux of diffusion probability and the diffusion propagator if $\mathbf{J}(\mathbf{r}_0,\mathbf{r}_1,t)$ and $\nabla P(\mathbf{r}_0,\mathbf{r}_1,t)$ are collinear. However, by replacing D with a symmetric, second-order diffusion tensor, $\mathbf{D}$, Eq. (13) becomes

$$\mathbf{J}\left(\mathbf{r}_0,\mathbf{r}_1,t\right) = -\mathbf{D}\nabla P\left(\mathbf{r}_0,\mathbf{r}_1,t\right)$$

$$\begin{pmatrix} J_{Px} \\ J_{Py} \\ J_{Pz} \end{pmatrix} = \begin{pmatrix} D_{xx} & D_{yx} & D_{zx} \\ D_{xy} & D_{yy} & D_{zy} \\ D_{xz} & D_{yz} & D_{zz} \end{pmatrix} \begin{pmatrix} \dfrac{\partial P}{\partial x} \\ \dfrac{\partial P}{\partial y} \\ \dfrac{\partial P}{\partial z} \end{pmatrix} . \tag{32}$$

The diagonal elements of **D** relate the components of $\mathbf{J}(\mathbf{r}_0,\mathbf{r}_1,t)$ and $\nabla P(\mathbf{r}_0,\mathbf{r}_1,t)$ which are parallel to each other; the off-diagonal components, on the other hand, couple the components of $\mathbf{J}(\mathbf{r}_0,\mathbf{r}_1,t)$ and $\nabla P(\mathbf{r}_0,\mathbf{r}_1,t)$ which are orthogonal to each other [114-116]. As **D** is a symmetric tensor (i.e., $D_{ij} = D_{ji}$), it possesses a subset of six independent elements, D_{xx}, D_{yy}, D_{zz}, D_{xy}, D_{xz}, and D_{yz}, with which it is possible to reconstruct the entire tensor. When the off-diagonal components of the tensor are zero (i.e., the tensor is diagonalised) the diagonal elements of **D** are termed principal diffusion coefficients of the diffusion tensor, and are equivalent to the eigenvalues of the tensor [117]. The nature and determination of the eigenvalues of **D** will be explained in further detail below.

An ADC associated with an arbitrary direction vector $\hat{\mathbf{u}}$ can be determined from **D** using matrix multiplication

$$D\left(\mathbf{u}\right) = \hat{\mathbf{u}}^{\mathrm{T}}\mathbf{D}\hat{\mathbf{u}}\,, \tag{33}$$

where ^{T} indicates the vector transpose. This relationship can be used to incorporate **D** into the Stejskal-Tanner equation; if $\hat{\mathbf{u}}$ is collinear with $\mathbf{g}$, Eq. (33) can therefore be substituted into Eq. (30), yielding [114]

$$E\left(\mathbf{g}\right) = \exp\left(-\gamma^2\delta^2\left(\Delta-\delta/3\right)\mathbf{g}^{\mathrm{T}}\mathbf{D}\,\mathbf{g}\right). \tag{34}$$

Recalling Eq. (31), Eq. (34) can also be reduced to a straightforward, linear relationship between the parameters of the magnetic diffusion gradient and the attenuated diffusion-weighted MR signal. To do so, Eq. (33) is first rewritten as a mathematical series. As **D** is symmetric, Eq. (33) can be rewritten as

$$D(\mathbf{u}) = \sum_{i=1}^{3}\sum_{j=1}^{3} u_i u_j D_{ij} = \begin{array}{c} u_x u_x D_{xx} + u_y u_y D_{yy} + u_z u_z D_{zz} \\ + 2u_x u_y D_{xy} + 2u_x u_z D_{xz} + 2u_y u_z D_{yz} \end{array} . \tag{35}$$

This expansion can be written as

$$D(\mathbf{u}) = \mathbf{U} : \mathbf{D} = \sum_{i=1}^{3}\sum_{j=1}^{3} u_i u_j D_{ij} . \tag{36}$$

where **U** is a symmetric, second order direction tensor, the elements of which are equal to $u_i u_j$ and **U** : **D** is the tensor dot product (i.e., scalar product) of the two tensors**.**

Assuming for now that only one *b*-value is used for all diffusion measurements, **U** can be multiplied by *b* to create a second order diffusion-weighting tensor, **b**, which describes the diffusion magnetic gradient in three dimensions, i.e.

$$\mathbf{b} = b\begin{pmatrix} u_x u_x & u_y u_x & u_z u_x \\ u_x u_y & u_y u_y & u_z u_y \\ u_x u_z & u_y u_z & u_z u_z \end{pmatrix} = \gamma^2 \delta^2 \left(\Delta - \delta/3\right)\begin{pmatrix} g_x g_x & g_y g_x & g_z g_x \\ g_x g_y & g_y g_y & g_z g_y \\ g_x g_z & g_y g_z & g_z g_z \end{pmatrix}. \tag{37}$$

Replacing **U** with **b** in Eq. (36) yields

$$\mathbf{b} : \mathbf{D} = \sum_{i=1}^{3}\sum_{j=1}^{3} b_{ij} D_{ij} = b_{xx} D_{xx} + b_{yy} D_{yy} + b_{zz} D_{zz} + 2b_{xy} D_{xy} + 2b_{xz} D_{xz} + 2b_{yz} D_{yz} . \tag{38}$$

Eq. (38) can now be substituted into Eq. (31); effectively, *b* and *D* are replaced with the tensor dot product of their respective tensors, **b** and **D** [114], yielding

$$\ln E = -\mathbf{b} : \mathbf{D} = -b_{xx} D_{xx} - b_{yy} D_{yy} - b_{zz} D_{zz} - 2b_{xy} D_{xy} - 2b_{xz} D_{xz} - 2b_{yz} D_{yz} . \tag{39}$$

Rewriting Eq. (39) as a system of linear equations for *n* unique diffusion gradient unit vectors therefore yields

$$
\begin{aligned}
\ln E(\mathbf{g}_1) &= -b(\mathbf{g}_1)_{xx} D_{xx} - b(\mathbf{g}_1)_{yy} D_{yy} - b(\mathbf{g}_1)_{zz} D_{zz} \\
&\quad -2b(\mathbf{g}_1)_{xy} D_{xy} - 2b(\mathbf{g}_1)_{xz} D_{xz} - 2b(\mathbf{g}_1)_{yz} D_{yz} \\
\ln E(\mathbf{g}_2) &= -b(\mathbf{g}_2)_{xx} D_{xx} - b(\mathbf{g}_2)_{yy} D_{yy} - b(\mathbf{g}_2)_{zz} D_{zz} \\
&\quad -2b(\mathbf{g}_2)_{xy} D_{xy} - 2b(\mathbf{g}_2)_{xz} D_{xz} - 2b(\mathbf{g}_2)_{yz} D_{yz} \quad . \\
&\quad \vdots \\
\ln E(\mathbf{g}_n) &= -b(\mathbf{g}_n)_{xx} D_{xx} - b(\mathbf{g}_n)_{yy} D_{yy} - b(\mathbf{g}_n)_{zz} D_{zz} \\
&\quad -2b(\mathbf{g}_n)_{xy} D_{xy} - 2b(\mathbf{g}_n)_{xz} D_{xz} - 2b(\mathbf{g}_n)_{yz} D_{yz}
\end{aligned}
\tag{40}
$$

The independent elements of **D** can then be determined from Eq. (40) using an appropriate method for solving a system of linear equations. These methods can be classified as being either an iterative (i.e., a process that repeatedly refines estimations of the elements of **D**), or a direct (i.e., the system of linear equations is rewritten in the form of vectors and matrices, so that elements of **D** can be calculated directly by matrix multiplication) reconstruction approach. Further details regarding iterative and direction reconstruction methods can be found in Appendix B. As **D** possesses six independent elements, the system of linear equations must contain a minimum of six equations in order to reconstruct the diffusion tensor. Consequently, *q*-space must be sampled in at least six points of a single *q*-shell in addition to the origin of *q*-space (i.e., the diffusion-unweighted MR signal) [114]. These first six points must be unique; they may not be antipodal or have more than two points sharing the same plane [118]. Ideally these points will be spaced evenly over the surface of the *q*-shell to reduce directional bias in the diffusion measurements. Including additional diffusion measurements (i.e., with **q** oriented at different directions) in the system of linear equations (i.e., overdetermining) will assist the reconstruction by reducing the effect of MR signal noise on the diffusion measurements and improving the angular resolution of **D**.

Once **D** has been determined, the information it contains can be extracted and visualised. There are many ways that this can be accomplished. For example, using Eq. (33) and a set of gradient directions defined on the surface of a sphere, the ADC with respect to each of these directions can be expressed as the radius of a function in spherical coordinates (Figure 25A) [114, 119]. Typically these apparent diffusivity profiles are represented by an isosurface (i.e., a surface which passes through the points described by the scaled vectors) to assist in visualisation (Figure 25B). The

diffusivity profile of isotropic diffusion will be a sphere, while anisotropic will be distinctly peanut shaped.

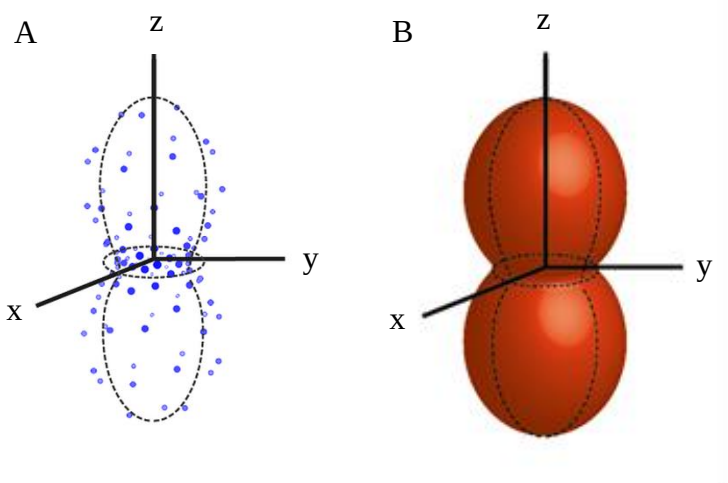

Figure 25: (A) A three-dimensional apparent diffusivity profile created by plotting the ADCs associated with ninety-six different gradient directions as the radius of a function in spherical coordinates. The ADCs were calculated using Eq. (33) and a diagonalised diffusion tensor (D_{xx} = 0.425×10^6 s m^{-2}, D_{yy} = 0.425×10^6 s m^{-2}, D_{zz} = 1.90×10^6 s m^{-2}). The x, y, and z axes correspond to where the projected ADC equates to D_{xx}, D_{yy} and D_{zz}, respectively (unit length of each axes is not to scale). (B) The same apparent diffusivity profile, but represented as an isosurface.

4.2.1 Eigenvectors, eigenvalues and useful scalars of the diffusion tensor

Since **D** is a square matrix (see Eq. (32)), it can be decomposed into is corresponding eigenvectors and eigenvalues [117]. These components of the tensor are rotationally invariant, and are highly useful when analysing and comparing complicated porous structures.

An eigenvector, $\boldsymbol{\upsilon}$, is a unit vector that when multiplied by a square matrix such as **D** will result in itself multiplied by a scalar, λ (i.e., its eigenvalue), i.e., [120]

$$\mathbf{D}\boldsymbol{\upsilon}_i = \lambda_i \boldsymbol{\upsilon}_i . \tag{41}$$

Since **D** is a third rank tensor it possesses three eigenvectors and three corresponding eigenvalues. **D** is also a positive-definite matrix; its eigenvalues are real, positive values and its eigenvectors form a complete orthonormal basis, i.e.,

$$\boldsymbol{\upsilon}_i \cdot \boldsymbol{\upsilon}_j = \begin{cases} 0 & i \neq j \\ 1 & i = j \end{cases} . \tag{42}$$

To calculate the eigenvalues and eigenvectors of **D**, Eq. (41) is rewritten as [120]

$$\left(\mathbf{D} - \lambda \mathbf{I}\right)\boldsymbol{\upsilon} = 0 . \tag{43}$$

As $\boldsymbol{\upsilon}$ will be a non-zero vector and a non-trivial solution is expected from Eq. (43), the determinant of **D** – λ**I** must be zero [120]. Thus,

$$\det\left(\mathbf{D} - \lambda \mathbf{I}\right) = 0$$
$$\det\begin{bmatrix} D_{xx} - \lambda & D_{yx} & D_{zx} \\ D_{xy} & D_{yy} - \lambda & D_{zy} \\ D_{xz} & D_{yz} & D_{zz} - \lambda \end{bmatrix} = 0 . \tag{44}$$

Rewriting Eq. (44) as a polynomial [120] yields

$$\begin{aligned} &\left(D_{xx} - \lambda\right)\left(D_{yy} - \lambda\right)\left(D_{zz} - \lambda\right) + 2D_{xy}D_{xz}D_{yz} \\ &-2D_{xz}\left(D_{yy} - \lambda\right) - 2D_{yz}\left(D_{xx} - \lambda\right) - 2D_{xy}\left(D_{zz} - \lambda\right) = 0 \end{aligned} . \tag{45}$$

Finding the roots of Eq. (45) will therefore yield the eigenvalues of **D**. Once the eigenvalues are known, the eigenvectors can be calculated by rewriting Eq. (41) as a system of linear equations, i.e., [120]

$$\begin{aligned} D_{xx}\boldsymbol{\upsilon}_x + D_{yx}\boldsymbol{\upsilon}_y + D_{zx}\boldsymbol{\upsilon}_z &= \lambda\boldsymbol{\upsilon}_x \\ D_{xy}\boldsymbol{\upsilon}_x + D_{yy}\boldsymbol{\upsilon}_y + D_{zy}\boldsymbol{\upsilon}_z &= \lambda\boldsymbol{\upsilon}_y \\ D_{xz}\boldsymbol{\upsilon}_x + D_{yz}\boldsymbol{\upsilon}_y + D_{zz}\boldsymbol{\upsilon}_z &= \lambda\boldsymbol{\upsilon}_z \end{aligned} . \tag{46}$$

Solving Eq. (46) for each eigenvalue will hence result in the components of the corresponding eigenvector. When eigenvalues are used to describe anisotropic diffusion, one or more of the eigenvalues of **D** will differ from the remainder (the eigenvalues will be equal in value when diffusion is isotropic). The eigenvector associated with the largest eigenvalue (i.e., the principal eigenvector, $\boldsymbol{\upsilon}_1$) indicates the direction of least diffusion restriction [117]. In ordered structures, such as muscle fibres and brain white matter, the principal eigenvector is usually assumed to be parallel to the longest axis of the restricting microstructure (e.g. the length of a cylinder) [114]. Image maps of $\boldsymbol{\upsilon}_1$ are highly useful in determining connections

between restricting microstructures in neighbouring voxels. These maps can either be visualised as a two or three-dimensional field of vectors (Figure 26A) [121] or as a diffusion encoded colour image (Figure 26B) [122]. In the latter case, the hue of the voxel indicates the orientation of υ_1. The intensity of coloration can also be employed to provide additional diffusion information, such as the degree of diffusion anisotropy (see below). For a more complete representation of three-dimensional diffusion the three orthogonal eigenvectors of **D** can be scaled by their respective eigenvalues and plotted in a three-dimensional space. When this simplified apparent diffusivity profile is converted into an isosurface, it is known as a diffusion ellipsoid (Figure 26C) [117].

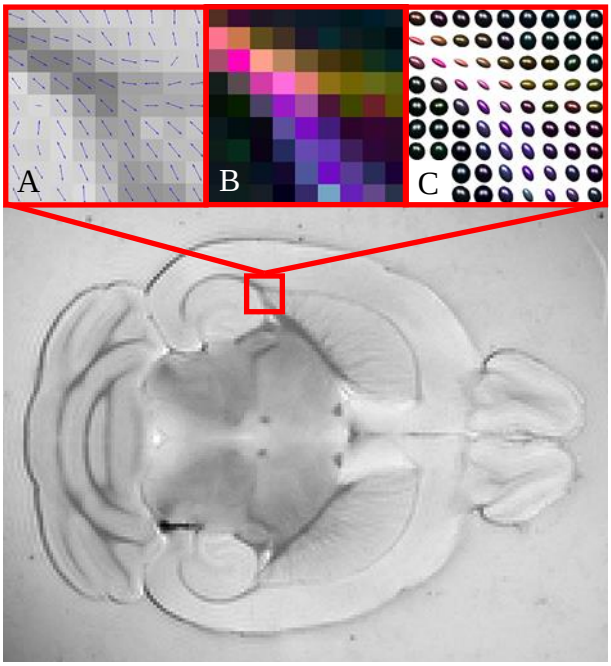

Figure 26: Three different ways of representing three-dimensional diffusion in a mouse brain. Two-dimensional vector maps (A) and diffusion colour encoded images (B) indicate the orientation of the principal eigenvector. Diffusion ellipsoids can be used instead to create a complete representation of three-dimensional diffusion (C). The three diffusion tensor images of the mouse brain were created from a set of thirty-six diffusion-weighted MR images acquired using a Bruker 500 MHz wide bore NMR spectrometer. The parameters used included three different *b*-values (60×10^6 s m^{-2}, 239×10^6 s m^{-2} and 537×10^6 s m^{-2}) and twelve different diffusion gradient directions (the vertices of an icosahedron in Cartesian coordinates). Voxel size is $98 \times 98 \times 500$ µm. Special thanks to Dr T. Stait-Gardner for supplying the mouse brain (under tissue sharing arrangements).

In addition to eigenvalues and eigenvectors, a number of invariant scalar features can also be extracted from **D**. These scalar features are often useful for making comparisons between different diffusion restricting systems. One example is the mean diffusivity, $\langle \mathbf{D} \rangle$, which can be calculated by finding the mean of the trace (i.e., the sum of the diagonal elements of the tensor) of **D**, [123] i.e.,

$$\langle \mathbf{D} \rangle = \left(D_{xx} + D_{yy} + D_{zz} \right) / 3 . \tag{47}$$

Since the trace is an invariant property and not dependent on any particular coordinate system, $\langle \mathbf{D} \rangle$ is also equivalent to the mean of the eigenvalues of **D** [123]. Maps of the mean diffusivity are capable of detecting small changes in the permeability of porous microstructures, such as changes to cell membrane permeability in the case of ischemic cell death [124, 125], as will be demonstrated later (see Chapter 8 - Time course study of grape berry split using diffusion MRI).

The components of the diffusion tensor can also be used to quantify the overall anisotropy of a diffusivity profile with a scalar known as a diffusion anisotropy index (DAI). Of the many DAI variants that exist, the three most frequently cited are the fractional anisotropy (FA), volume ratio (VR) and relative anisotropy (RA) indices [126-128]. These three DAIs measure the overall deviation of the eigenvalues/diagonal elements of **D** from its mean diffusivity, i.e.,

$$\mathrm{FA} = \sqrt{\frac{3}{2} \frac{\left(D_{xx} - \langle \mathbf{D} \rangle \right)^2 + \left(D_{yy} - \langle \mathbf{D} \rangle \right)^2 + \left(D_{zz} - \langle \mathbf{D} \rangle \right)^2}{D_{xx}^2 + D_{yy}^2 + D_{zz}^2}} \tag{48}$$

$$\mathrm{RA} = \sqrt{\frac{1}{6} \frac{\left(D_{xx} - \langle \mathbf{D} \rangle \right)^2 + \left(D_{yy} - \langle \mathbf{D} \rangle \right)^2 + \left(D_{zz} - \langle \mathbf{D} \rangle \right)^2}{\langle \mathbf{D} \rangle^2}} \tag{49}$$

$$\mathrm{VR} = 1 - \frac{D_{xx} D_{yy} D_{zz}}{\langle \mathbf{D} \rangle^3} . \tag{50}$$

Eqs. (48) – (50) include scaling factors so that each calculated DAI has a value between zero (isotropic diffusion) and one (complete anisotropic diffusion). Of these three DAIs, FA indices are the most featured in the literature; FA indices are more sensitive to variations in anisotropy than RA and VR indices and also have a lower sensitivity to errors in **D** (Figure 27A) [126-128]. However, both RA and VR indices

possess useful qualities. For example, VR indices exhibits a stronger contrast than FA between image regions with different degrees of anisotropy (Figure 27C), which could potentially be useful for biological tissue segmentation. The characteristics of RA indices are between those of FA and VR indices. RA indices have a moderate level of anisotropic detail and region contrast, as well as a moderate susceptibility to errors in **D** (Figure 27B), offering a compromise between the other two indices [126-128]. An example of the use of DAIs in clinical studies has been in the investigation of neurological impairment after traumatic brain injury [129, 130]. These injuries altered the coherence of microstructure within the affected region of brain tissue, resulting in highly noticeable changes in diffusion anisotropy.

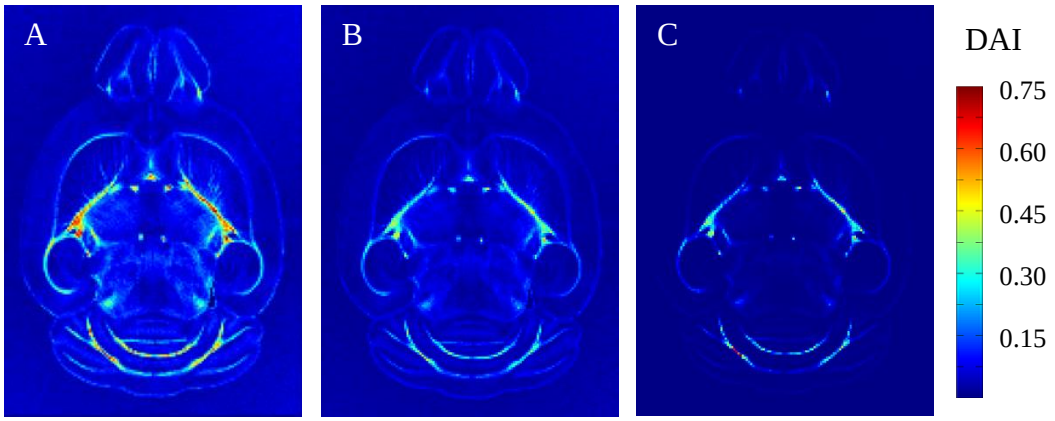

Figure 27: Comparing FA (A), RA (B) and VR (C) maps of a mouse brain. Although all three DAI images vary between zero (isotropy) and one (complete anisotropy), the tissue contrast between the three images differs. The three DAI images of the mouse brain were created from a set of thirty-six diffusion-weighted MR images acquired using a Bruker 500 MHz wide bore NMR spectrometer. The parameters used included three different *b*-values (60×10^6 s m^{-2}, 239×10^6 s m^{-2} and 537×10^6 s m^{-2}) and twelve different diffusion gradient directions (the vertices of an icosahedron in Cartesian coordinates). Voxel size is $98 \times 98 \times 500$ µm. Special thanks to Dr T. Stait-Gardner for supplying the mouse brain (under tissue sharing arrangements).

As DTI requires a minimum of seven images to reconstruct **D**, the total acquisition time of DTI can be kept relatively short compared with other three-dimensional diffusion MRI technique (see Appendix A), especially when a fast diffusion MRI sequence such as echo-planar PGSE imaging [131] is employed. DTI it is most effective when the voxels of its images contain only a single fibre population (i.e.,

anisotropically diffusion restricting microstructures within the voxel all having a similar orientation. For example, a voxel containing aligned elongated cells, or a voxel containing coherent, fibrous protein structures, such as collagen. Figure 28A). DTI has been used to great effect in skeletal muscles [87, 132] and the spinal cord [130, 133, 134]. However, **D** possesses only a single principal eigenvector; as a consequence, it is impossible to correctly infer the shape and orientation of the restricting microstructures when multiple fibre populations are present within a voxel (Figure 28B – D). This can be problematic in complicated diffusion restricting systems, such as brain white matter [86, 94], and in determining the connections between separated brain regions [128, 135, 136].

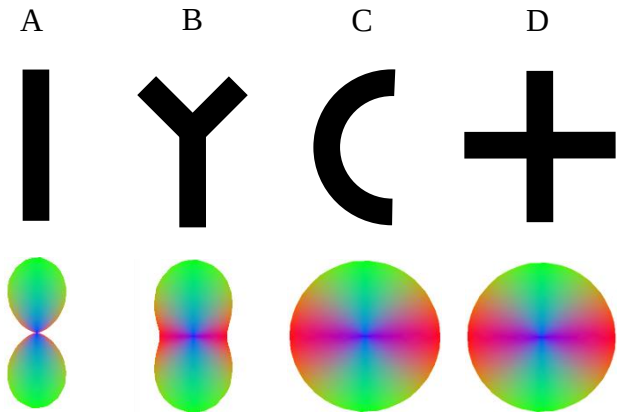

Figure 28: Examples of different fibrous microstructure configurations with a voxel (top) and their corresponding three-dimensional apparent diffusivity profiles (bottom). These diffusivity profiles were created using a second order diffusion tensor. The diffusion profile associated with a single fibre population (A) can be readily interpreted to determine its orientation. However, the diffusion profile cannot convey the orientation of these fibrous structures when they diverge (B) or bend (C) or intersect (D).

4.3 Bessel Fourier orientation reconstruction imaging

One advantage that several diffusion MRI techniques possess over DTI is their ability to reconstruct the EAP. Thus, these diffusion MRI techniques can simultaneously capture both the angular and radial components of the diffusion-weighted MR signal. This information can potentially be used to determine the orientations of overlapping diffusion restricting microstructures as well as estimate the size, shape and density of diffusion restricting microstructures. As discussed in Appendix A, diffusion MRI techniques capable of reconstructing the EAP from the diffusion-weighted MR signal include DSI [101], DOT imaging [137], DPI [138], SPFI [139] and BFOR imaging [140, 141]. Of the listed diffusion MRI techniques, BFOR imaging appears to be particularly promising. BFOR imaging was specifically designed to accommodate diffusion-weighted images with a low SNR and diffusion data with relatively few samples of *q*-space (both in terms of the number of *q*-shells and the number of points sampled on each *q*-shell).

The BFOR algorithm assumes that the diffusion-weighted MR signal satisfies the diffusion (or heat) equation (cf. Eq. (14)) [140, 141],

$$\nabla^2 E(\mathbf{q},t) = \frac{\partial E(\mathbf{q},t)}{\partial t} \ . \tag{51}$$

The diffusion equation is a generalisation of the Laplace equation (i.e., $\nabla^2 E(\mathbf{q}) = 0$); these two different expressions become equal when the former reaches the steady state (i.e., $t \rightarrow \infty$). Since the diffusion equation is the generalised case, it imposes few constraints when solving a given problem. Additionally, the dependence of the MR signal attenuation on t will later prove useful when smoothing the EAP.

In order to find the solution of Eq. (51), the expression can be treated as a Cauchy problem with the boundary condition [141, 142]

$$\nabla^2 \psi_i(\mathbf{q}) = -\lambda_i \psi_i(\mathbf{q}) \tag{52}$$

where $\psi_i(\mathbf{q})$ and λ_i are the i-th eigenfunctions and eigenvalues of the Laplace operator, respectively. The solution to Eq. (51) is then given by [143],

$$E(\mathbf{q},t)=\sum_{i=0}^{\infty}c_i\exp(-\lambda_i t)\psi_i(\mathbf{q}) \tag{53}$$

where c_i are the coefficients of the expansion. Thus by finding the eigenfunctions and eigenvalues of the Laplace operator, the coefficients of the series can be calculated. The solution for the Cauchy boundary condition can be derived by separating $\psi_i(\mathbf{q})$ into its angular and radial components [140, 141], i.e.,

$$\psi_i(\mathbf{q})=R_i(q)Y(\theta,\varphi), \tag{54}$$

Rewriting Eq. (52) in spherical coordinates yields

$$\begin{aligned}\nabla^2\psi_i(\mathbf{q})&=\left[\frac{1}{q^2}\frac{\partial}{\partial q}\left(q^2\frac{\partial}{\partial q}\right)+\frac{1}{q^2\sin\theta}\frac{\partial}{\partial\theta}\left(\sin\theta\frac{\partial}{\partial\theta}\right)+\frac{1}{q^2\sin^2\theta}\frac{\partial^2}{\partial\varphi^2}\right]\psi_i(\mathbf{q})\\&=-\lambda_i\psi_i(\mathbf{q})\end{aligned} \tag{55}$$

Thus by using the technique of separation by variables (see Appendix C), it can found that Eq. (55) will possess two solutions,

$$\frac{q^2}{R_i(q)}\frac{d^2R_i(q)}{dq^2}+\frac{2q}{R(q)}\frac{dR_i(q)}{dr}+q^2\lambda_i=\lambda_i \tag{56}$$

and

$$\left[\frac{1}{Y(\theta,\varphi)\sin\theta}\frac{\partial}{\partial\theta}\left(\sin\theta\frac{\partial Y(\theta,\varphi)}{\partial\theta}\right)+\frac{1}{Y(\theta,\varphi)\sin^2\theta}\frac{\partial^2Y(\theta,\varphi)}{\partial\varphi^2}\right]=\lambda\,. \tag{57}$$

where λ in this context is a constant, and $R(q)$ and $Y(\theta,\varphi)$ represent the radial and angular components of the attenuated diffusion-weighted MR signal, respectively. Upon further separation by variables, it can be shown that $Y(\theta,\varphi)$ consists of spherical harmonic functions (see Appendix C), a set of orthogonal basis functions which are highly useful for approximating functions on the surface of a sphere. As such, spherical harmonic functions are well suited to capturing the angular component of the attenuated diffusion-weighted MR signal. Spherical harmonic functions are given by [144, 145]

$$Y_l^m(\theta,\varphi)=\sqrt{\frac{2l+1}{4\pi}\frac{(l-m)!}{(l+m)!}}\exp(im\varphi)\mathfrak{P}_l^m(\cos\theta)\,. \tag{58}$$

where $\mathfrak{P}_l^m(\cdot)$ are the associated Legendre polynomials of the first kind (i.e., l is an integer describing the angular order of the polynomial and m is an integer describing the degree of the polynomial). If $R(q)$ is redefined so that

$$\mathfrak{R}_i(q) = \sqrt{\frac{\pi}{2q\sqrt{\lambda_i}}} R_i(q) \ , \tag{59}$$

Eq. (56) can then be rewritten, using the relation

$$\frac{d}{dq}\sqrt{\frac{\pi}{2q\sqrt{\lambda_i}}} = -\frac{1}{2q}\sqrt{\frac{\pi}{2q\sqrt{\lambda_i}}} \ , \tag{60}$$

as [140, 141]

$$q^2 \frac{d^2\mathfrak{R}_i(q)}{dq^2} + q\frac{d\mathfrak{R}_i(q)}{dr} + \left[q^2\lambda_i - (l+1/2)^2\right]\mathfrak{R}_i(q) = 0 \, . \tag{61}$$

This expression is a scaled version of the Bessel differential equation [146]. Therefore the solution to Eq. (61) is

$$\mathfrak{R}_i = J_{l+1/2}\left(q\sqrt{\lambda_i}\right) \tag{62}$$

where $J_{l+1/2}(x)$ is a Bessel function of the first kind. Upon converting $J_{l+1/2}(x)$ into its corresponding spherical Bessel function of the first kind, $j_l(x)$, the solution of Eq. (56) becomes (Eq. 10.1.1 of [147])

$$R_i(q) = j_l\left(q\sqrt{\lambda_i}\right). \tag{63}$$

The spherical Bessel functions and the spherical harmonic functions can then be multiplied together to yield an orthonormal basis [140, 141],

$$\psi(\mathbf{q}) = \sum_{n=1}^{\infty}\sum_{l=0}^{\infty}\sum_{m=-l}^{l} C_{nl}^{\ m} j_l\left(q\sqrt{\lambda_{nl}}\right) Y_l^m(\mathbf{q}'), \tag{64}$$

where $C_{nl}^{\ m}$ are the coefficients of the expansion. As spherical Bessel functions indefinitely oscillate about zero, a radial distance in q-space must be defined as the point at which the radial component of the diffusion-weighted MR signal finally decays to zero. In practice, τ is defined as the largest q-value plus the difference

between q-values used (i.e., $q' + \Delta q$) [140, 141]. Since the radial component of the diffusion-weighted signal is assumed to decay to zero at τ, it can be inferred that

$$R_{nl}(\tau) = j_l\left(\tau\sqrt{\lambda_{nl}}\right) = 0\,. \tag{65}$$

The values of $\tau\sqrt{\lambda_{nl}}$ which satisfy Eq. (65) are known as the roots of the spherical Bessel function of the first kind. Thus if α_{nl} is designated as the n-th root of the l-th order spherical Bessel function of the first kind, the eigenvalues of the Laplace operator are given by

$$\lambda_i = \frac{\alpha_i^2}{\tau^2}\ . \tag{66}$$

Therefore, by combining Eqs. (53), (64) and (66), and truncating the expansion to a particular radial, N, and angular order, L, the diffusion-weighted MR signal can be expanded as [140, 141]

$$E(\mathbf{q}) = \sum_{n=1}^{N}\sum_{l=0}^{L}\sum_{m=-l}^{l} C_{nl}^{\ m} \exp\left(-\frac{\alpha_{nl}^2 t}{\tau^2}\right) j_l\left(\frac{\alpha_{nl} q}{\tau}\right) Y_l^m(\mathbf{q}') \tag{67}$$

where all of the coefficients featured in these equations have been combined into $C_{nl}^{\ m}$. The coefficients of Eq. (67) can then be calculated by using this expression as the basis for a system of linear equations. Written as a matrix operation, Eq. (67) becomes

$$\mathbf{E} = \mathbf{ZC} \tag{68}$$

where $\mathbf{C}$ is a vector containing the coefficients of Eq. (67) and

$$\mathbf{Z} = \begin{bmatrix} j_0\left(\frac{\alpha_{0,0} q_1}{\tau}\right) Y_0^0(\mathbf{u}_1) & j_2\left(\frac{\alpha_{0,2} q_1}{\tau}\right) Y_2^{-2}(\mathbf{u}_1) & \cdots & j_l\left(\frac{\alpha_{NL} q_1}{\tau}\right) Y_L^L(\mathbf{u}_1) \\ j_0\left(\frac{\alpha_{0,0} q_2}{\tau}\right) Y_0^0(\mathbf{u}_1) & j_2\left(\frac{\alpha_{0,2} q_2}{\tau}\right) Y_2^{-2}(\mathbf{u}_1) & \cdots & j_l\left(\frac{\alpha_{NL} q_2}{\tau}\right) Y_L^L(\mathbf{u}_1) \\ \vdots & \vdots & & \vdots \\ j_0\left(\frac{\alpha_{0,0} q_K}{\tau}\right) Y_0^0(\mathbf{u}_N) & j_2\left(\frac{\alpha_{0,2} q_K}{\tau}\right) Y_2^{-2}(\mathbf{u}_N) & \cdots & j_l\left(\frac{\alpha_{NL} q_K}{\tau}\right) Y_L^L(\mathbf{u}_N) \end{bmatrix}. \tag{69}$$

Since the diffusion signal is considered to be acquired when t = 0, the exponential function featured in Eq. (67) is excluded from **Z** [140, 141]. Since BFOR MRI uses the spherical harmonic series to model the angular component of the diffusion-weighted MR signal, the minimum number of points that must be sampled on each q-shell is given by Eq. (116). The number of q-shells that must be sampled, on the other hand, is equal to the radial order by which Eq. (67) was truncated.

If **Z** is an ill-conditioned matrix, the Laplace-Beltrami operator can be used to regularise the matrix [148, 149]. This matrix regularisation helps smooth spherical functions by penalising higher order tensor terms which do not significantly improve the accuracy of the reconstruction. This in turn improves the robustness of the matrix pseudo-inversion of **Z**. To perform Laplace-Beltrami, Eq. (68) is rewritten as

$$\mathbf{C} = \left(\mathbf{Z}^{\mathrm{T}}\mathbf{Z} + \lambda_L \mathbf{L} + \lambda_N \mathbf{N}\right)^{-1} \mathbf{Z}^{\mathrm{T}}\mathbf{E} \tag{70}$$

where λ_L is the angular regularisation constant, **L** is the angular regulation matrix, λ_N is the radial regularisation constant and **N** is the radial regulation matrix. The **L** and **N** matrices are diagonal matrices with entries $l^2\left(l+1\right)^2$ and $n^2\left(n+1\right)^2$, respectively. Appropriate values for regularisation constants will need to be carefully selected in order to ensure that the higher order terms of **C** are not over smoothed. Useful values for the regularisation constants can be found using the L-curve numerical method [150], or by simple trial-and-error.

Once the expansion coefficients of Eq. (68) have been calculated using a matrix inversion, the EAP can be reconstructed using Eq. (26). However, this first requires that the plane wave featured in Eq. (108) be rewritten in terms of spherical wave functions, i.e.

$$\mathfrak{W} = \exp\left(-2\pi i \mathbf{q}\cdot\mathbf{R}\right) = 4\pi \sum_{l=0}^{\infty}\sum_{m=-1}^{l}\left(-i\right)^l J_l\left(2\pi q R\right) Y_l^m\left(\mathbf{q}'\right) Y_l^m\left(\mathbf{R}'\right)^* . \tag{71}$$

Substituting Eq. (71) into Eq. (26) will yield

$$\bar{P}\left(R_0\mathbf{R}'\right) = \sum_{l=0}^{\infty}\sum_{m=-1}^{l}\left(-i\right)^l Y_l^m\left(\mathbf{R}'\right)\int Y_l^m\left(\mathbf{q}'\right)^* I_l\left(\mathbf{q}'\right) d\mathbf{q}' \tag{72}$$

where

$$I_l\left(\mathbf{q}'\right)=4\pi\int_0^\infty q^2 j_l\left(2\pi q R_0\right)E\left(\mathbf{q}'\right)dq\,. \tag{73}$$

Solving and truncating this resultant expression with Eq. (67) yields [140, 141]

$$\bar{P}\left(\mathbf{R},t\right)=2\tau\sqrt{2\pi^3}\sum_{n=1}^{N}\sum_{l=1}^{L}\sum_{m=-l}^{l}\left(\begin{array}{c}\left(-1\right)^{l/2}C_{nlm}\exp\left(-\dfrac{\alpha_{nl}^2 t}{\tau^2}\right)Y_l^m\left(\mathbf{R}'\right)\\ \times\dfrac{\sqrt{\alpha_{nl}}\,J_{l-1/2}\left(\alpha_{nl}\right)j_l\left(2\pi\tau R\right)}{4\pi^2R^2-\dfrac{\alpha_{nl}^2 t}{\tau^2}}\end{array}\right). \tag{74}$$

Since the solution of this equation will decrease exponentially as t increases, t can be adjusted so as to smooth out high frequency noise in the measured MR signal. Once $\bar{P}$ (**R**,t) has been determined for a large set of **R** defined on the surface of a sphere, the probability isosurface can be plotted by expressing $\bar{P}$ (**R**,t) as the radius of a function in spherical coordinates (see Figure 25). The resultant probability profile will have high angular contrast and low susceptibility to signal noise (Figure 29). A MATLAB script written in-house for processing diffusion MRI data via BFOR imaging, and displaying the processed data as a field of probability isosurfaces, is included in Appendix D.

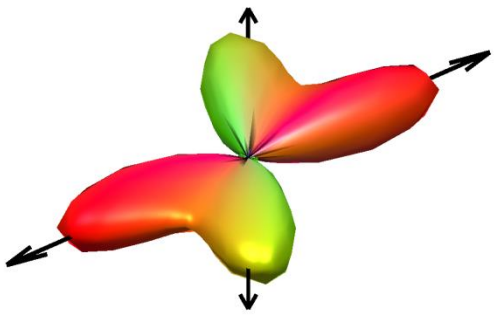

Figure 29: BFOR EAP profile of water diffusing through two overlapping fibres separated by 45° as simulated in MATLAB. The parameters used for the simulations included 200 diffusion gradient directions, b = 74, 297, 668, 1187, 1854, 2670 ($\times 10^6$ s m^{-1}), δ = 2.5 ms and Δ = 30 ms. The maximum spherical harmonic order of the reconstructions was six and the maximum radial order was five. The fibres were simulated as cylinders with a 5 μm radius and 100 μm length.

Similarly to DTI, a number of useful scalars can be calculated from the EAP; for example, the generalised fractional anisotropy (GFA) index, which is calculated by modifying the definition of the FA index (cf. Eq. (48)) [151], yielding

$$\mathrm{GFA} = \frac{\mathrm{std}\left(P\left(\mathbf{R}\right)\right)}{\mathrm{rms}\left(P\left(\mathbf{R}\right)\right)} = \sqrt{\frac{\int\left(P\left(\mathbf{R}\right)-\left\langle P\right\rangle\right)^2 d\mathbf{w}}{\int P\left(\mathbf{R}\right)^2 d\mathbf{w}}} = \sqrt{\frac{n}{n-1}\frac{\sum_{i=1}^{n}\left(P\left(\mathbf{R}_i\right)-\left\langle P\right\rangle\right)^2}{\sum_{i=1}^{n}P\left(\mathbf{R}_i\right)^2}} \tag{75}$$

The zero displacement probability, $\bar{P}(0)$, can also be calculated from the reconstructed EAP [140]. $\bar{P}(0)$ describes the likelihood of individual particles having no net displacement during the diffusion period. This probability will increase as the restricting microstructure becomes narrower. Thus, this value can be used as another measure of diffusion anisotropy. An analytical expression for the zero displacement probability can be calculated by solving Eq. (74) with **R** = 0, i.e.,

$$\bar{P}\left(0\right) = \tau^3\sqrt{4\pi}\sum_{n=1}^{N}C_{n1}\frac{\left(-1\right)^{n+1}}{\alpha_{n0}^2} \ . \tag{76}$$

Finally, the MSD of the EAP can be calculated by exploiting the relationship between the Laplacian of $E(0)$ and the MSD [140]. This will yield

$$\left\langle \mathbf{R}^2 \right\rangle = \frac{1}{8\pi^{5/2}\tau^2}\sum_{n=1}^{N}C_{n1}\alpha_{n0}^2 \ . \tag{77}$$

The greatest limitation of BFOR MRI is that the radial basis does not naturally decay to zero. While this does not affect the accuracy of the angular component reconstruction of the EAP, it will affect the reconstruction of the radial component [140]. Additionally, BFOR imaging was developed with the intention of characterising narrow cellular and tissue structures, such as white matter neural connectors. BFOR imaging may therefore prove to be an unsuitable diffusion MRI method for characterising biological structures which are considerably wider, such as the pericarp cells of grape berries (see Chapter 6 - Assessing the use of BFOR imaging for botanical studies).

Chapter 5 - Materials and methods

5.1 Botanical specimen handling

Botanical specimens examined within this thesis included grape berries (*Vitis vinifera* L.), olives (*Olea europaea* L.) and calamondins (*Citrofortunella macrocarpa*). The examinations of the olives and calamondins were included primarily to support, or provide complementary comparisons, for the grape berry studies. All botanical specimens were stored at 4 °C while not in use. Once selected for imaging, the specimen had approximately 30 minutes to equilibrate to 22.0 ± 0.1 °C during the spectrometer setup and calibration stages. Botanical specimens were dried at 70 °C after imaging to determine the dry weight. When a grape berry was imaged, the total soluble solids was estimated based on the average of three refractormeter (PAL-1, Atago Co., Ltd., Tokyo, Japan) readings obtained from berries of the same bunch.

5.2 Grape berry growing conditions

All wine grape berries, cv. Semillon (clone DA16162, own roots), examined within this thesis were obtained from 18 grapevines grown in a glasshouse at the National Wine & Grape Industry Centre, Wagga Wagga, NSW, Australia. The plants were maintained in 35 L pots containing sandy loam. In late winter each plant was pruned to a pair of two-bud spurs and brought into the glasshouse to commence a fifth season of vegetative growth. Average daily maximum/minimum temperature and relative humidity in the glasshouse across the growing season were 30/17 °C and 75/40%, respectively. Each plant was watered beyond field capacity four times per day via a pair of drip emitters. Diluted fertiliser (Megamix Plus, Rutec Pty Ltd, Tamworth, Australia, 20 mL per plant) was applied fortnightly to the soil and wettable sulphur/tribasic copper sulphate was sprayed on the shoots. The shoots were trained vertically and pruned to one inflorescence each approximately six weeks after

bud burst. The date of bud burst was assessed on each bud [32] and the date of flowering (approximately 100 % capfall) was assessed on each inflorescence. All table grapes, cv. seedless Thompson and cv. Red Globe, examined within this thesis were obtained from a local green grocer, Campbelltown, NSW.

5.3 MRI hardware and software

All MRI was performed on a 500 MHz (11.7 T) wide-bore nuclear magnetic resonance spectrometer (AVANCE II; Bruker Biospin Co., Ltd., Germany), equipped with triple axis gradients capable of generating 1.5 T m^{-1} magnetic field gradients. This spectrometer was located in the Biomedical Magnetic Resonance Facility at the Campbelltown Campus of the University of Western Sydney, NSW, Australia. Each imaging experiment employed a 30 mm birdcage radio frequency coil insert. Bruker MRI sequences were used with minor adjustments as noted in the descriptions of each experiment. The interior temperature of the spectrometer was maintained at 22.0 ± 0.1 °C during the course of the experiments. Data acquisition, post-processing and imaging was controlled from a computer terminal running a Linux operating system, using ParaVision (version 5.1; Bruker Biospin Co., Ltd.). Image analysis and additional post-processing was performed on a separate computer terminal running Microsoft Windows 7. The raw MRI data were imported into MATLAB (8.0.0.783, the MathWorks, USA) for analysis. The MATLAB scripts used in conducting the analysis of the results were created in-house.

5.4 MRI pulse sequences and parameters

The MRI pulse sequences employed during the studies contained within this thesis included fast low angle shot (FLASH) MRI, multi-slice multi-echo (MSME) MRI, relaxation enhancement and variable repetition time (RARE VTR) MRI and PGSE echo planar DTI.

FLASH MRI was used to produce two-dimensional MR images weighted by spin-density. These spin-density MR images were typically employed to check the

position of the grapes within the NMR spectrometer and confirming the formation of splits in the epidermis of the berries. The FLASH MRI pulse sequence is similar to the spin-density MRI pulses sequence presented earlier (Figure 7), except the π rf pulse is excluded and the $\pi/2$ rf pulse is replaced with an rf pulse which rotates spins by α (where $\alpha \leq \pi/2$) [152].

MSME MRI was used to produce two-dimensional images weighted by spin-spin relaxation. These spin-spin relaxation images were used to observe structural features of the grape berries. The MSME MRI pulse sequence is similar to the CPMG MRI pulse sequence presented earlier (Figure 12), except it has been modified to acquire MR data from multiple image within one pass of the MRI pulse sequence [153].

RARE VTR MRI was used to produce sets of two-dimensional images weighted by varying degrees of spin-spin and spin-lattice relaxation. These relaxation weighted images were primarily used to examine the vascular/extra-vascular transport of paramagnetic ions throughout the grape berry pericarp. The RARE VTR MRI pulse sequence is similar to the CPMG MRI pulse sequence presented earlier (Figure 12) except multiple sets of spin-echo images are acquired and TR is varied between these different image sets [154].

PGSE echo planar DTI was used to produce two-dimensional images weighted by diffusion. These diffusion-weighted images were used to study the morphology of grape berry tissues, or changes in berry morphology/physiology over time due to experimental treatments. Echo planar PGSE is a modification of the PGSE pulse sequence presented earlier (Figure 21) allowing the acquisition of the entire image in a small number of segments rather than acquiring each individual line of voxels along the phase spatial encoding direction of the image [114, 131].

The MRI pulse sequence parameters (including FOV, MTX, THK, TR, TE and NA, as well as the number of echoes, δ and Δ if applicable) are listed with each MRI experiment. The voxels sizes of the MR images included in this thesis are indicated in the corresponding figure captions.

5.5 Confocal microscopy

All microscopy images include in this thesis were acquired using a confocal microscope (LSM5 Pascal; Zeiss, Germany) employing a 488 nm Argon laser and a 10 × objective Plan-Apochromatic lens. The microscopy images were acquired from a computer terminal running a Windows 7 operating system using Zen 2009 (Zeiss, Germany).

Chapter 6 - Assessing the use of BFOR imaging for botanical studies

6.1 Introduction

Having reviewed both DTI and BFOR, it is apparent that both techniques have a number of associated advantages. For example, DTI is highly robust and requires fewer diffusion-weighted MR images than BFOR imaging. DTI is also a well-established diffusion MRI technique; it has already been employed in previous studies to examine the morphology of fibrous botanical samples such as celery and asparagus [24, 155-157]. BFOR imaging, on the other hand, can better capture complicated angular and radial components of the diffusion-weighted MR signal. However, as previously mentioned, BFOR imaging was originally designed with intention of characterising narrow cells and tissue structures, such as studies of brain white matter. As neural fibres measure only a few micrometres in diameter [158, 159], BFOR imaging may struggle to accurately reconstruct the angular characteristics of microstructures which are considerably wider (see Section 1.1.1 Cell sizes of the grape berry pericarp tissues). This capability must be tested to determine the suitability of BFOR imaging for studying botanical specimens.

The objective of the experiments described in the current chapter was to assess the capabilities of BFOR imaging. The articles that describe the original implementation of BFOR imaging focussed primarily on testing its ability to reconstruct features from the radial component of the EAP (i.e., MSD, P_0 and GFA) [140, 141]. To provide a contrast to these previous tests, this investigation instead focused on testing the accuracy of the angular reconstruction of the EAP. This was done by measuring the deviation of the EAP isosurface maxima from the true orientation of two distinct and overlapping simulated fibre populations. These simulations included the reconstruction of EAP isosurfaces for different spherical harmonic orders, degrees of MR signal-to-noise and fibre geometries. In previous tests of the capabilities of BFOR imaging the attenuation of the diffusion-weighted MR signal was simulated

using a three-dimensional bi-exponential diffusion model [140, 141]. A disadvantage of using this model to simulate the diffusion-weighted signal is that its physiological implications [160, 161], and the dimensions of the diffusion restricting microstructure being simulated, are not clear. Consequently, for this investigation the simulated diffusion data was created using an eigenvalue expansion of the diffusion propagator within a cylindrical geometry [162-165] which would reasonably approximate the size and shape of grape berry mesocarp cells.

6.2 Method

6.2.1 Diffusion model for data simulation

The attenuation of the diffusion-weighted MR signal was simulated using the Fourier relationship between E and the EAP (see Eq. (26)). This involved calculating the EAP via the eigenvalue expansion of the diffusion propagator within a cylindrical geometry [162-165] before substituting EAP into Eq. (26), under the SGP condition, to yield E for a number of different $\mathbf{q}$ (see Section 6.2.2 Independent simulation parameters and 6.2.3 Dependent simulation parameters). The diffusion experiments were all simulated in MATLAB; special thanks go to Benjamin Moroney for sharing his MATLAB code for simulating the diffusion data using this method.

6.2.2 Independent simulation parameters

The parameters selected for the simulation of the attenuated diffusion-weighted MR signal were chosen so as to be similar to those used in the original articles [140, 141]. Thus, $E(\mathbf{q})$ was calculated using, Δ = 50 ms, δ = 1 ms, q-values 50, 100, 150, 200, 250, 300 $\times$ 10^3 m^{-1} (i.e., b-values 124, 497, 1118, 1987, 3104, 4470 $\times$ 10^6 s m^{-2}) and $D = 2.3 \times 10^{-9}$ m^2s^{-1}. The attenuated diffusion-weighted MR signal was simulated for 100 directions evenly spaced over the surface of each q-shell using an electrostatic repulsion model. δ was kept much shorter than in the papers cited above in order to meet the SGP condition. The BFOR reconstruction was performed with N = 6 and τ = 350 $\times$ 10^3 m^{-1}. $R = 50 \times 10^{-6}$ m and t = 0 for the respective reconstruction and smoothing of the probability isosurface. Two overlapping cylindrical geometries

were simulated in each experiment. The length of the restricting cylindrical geometry was maintained at 250 μm.

6.2.3 *Dependent simulation parameters*

Rician noise [166, 167] was added to simulated $E(\mathbf{q})$ values in order to achieve SNRs of 10, 50 and 100. These respectively indicate low, moderate and high MR signal-to-noise. The harmonic order of the spherical harmonic functions used in the processing of the diffusion data included L = 4, 6, 8 and 10. Three different diameters for the cylindrical geometry were included in the simulation, including d = 5, 25 and 50 μm, and the two simulated fibres were separated by 0°, 30°, 45°, 60° and 90° (a fibre separation of 0° yields the same result as a single simulated fibre). Each combination of the parameters listed in this section was tested, resulting in 180 different experiments. A hundred simulations were run for each of these experiments for statistical analysis. The coefficients of the Bessel-Fourier expansion (see Eq. (67) were angularly and radially regularised before being used to calculate the EAP [168] in order to smooth the probability isosurfaces. The values of these regularisation constants depended upon the SNR and the width of the cylinder used in the simulation (Table 1).

Table 1: The constants employed to regularise the angular component of the Bessel-Fourier expansion coefficients. The constants used to regularise the radial component were ten times the magnitude of the values in this table.

	Width		
SNR	d = 5 μm	d = 25 μm	d = 50 μm
10	1	1	1
50	100×10^{-3}	1	1
100	1×10^{-6}	1	1

6.2.4 *Real data from a botanical system*

To conclude the test, BFOR imaging was used to reconstruct diffusion data acquired from a real botanical system. As the structure of the grape berry mesocarp is quite

simple, the botanical specimen selected was a ripe calamondin. The flesh of the calamondin is divided into a number of self-contained segments (i.e. multiple carpels fused together). The calamondin carpels in turn consist of irregularly shaped pulp vesicles [169]. These vesicles are large plant cells, measurable on the millimetre scale and visible to the eye. Since it is possible to achieve an image voxel size on the micrometre scale, the reconstructed EAP isosurfaces will reflect the internal structures of the cell.

A PGSE echo planar DTI sequence was used to produce two-dimensional diffusion-weighted images of the calamondin. The sequence parameters used included THK 1 mm, MTX 128 × 128, δ 1 ms, Δ 70 ms, TE 76 ms, TR 11000 ms and NA 2. Five diffusion measurements, b = 500, 1000, 1500, 2000 and 3000 × 10^6 s m^{-2} ($q \approx$ 85, 120, 147, 169, 208 × 10^3 m^{-1}) were performed along forty-two directions (the vertices of a pentakis icosidodecahedron). One S_0 image was also acquired in order to normalise the diffusion weighted images. The total acquisition time was ~16.5 h. Diffusion data from a single transverse slice of the calamondin was acquired, located near the equator of the fruit. The acquired diffusion data was reconstructed using DTI and BFOR imaging. For the BFOR image reconstruction, L = 4 and τ = 350 × 10^3 m^{-1}. The EAP was reconstructed with N = 1 and N = 5. The DTI and BFOR images were reconstructed as maps of diffusion ellipsoids and probability isosurfaces respectively. To smooth the BFOR probability isosurfaces, R = 350 × 10^{-6} m and t = 0. The expansion coefficients were regularised using an angular/radial regularisation constant of 3 × 10^3 or 30 × 10^3, respectively

6.3 Results

6.3.1 Simulated data

The results of the simulations for angular orders 4, 6, 8 and 10 are presented in the tables below (Table 2 through Table 5, respectively). The effect of the width of the cylindrical geometry on the accuracy of the reconstructed fibre orientations was quite marked. For example, diffusion data with a moderate or a high SNR simulated from a pair of 5 μm diameter cylinders could be used to determine their orientations with a mean deviation from the ground truth by less than 5° for most cases. However, for

50 μm diameter cylinders, the reconstructed fibre orientation notably deviated from the ground truth except for fibre separations of 0 and 90°. There were difficulties in resolving the two simulated fibres when they were only separated by a small degree of separation (i.e., 30 μm). Only when the spherical harmonic order of the Bessel-Fourier expansion was high (i.e., L = 10) could two pairs of local maxima be observed. However, increasing the spherical harmonic order also resulted in a higher sensitivity to MR signal-to-noise.

6.3.2 Real data

The diffusion data were reconstructed within a selected region of interest which included multiple calamondin vesicles (Figure 30). As previously described [169], these vesicles were irregular in both size and shape. The dimensions of the vesicles within the region of interest varied between 0.5 and 4 mm. The diffusion data were reconstructed as DTI, QBI and BFOR images (Figure 31). The principal orientation of the diffusion ellipsoids from the diffusion tensor image was comparable to the probability isosurfaces of both BFOR images. The probability isosurfaces that constituted the BFOR (N = 5) image tended to be more elongated than the probability isosurfaces of the BFOR (N = 1) image. This indicates that the voxels of the BFOR image typically possess a single principal orientation population.

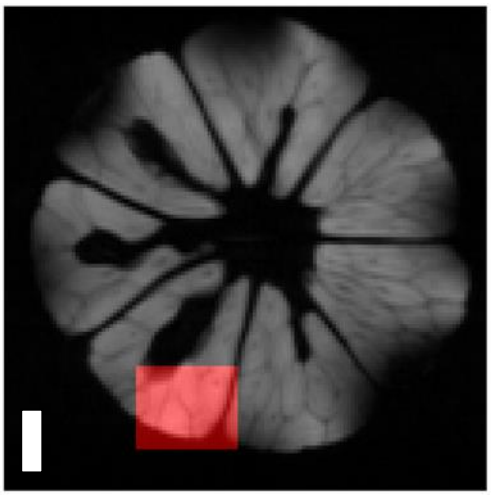

Figure 30: Transverse diffusion-unweighted image of the calamondin. The region of interest is highlighted in red. Scale bar; 3 mm.

Table 2: The deviation of the reconstructed simulated fibre orientations from the ground truth (in degrees). The reconstruction was performed with a spherical harmonic order of four.

Fibre separation	SNR 10			SNR 50			SNR 100		
	d = 5 μm	d = 25 μm	d = 50 μm	d = 5 μm	d = 25 μm	d = 50 μm	d = 5 μm	d = 25 μm	d = 50 μm
0°	0.00 ± 0.00	4.88 ± 2.14	11.77 ± 6.72	0.00 ± 0.00	0.00 ± 0.00	1.62 ± 2.01	0.00 ± 0.00	0.00 ± 0.00	0.08 ± 0.56
30°	15.22 ± 0.09	15.68 ± 0.57	18.55 ± 4.29	15.26 ± 0.00	15.20 ± 0.12	15.25 ± 0.23	15.26 ± 0.00	15.23 ± 0.08	15.23 ± 0.10
45°	22.59 ± 0.09	23.05 ± 0.45	23.81 ± 3.23	22.52 ± 0.05	22.96 ± 0.08	23.19 ± 0.22	22.50 ± 0.02	23.00 ± 0.03	23.07 ± 0.23
60°	2.68 ± 1.21	26.27 ± 8.46	26.69 ± 7.88	2.93 ± 0.00	23.55 ± 8.60	29.69 ± 3.02	2.93 ± 0.00	13.06 ± 5.05	29.86 ± 1.60
90°	0.75 ± 1.11	10.26 ± 6.95	29.06 ± 14.28	0.00 ± 0.00	0.63 ± 1.16	3.86 ± 1.82	0.00 ± 0.00	0.00 ± 0.00	1.39 ± 1.41

Table 3: The deviation of the reconstructed simulated fibre orientations from the ground truth (in degrees). The reconstruction was performed with a spherical harmonic order of six.

Fibre separation	SNR 10			SNR 50			SNR 100		
	d = 5 μm	d = 25 μm	d = 50 μm	d = 5 μm	d = 25 μm	d = 50 μm	d = 5 μm	d = 25 μm	d = 50 μm
0°	0.00 ± 0.00	6.81 ± 3.68	16.95 ± 9.81	0.00 ± 0.00	0.37 ± 1.21	3.20 ± 2.17	0.00 ± 0.00	0.04 ± 0.40	0.65 ± 1.51
30°	15.14 ± 0.13	16.52 ± 2.65	21.48 ± 8.54	15.23 ± 0.08	15.19 ± 0.18	15.33 ± 0.35	15.26 ± 0.00	15.22 ± 0.09	15.26 ± 0.23
45°	1.48 ± 1.50	20.72 ± 5.69	23.30 ± 7.26	0.00 ± 0.00	23.05 ± 0.26	22.92 ± 1.43	0.00 ± 0.00	23.10 ± 0.12	23.20 ± 0.59
60°	2.20 ± 1.18	17.31 ± 8.86	29.87 ± 15.71	1.08 ± 0.53	4.51 ± 0.97	16.59 ± 10.53	0.98 ± 0.28	3.67 ± 0.80	7.70 ± 2.95
90°	0.98 ± 1.37	15.21 ± 7.17	29.72 ± 13.95	0.00 ± 0.00	1.96 ± 1.51	6.17 ± 2.18	0.00 ± 0.00	0.40 ± 0.89	2.74 ± 1.56

Table 4: The deviation of the reconstructed simulated fibre orientations from the ground truth (in degrees). The reconstruction was performed with a spherical harmonic order of eight.

Fibre separation	SNR 10			SNR 50			SNR 100		
	d = 5 µm	d = 25 µm	d = 50 µm	d = 5 µm	d = 25 µm	d = 50 µm	d = 5 µm	d = 25 µm	d = 50 µm
0°	3.82 ± 1.49	37.37 ± 25.70	39.44 ± 23.91	0.00 ± 0.00	1.04 ± 1.84	3.95 ± 2.03	0.00 ± 0.00	0.28 ± 1.02	1.58 ± 2.00
30°	13.26 ± 4.29	40.26 ± 17.79	38.19 ± 17.29	15.27 ± 0.05	15.25 ± 0.25	15.55 ± 1.14	15.28 ± 0.03	15.20 ± 0.16	15.39 ± 0.30
45°	4.08 ± 1.70	40.36 ± 19.09	41.68 ± 18.31	1.69 ± 0.71	23.06 ± 0.94	21.57 ± 4.55	1.97 ± 0.20	23.24 ± 0.40	22.33 ± 1.56
60°	4.86 ± 1.22	36.64 ± 21.36	39.97 ± 20.68	1.48 ± 0.00	5.08 ± 1.22	13.08 ± 6.71	1.48 ± 0.00	4.01 ± 0.80	7.81 ± 3.72
90°	4.02 ± 1.66	46.21 ± 18.99	43.06 ± 19.74	0.00 ± 0.00	3.14 ± 1.64	8.11 ± 2.99	0.00 ± 0.00	0.78 ± 1.13	4.00 ± 1.72

Table 5: The deviation of the reconstructed simulated fibre orientations from the ground truth (in degrees). The reconstruction was performed with a spherical harmonic order of ten.

Fibre separation	SNR 10			SNR 50			SNR 100		
	d = 5 µm	d = 25 µm	d = 50 µm	d = 5 µm	d = 25 µm	d = 50 µm	d = 5 µm	d = 25 µm	d = 50 µm
0°	2.99 ± 2.17	44.73 ± 24.00	46.84 ± 24.20	3.98 ± 0.00	1.74 ± 2.26	5.39 ± 2.46	3.98 ± 0.00	0.16 ± 0.78	2.73 ± 2.22
30°	9.76 ± 6.31	40.98 ± 19.00	39.62 ± 18.74	3.31 ± 0.44	15.27 ± 1.29	14.78 ± 2.66	3.21 ± 0.00	15.28 ± 0.27	15.50 ± 0.35
45°	6.77 ± 4.77	46.88 ± 19.09	44.83 ± 20.82	2.10 ± 0.52	21.09 ± 4.03	22.84 ± 9.78	1.99 ± 0.00	22.42 ± 2.58	22.98 ± 7.41
60°	7.26 ± 4.43	39.63 ± 19.80	42.40 ± 20.50	3.95 ± 0.48	6.04 ± 1.54	12.33 ± 5.34	3.75 ± 0.46	4.41 ± 1.37	8.48 ± 2.87
90°	7.92 ± 5.90	44.76 ± 18.62	41.53 ± 16.97	1.99 ± 0.00	4.26 ± 1.63	9.47 ± 2.61	1.99 ± 0.00	2.08 ± 1.52	5.17 ± 1.81

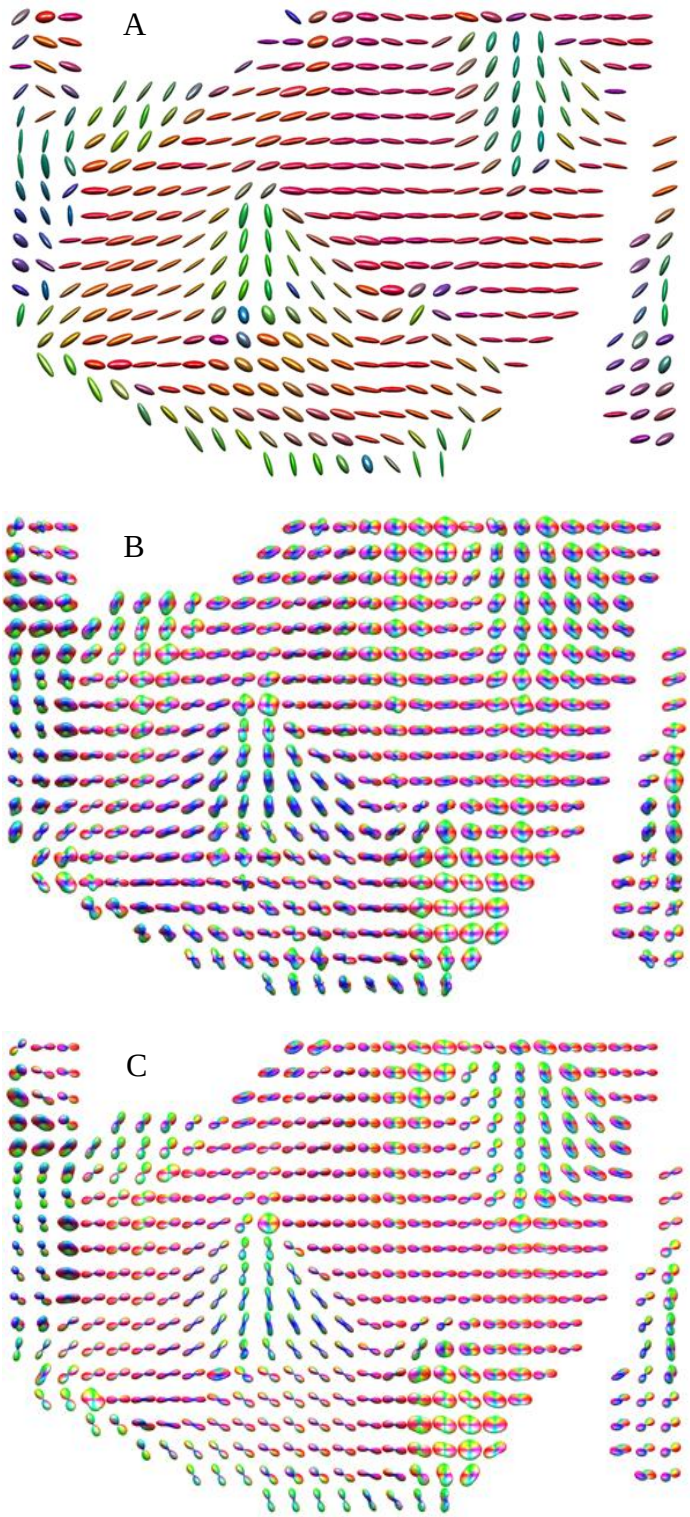

Figure 31: DTI (A), BFOR (N = 1) (B) and BFOR (N = 5) (C) profile of water diffusing through the calamondin region of interest (see Figure 30). When performing the BFOR reconstructions, L = 4 and $\tau = 350 \times 10^3$ m^{-1}. The MRI pulse sequence parameters used for the acquisition included THK 1 mm, MTX 128 × 128, δ 1 ms, Δ 70 ms, TE 76 ms, TR 11000 ms and NA 2. Five diffusion measurements, b = 500, 1000, 1500, 2000 and 3000 × 10^6 s m^{-2} ($q \approx$ 85, 120, 147, 169, 208 × 10^3 m^{-1}) were performed along forty-two directions (the vertices of a pentakis icosidodecahedron).

6.4 Discussion

The results of simulated diffusion data experiments indicate that BFOR imaging is well suited to reconstructing the orientation of complicated diffusion restricting structures consisting of narrow fibres, such as brain matter and muscle tissue. However, it could be inferred from the results that this method will not be suited to the examination of tissues consisting of fibres 50 μm or wider. By increasing the length of the 50 μm simulated cylindrical geometry, the deviation of the deduced fibre orientation from the ground truth was reduced. Therefore the decrease in the accuracy of the reconstructed probability isosurface with respect to cylindrical width was linked to the anisotropy of the diffusion restricting simulated geometry. Consequently, BFOR imaging can be employed for wide fibrous tissue structures, provided that they are highly elongated and the diffusion period is long (i.e., ≥ 50 ms). This technique is suited to the characterisation of the plant vasculature, roots, stems and petioles due to the elongated fibres that comprise these tissues. However, less anisotropic biological structures can potentially be examined by decreasing the spherical harmonic order of the Bessel-Fourier expansion and ensuring that the diffusion-weighted images have a high SNR. While expansions of the MR signal at low spherical harmonic orders result in probability isosurfaces with poor angular resolution, expansions at high spherical harmonic orders are much more sensitive to MR signal noise as the more complicated isosurface fits more closely to noisy diffusion data.

The BFOR images reconstructed from the diffusion data acquired from the calamondin were a promising indicator of the suitability of this diffusion MRI technique for imaging complicated botanical systems. The calamondin presented a special challenge as the large size of its vesicles meant that a subcellular image resolution was achievable. While the vesicles of the calamondin were irregular in shape, there was a preference for radial cell elongation. However, within the cells much more diverse environments are possible. To provide a standard with which to compare the reconstructed BFOR images, the diffusion data was also reconstructed as a DTI image. Due to the low anisotropy of the vesicle microstructure, the spherical harmonic order of the BFOR reconstructions was kept relatively low (i.e. $L = 4$).

Overall, both BFOR images compared favourably with the DTI image, with the shape of the BFOR (N = 5) probability isosurfaces tending to fall somewhere between that of diffusion ellipsoids and the BFOR (N = 1) probability isosurfaces. The BFOR probability isosurfaces typically exhibited a single pair of maxima, indicating only one principal direction of diffusion within the voxel. However, in some regions of the cell, the shape of the probability isosurface indicated that there was more than one preferred diffusion direction population present. These voxels likely reflect the anisotropic microstructure of cellular organs.

6.4.1 Selecting probability isosurface smoothing constants

Selecting an appropriate set of constants to smooth reconstructed probability isosurfaces was important to consider when processing the diffusion data. The choice of these constants was made to maximise the smoothness of the isosurface while sacrificing as little angular resolution as possible. The smoothness of the reconstructed isosurface was largely dictated by the choice of the angular and radial regularisation constants. The value of these two regularisation constants was in turn dependent on two primary factors; the width of the cylindrical geometry and the maximum harmonic order of the spherical harmonic functions used in the diffusion model. Probability isosurfaces reconstructed from diffusion models with a high harmonic order (i.e., 8 or 10) generally required regularisation constants much smaller than one to ensure the smoothness of the surface. As the width of the simulated fibre increased, the value of regularisation constants had to be likewise increased in order to smooth the isosurface. This is because the effect of MR signal noise has a stronger influence over the shape of the isosurface when the cylindrical geometry is less anisotropic.

The regularisation constants were not changed between experiments which differed only by SNR or the degree of separation between simulated fibres. This is because a pair of regularisation constants that were suitable for regularising the coefficients of the Bessel-Fourier expansion when the diffusion data had a low SNR was also suitable for coefficient regularisation when the diffusion data has high SNR. Likewise, a pair of regularisation constants that were suitable for regularising the coefficients of the Bessel-Fourier expansion when the simulated fibres were

separated by a small degree was also suitable for coefficient regularisation when the fibres had a higher degree of separation. It was observed that probability isosurfaces reconstructed from diffusion data with a high SNR and/or with a low spherical harmonic order could be regularised with a wider range of regularisation constants without notably changing the shape of the isosurface. Another reason for not changing the regularisation constants due to variations in the degree of separation between simulated fibres is that this would require *a priori* information regarding the restricting microstructure.

The use of t as smoothing factor was found too unreliable for use in these tests. Values of t greater than zero radically smoothed and altered the probability of the isosurface but did not approach a stable shape unlike when regularising the coefficients of the Bessel-Fourier expansion. It was therefore impossible to discern the correct shape of the isosurface without *a priori* knowledge of the diffusion restricting system by employing this smoothing factor. This finding is unfortunate as the inclusion of t in Eq. (74) offered a potential method for controlled isosurface smoothing and an additional advantage over other diffusion MRI techniques, such as *q*-ball imaging and diffusion propagator imaging (see Appendix A - *q-ball* imaging and Appendix A - Diffusion propagator imaging), where isosurface smoothing cannot be controlled.

To accommodate the presence of both high and low anisotropy diffusion restricting microstructure within a diffusion-weighted image, a hybrid spherical harmonic order scheme could be employed. The diffusion data could first be processed using *q*-ball imaging in order to estimate the GFA (see Appendix A - *q-ball* imaging). Regions which have a high GFA could be modelled using BFOR at a high spherical harmonic order of regions while regions with a low GFA could be modelled at a lower spherical harmonic order. However, the coefficients of the Bessel-Fourier expansion relating to these different regions must be regularised with different constants in order to ensure that the probability isosurface remains smooth.

The results of the simulations indicate that BFOR imaging is not well suited to imaging grape berries. The large dimensions of the grape berry cells (see Section 1.1.1 Cell sizes of the grape berry pericarp tissues) could result in a poor fit using BFOR imaging. Additionally, from previous observations gathered using traditional

optical microscopy [4, 27], it is known that the bulk of the grape berry consists of radially elongated parenchyma. Consequently, there is a great likelihood that only one principal direction of diffusion will exist per voxel. Hence from this point forward, the diffusion-weighted images of the grape berry pericarp will be processes using DTI. However, it will be noted here that BFOR imaging could potentially prove useful for studying narrow and complicated plant tissue structures, such as root systems and leaf petioles.

Chapter 7 - Diffusion MRI of grapes at different stages of development

[The results contained within this chapter were presented in 'Dean, R. J., T. Stait-Gardner, S. J. Clarke, S. Y. Rogiers, G. Bobek and W. S. Price (2014). "Use of diffusion magnetic resonance imaging to correlate the developmental changes in grape berry tissue structure with water diffusion patterns." *Plant Methods* 10, 35.']

7.1 Introduction

Having selected DTI as the diffusion MRI method of choice for investigating the tissues of the grape berry pericarp, the diffusion MRI investigation of pericarp morphology could commence. The first objective of the relaxation and diffusion MRI experiments was to verify whether they can accurately reflect the relative size, orientation and organisation of the cells that constitute the different tissues of the grape berry pericarp. As previous MRI studies of grape berry tissue structure have focussed on grape berries at single time-points, the second objective of the study was to examine structural changes across grape berry development via diffusion and relaxation MRI. A brief and complementary MRI study on mature olives was also included in this chapter in order to determine the applicability of relaxation and diffusion MRI to fruits and vegetable with high natural oil content. Natural oils extracted from plant materials, such as olive, coconut, corn and palm oil, are often highly valued commodities [170]. As natural oils are highly hydrophobic, it is reasonable to hypothesise that diffusing water molecules are likely to treat small droplets of oil encountered in the cell cytoplasm [171] as diffusion restricting obstacles. Depending on the concentration of oil in the cytoplasm, water diffusion could potentially be heavily restricted. High concentrations of oil in the cell cytoplasm could prevent water molecules to reaching and probing surrounding

diffusion restricting cellular boundaries. Consequently, it may prove that diffusion MRI is unsuitable for examining the morphology of fruits and vegetables with high oil content. Mature olives were determined to be an ideal candidate for this complementary study as they are also comparable to grape berries in terms of their internal tissue structure and cellular dimensions [172, 173].

7.2 Materials and methods

7.2.1 Experimental procedures

Berries were sampled fortnightly for imaging, beginning four weeks after flowering and ending three months later. To minimise developmental variability at each sampling event, grape bunches were assigned to classes according to flowering date (28, 41, 55, 70, 84, 95 and 109 DAF respectively). Seven bunches were randomly chosen per sampling event. Each sample consisted of the distal portion of the bunch (approximately 10 berries), which were obtained by cutting the rachis while it was momentarily submersed in tap water. The detached, distal portion of the bunch was wrapped in a moist paper towel, placed in a zip-lock bag and shipped overnight to the Biomedical Magnetic Resonance Facility. Three berries were examined per age class (for a total of twenty-one grape berries) to monitor changes in the diffusion pattern across the berry over the course of its development. Berries of an average size (with respect to the bunch) were cut 3 to 4 mm above the pedicel. All MRI protocols were completed within 11 hours of berry detachment. Three detached, mature olives, cv. Correggiolla, were also imaged over the course of this study to offer a comparison to the grape berries. These two different fruits were imaged using the MRI sequences described below.

7.2.2 MRI pulse sequence protocols for the grape berries

A MSME MRI sequence was employed to produce two-dimensional images of the grape berries which were weighted by spin-spin relaxation. The sequence parameters used included THK 1 mm, MTX 256 × 256, a train of 16 echoes spaced 10 ms apart, TR 5 s and NA 2 (total acquisition time ~32 min). A PGSE echo planar DTI

sequence was used to produce three-dimensional images of the grape berries weighted by diffusion. The sequence parameters used included THK 1 mm, MTX 128 × 128, δ 1 ms, NA 1 and 13 segments. Two diffusion measurements (b weighting of 250 and 500 s mm^{-2}) were performed along forty-two directions (the vertices of a pentakis icosidodecahedron). One S_0 image (which had a negligible diffusion weighting) was also acquired in order to normalise the diffusion weighted images. The echo-planar DTI pulse sequence parameters were set in order to maximise the length of Δ and minimise the loss of MR signal due to spin-spin relaxation. Additionally, the TR was adjusted to be five times the length of the maximum spin-lattice relaxation time (5 × T_1) of each grape berry in order to minimise unintended spin-lattice relaxation weighting. Due to differences in the spin-spin and spin-lattice relaxation properties of the berries grape across their development, Δ, TE and TR were adjusted for each age class of grape berry (total acquisition time ~2.1 – 3.8 h) (Table 6).

Table 6: Summary of the Δ, TE and TR values used for the DTI sequences. These values were adjusted for each age class of grape berry due to changes in the transverse and spin-lattice relaxation properties of the berries across their development.

Berry age (DAF)	Δ (ms)	TE (ms)	TR (ms)
28	25	40	12500
41	50	65	15000
55	50	60	15000
70	50	60	10000
85	25	35	8000
95	25	35	7000
109	25	35	7000

7.2.3 MRI pulse sequence protocols for the olives

A MSME MRI sequence was employed to produce two-dimensional images of the olives which were weighted by spin-spin relaxation. The sequence parameters used included THK 1 mm, MTX 64 × 64, a train of 16 echoes spaced 10 ms apart, TR 5 s and NA 4 (total acquisition time ~16 min). A PGSTE DTI pulse sequence was employed to produce three-dimensional images of the olives which were weighted by diffusion. A faster (i.e. echo planar variant) diffusion MRI sequence could not be employed due a noticeable loss of radio-frequency magnetic pulse power arising from the high concentration of salt in the olives. Additionally, since a low mean diffusivity coefficient was expected for the olive pericarp tissue, a lengthy diffusion period was imposed to ensure that diffusing water molecules had ample time to probe restricting tissue microstructures. Consequently, a PGSE DTI sequence could not be employed due to prohibitive MR signal loss arising from spin-spin relaxation.

The sequence parameters of the PGSTE DTI pulse sequence used included THK 1 mm, MTX 64 × 64, δ 6 ms, Δ 80 ms, TE 20 ms, TR 3500 ms and NA 4 (total acquisition time ~10 h). Two diffusion measurements (b weighting of 80000 and 160000 s mm^{-2}) were performed along twenty directions (the vertices of a dodecahedron). One S_0 image was also acquired in order to normalise the diffusion weighted images. For the analysis of the spin-spin relaxation and DT images of the olive, the pericarp was treated as a single tissue. This was due to the large voxel size of the images (i.e., 390 × 390 × 1000 μm) and lack of distinctive tissue types visible in the images.

7.2.4 MR image analysis

Each constituent tissue of the grape berry pericarp (see Section 1.1 The tissues of the grape berry pericarp and Figure 32) was analysed independently from all other regions by the application of image masks. For the analysis of the relaxation images, a mean T_2 was determined for each of the pericarp tissues, from each grape berry in the same age group. A standard error was also calculated for each tissue based on the mean T_2 values across each respective age group. The acquired DT image data, on the other hand, was used to create three images of each grape berry; a diffusivity map (a map of the average ADC for each voxel), a diffusion vector field map and a

diffusion colour map (to indicate the direction of least restricted diffusion). The DT colour maps used a symmetrical additive red/blue/green colour scheme to represent that the direction of least restricted diffusion in each voxel was horizontal/longitudinal/ perpendicular with respect to the FOV. Mean diffusivity values and accompanying standard errors were calculated from diffusivity maps on a per tissue basis.

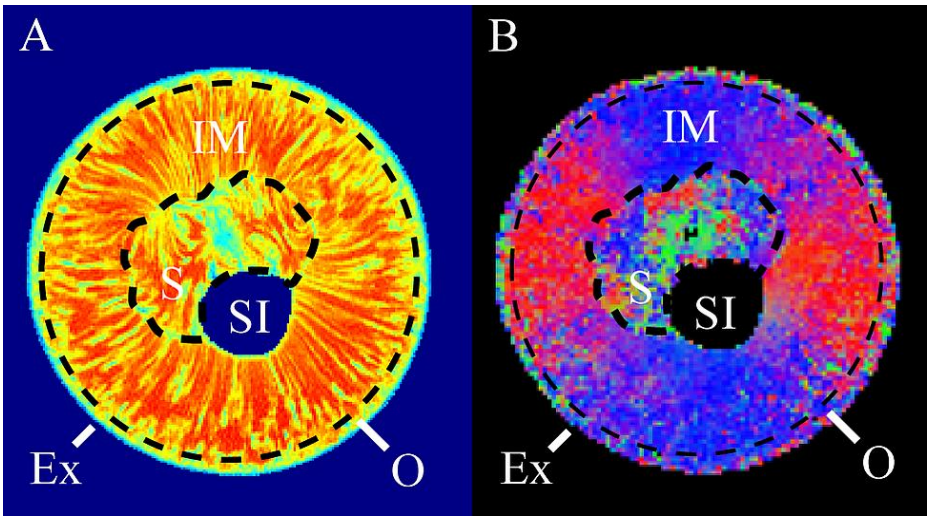

Figure 32: Tissue regions of the grape berry (transverse plane). Here the five tissue regions of the grape berry are provided with reference to a spin-spin relaxation image (A) and a diffusion tensor image (B). Ex: exocarp, OM: outer mesocarp, IM: inner mesocarp, S: septum, SI: seed interior. The outer, black dashed curve indicates the border between the outer mesocarp and the inner mesocarp while the inner, black dashed curve indicates the border between the inner mesocarp and the septum.

A high spatial resolution diffusion tensor (DT) image of a grape berry 55 DAF was used to confirm whether the radial striation patterns visible in the relaxation images were linked to variations in cellular size across the inner mesocarp tissue. This was done by using the S_0 image (which has a small T_2 weighting, and had visible striation patterns in the inner mesocarp region) to create an MR signal intensity threshold mask. The threshold value was qualitatively chosen in order to divide the inner mesocarp into radial bands of voxels with ‘relatively high’ and ‘relatively low’ signal intensity. The image mask was then applied to the DT image data to create two populations of voxels. The three eigenvalues of the DT (i.e. three orthogonal ADCs,

the largest of which corresponds to the direction of least diffusion restriction) for each voxel were averaged over the two populations. This resulted in two groups of primary, secondary and tertiary eigenvalues. The mean primary eigenvalue was proportional to the average length of the cells in the voxel, while the mean secondary and tertiary eigenvalues corresponded to either the average width or depth of the cells (see Section 4.2.1 Eigenvectors, eigenvalues and useful scalars of the diffusion tensor). The Tukey-Kramer test [174, 175] (P = 0.05) was then performed to determine whether differences between corresponding mean eigenvalues were statistically significant, which would indicate if there was a significant difference in average cell size across the bands of the inner mesocarp striations.

7.3 Results

The grape berries increased in size and weight and then declined as the berries progressed through the ripening and senescence phases (Figure 33). The concentration of soluble solids in the grape berries increased sigmoidally with respect to time (adjusted R^2 = 0.99). Véraison occurred at approximately 60 – 65 DAF, and full ripeness was placed at 95 DAF (based on the mean concentration of soluble solids of the sampled berries which plateaued at 26 °Brix).

The spin-spin relaxation images of the outer mesocarp generally lacked consistent or well defined features (Figure 34 and 35). The mean T_2 of the outer-mesocarp tended to be longer than those of the exocarp, but shorter than other tissues (Figure 36). The diffusion vectors had a rotational dependency (Figure 37, 38 and 39) and were aligned so as to radiate from the centre of the fruit. In pre-véraison berries, the diffusivity values of the outer mesocarp were amongst the highest observed. For post-véraison grape berries, however, the mean diffusivity values of the outer mesocarp declined further than other tissues (Figure 40).

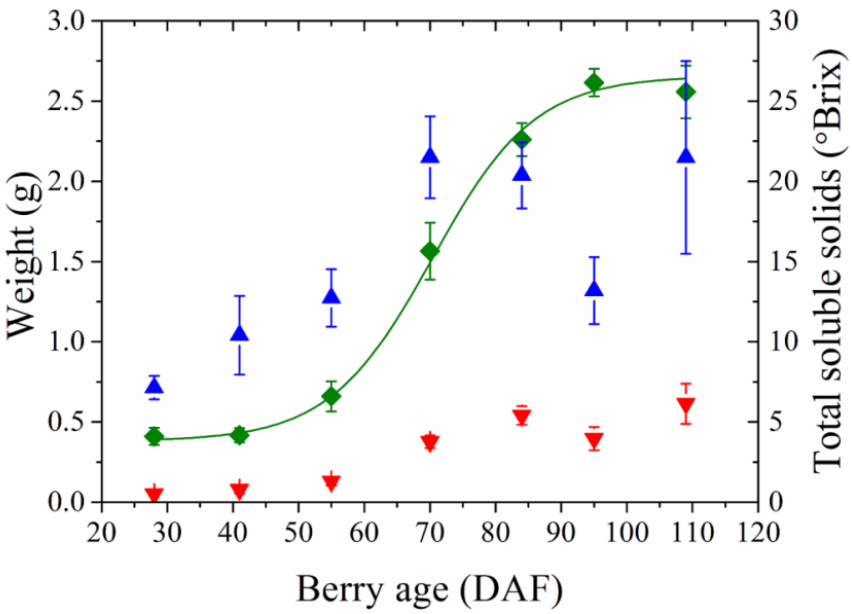

Figure 33: The physical characteristics of the grape berries. The concentrations of soluble solids of the grape berries (♦), as well as the fresh weight (▲) and dry weights (▼) of the berries, are presented with respect to the number of days after flowering. A sigmoidal function (solid green curve) of the form $a_1 + (a_1 + (a_2 - a_1)/(1 + \exp(-\mathrm{DAF} - x_0)/w))$ was fitted to the soluble solids values by nonlinear regression (adjusted $R^2 = 0.99$), where $a_1 = 26.1$ (the approximate maximum soluble solids value), $a_2 = 3.9$ (the approximate minimum soluble solids value), $x_0 = 69.7$ (the inflection point) and $w = 7.4$ (the change in DAF which yielded the greatest change in the soluble solids value). The error bars reflect the standard deviation of soluble solids values at each time point.

A notable feature in the spin-spin relaxation images of the inner mesocarp was the clear radial striation patterns with distinctly different (Tukey-Kramer test, $P = 0.05$) T_2 values. These patterns were observed in both transverse and longitudinal image orientations for the inner mesocarp (Figure 34 and 35) of grape berries between 28 DAF and 109 DAF. The striation pattern radiated throughout the entire sub-tissue, starting close to the septum and vascular systems at the centre of the berry (i.e., at the ovular and axial vascular network), and terminating at the interface between the inner and outer mesocarp. Additionally, upon analysing the high resolution DT image of a grape berry 55 DAF (Figure 41), a statistically significant difference (Tukey-Kramer test, $P = 0.05$) was noted between the mean secondary and tertiary eigenvalues across the striation bands (Table 7).

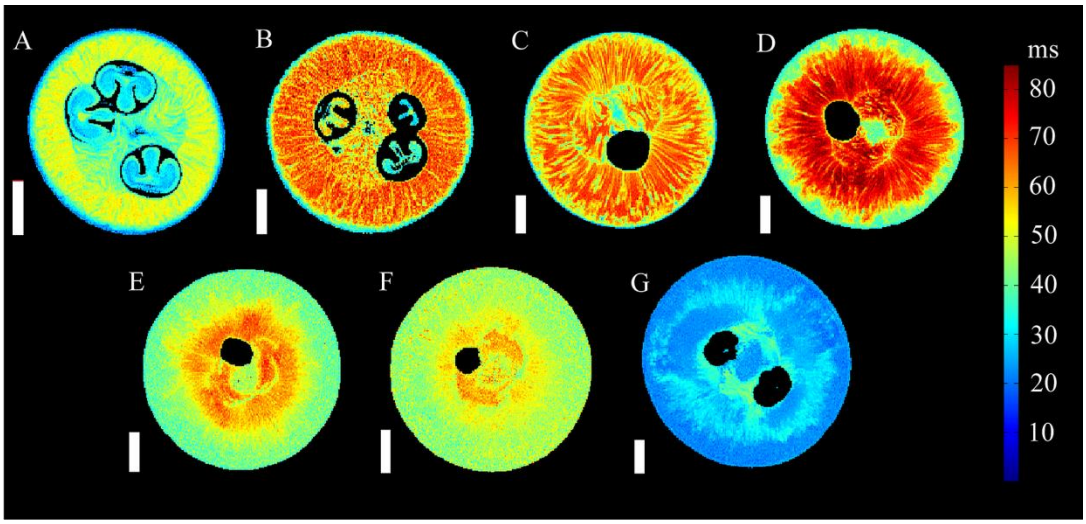

Figure 34: Spin-spin relaxation images of grape berries at seven different stages of berry development in the transverse plane. The images include three pre-véraison grapes, at 28 DAF (A, voxel size 59 × 59 × 1000 µm), 41 DAF (B, voxel size 78 × 78 × 1000 µm) and 55 DAF (C, voxel size 78 × 78 × 1000 µm), a grape undergoing véraison at 70 DAF (D, voxel size 82 × 82 × 1000 µm), a ripening grape at 85 DAF (E, voxel size 74 × 74 × 1000 µm), a grape which is at maturity at 95 DAF (F, voxel size 63 × 63× 1000 µm) and a post-maturity berry at 109 DAF (G, voxel size 86 × 86 × 1000 µm). The spin-spin relaxation values are indicated by the colour bar to the right of the figure. Scale bar: 3 mm.

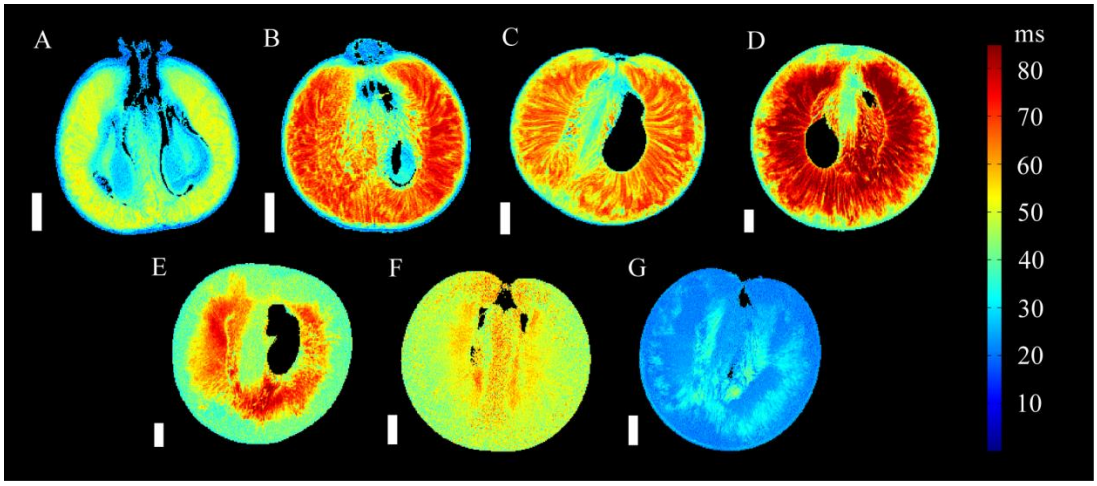

Figure 35: Spin-spin relaxation images of the same grape berries from Figure 34 at seven different stages of berry development but in the longitudinal plane. The images include three pre-véraison grapes, at 28 DAF (A, voxel size 59 × 59 × 1000 µm), 41 DAF (B, voxel size 78 × 78 × 1000 µm) and 55 DAF (C, voxel size 78 × 78 × 1000 µm), a grape undergoing véraison at 70 DAF (D, voxel size 133 × 133 × 1000 µm), a ripening grape at 85 DAF (E, voxel size 82 × 82 × 1000 µm), a grape which is at maturity at 95 DAF (F, voxel size 63 × 63 × 1000 µm) and a post-maturity berry at 109 DAF (G, voxel size 86 × 86 × 1000 µm). The spin-spin relaxation values are indicated by the colour bar to the right of the figure. Scale bar: 3 mm.

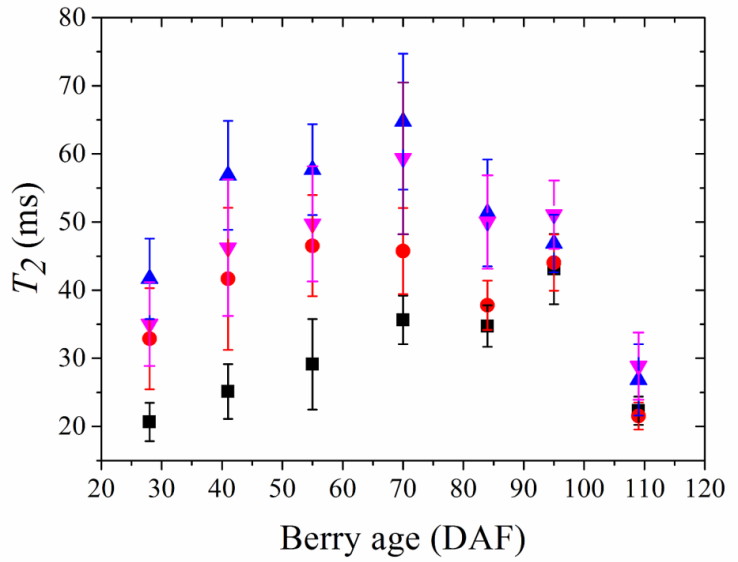

Figure 36: Transverse (T_2) relaxation of the major tissue groups of the grape berry with respect to berry age (transverse plane). The spin-spin relaxation values for the exocarp (■), outer mesocarp (●), inner mesocarp (▲) and septum (▼). The error bars are given by the standard deviation of the spin-spin relaxation values at each time point.

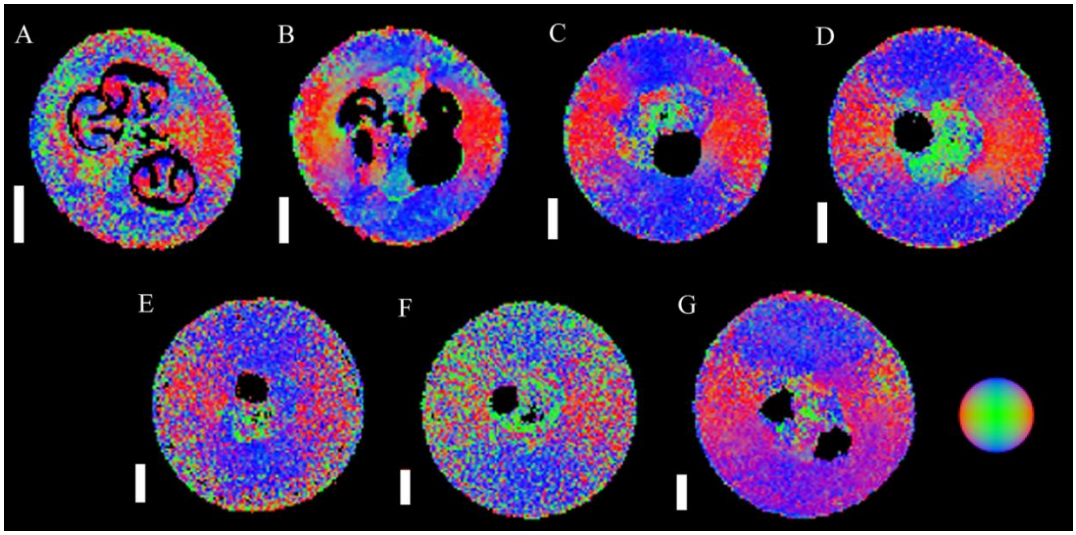

Figure 37: DT images of grape berries at seven different stages of berry development in the transverse plane. The images include three pre-véraison grapes, at 28 DAF (A, voxel size 117 × 117 × 1000 µm), 41 DAF (B, voxel size 156 × 156 × 1000 µm) and 55 DAF (C, voxel size 156 × 156 × 1000 µm), a grape undergoing véraison at 70 DAF (D, voxel size 164 × 164 × 1000 µm), a ripening grape at 85 DAF (E, voxel size 148 × 148 × 1000 µm), a grape at maturity at 95 DAF (F, voxel size 125 × 125 × 1000 µm) and a post-maturity berry, at 109 DAF (G, voxel size 171 × 171 × 1000 µm). The colours in the figure indicate the direction of least restricted diffusion (bottom right glyph). Scale bar: 3 mm.

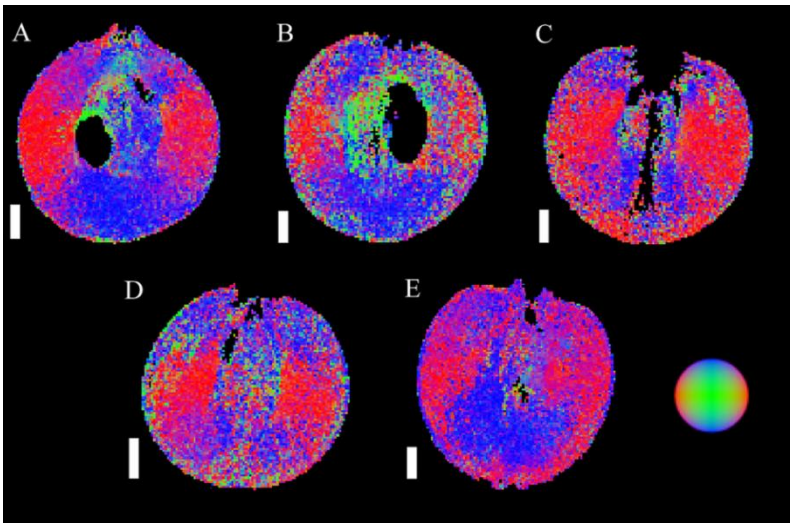

Figure 38: DT images of the same grape berries from Figure 37 at five different stages of berry development but in the longitudinal plane (data not available for 28 and 41 DAF). The images include a pre-véraison grape at 55 DAF (A, voxel size 156 × 156 × 1000 µm), a grape undergoing véraison at 70 DAF (B, voxel size 164 × 164 × 1000 µm), a ripening grape at 85 DAF (C, voxel size 172 × 172 × 1000 µm), a grape which is at maturity at 95 DAF (D, voxel size 125 × 125 × 1000 µm) and a post-maturity berry at 109 DAF (E, voxel size 172 × 172 × 1000 µm). The colours in the figure indicate the direction of least restricted diffusion (bottom right glyph). Scale bar: 3 mm.

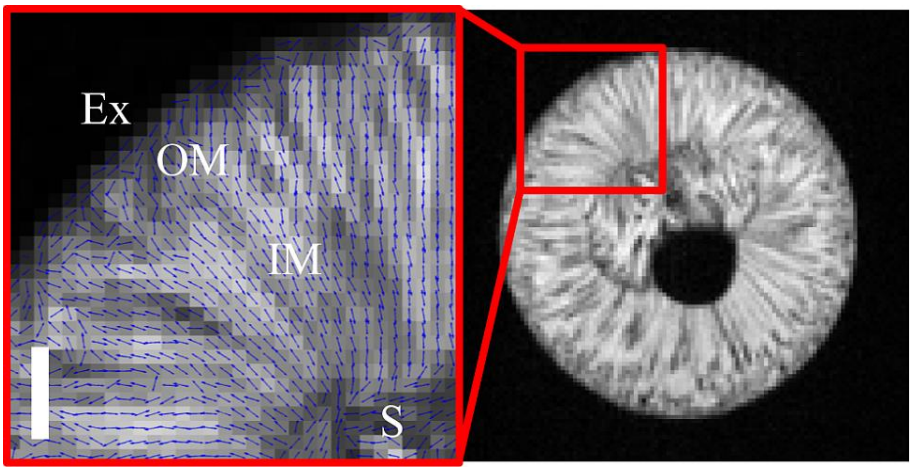

Figure 39: Diffusion vector field map overlaying the S_0 image of a grape berry 41 DAF (transverse plane). The diffusion vectors (blue arrows) indicate the direction of least restricted diffusion in each voxel. Voxel size: 156 × 156 × 1000 µm, bar length: 1000 µm.

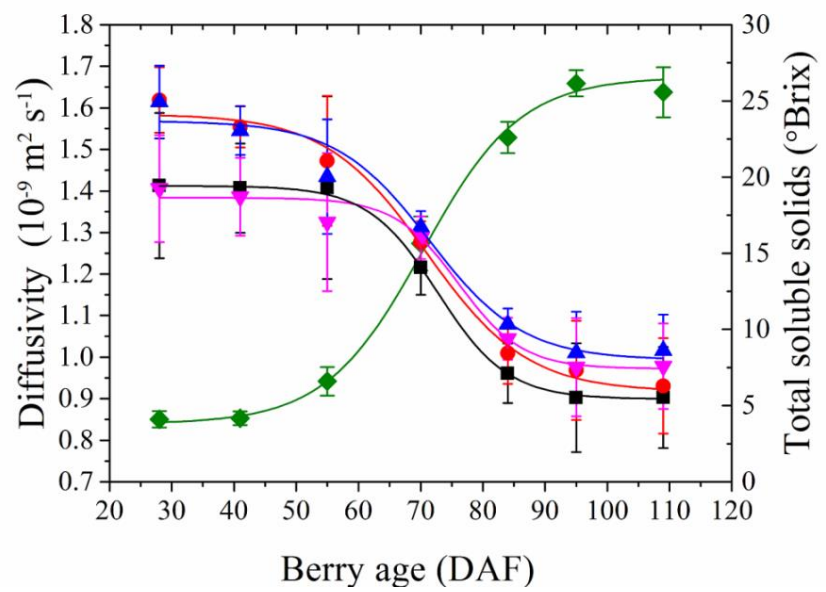

Figure 40: Mean ADC of the major tissue groups of the grape berry with respect to berry age. The total soluble solids with respect to berry age are also shown. The mean ADC for the exocarp (■), outer mesocarp (●), inner mesocarp (▲) and septum (▼) decrease sigmoidally (adjusted R^2 = 0.99) with respect to sigmoidally increasing (adjusted R^2 = 0.99) dissolved solids content (♦). The error bars reflect the standard deviation of the mean ADC at each time point.

Table 7: Each eigenvalue is expressed as the mean of the diffusion tensor eigenvalues (ADCs). The standard error was not included as it was insignificant (< 1% of the values listed). Asterisks denote values between which there was no statistically significant difference (Tukey-Kramer test, *P* = 0.05).

	Mean primary eigenvalue ($\times 10^{-9}$ m^2 s^{-1})	Mean secondary eigenvalue ($\times 10^{-9}$ m^2 s^{-1})	Mean tertiary eigenvalue ($\times 10^{-9}$ m^2 s^{-1})
Striation bands with high signal intensity	1.53*	1.44	1.36
Striation bands with low signal intensity	1.54*	1.41	1.30

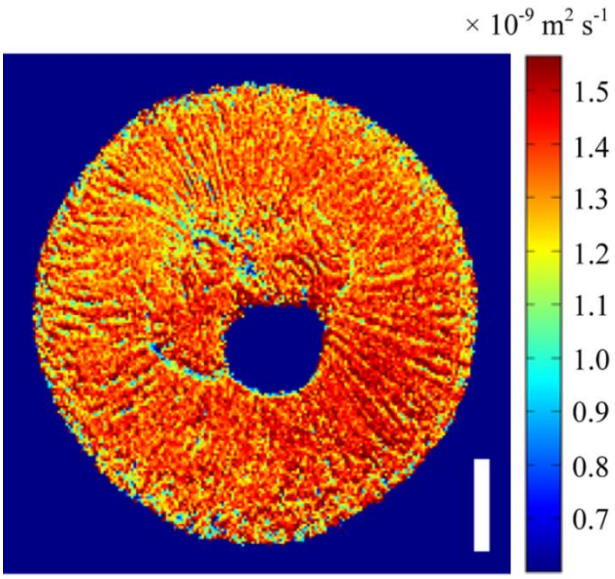

Figure 41: Mean ADC map of a grape berry 55 DAF (transverse plane). Voxel size 78 × 78 × 1000 µm, bar length: 3000 µm.

Prior to 95 DAF, the mean T_2 of the inner mesocarp was consistently higher than other tissues (Figure 36). After the concentration of soluble solids plateaued, the mean T_2 of this tissue declined, accompanied by a partial loss of its radial striation pattern. The diffusion vectors of the inner mesocarp had a rotational dependency similar to that of the outer mesocarp. For most of berry development, the inner mesocarp was also consistently associated with the largest mean diffusivity values, relative to the other tissues examined (Figure 40). Furthermore, the diffusion vectors were predominantly parallel to the radial striation bands (Figure 37 – 39), except for grape berries 28 DAF or past 95 DAF (Figure 42). However, upon approaching full ripeness, regions of the berry inner mesocarp exhibited a loss of coherence in orientation of diffusion anisotropy (Figure 42). This was accompanied by a decline in T_2 values and partial loss of the radial striation pattern in the spin-spin relaxation images of these same regions.

The septum was readily distinguishable from the surrounding mesocarp tissue in the spin-spin relaxation images. This was due to the presence of curved striation patterns which were perpendicular to the striation patterns of the inner mesocarp (Figure 34 and 35). These striation patterns were curled about the central vascular bundles and extended through the septum to the seeds and locules. Prior to 95 DAF, the mean T_2

of the septum was consistently higher than the exocarp, but lower than the inner mesocarp. After 95 DAF, the septum had the highest mean T_2 (Figure 36). Unlike the inner mesocarp, the diffusion vectors of the septum were not consistently parallel to the striation patterns of the tissue (Figure 37 – 39). The anisotropic diffusion pattern of the septum differed on a per berry basis. The septal-mesocarp boundary could be discerned by abrupt changes in the local orientation of diffusion vectors. The mean diffusivity value of the septum was the lowest of all the examined tissues pre-véraison, but had a mean diffusivity greater than that of the exocarp and outer mesocarp post-véraison (Figure 40).

In the grape seed interior, the nucellus (located towards the bulbous distal end of the seed) was identified in grape berries aged 28 and 41 DAF. It could be readily identified in berries of this age, as it occupies a sizeable portion of the seed and has a stylised '3' shape when imaged through the transverse plane [176]. The nucellus demonstrated a highly characteristic anisotropic diffusion pattern which was rotationally dependent, similar to the anisotropic diffusion pattern of the inner mesocarp tissue (Figure 37, 38 and 43). After 41 DAF, the MR signal from this region decayed too rapidly to be visible in the DT and spin-spin relaxation images.

The spin-spin relaxation images of the mature olive pericarp, in comparison to the grape berry pericarp, lacked well-defined macroscopic features such as the radial striation patterns previously noted [27, 176]. However, the anisotropic diffusion patterns (Figure 44, A) and diffusion vectors (Figure 44, B) associated with the olive pericarp exhibited a rotational dependency and were aligned so as to radiate from the centre of the fruit. The mean T_2 of the olive pericarp was determined to 45 ± 3 ms across the imaged olives while the mean diffusivity value of the olive pericarp was $6.07 \pm 0.46 \times 10^{-12}$ m^2 s^{-1}.

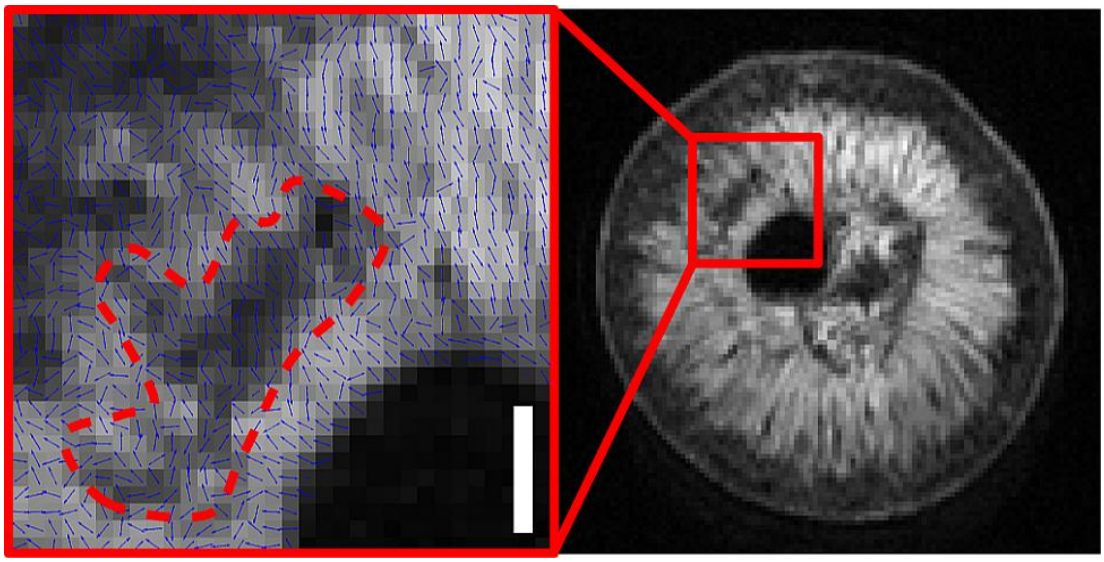

Figure 42: Diffusion vector field map overlaying the S_0 image of a grape berry 109 DAF (transverse plane). The orientation of diffusion vectors are indicated by the blue arrows. There was a loss of diffusion-weighted signal in the region denoted by the red dashed line. Voxel size: 133 × 133 × 1000 µm, bar length: 1000 µm.

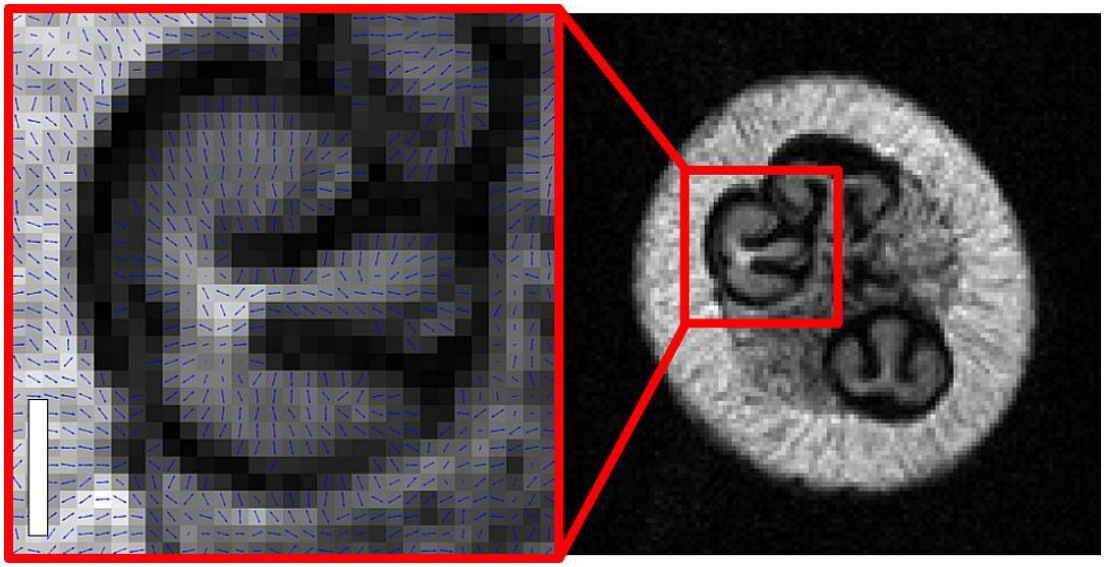

Figure 43: Diffusion vector field map overlaying the S_0 image of a grape berry seed interior 28 DAF (transverse plane). The diffusion vectors (blue arrows) indicate the direction of least restricted diffusion. Voxel size: 117 × 117 × 1000 µm, bar length: 1000 µm.

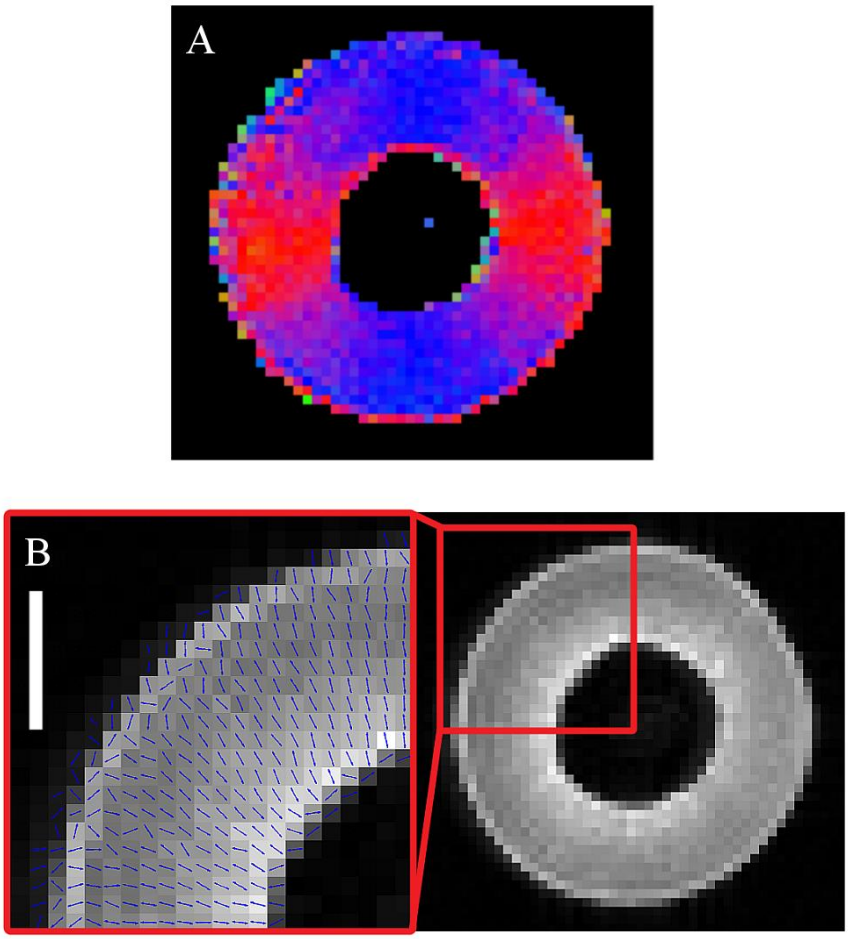

Figure 44: DT and diffusion vector field images of a mature olive (transverse plane). The DT image (A, voxel size 390 × 390 × 1000 μm) and diffusion vector map (B, voxel size 390 × 390 × 1000 μm) of an olive pericarp. Bar length 1000 μm.

7.4 Discussion

7.4.1 Analysis of the grape berry MRI experimental results

The anisotropic diffusion patterns observed in the grape berry pericarp were due to the restricting effects of cell membranes on diffusion. For example, in the mesocarp of grape berries 28 DAF, the diffusion anisotropy exhibited low coherence. This was because the parenchyma cells of the mesocarp were not fully elongated [177], as demonstrated by confocal microscopy (Figure 45). Between 41 DAF and 95 DAF, however, the anisotropic diffusion pattern was radially dependent, thus reflecting the radial orientations of the elongated inner mesocarp cells [4, 27, 177], as shown by confocal microscopy (Figure 46).

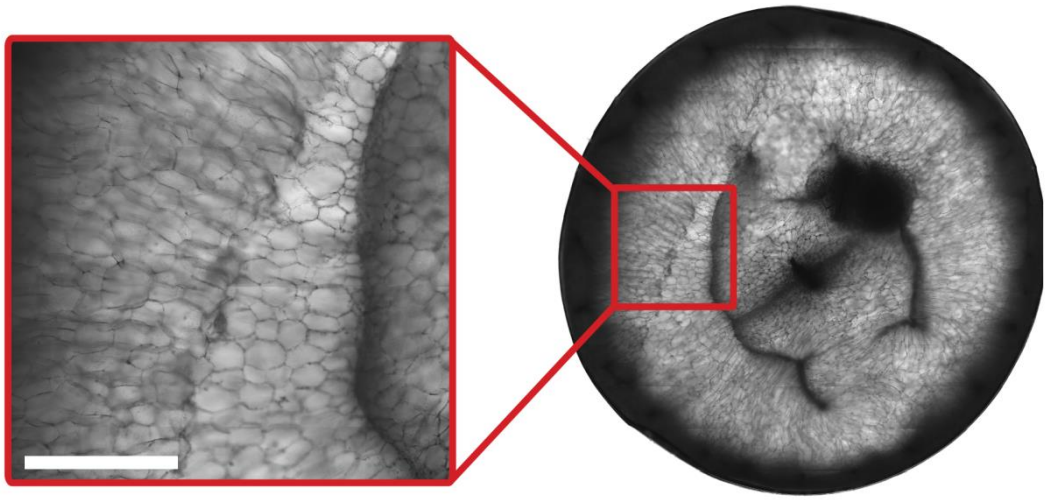

Figure 45: Confocal micrograph of the pericarp of a grape berry prior to véraison 41 DAF (transverse plane). Scale bar; 1000 μm.

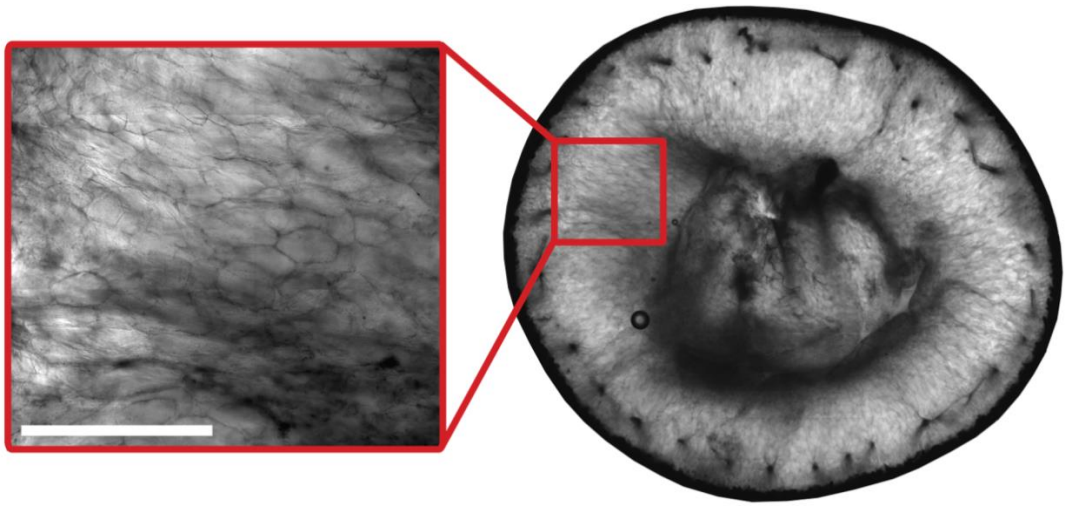

Figure 46: Confocal micrograph of the pericarp of a grape berry undergoing véraison 55 DAF (transverse plane). Scale bar; 1000 μm.

Between 85 and 109 DAF, the T_2 values for all berry tissues noticeably decreased. The decline of T_2 values would begin at the interface between the outer and inner mesocarp, and would steadily shift toward the centre of berry as the grape approached full ripeness. An increase in cellular fluid viscosity could reduce the rotational velocity of spin bearing molecules in the berry; however, there is no straightforward relationship between the observed spin-spin relaxation rate and the measured concentration of soluble solids in the final stages of berry ripening. It is also doubtful that the increased spin-spin relaxation rate could be caused by a sudden

influx of free paramagnetic ions. Due to the small width of the voxels constituting the T_2 images (i.e. 60 – 80 μm) the read gradients of the T_2 MR imaging sequence may have caused unaccounted diffusion-weighted signal relaxation [178]. However, this seems unlikely, as T_2 MR images have previously been taken of a geranium leaf petiole with a voxel width of 39 μm [19]. Despite the small voxel width, these images exhibited a strong contrast between the primary tissues of the petiole. The maximum observed T_2 value of the petiole was also less than 85 ms, similar to the maximum observed T_2 values of the grape berries. It is possible that the observed decrease in T_2 values is linked to apoptotic cell death occurring throughout the berry mesocarp. Programmed cell death has been observed across the mesocarp of certain wine grape berries during the later stages of ripening [179, 180]. Although Semillon grape berries were not included in these studies, for the varieties tested cellular vitality began to decrease at a point between 85 and 109 DAF, which also corresponded with the occurrence of a noticeable decrease in T_2 across the tissues of the Semillon grape berry (Figure 36). Apoptotic cell death has previously resulted in decreases of T_2 and apparent diffusivity values relative to their healthy counterparts [181] and it would also explain the loss of diffusion vector coherence observed late in berry ripening. The sigmoidal decrease in apparent diffusivity with respect to berry age could also be potentially associated with the sigmoidal increase in sugar concentration within the grape berry (Figure 40). The increased sugar concentration could be increasing viscosity in the cell vacuoles where sugars and other solutes are stored [182, 183]. As diffusing water molecules assist in transporting these sugars across the grape berry pericarp, this potential relationship could have important implications for sugar accumulation rates in the grape berry and hydraulic resistance across the grape berry and should be explored further detail in a future study to determine if these two factors are related.

The radial striation patterns noted in the grape berry mesocarp were also noted in the spin-spin relaxation MR images of a previous investigation [27]. By comparing their spin-spin relaxation MR images to bright field light micrographs they had taken of the berry inner mesocarp, the authors of this previous study suggested that these patterns arise in the MR images due to the arrangement of alternately sized radially elongated parenchyma cells in the grape berry mesocarp tissue. The results of the current study agree with this theory. There was no statistically significant difference

between mean primary eigenvalues from striation bands with ‘relatively high’ and ‘relatively low’ MR signal intensity, thus indicating that the cells belonging to both populations have the same mean length. However, there was a statistically significant difference between the mean secondary and tertiary eigenvalues of the two populations. The ‘relatively low’ MR signal intensity population was associated with the lower eigenvalues, indicating that the cells belonging to this population were less wide than their counterparts in the ‘relatively high’ MR signal intensity population. As the parenchyma cells are radially elongated in grape berries older than 28 DAF, the spin-spin relaxation striation patterns thus aligned with the anisotropic diffusion patterns in the mesocarp of these berries. The spin-spin relaxation images of the septum demonstrated striation patterns similar to those found in the inner mesocarp. It is therefore likely that the septal cells are grouped in bands of cells which alternate. However, the orientation of anisotropic diffusion within the septum was largely not aligned with these septal striation bands; this indicates that the septal cells are not radially aligned with the striation bands. This agrees with previous descriptions of the septum, which states that the septal cells are irregular in shape and orientation [4].

The rotationally dependent anisotropic diffusion patterns noted in the outer edge of young seed nucelli are due to the diffusion of water through the seed integument. These cells are known to be tabular in shape and are radially arranged [184]. However, after 41 DAF, there was a decline in the measurable MR signal from the integument tissue due to tissue dehydration and mechanical hardening. Concurrently, the seed nucellus deteriorated and is replaced by the liquid endosperm [185, 186]. The liquid endosperm has a spin-spin relaxation significantly less than 30 ms (~10 ms). As a result, after 41 DAF the MR signal from the seed interior decayed too rapidly for the imaging protocols used in the current study.

7.4.2 Analysis of the mature olive MRI experimental results

Due a noticeable loss of radio-frequency magnetic pulse power, fast diffusion MRI sequences could not be used, which increased the length of the total image acquisition. This loss of radio-frequency magnetic pulse power was attributed to the high salt content of the fruit. The number of image averages and the size of the image

voxel were thus increased to compensate for this loss of signal. Consequently, the diffusion MRI images still possessed a good signal-to-noise ratio and a voxel volume less than 1 mm^3. The low mean diffusivity value of olive pericarp also necessitated the use of very high diffusion magnetic gradients to perform the diffusion measurements and a lengthy diffusion period was used to ensure that the slowly diffusing molecules had sufficient time to probe the restricting tissue microstructure. To prevent prohibitive MR signal loss arising from spin-spin relaxation, a PGSTE MRI sequence was employed instead of a PGSE MRI sequence.

The radial anisotropic diffusion pattern observed in the olive pericarp indicated that the cells of the mesocarp were radially elongated. This results agrees with what is known of the olive mesocarp structure [187] and appeared similar to that of a Semillon grape berries at véraison. Additionally, the mean T_2 value of the olive pericarp was comparable to those of a Semillon grape berry pericarp at véraison, which is not unexpected given that olives and grape berries have similar cellular dimensions [172, 173].

These results indicate that diffusion MRI can be successfully used to investigate morphological and physiological features of plant tissues with high oil content. As was hypothesised, there was a large difference between the mean ADC of the olive pericarp and the grape berry pericarp tissues, which was attributed to the presence of oil droplets in the olive pericarp cell cytoplasm [171]. This area of research deserves further investigation, as these low rates of diffusivity could hold a number of practical implications for transpiration, drying and water/solute transportation rates within olives and other plant tissues with high oil content.

7.4.3 Practical implications of this research for other plant tissues and organs

The results of this study demonstrate that relaxation and diffusion MR images reflect both grape berry and olive morphology. This study also provides a novel and non-invasive perspective on the development changes that occur in grape berries as they ripen, in addition to a supplying a library of images and relaxation/diffusion data for comparisons to treated grape berries in sequence chapters. The question remains as to

the applicability of relaxation and diffusion MRI in the examination of other plant species and organs. It is expected that these MRI techniques can be applied broadly across botanical studies for the non-invasive study of many different important aspects of plant biology. However, its applicability will be dependent upon the amount of unbound water the organ contains. Tissues with low water content, such as the solid endosperm of seeds and the cotyledons of beans, will be difficult to examine, although anisotropic water movement has been previously been successfully demonstrated using diffusion MRI in macadamia nuts [188]. Tissues consisting of smaller cells will be easier to examine than tissues with larger cells; however, providing that Δ is long enough to ensure that a large population of water molecules are able to interact with the surface of the cellular boundaries, diffusion anisotropy will be evident. Upon considering these limitations, good botanical candidates for future relaxation and diffusion MRI studies are hypothesised to include other sink organs, plant stems, petioles and root systems.

7.4.4 Comparing the results of the study to the literature

In a recent study, DT images of the grape berry vascular system were reconstructed [156]. However, the orientation of anisotropic diffusion within the berry pericarp was also visible in these images. The anisotropy of these observed diffusion patterns did not correlate with the results from the current study, nor the known pericarp tissue structure. While the experimental procedures employed in both studies were largely similar, they differed in two important respects. First, the TE of the PGSE MRI pulse sequence used in the previous study was shorter than those used in the current study. TE limits the maximum length of Δ, so although the length of Δ was not specified in the study by Gruwel et al., it can be inferred from the TE used (26 ms) that it was less than the shortest Δ employed in the current study. This difference is noteworthy because as Δ increases, the water molecules have more time to displace further from their origin and interact with different physical structures. The cells of the berry vasculature are less wide than the cells that make up the mesocarp, thus a short Δ relative to that used in the current study remains appropriate for probing the cellular membranes of the xylem and phloem. However, in regions where the average cell size is much larger, (e.g. the inner mesocarp) the diffusion anisotropy patterns are more likely to be observed due to interactions with cellular components rather than

the cellular membrane. As a result, the observations from both the current study and that of Gruwel et al. could be considered accurate; however, they are observations of the effects of different restricting structures (i.e., the results of Gruwel et al. are on a shorter length scale than the results of the current study).

The second difference between the present study and that of Gruwel et al was the diffusion gradient schemes employed. Gruwel et al. performed diffusion measurements along six unique diffusion gradient vectors. While this is the minimum required for DTI, it is possible that gradient cross-terms (from the imaging and diffusion gradients) have affected the diffusion weighting of the images. The current study used forty-two different diffusion gradient vectors (i.e., twenty-one unique directions and their corresponding opposite). The inclusion of gradient vectors and their corresponding opposite gradient vectors reduces the effects of potential gradient cross-terms [22, 104]. Using a large number of unique diffusion gradient vectors also reduces potential directional bias when reconstructing **D**.

Chapter 8 - Time course study of grape berry split using diffusion MRI

[The results contained within this chapter presented in an article which has been recently accepted for publishing. 'Dean, R. J., T. Stait-Gardner, S. J. Clarke, S. Y. Rogiers, G. Bobek and W. S. Price (2015). "Time course study of grape berry split using diffusion MRI". *Australian Journal of Grape and Wine Research.*]

8.1 Introduction

Having found a strong correlation between the known morphology and the anisotropy diffusion patterns of healthy grape berries at a large number of different development stages, the next step is to apply treatments to test the sensitivity of relaxation and diffusion measurements to changes in grape berry biology. For example, the sensitivity of diffusion measurements to changes in the microstructure of the grape due to physical damage through fruit split. Fruit splitting (also known as fruit cracking) is a widely recognised source of fruit loss in viticulture commonly associated with periods of high rainfall [189]. The cool, damp conditions promote the osmotic uptake of water into the berry while also inhibiting water loss via transpiration. This net uptake of water increases turgor pressure within the berry and can eventually lead to the mechanical failure of the epidermis. The resultant wounds in the berry epidermis encourage berry desiccation and greatly increase the probability of microbial infection, such as *Botrytis cinerea*, leading to reduced crop yields and berry quality [190].

There are a number of intrinsic factors that influence the susceptibility of grapes to fruit split. For example, these factors can include the tensile strength, elastic modulus and thickness of the berry epidermis [191, 192], the presence of lenticels [193], the shape of the berry and how tightly the berries are pressed together within the bunch

[194]. In certain cultivars of wine grapes, the developmental stage of the berry also plays a role. For example, in post-véraison Riesling grapes, mismatches in berry surface expansion and the disposition of the cuticular membrane place strain on the berry epidermis and increase the chance of microcracks and splits forming [195]. Conversely, Shiraz grapes become less likely to split as they approach maturity due to a decrease in internal turgor, resulting from widespread cell death in the berry mesocarp [196].

To provide some context regarding the internal pressure required to split the epidermis of a table grape, some examples of grape berry internal turgor pressure are included here. Pre-dawn the internal turgor pressures of table grape cultivars will be within the vicinity of 5 kPa to 38 kPa [191, 197]. However, the internal turgor pressure at which table grape berries split (i.e., the critical turgor pressure) will be in the vicinity of 1.5 to 3.7 MPa [192, 198] and the linear strain on the berry epidermis will be in the vicinity of 0.027 to 0.142 [191, 198].

The primary objective of the current study was to investigate physical changes that occur in the berry mesocarp preceding and following the formation of fruit splits by the non-invasive examination of tissue structure using features of the diffusion tensor, particularly ADCs. As ADCs reflect the features of the restricting microstructure (e.g. relative cell size and cellular membrane permeability), as previously demonstrated (see Chapter 7 - Diffusion MRI of grapes at different stages of development). Changes in these values in the grape berry immediately preceding, or following, the formation of a split in the berry epidermis can thus be used as an indication of tissue structure alteration.

8.2 Methods

8.2.1 Experimental procedures

The *V. vinifera* berries used in this study were a table grape variety, cv. Thompson seedless, purchased from a local green grocer, Campbelltown, NSW, Australia. Over the course of this investigation, thirty-six grapes berries were selected at random, cut from the bunch three to four millimetres proximal to the receptacle (the pedicel junction with the berry), then weighed. These berries were individually inspected for

obvious blemishes (e.g. tissue bruising and fruit split) and the damaged berries discarded. The undamaged berries were then randomly assigned to one of the following groups; twelve to the control group, twelve to the first experimental group and twelve to the second experimental group. Individual berries were sealed in a 25 mm diameter plastic vial and held in position by a pair of four pronged acrylonitrile butadiene styrene holders designed specifically for this purpose. The grapes in the first experimental group were wrapped in damp tissue before being sealed upside down in a vial which had been filled with sufficient distilled water to ensure the pedicel and receptacle were immersed. This experimental group would represent grape berries experiencing damp field conditions. The grapes in the second experimental group had sufficient distilled water added to their vials to completely immerse the berries, including the pedicel and receptacle. As the number and severity of microcracks in the berry surface is aggravated by water [199], this would greatly improve the chance of observing the formation of berry splits during the period available for MRI. The grapes assigned to the control group had no water added to their vials. From each group of twelve, three grape berries were imaged, one at a time. The weight of the individual berries in each group was recorded within an hour before and after imaging to determine the change in fresh weight.

8.2.2 MRI pulse sequence protocols

Grape berries were imaged using the MRI protocols described below. Five transverse images of the berry were acquired concurrently, spaced evenly over the longitudinal axis of the berry. The imaging protocols alternated between a FLASH MRI sequence and a PGSE echo planar DTI sequence to produce diffusion weighted images.

The FLASH imaging sequence was used to produce two-dimensional images of the grape berries weighted by spin-density. These images were chiefly used to confirm the formation of fruit splits in the berry epidermis. The protocol parameters used included THK 1 mm, MTX 256 × 256, a flip angle of 30°, TE 6 ms, TR 100 ms and NA 6 (total acquisition time ~3 min). The EPI DTI sequence was used to produce two-dimensional diffusion-weighted images of the berries. The protocol parameters used included THK 1 mm, MTX 128 × 128, δ 1 ms, Δ 25 ms, TE 32 ms, TR 8000 ms and NA 1. Diffusion was measured along twelve different directions (the vertices of

an icosahedron) using a single diffusion gradient strength (*b* weighting of 800 s mm^{-2}). One image with a negligible diffusion weighting was also acquired in order to normalise the diffusion weighted images (total acquisition time ~ 25 min).

8.2.3 Cell vitality staining

After the scans were completed, three berries from the control group and one from each experimental group were sectioned transversely. These sections were made so as to mimic the transverse slices of the acquired magnetic resonance images. A 6 μM solution of fluorescein diacetate (FDA; Sigma-Aldrich, USA) in acetone was applied in excess to the cut surface of the grape berry sections and left to incubate for 15 min [179]. The excess FDA solution was then blotted from the cut surface of the berry and a phosphate buffer solution was applied to the cut surface in its stead (Sigma-Aldrich, USA). The sectioned berries were then examined using a confocal microscope. To confirm that only vital cells exhibited fluorescence, one of the control grapes was microwaved for 30 s at 1100 W before the FDA was applied. This berry exhibited a muted fluorescent response, indicating the mesocarp cells had a damaged cellular membrane and/or non-living cytoplasm. Another control berry was also examined under the 488 nm laser without first applying the FDA solution and no auto-florescence was noted.

8.2.4 Determining the cause of cell vitality loss

To determine the cause of cell death, a small incision was made along the length of six additional Thompson seedless grape berries using a razor blade. Two of these pre-split berries were fully immersed in water, two were fully immersed in Fomblin Y (Solvey Solexis, USA), a biologically and chemically inert oil, and the remainder left dry. These berries were then imaged over a period of twenty hours using the diffusion MRI protocol previously described. These berries were then sectioned transversely and the cells stained using the method described above, except the grape berries that had been immersed in Fomblin were stained using a 100 μM solution of propidium iodine (PI; Sigma-Aldrich, USA) in a phosphate buffer solution.

8.3 Results

Over the twenty hour period of imaging the mean fresh weight of the berries in the control group berries decreased by 1.3 ± 0.6%. None of the berries in the control group showed evidence of fruit split during this time period. The mean fresh weight of the berries in the pedicel immersion experimental group increased by 1.3 ± 0.9% during the twenty hour period of their detachment from the bunch. Three of the berries exhibited splits in the epidermis about the stylar remnant. None of these splits intersected any of the image slices. The mean fresh weight of the berries in the wholly immersed experimental group increased by 4.4 ± 0.6% during the twenty hour period of their detachment from the bunch. Ten of twelve berries in this experimental group bore one or more splits in their epidermis. These splits ran longitudinally between the pedicel and stylar remnant, the majority of which were located within 5 mm of either the pedicel (54% of splits) or the stylar remnant (31% of splits).

8.3.1 Diffusion MR image results

The grape berries in the control and the experimental groups had an initial mean ADC of $1.1 \pm 0.1 \times 10^{-9}$ m^2 s^{-1} across the berry pericarp. The berries in the control and the immersed pedicel groups exhibited no significant variance (Tukey-Kramer test, $P < 0.05$) in the pericarp ADCs over the course of twenty hours of diffusion imaging. The grapes in the wholly immersed experimental group exhibited no significant variance (Tukey-Kramer test, $P < 0.05$) in the pericarp ADCs prior to the formation of a split in the berry epidermis (Figure 47A). Upon the formation of a split in the berry epidermis, the mean ADC of the tissue around the split increased to $1.5 \pm 0.1 \times 10^{-9}$ m^2 s^{-1} (Figure 47B and C). As time progressed the region of affected tissue continued to increase in size (Figure 47D to H). At the end of the twenty hour period, the area of affected tissue varied widely between berries and the location of the image slice. The region of affected tissue penetrated as far as 3 mm from the split in the grape berry epidermis.

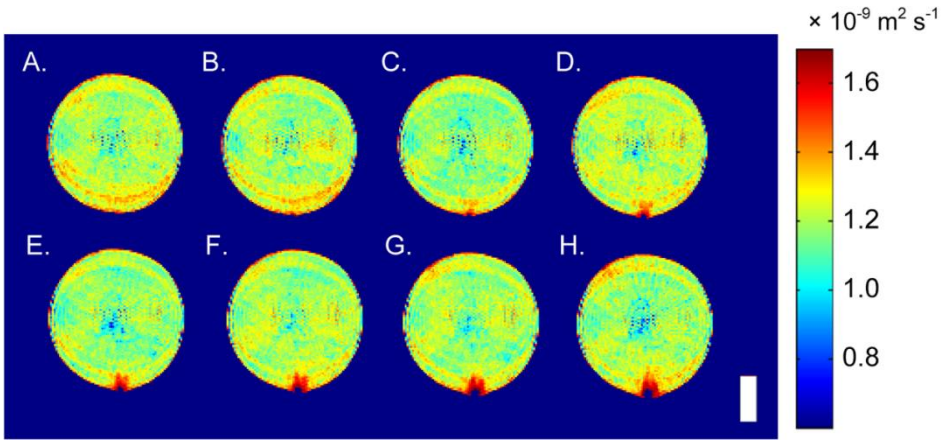

Figure 47: The development of a single split in the epidermis of a mature table grape, cv. Thompson seedless, and its effect on the mesocarp tissue. (A) An ADC map acquired one hour after the berry was fully immersed in water. (B – H) ADC maps acquired nine to fifteen hours after the berry was fully immersed in water (each image thereafter was acquired an hour apart). The diffusivity of the different tissue regions is as indicated by the colour scale. Scale bar; 6 mm.

8.3.2 Increased apparent diffusivity is linked to cell death

The FDA staining of the sectioned control grapes together with the berries which had only their pedicels immersed in water revealed a strong fluorescent response from all regions of the berry pericarp. This indicated that the cells of the berry pericarp maintained vitality after the twenty hours spent detached from the grape bunch. The sectioned and FDA stained grape berries which had been fully immersed in water exhibited a strong fluorescent response from most regions of the grape berry pericarp. However, the tissue immediately adjacent to splits in the grape berry epidermis showed a highly muted fluorescent response after splitting had occurred, indicating that the cells in the regions about the splits were non-vital (Figure 48). These regions of non-vital cells matched the size and shape of the regions of increased apparent diffusivity about the splits in the epidermis. This relationship was also observed in water immersed berries where the epidermis had been damaged with a razor blade (Figure 49A and Figure 50). In contrast, Fomblin immersed berries and the berries that were left dry exhibited no increase in apparent diffusivity (Figure 49B and C).

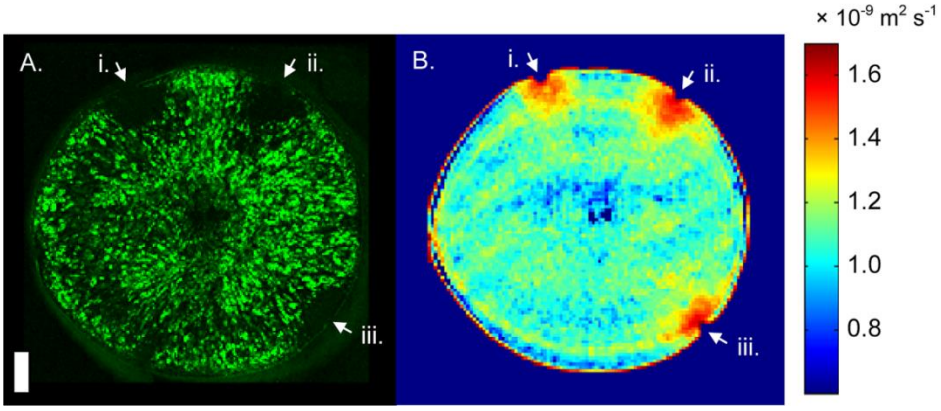

Figure 48: The relationship between cell vitality (A) and apparent diffusivity (B) within the mesocarp of a mature table grape, cv. Thompson seedless from the wholly immersed experimental group. The berry has developed three separate splits (i, ii and iii). Vital cells in (A) are bright green while non-vital cells have a muted response. The apparent diffusivity values are indicated by the colour scale. Scale bar; 3 mm.

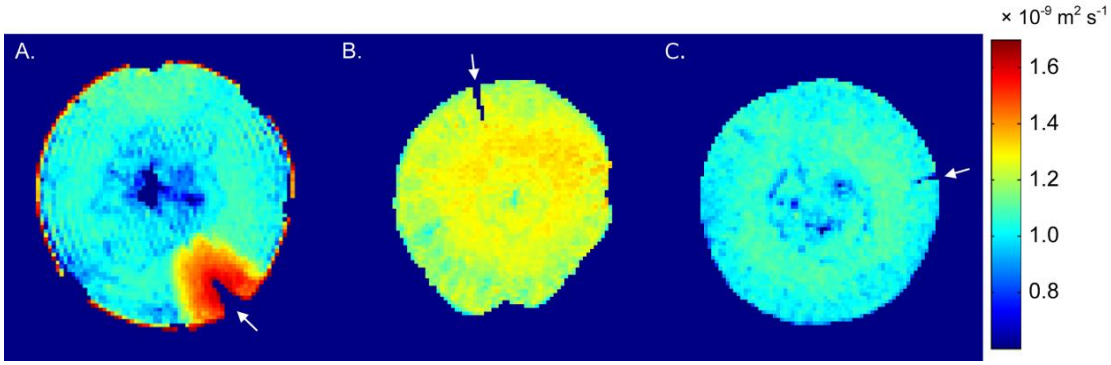

Figure 49: Determining the cause of cell death in split table grapes, cv. Thompson seedless. (A) A mean diffusivity map of a grape berry with an incision (indicated by the white arrow) in the berry epidermis after twenty hours wholly immersed in water at 22.0 ± 0.1 °C. (B) A mean diffusivity map of a grape berry with an incision (indicated by the white arrow) in the berry epidermis after twenty hours immersed in 22.0 ± 0.1 °C Fomblin oil. (C) A mean diffusivity map of a grape berry with an incision in the berry epidermis after twenty hours left dry.

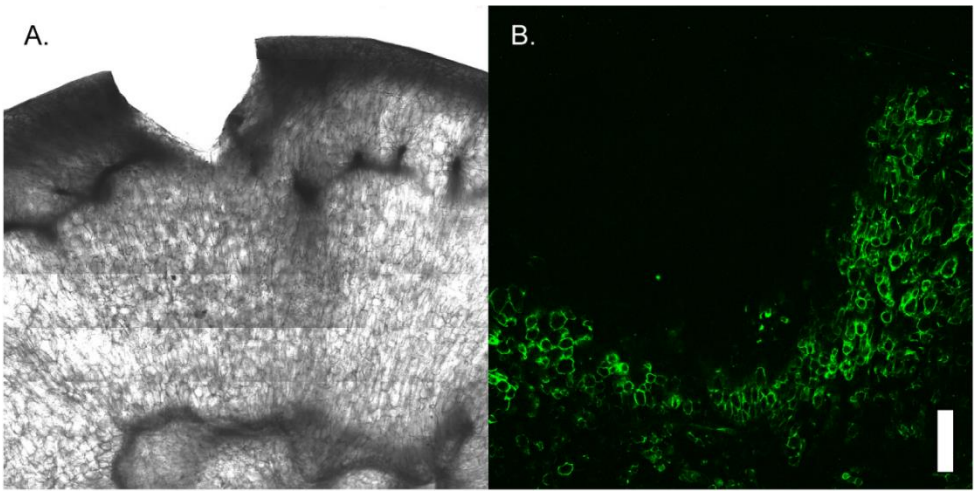

Figure 50: Morphological (A) and cell vitality (B) images of the same split in a mature table grape, cv. Thompson seedless, twenty hours after water immersion. Vital cells in image B are bright green while non-vital cells have a muted response. Scale bar; 1 mm.

8.3.3 Regional expansion of the berry mesocarp

To examine the expansion of the pericarp tissue, void spaces at the centre of the berry left from the abortion of the grape seeds were used as reference points to align MR images acquired at different time points. Upon overlaying these images it was found that the berry pericarp underwent one or more regional expansions rather than a uniform expansion (Figure 51). All splits observed in the MR images were located within or on the edge of a region of the berry which had undergone a regional expansion.

8.4 Discussion

8.4.1 Analysis of the diffusion MR images

Prior to the formation of splits in the berry epidermis, the ADCs across the pericarp of the Thompson seedless grape berries were in the vicinity of the ADCs of Semillon grape berries passing through véraison (see Figure 40). However, once a split formed in the berry epidermis, there was an immediate change to diffusion restriction in the region of tissue surrounding the wound. While the increase in mean apparent diffusivity could potentially reflect either a substantial change in parenchyma cell

size or a change in cell membrane permeability, there was a close correlation between regions of increased apparent diffusivity and the regions of tissue about the split which exhibited a muted fluorescence response when stained with FDA (Figure 48). Since FDA requires cellular enzymatic activity to activate its fluorescence, and an intact cellular membrane to retain the activated dye, the cells within the region of muted fluorescent response must have undergone ischemic cell death, and were no longer vital.

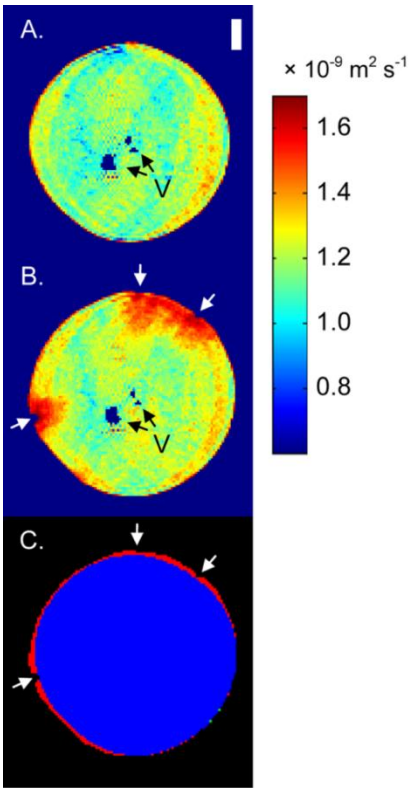

Figure 51: The regional expansion of a mature table grape, cv. Thompson seedless, immersed in water at 22.0 ± 0.1 °C for approximately twenty hours. (A) An ADC map of the grape berry two hours after the berry was fully immersed in water; no splits were evident. (B) An ADC map of the grape berry twenty hours after immersion; three splits were visible in the berry epidermis (indicated with white arrows). (C) Image A (the blue region) overlaying image B (red region). Scale bar; 3 mm. (V) Void spaces, indicated by the black arrows.

The increase in apparent diffusivity in regions of non-vital mesocarp cells in the split grape berries contrasts interestingly with the discussion arising from the results of the preceding study (cf. Section 7.4 Discussion), in which a decrease in apparent diffusivity in the berry mesocarp was attributed to apoptotic cell death (see Figure

40). It is probable that these differences in apparent diffusivity are reflective of the two different mechanisms of cell death. For example, ischemic cell death results in the rupturing of cellular membranes [200], allowing water to diffuse through the injured tissue more easily. Apoptosis, on the other, results in the collapse of cell via shrinkage and does not result in the cellular membrane rupturing [200]. As the cells shrink and become denser, diffusion restriction would be expected to increase on the length scale probed by the diffusing water, hence resulting in a decrease of apparent diffusivity.

To determine whether the cause of the cell death was due to physical trauma, oxygen shock, or related to the imbibition of water, an incision was made in the epidermis of six Thompson seedless grape berries with a razor blade and then either wholly immersed in water, Fomblin oil, or left dry. The cut berries that had been immersed in water exhibited increases in apparent diffusivity (Figure 49A) and widespread cell death in the pericarp tissue surrounding the split (Figure 50). In the absence of water, there was no localised increase in apparent diffusivity around the epidermal splits (Figure 49B and C) and no widespread cell death was observed in these tissue regions. Therefore, the ischemic cell death of the pericarp tissue was attributed to the imbibition of water, rather than physical trauma or oxygen shock.

Initially the cell vitality assays performed on the Fomblin immersed grape berries made use of FDA to stain cells which were vital. Despite exhibiting no change in apparent diffusivity around the incisions, the pericarp cells adjacent to the incisions of the Fomblin immerse berries appeared to be non-vital. This finding noticeably differed from all other results within this investigation. However, upon staining the Fomblin immersed grape berries with PI, a fluorescent dye that stains non-vital cells, no evidence of cell death was observed in the vicinity of any the incisions (Figure 52). From this result, and due to the consistency between the apparent diffusivity images and the cell vitally images for the other experiments, it was concluded that the presence of Fomblin did not trigger cell death in the grape berry mesocarp. In order to determine the reasons for why the FDA did not stain the mesocarp cells adjacent to the splits of the Fomblin immersed grape berries, further investigation is required. It is possible that the Fomblin oil was able to permeate the pericarp tissue surrounding the incisions or was smeared across the cut surface during hand sectioning, preventing the FDA from staining vital mesocarp cells in these regions.

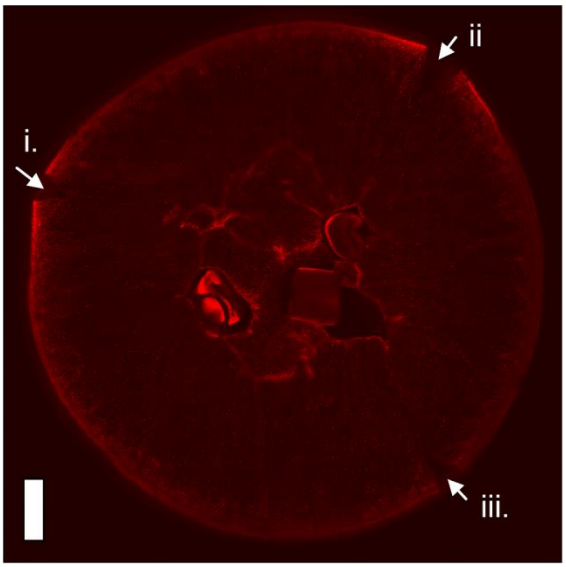

Figure 52: Cell vitality image of three artificial splits in the berry epidermis twenty hours after Fomblin immersion. The three splits (i, ii and iii) are indicated with white arrows. Non-vital cells are bright red while vital cells exhibit a muted response. Scale bar; 3 mm.

The sugar content of the imaged grape berries was considered largely inconsequential to the results of the current study. While grape berries with higher sugar contents will have a higher osmotic potential, the experiments in this work only required that the berries split/imbibed water during the period the berries were immersed. Consequently, the berry cultivar chosen for these experiments (i.e., Thompson seedless) was considered to be more influential over the outcomes of the study than the small variations in sugar concentration between berries. Thompson seedless were an excellent cultivar for the current study as these grapes maintain cell vitality and turgor pressure through to maturity [179], and hence remain susceptible to berry splitting well after véraison.

8.4.2 Analysis of the berry mesocarp regional expansion

Fruit splits were only observed in regions of the epidermis where the pericarp tissue had undergone regional tissue expansion. A regional expansion will concentrate deformation stress in a small area of the epidermis, thus increasing the likelihood of the epidermis failing. The occurrence of regional expansions rather than uniform expansion could affect the outcome of previous mechanical stress models of grape

berry undergoing fruit split [193, 194], as these models assume that the internal pressure placed on the epidermis is uniform.

It is difficult to determine whether the regional expansion of the tissue precedes the formation of a split in the berry epidermis. This is because it is unlikely that the splits originated in the same plane as the MR images. If a split were to form outside of the imaging slice, and then propagate along the length of the grape berry out into an image slice, the region of expanded tissue would be observed first (Figure 53). This question could be resolved if the entire grape berry volume could be imaged. This additional information could also be used to determine the volume of the regional tissue expansions and thus determine the distribution of water taken into the grape berry. However, this is not currently feasible as it would take many hours to acquire images of the entire berry volume.

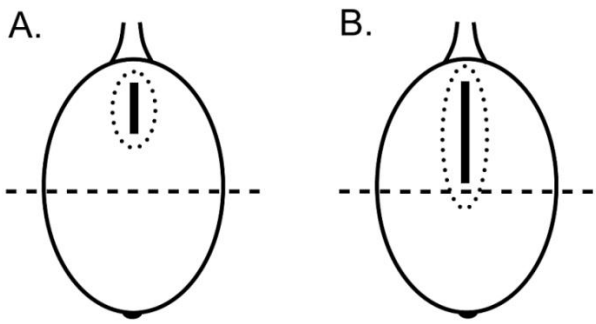

Figure 53: Longitudinal schematic of a grape berry explaining how regional tissue expansions could be observed prior to split formation. (A) A split (thick vertical line) in the grape berry epidermis occurs some distance from the image slice (dashed horizontal line). As water enters the split, regional tissue expansion occurs (dotted circle). (B) The split propagates along the length of the berry towards the image slice. Due to regional tissue expansion about the split, this expansion is observed to precede the split in the image.

8.5 Practical implications of these findings

The results of the wholly immersed experimental group represent the worst-case-scenario for fruit splitting. Although the majority of water enters the berry through the pedicel and receptacle [201, 202], fully immersing grape berries in water provided ample opportunity for osmotic imbibition through splits and microcracks in the berry surface. Due to the link between tissue ischemic cell death and the uptake

of water through the splits in the berry epidermis, it can be hypothesised that a grape berry whose surface is left exposed to standing water after the formation of fruit splits is more likely to exhibit localised cell death in the grape pericarp than a fruit whose surface split but subsequently remained dry. Therefore, the surface of grape berries should be kept dry after they split, if possible, to mitigate further tissue damage. The amount of water left standing on the berry surface after splitting occurs could also correspond with increased fungal infection rates across crops as the presence of dead tissue about the open wounds in the berry epidermis would provide an ideal environment for plant pathogens, such as *Botrytis cinerea*, to become established. Follow up rain events could hence prove more important than the initial fruit split-inducing event for grape cultivars, particularly those which are not prone to fruit abscission and could impact on fungal control practices.

Chapter 9 - The diffusive transport of manganese in the grape berry

9.1 Introduction

The grape-vine absorbs a variety of metal ions from the soil in order to maintain its numerous physiological activities, and the concentrations of these metal ions potentially influence the quality, taste and production of viticultural goods [203-205]. Examples of metal ions found in the grape berry include potassium, iron, zinc, copper, magnesium, calcium and manganese [206, 207]. A number of studies have already been conducted which examined the vasculature transport/unloading of photosynthates in grapes as well as other fruits/sink organs [6-8, 14, 208-211]. These previous studies typically employed radioactively or fluorescently labelled tracer compounds to examine the photosynthate transport pathway [8, 14, 210, 211]. From these previous studies it was determined that these large molecular weight organic compounds, delivered to the grape berry via the phloem, are transported through the pericarp initially via the symplasmic (intercellular) pathway. At the onset of ripening, the transport of labelled photosynthates and tracer compounds shift to the apoplasmic (extracellular) pathway. Metal ions, on the other hand, can be either phloem or xylem mobile [206]. The transport of metal ions through the grape berry pericarp is not as well understood, although it has been previously demonstrated in tomatoes that the ratios of the apoplasmic and bulk pericarp sap concentrations of metal ions vary between elements and with respect to berry age [212]. Due to differences between the mechanisms that used to transport photosynthates and metal ions, the spatial distribution and of these solutes in the grape berry pericarp could differ significantly.

The objective of the current investigation was to employ MRI to non-invasively study the vascular/extra-vascular transport of manganese through the grape berry pericarp. Manganese is a xylem-mobile metal ion and, as mentioned above, it naturally accumulates in grape berries. Manganese is a micronutrient required for the synthesis of chlorophyll [185], enzymes [213] and glucosyltransferases [214]; it is

typically non-harmful to the grape vine but it can accumulate in toxic quantities when the grape vine grows in acidic soils [207, 215]. While MRI has been previously employed to directly observe the spatial distribution of ^{1}H-rich compounds such as water, sugar and lipids in the grape berry [26, 27, 176], manganese has a much smaller gyromagnetic ratio than ^{1}H (66.4×10^{6} rad s^{-1} T^{-1}). It is also be present in the grape berry in far smaller quantities than ^{1}H, making direct observations of manganese difficult. However, manganese is paramagnetic; consequently this study employed manganese ions as a paramagnetic relaxation contrast agent (see Section 2.6.1 Paramagnetic relaxation contrast agents), indirectly observing its uptake and subsequent transport via its effect on the spin-lattice relaxation rate of water. Studies of manganese transport and spatial distribution in the grape berry pericarp may also assist in transport studies of diamagnetic calcium. Calcium is also xylem mobile [206] and certain ion transport channels/mechanisms have been determined to transport both calcium and manganese [216-218]. Calcium is an important macronutrient for many fruits; amongst other health problems, a deficiency of calcium in a fruit can result in increased occurrences of fruit split [219, 220].

9.2 Methods

9.2.1 Experimental procedures

The grape berries used in this study were a table grape variety, cv. Red Globe. Over the course of this investigation, eight grapes berries were selected at random and cut from the bunch three to four millimetres above the pedicel. These berries were visually inspected for obvious blemishes (e.g. tissue bruising and fruits split) before four were randomly assigned to the control group and the remainder to the experimental group.

Each berry was placed upside down in separate 25 mm diameter plastic vials, and held in position by a pair of four pronged acrylonitrile butadiene styrene holders designed specifically for this purpose. The experimental grapes had a sufficient amount of 10 mM manganese chloride ($MnCl_2.4H_2O$, Sigma Aldrich) solution added to their vial to immerse the stem and pedicel of the berry. This manganese chloride solution was less concentrated than what is typically used for mammalian studies

[60, 221] in order to minimise additions to the endogenous manganese pool. The control grapes instead had a sufficient amount of distilled water added to their vial to ensure the pedicel and receptacle was immersed. Each grape berry was imaged over an immersion period of nineteen hours using the MRI protocols described below.

9.2.2 MRI pulse sequence protocols

The RARE VTR MRI pulse sequence was employed to produce a set of two-dimensional images which were weighted by varying degrees of longitudinal and spin-spin relaxation. The sequence parameters used included THK 1 mm, MTX 256 × 256, a train of 5 echoes (10, 30, 50, 70 and 90 ms), TR of 5550, 3000, 1500, 800 and 536 ms and NA 1 (total acquisition time ~18 min). Fives image slices of the grape berry were acquired concurrently, spaced 5 mm apart (Figure 54). To better visualise reductions in T_1 over time, the reconstructed T_1 maps of each image slice were also normalised with respect to the T_1 map of that image slice at time zero (i.e., $T_1{*}(t_n) = T_1(t_n)/T_1(t_0)$ where t_n is the time point of interest, t_0 represents time zero and T_1* is the normalised T_1).

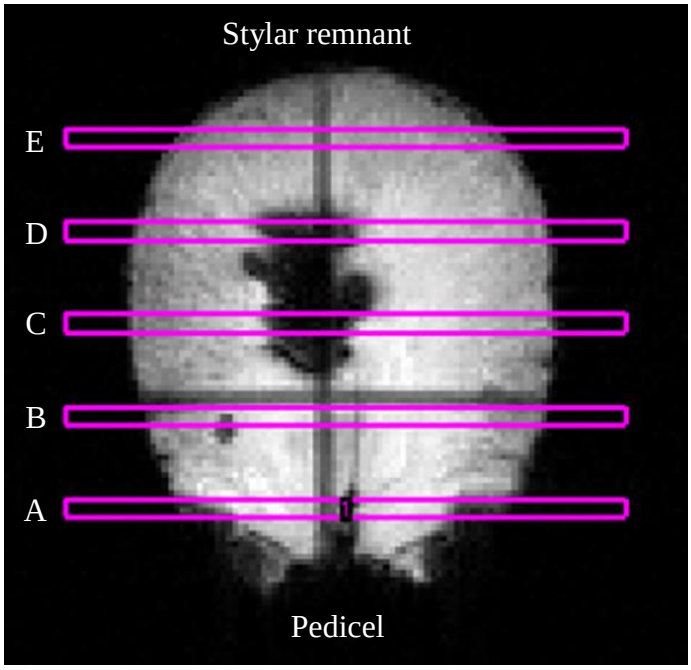

Figure 54: Longitudinal proton-density image of an experimental grape berry, cv. Red Globe at maturity. The locations of the image slice relative to the grape berry are indicated in pink.

The EPI DTI MRI pulse sequence was used to produce two-dimensional diffusion-weighted images of the berries. The protocol parameters used included THK 1 mm, MTX 128 × 128, δ 1 ms, Δ 35 ms, TE 42 ms, TR 8000 ms and NA 1. The image was acquired in nine segments. Diffusion was measured along 15 different antipodal pairs of directions spaced evenly over a sphere, using a single diffusion gradient strength (*b* weighting of 800 s mm^{-2}). One image with a negligible diffusion weighting was also acquired in order to normalise the diffusion weighted images (total acquisition time ~ 37 min). All MR imaging protocols for individual berries were completed within nineteen hours of detachment from the bunch.

9.2.3 Influence of pericarp cells on manganese transport

To demonstrate the influence grape berry pericarp cellular membranes have on the distribution of manganese throughout the tissue, two additional Red Globe grapes were each microwaved three times at 770 W in order to disrupt their cellular membranes. Each period of irradiation lasted 7 s and the grapes were left to rest for two minutes in-between these periods. The pedicel and receptacle of the grape berries were wrapped with damp tissue paper prior to their irradiation to prevent their desiccation during the microwaving process. After their third dose of microwave radiation, the berries were left to rest for 30 min to allow their return to room temperature (22.0 ± 0.1 °C). The two microwaved grape berries were then imaged using the experimental procedures outline for the grape berries in the experimental group, as listed above.

9.3 Results

At time zero a number of the morphological features of the grape berry could be distinguished in the T_1 relaxation MR images. These features include the central and peripheral vascular bundles, locules and the liquid endosperm of the seeds (Figure 55). No splits were noted in the epidermis of the control berries or the experimental berries after this period of partial immersion. No significant changes (Tukey-Kramer test, $P = 0.05$) in T_1 were noted in the relaxation images of the control grape berries over the nineteen hour period they spent partly immersed in water. Conversely, the

experimental grapes exhibited significant reductions (Tukey-Kramer test, $P = 0.05$) in T_1 during their nineteen hour period of partial immersion in the manganese chloride solution (Figure 56).

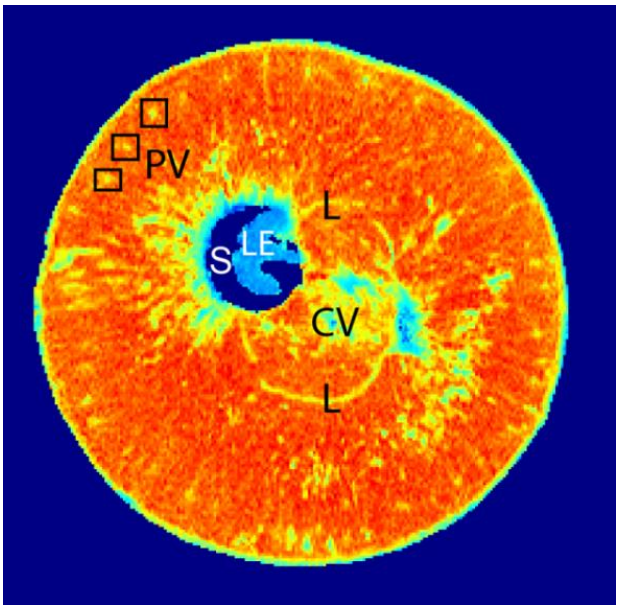

Figure 55: Structural features of an experimental grape berry, cv. Red Globe, visible in a transverse T_1 relaxation image of ^{1}H at ambient temperature (22.0 ± 0.1 °C) at time zero. The image was acquired using a VTR RARE MRI pulse sequence. (PV) peripheral vasculature, (CV) central vasculature, (L) locule, (S) seed, (LE) liquid endosperm.

These reductions were first observed in the image slice closest to the pedicel of the grape berry in the peripheral vasculature of the berry. This was followed by T_1 reductions in the mesocarp tissue immediately adjacent to the peripheral vasculature (Figure 57). Localised reductions in T_1 around sections of the peripheral vasculature were subsequently observed in image slices further away from the pedicel. A significant reduction in T_1 was observed around the central region of the image closest to the pedicel, corresponding with the berry brush. However, no reduction in T_1 was observed about the central or ovular vasculature (Figure 58), or in the liquid endosperm of the berry seeds. The final area and distribution of these regions of T_1 reduced pericarp tissue varied greatly across the experimental grape berries and between image slices (Figure 59).

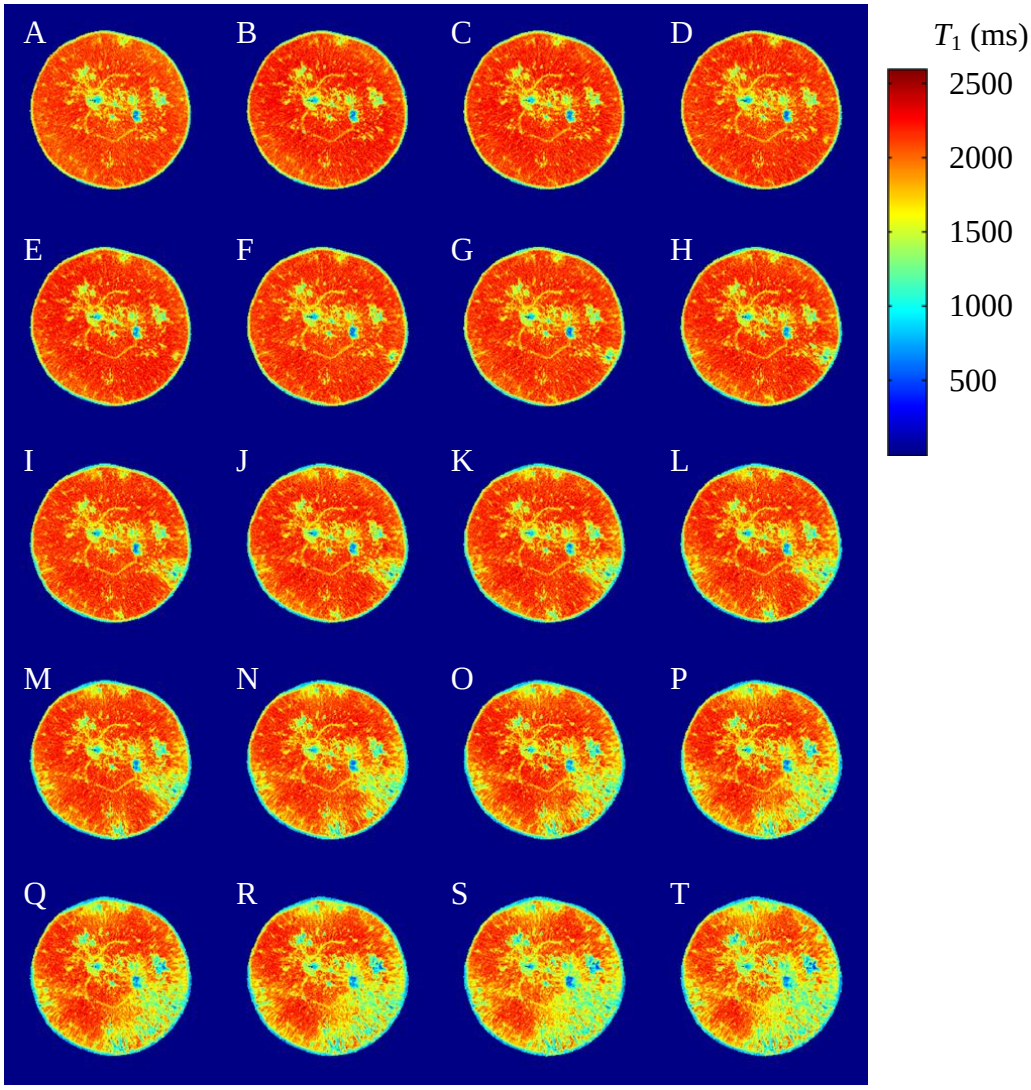

Figure 56: T_1 changes in a grape berry, cv. Red Globe, over nineteen hours of partial immersion in a 10 mM manganese chloride solution. All images were from the image slice second closest to the grape berry pedicel. (A) T_1 image of the experimental grape berry at time zero. (B – T) T_1 images of the experimental grape berry at hours one to nineteen.

The area of these T_1 reduced regions as a percentage of the total area of the pericarp tissue in the image slice tended to decrease with increasing distance from the berry pedicel (Table 8), as did the rate of growth of the affected area of tissue (Figure 60).

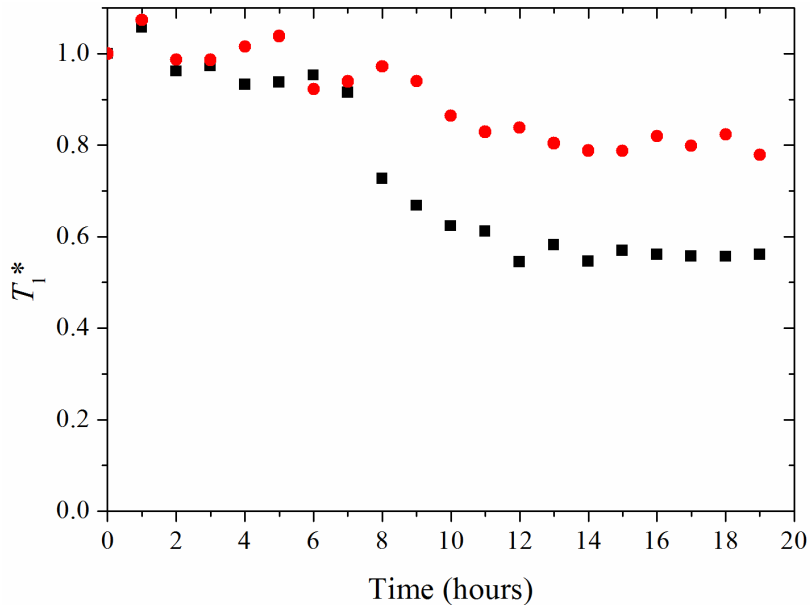

Figure 57: Contrasting changes in the normalised T_1 (T_1*) of two sampled points in a selected experimental grape berry, vasculature tissue (black ■) and extra-vascular tissue (red ●), with respect to time. The two points were located ~350 µm apart.

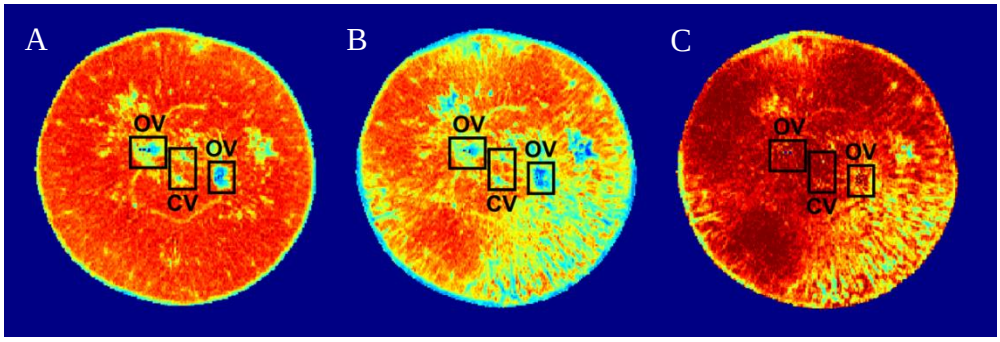

Figure 58: T_1 changes around the central (CV) and ovular vasculature (OV) of a grape berry, cv. Red Globe, partially immersed in a 10 mM manganese chloride solution. All images were from the image slice second closest to the grape berry pedicel. (A) T_1 image at time zero. (B) T_1 image of the same grape berry after nineteen hours. (C) Normalised T_1 image of (B) with respect to (A) in order to better visualise spatial contrast in T_1 values.

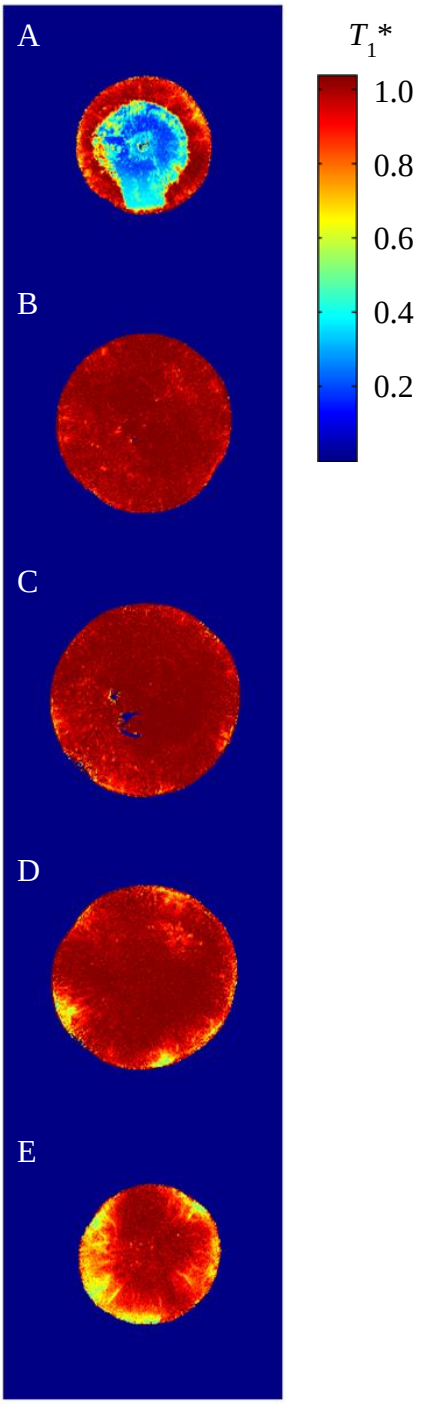

Figure 59: Five T_1 image slices (see Figure 54) of an experimental grape berry, cv. Red Globe, after nineteen hours of partial immersion in a 10 mM manganese chloride solution. These image slices are spaced 5 mm apart along the longitudinal axis of the berry, from the proximal end at the pedicel junction (A) to the distal end at the stylar remnant (E). These images have been normalised with respect to the five T_1 images of the grape berry acquired at time zero in order to better visualise changes in T_1.

Table 8: The area of T_1 reduced pericarp for each image slice (see Figure 54), averaged across the four experimental grape berries, after nineteen hours of partial immersion in a 10 mM manganese chloride solution. The error provided is the standard deviation of the areas between the grape berries.

Image Slice	Pericarp area with reduced T_1 (% of total pericarp area)
A	78 ± 9
B	33 ± 24
C	20 ± 15
D	18 ± 5
E	29 ± 16

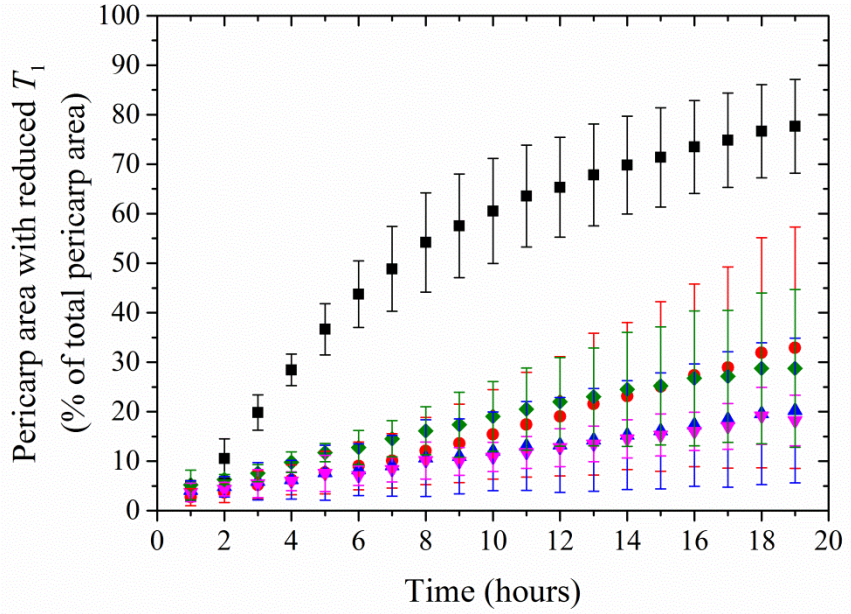

Figure 60: The area of the T_1 reduced pericarp in each image slice with respect to time (averaged over the four experimental grape berries). Image slice A (black ■), image slice B (red ●), image slice C (blue ▲), image slice D (magenta ▼), image slice E (green ♦). The error bars reflect the standard deviation of the area of T_1 reduced pericarp between the experimental grape berries.

On average, the weight of the experimental grapes increased by 41.33 ± 10.69 mg during its nineteen hours of partial immersion. Therefore the manganese content of the grape berries increased by 22.7 ± 5.9 μg over the course of the experiment. This was higher than the amount of manganese typically present in the grape berry, which

should be in the vicinity of 2.3 μg per berry [206]. As the concentration of manganese within the pericarp tissues of the grape berry increased, there was a gradual loss of diffusion-weighted MR signal from paramagnetically enhanced spin-spin relaxation. This problem was exacerbated by the EPI modification of the DTI pulse sequence used to acquire the images. Despite this loss of MR signal, apparent diffusivity within the five image slices remained relatively consistent over the nineteen hours of partial immersion in the manganese chloride solution (Figure 61).

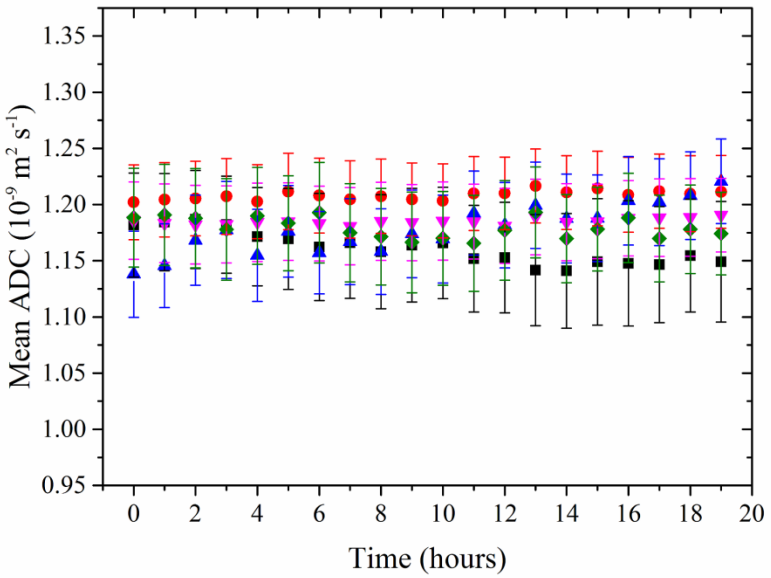

Figure 61: The mean ADC of each image slice, averaged across all of the experimental grape berries. Image slice A (black ■), image slice B (red ●), image slice C (blue ▲), image slice D (magenta ▼), image slice E (green ♦). The error bars reflect the standard deviation of the ADCs.

9.3.1 The results of irradiating grapes with microwaves

At time zero, the microwaved grape berries exhibited a reduced T_1 and a lack of structural details in the inner mesocarp region of the grape berry relative to un-microwaved grape berries (Figure 62A – E, cf. Figure 55).

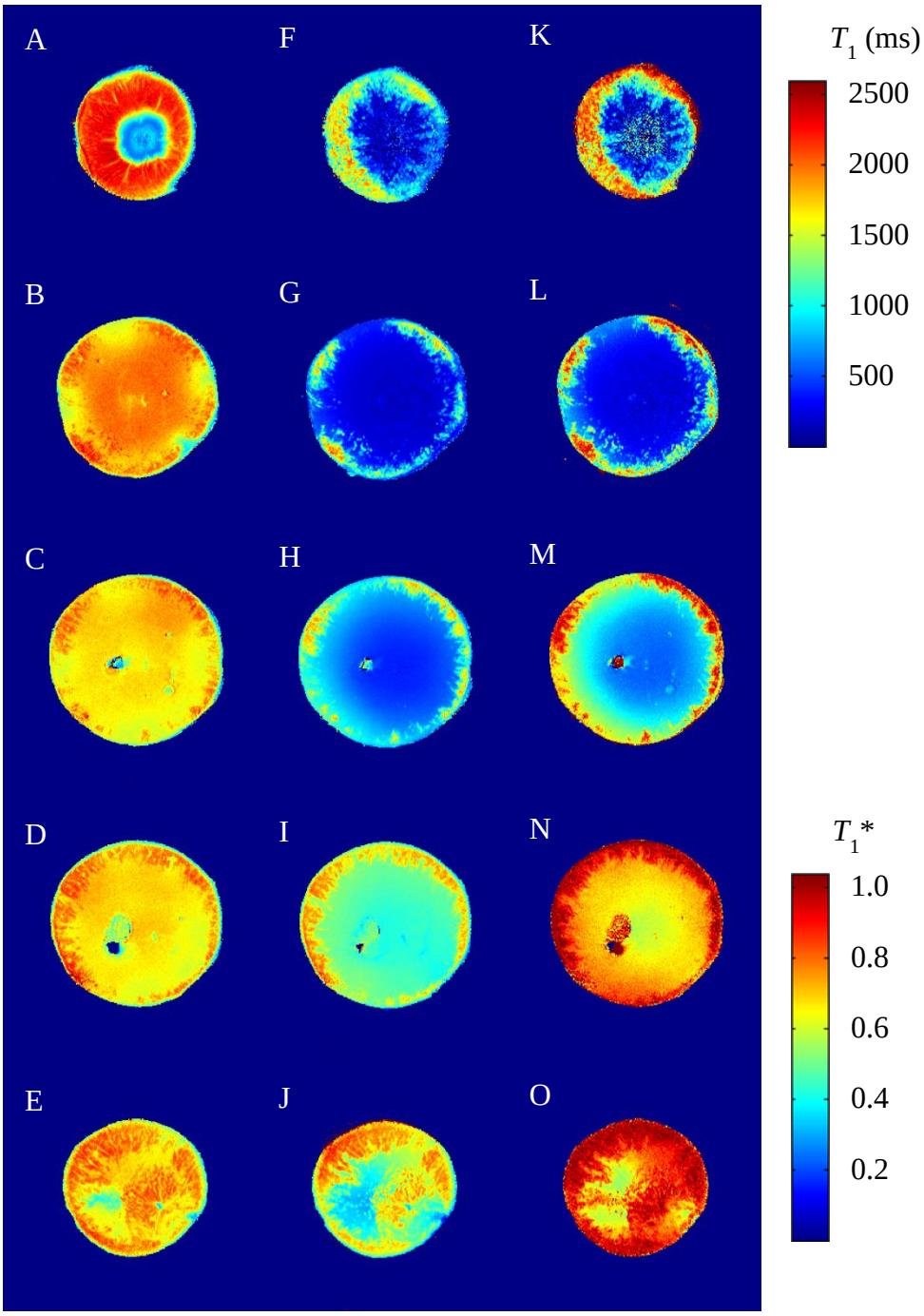

Figure 62: Comparison of T_1 images across five slices of a microwaved grape berry, cv. Red Globe, at time zero (A – E) and nineteen hours (F .– J) after partial immersion in a 10 mM solution of manganese chloride. Images F .– J have also been normalised with respect to images A – E in order to better visualise changes in T_1 (K – O).

Over the nineteen hours of their partial immersion in the manganese chloride solution, T_1 values across the inner pericarp of the microwaved grape berries significantly decreased (Figure 62F – J). Rather than entering the image slice from the grape peripheral vasculature, the reduction of T_1 in the microwaved berries originated close to the centre of the grape berry (Figure 63). The degree and extent of T_1 relaxation was noticeably greater in the microwaved grapes than in berries that had not been subject to microwave radiation (Figure 63, cf. Figure 56), as was the rate of change of the T_1 reduced pericarp tissue area (Figure 64, cf. Figure 60).

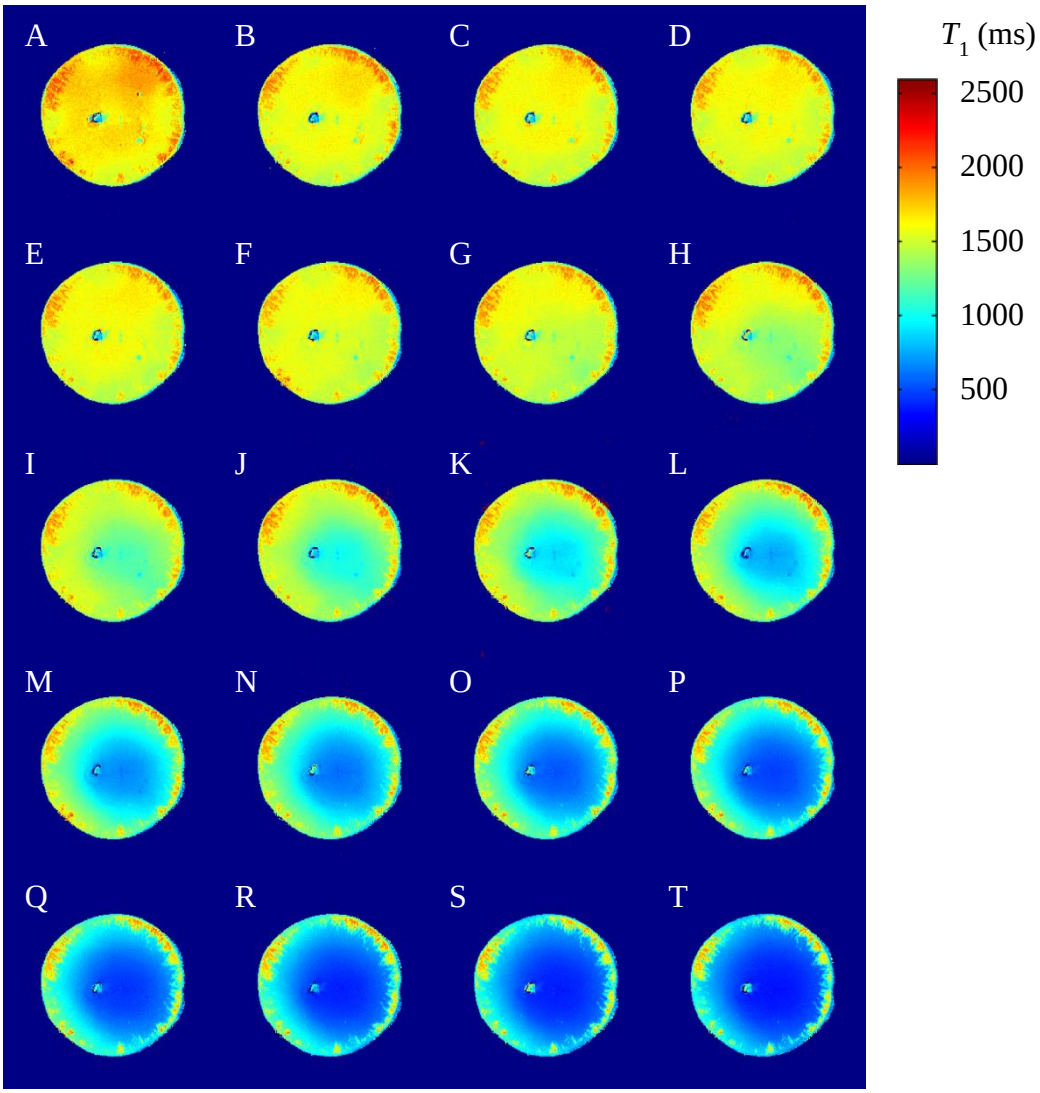

Figure 63: T_1 changes in a grape berry, cv. Red Globe, over nineteen hours of partial immersion in a 10 mM manganese chloride solution. All images were from the image slice third closest to the grape berry pedicel. (A) T_1 image of the microwaved experimental grape berry at time zero. (B – T) T_1 images of the microwaved experimental grape berry at hours one to nineteen.

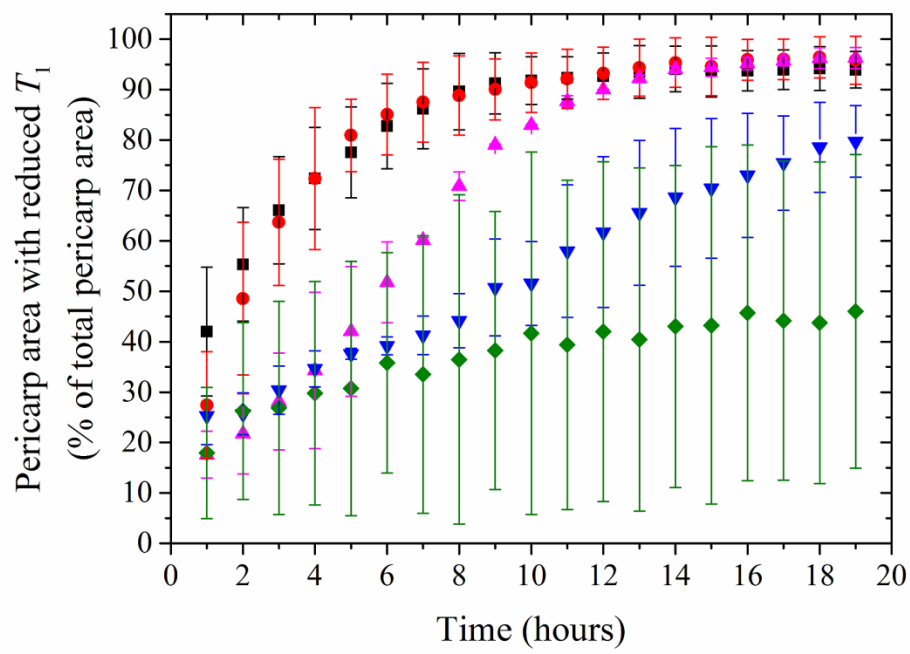

Figure 64: The area of the T_1 reduced pericarp in each image slice with respect to time (averaged over the two microwaved grape berries). Image slice A (black ■), image slice B (red ●), image slice C (blue ▲), image slice D (magenta ▼), image slice E (green ♦). The error bars reflect the standard deviation of the area of T_1 reduced pericarp between the microwaved grape berries.

9.4 Discussion

The results of the current study indicated that paramagnetic metal ions have great potential to act as tracers of vascular/extra vascular transport investigations. The widespread T_1 reductions in the pericarp of the experimental grape berries indicated the successful uptake of manganese into the vasculature of the berry pedicel, primarily the xylem [206], and the subsequent exiting of manganese ions from the berry vasculature into the pericarp tissue (Figure 56). This was also supported by the absence of T_1 reduction observed in the control berries. The presence of additional manganese in the experimental grape berries was not found to change the apparent diffusivity of the affected tissue (Figure 61). Therefore there was no noticeable change in intracellular viscosity, effect on cellular membrane permeability or evidence of cell death. The peripheral vasculature was the preferred system for manganese delivery within the grape berry, as there was little to no reductions in T_1 in or about the central and ovular vasculature (Figure 58).

The area of T_1 reduced pericarp tissue tended to decrease with increasing distance from the berry pedicel (Table 8), as did the rate of growth of these affected regions (Figure 60). However, the image slice furthest from the pedicel did not follow this trend. This is because the density and curvature of the berry vascular bundles in this image slice. This increases the probability of observing the unloading of manganese within the image slice. The area growth rate of T_1 reduced pericarp tissue in the image slice closest to the pedicel began to slow after eight hours of partial immersion (Figure 60). Thus the rate of concentration change for the manganese within the tissues of this image slice decreased with respect to time, indicating an approach towards system equilibrium as outlined by Fick's laws. (see Section 3.1 Diffusion processes). This reduction in manganese uptake is therefore consistent with a mutual diffusion dominated transport process. Unfortunately, the actual concentration of manganese in the tissue is difficult to quantify using paramagnetic enhanced spin-lattice relaxation MRI, as the relationship between the measured MR signal intensity and manganese concentration is relative [222]. The consistency of the mean ADCs exhibited in the experimental grape berries across the nineteen hours of partial immersion in the manganese chloride solution demonstrates that the uptake of manganese did not noticeably increase intracellular viscosity or influence cellular membrane permeability.

9.4.1 Evidence for controlled diffusive transport

The results of this study indicate that once manganese entered the experimental grape berry peripheral vasculature, a difference in manganese ion concentration was established and maintained between the vasculature and the surrounding extra-vascular tissue (Figure 57). However, if the exiting of manganese ions from the berry xylem was driven by mutual diffusion processes alone, it is expected that manganese would exit from all points of the peripheral vasculature and into the surrounding tissue. However, many extra-vascular regions adjacent to the peripheral vasculature of the experimental grape berries exhibited no appreciable reductions in T_1 relaxation despite other regions exhibited much greater reductions in T_1. Additionally, there were occasions when images slice further from the berry pedicel exhibited reductions in T_1 relaxation in the berry pericarp to a greater extent than images slices closer to the berry pedicel (Figure 59 and 60). This variation in manganese distribution

between image slices could be due to bifurcations and xylem unloading mechanisms within the berry vasculature influencing the spatial distribution of manganese ‘downstream’ of the berry pedicel.

Further evidence for controlled diffusive transport of metal ions in the experimental grape berries was provided by the two Red Globe table grapes which were briefly microwaved in order to disrupt the membranes of their pericarp cells. This disruption was indicated by the observed widespread reduction in T_1 in the microwaved grape berries and the loss of detailed tissue structure in inner mesocarp region (Figure 62A – E). The disruption of the inner mesocarp cellular membranes was also reflected in the rate at which the manganese entered the inner mesocarp of the microwaved grape berries and its spatial distribution in the tissue. For example, the rate of the area of the T_1 reduced pericarp tissue changed faster in microwaved berries than in the experimental grapes (Figure 64, cf. Figure 60). This rate of change also slowed in the image slices with time, reflecting the driving mutual diffusion process. Additionally, from the T_1 images (Figure 63) it appears that the reduction of T_1 in the microwaved grape berries began in the central tissue of the grape berry, rather than near the peripheral vasculature, and that the spatial distribution of the manganese within these berries was more isotropic when compared with the more anisotropic distributions of their un-microwaved counterparts (Figure 56). Importantly, the distribution of manganese in the microwaved grape berries was also noticeably more homogeneous than in the grape berries which had not been irradiated. For these results, the transport of manganese between pericarp cells must be controlled.

The microwaved grape berries exhibited lower T_1 values after nineteen hours of partial immersion in the manganese chloride solution compared to their un-microwaved counterparts. This difference in T_1 could potentially be attributed to microwave damage to the berry pedicel, receptacle and/or the epidermal tissue surrounding the receptacle providing an easier point of ingress for the aqueous manganese. However, the overall increase in microwaved grape berry weight after nineteen hours of partial immersion in the manganese chloride solution (33.50 ± 19.09 mg) was not greater than the increased weight of the experimental grape berries. This indicates that the microwaved grape berries did not necessarily take up more manganese than the un-microwaved berries. It is possible that the manganese

ions taken up by the experimental grape berries are being stored in parenchyma cells in such a way that limits the contact of these ions with mobile water molecules.

9.4.2 Comparing the results of the study to the literature

A number of studies have been previously conducted to order to investigate xylem transport using xylem tracers. These tracers largely consisted of xylem-mobile dyes, such acid/basic fuchsin [223-225] and eosin yellow [14]. However, these organic molecules have a much greater molecular weight than manganese ions, and were largely confined to the berry peripheral vasculature. Paramagnetically enhanced relaxation MRI, on the other hand, offers the novel possibility of non-invasively tracing the transport of metal ions native to the grape berry, their exiting of the xylem and their subsequent transport across the grape berry pericarp.

Other previous studies, which employed phloem tracers instead of xylem tracers, also offer interesting comparisons for the results of this investigation. For example, from the results of the current study it appears that the percentage area of the T_1 reduced tissue tends to be greater in image slices closer to the berry pedicel. A similar result was obtained in a previous study in which the uptake of ^{14}C labelled sucrose into the grape berry via the pedicel was observed [14]. However, these results disagree with those of another previous study [8], which indicate that ^{14}C labelled photosynthates appear to be evenly unloaded across the length of the berry peripheral vascular system. One difference between these three studies was the method used to deliver the tracer molecules to the berry pedicel. In the current study and the study of Findlay et al., a highly concentrated solution containing the tracer molecules was applied directly to the freshly cut berry pedicel. However, Zhang et al. used a fine wick to deliver small amounts of the labelled photosynthates to the pedicel of the berry over a longer period of time (72 hours). In the current study, manganese was supplied to the experimental grape berries at non-physiological concentrations to ensure strong contrast in the relaxation images. Any potential problems arising from this could be reduced by developing a method of delivering a more dilute solution of manganese to the berry pedicel in smaller quantities over a longer period of time, or by introducing the manganese at a more basal site. However, this will result in significantly decreased contrast in the relaxation MR images.

Chapter 10 - Conclusions

In this chapter, conclusions are drawn from the studies within the thesis to demonstrate the contributions of this research to furthering knowledge of grape berry morphology and physiology and how these contributions relate to one another. This chapter also includes an assessment of whether the research presented here met its intended objectives.

The first objective of this thesis was to determine the applicability of different diffusion MRI techniques for the processing of MR data acquired during studies of grape berry morphology. From the extensive list of diffusion MRI techniques considered, two methods were short listed; DTI and BFOR imaging. DTI possesses advantages in its simplicity and robustness, while BFOR imaging is able to model more complex tissue geometries than DTI. However, the results of the BFOR imaging simulations found that BFOR imaging did not appear well suited to reconstructing the relatively wide microstructures expected in the grape berry pericarp. The probability isosurfaces reconstructed using BFOR imaging had a noticeably reduced ability to accurately reconstruct the simulated cell geometries wider than 10 µm. For this reason, DTI was selected for processing the data of the diffusion MRI studies contained within this thesis. As has been previously established, the bulk of the grape berry consists of radially aligned parenchyma cells. Therefore DTI would be sufficient for reconstructing the orientation of grape pericarp microstructures even with its relatively low angular contrast.

Having selected an appropriate diffusion MRI technique to analyse the diffusion MR data, the second objective of the thesis was to use diffusion MRI to study the morphology of healthy grape berries across their development. In addition to providing a novel prospective on grape berry development, this investigation also established a library of relaxation and diffusion MR images/values of normal grape berries for comparisons with the results of different grape treatments in following studies. The results of the DTI studies of the untreated grape berries demonstrated that diffusion anisotropy patterns correlated with the microstructure of the major pericarp tissues of cv. Semillon grape berries, including the exocarp, outer and inner mesocarp and seed interior development. Microstructural variations in the grape

berry tissues could also be inferred from the MR images which corresponded with well-known stages of grape berry development. For example, an increase in diffusion vector coherence between 28 and 41 DAF indicating the transition from non-elongated to radially elongated mesocarp cells, and the decrease of diffusion vector coherence/apparent diffusivity during ripening, likely the result of the widespread apoptotic cell death in the berry mesocarp. It is also possible that the sigmoidal decrease of apparent diffusivity with grape berry is related to the sigmoidal increase of berry sugar. This potential relationship could have important implications for sugar accumulation in grapes as well as the hydraulic resistance across the berry, and should be explored further in a future study. Another interesting feature observed in the diffusion MR images of the grape berry pericarp was the rotationally dependent anisotropic diffusion patterns noted in the seed integument of young grape berries. These diffusion patterns could only be observed early in the development of the grape berry, due to the dehydration of the seed integument and the replacement of the nucellus by the liquid endosperm. DTI could hence prove to be a useful tool for future studies of water transport across the seed coat while the seed is still maturing. Additionally, the analysis of diffusion MR images revealed that these striation patterns, readily visible in the relaxation images of the grape berry pericarp, corresponded with variations in apparent diffusivity. This result provided further evidence that the inner mesocarp striation patterns previously noted in the spin-spin relaxation weighted images from the studies of Pope et al. (1993) and Glidewell et al. (1997) arise due to variations in cell width across the striation bands.

Although the diffusion measurements were made from berries detached from the bunch and in a sealed environment, it is expected that an actively transpiring berry still attached to the vine would not exhibit a noticeable difference to the results presented here. As was previously explained, diffusion measurements are of the random, thermally driven movement of water molecules. These measurements will hence not be affected by uniform water flow caused by active transpiration. Differences between the acquisition parameters of the different diffusion MRI experiments in this thesis added an additional step of complexity when comparing diffusion results between studies. However, the TR and TE were maintained between diffusion MR images acquired in the same set; hence spin-spin and spin-lattice relaxation could be normalised from the diffusion MR images during their

reconstruction. Differences in Δ between diffusion MR images was more of a concern as it changes the length scale probed by diffusing water molecules. However, although the difference in Δ between the experiments contained within this thesis could appear significant, the difference in the RMSD (i.e. the length scale probed by the diffusing water) differs by a few micrometres, which is quite small relative to variations in grape berry cell size (see Section 1.1.1 Cell sizes of the grape berry pericarp tissues). It is therefore quite unlikely that differences in the MR experiment parameters would noticeably impact on any comparisons made between different grape berry diffusion experiments.

Having established a close relationship between the diffusion MRI images and the morphology of the grape berry, the third objective of this thesis was to investigate how changes to the grape berry morphology arising from berry diseases/physical injury could potentially provide information regarding the mechanism of important fruit afflictions, such as grape berry split. Table grapes, cv. Thompson seedless, were studied during this investigation due to their predisposition to splitting. No changes in the diffusion MR images were observed prior to the formation of a split in the berry epidermis that would indicate a change in berry morphology with the exception of localised expansions in the grape berry pericarp. However, the diffusion MR studies did reveal that a number of morphological and physiological changes occur in the berry pericarp once splits form in the berry epidermis. Significantly, there was an increase in the mean apparent diffusivity of the tissue surrounding these wounds relative to healthy tissue/grape berries. The increase in apparent diffusivity was attributed to ischemic cell death in the affected berry mesocarp tissue. This result contrasted interestingly with the decrease in apparent diffusivity observed in the Semillon grapes as a consequence of cell shrinkage from widespread apoptosis in the berry pericarp. Upon comparing water soaked pre-split berries to pre-split berries that had been immersed in Fomblin oil or left dry, it was concluded that ischemic cell death was triggered by the osmotic imbibition of water through the openings in the berry epidermis. In the context of a vineyard, the amount of standing water on the surface of split grape berries may be an important determinant of the cellular response of the fruit to this trauma, and the subsequent establishment of adventitious fruit pathogens.

The fourth and final objective of this thesis was to investigate how paramagnetically enhanced spin-lattice relaxation MRI could be used to investigate the transport and diffusion of manganese across the berry pericarp. This study differed somewhat from other investigations within this thesis; instead of making direct measurements of water diffusion in order to determine the morphology of the grape berry pericarp, indirect observations of the diffusion of paramagnetic ions were made to better understand this physiological process within the grape berry. This method is a highly novel approach; previous studies of vasculature and extra-vascular solute transport typically employ radioactively or fluorescently labelled compounds which are constrained to large molecule transport pathways. The relaxation MRI experiments revealed that manganese is preferentially transported across the length of grape berry by the peripheral vasculature. However, the manganese was not evenly distributed in the berry pericarp; some regions of the grape berry received a higher concentration of manganese than others over the nineteen hours the grape berry pedicels were immersed in the manganese solution. In some cases, image slices further from the berry pedicel exhibited more noticeable changes in T_1 than image slices closer to the pedicel. These results, in conjunction with the relaxation MRI experiments on microwaved grape berries, imply that the grape berry xylem is able to control the point at with manganese exits 'downstream' of the pedicel while the cellular membranes of the extra-vascular tissue cells are able to influence the spatial distribution of manganese within the pericarp tissue. Unlike large molecular weight xylem-mobile dyes, manganese can freely exit the xylem and diffuse through the berry pericarp, therefore serving as an excellent tracer for xylem vascular/extra-vascular metal ion transport. Other paramagnetic ions that the grape berry naturally accumulates, such as iron and copper, are likely to prove useful for studying vascular/extra-vascular metal ion transport as well. Future botanical investigations making use of paramagnetically enhanced relaxation MRI could prove to be very valuable in determining how botanical species are able to transport and store these materials.

Relaxation and diffusion MRI will be useful in the examination of the morphology and physiology of other plant species and organs, providing the constituent tissues contain sufficient unbound water. While tissues consisting of smaller cells are easier to investigate than tissues with larger cells, diffusion anisotropy will remain evident

if Δ is long enough to ensure that a large population of water molecules can interact with the surface of the cellular boundaries. The applicability of relaxation and diffusion MRI to the study of the biology of plant species with high oil contents is of great interest as natural plant oils are often highly valued botanical commodities. Although natural oils are hydrophobic, and diffusing water molecules treated droplets of oil encountered in cell cytoplasm as diffusion restricting obstacles, a short diffusion MRI investigation of mature olives found that diffusion MRI is quite possible on plant organs with high oil contents. Olives were an ideal candidate for this small study, as olives are comparable in size to grape berries and also have a similar internal structure and cellular dimensions, and the relaxation and diffusion results of this investigation neatly complemented the results of the grape berry MRI investigation.

In closing, this thesis has met all its intended objectives. It has demonstrated that diffusion MRI is an effective tool in the study of botany with MR images of the grape berry pericarp providing complementary information regarding grape morphology and physiology. The exciting results of the studies within this thesis also provide a strong foundation for future research into the use of novel MRI technologies for furthering our understanding of plant biology.

Appendices

Appendix A

The ability to determine the orientation of overlapping fibre populations is highly desirable for analysing complicated biological systems. As a result, there has been much interest from biomedical researchers since the inception of DTI to improve upon the limited angular resolution provided by the second order diffusion tensor. The objective of this appendix is to introduce and discuss a large variety of the three-dimensional diffusion MRI techniques available. Also included is an assessment of the requirements and capabilities of each of the listed techniques in their respective sections.

Higher order diffusion tensor imaging

Expanding on the concept of the diffusion tensor directly, the diffusion imaging technique known as higher order diffusion tensor imaging (HOTDI) replaces **D** with a tensor of a higher order. The increased dimensionality of higher order tensors allows for more complicated coupling between the components of **B** and the measured diffusion-weighted MR signal. As a result, HODTI provides a more complete description of diffusion anisotropy and correspondingly provides additional information regarding complicated restricting microstructures. Replacing **D** with a symmetric tensor of an arbitrary higher order is a straightforward process largely because the tensor product operation is allowed for any two tensors of equal rank. If **U** and **D** in Eq. (36) are replaced with tensors of some arbitrary order, the expression becomes [226],

$$D(\hat{\mathbf{u}}) = \mathbf{U}^{(l)} : \mathbf{D}^{(l)} = \sum_{i_1=1}^{3}\sum_{i_2=1}^{3}\cdots\sum_{i_l=1}^{3} u_{i_1}u_{i_2}\ldots u_{i_n} D_{i_1 i_2 \ldots i_l} \tag{78}$$

where $\mathbf{U}^{(l)}$ is an l-th order directional tensor, $\mathbf{D}^{(l)}$ is an l-th order diffusion tensor and i_l is the l-th spatial coordinate index of the subscripted tensor (i.e., $i_k = x, y, z$ where

$1 \le k \le l$). The order of $\mathbf{D}^{(l)}$ is generally restricted to an even integer; this is because the multiplication of an odd number of u components in Eq. (78) would imply that

$$D(-\hat{\mathbf{u}}) = -D(\hat{\mathbf{u}}) \tag{79}$$

and negative diffusion coefficients cannot exist for a real system (i.e., the values would be non-physical). Analogous to Eq. (37), multiplying $\mathbf{U}^{(l)}$ by b yields a tensor that describes a multi-dimensional description of the magnetic diffusion gradient, $\mathbf{b}^{(l)}$, i.e.,

$$\mathbf{b}^{(l)} = b\mathbf{U}^{(l)} . \tag{80}$$

The second order **b** and **D** tensors in Eq. (39) can then be replaced with $\mathbf{b}^{(l)}$ and $\mathbf{D}^{(l)}$,

$$\ln E(\hat{\mathbf{u}}) = -\mathbf{b}^{(l)} : \mathbf{D}^{(l)} = -\sum_{i_1=1}^{3}\sum_{i_2=1}^{3}\ldots\sum_{i_l=1}^{3} b_{i_1 i_2 \ldots i_l} D_{i_1 i_2 \ldots i_l} \tag{81}$$

While an l-th order diffusion tensor possesses 3^l elements, the symmetry of the tensor implies that (similarly to **D**) it contains a subset of independent elements. For example, $\mathbf{D}^{(4)}$ contains fifteen independent elements: D_{xxxx}, D_{yyyy}, D_{zzzz}, D_{xxxy}, D_{xxxz}, D_{xxyy}, D_{xxyz}, D_{xxzz}, D_{xyyy}, D_{xyyz}, D_{xyzz}, D_{xzzz}, D_{yyyz}, D_{yyzz} and D_{yzzz}.

The number of independent elements in a diffusion tensor of any order can be found by using an index replacement strategy. This strategy begins with $D_{xxx\ldots xx}$, an element of an l-th order diffusion tensor. As all the indices are identical, $D_{xxx\ldots xx}$ is an independent element of the tensor and is not equivalent to any other element in tensor. Now consider an element which differs by one index (i.e., one index of the element is either y or z). Recalling that the order of the element indices is not important due to the symmetry of the tensor, this replacement creates two new independent elements (i.e., $D_{xxx\ldots xy}$ and $D_{xxx\ldots xz}$). Likewise, if an element differs from $D_{xxx\ldots xx}$ by two indices and from $D_{xxx\ldots xy}$ and $D_{xxx\ldots xz}$ by one index this would lead to the creation of three additional independent elements (i.e., $D_{xxx\ldots yy}$, $D_{xxx\ldots yz}$ and $D_{xxx\ldots zz}$). Generalising this replacement strategy yields the relation

$$N = \sum_{x=1}^{l+1} x = 1 + 2 + 3 + \ldots + (l+1) = \frac{(l+1)(l+2)}{2} . \tag{82}$$

Since the independent elements can appear more than once in the array, the diffusion tensor is a multiset. The number of equivalent elements (i.e., the multiplicity of each element) in a multiset is given by

$$\frac{l!}{n_x!n_y!n_z!} \tag{83}$$

where n_x, n_y and n_z are respectively the number of the x, y and z components of the tensor. Using Eqs. (82) and (83), Eq. (81) can be easily rewritten as a system of linear equations. For example, in order to reconstruct a fourth order diffusion tensor, Eq. (81) can be expressed as

$$\begin{aligned}\ln E(\mathbf{u}) = &-b(\hat{\mathbf{u}})_{xxxx} D_{xxxx} - b(\hat{\mathbf{u}})_{yyyy} D_{yyyy} - b(\hat{\mathbf{u}})_{zzzz} D_{zzzz} \\ &-4b(\hat{\mathbf{u}})_{xxxy} 4D_{xxxy} - 4b(\hat{\mathbf{u}})_{xxxz} D_{xxxz} - 4b(\hat{\mathbf{u}})_{yyyx} D_{yyyx} \\ &-4b(\hat{\mathbf{u}})_{yyyz} D_{yyyz} - 4b(\hat{\mathbf{u}})_{zzzx} D_{zzzx} - 4b(\hat{\mathbf{u}})_{zzzy} D_{zzzy} \\ &-6b(\hat{\mathbf{u}})_{xxyy} D_{xxyy} - 6b(\hat{\mathbf{u}})_{xxzz} D_{xxzz} - 6b(\hat{\mathbf{u}})_{yyzz} D_{yyzz} \\ &-12b(\hat{\mathbf{u}})_{xxyz} D_{xxyz} - 12b(\hat{\mathbf{u}})_{yyxz} D_{yyxz} - 12b(\hat{\mathbf{u}})_{zzxy} D_{zzxy}\end{aligned} . \tag{84}$$

The elements of $\mathbf{D}^{(l)}$, for a particular order l, can hence be determined using a standard iterative or direct tensor reconstruction method (see Appendix B). As $\mathbf{D}^{(4)}$ contains fifteen independent elements, Eq. (84) can only be solved if the system contains a minimum of fifteen equations (i.e., q-space must be sampled on at least fifteen or more unique points of a single q-shell in addition to the origin of q-space).

Once the independent elements of $\mathbf{D}^{(l)}$ have been determined, the visualisation of the diffusion data can begin. Since higher order diffusion tensors are not matrices, linear algebraic operations, such as eigen-decomposition, are possible in theory but are not straightforward to implement [227, 228]. As a result, $\mathbf{D}^{(l)}$ is typically visualised as an apparent diffusivity profile by extrapolating ADCs from $\mathbf{D}^{(l)}$ using Eq. (78) for a large number of non-collinear $\mathbf{u}$, similar to how an apparent diffusivity profile can be created from $\mathbf{D}$. The profile can then be converted into an isosurface (Figure 65). However, the question remains as to what order of $\mathbf{D}^{(l)}$ is appropriate for a given restricted system. If the order of the tensor is too low, the angular resolution of the tensor will be insufficient to resolve the effect of restricting structure on the apparent diffusion profile. If the order of the tensor is too high, the total acquisition image time is significantly increased for little gain.

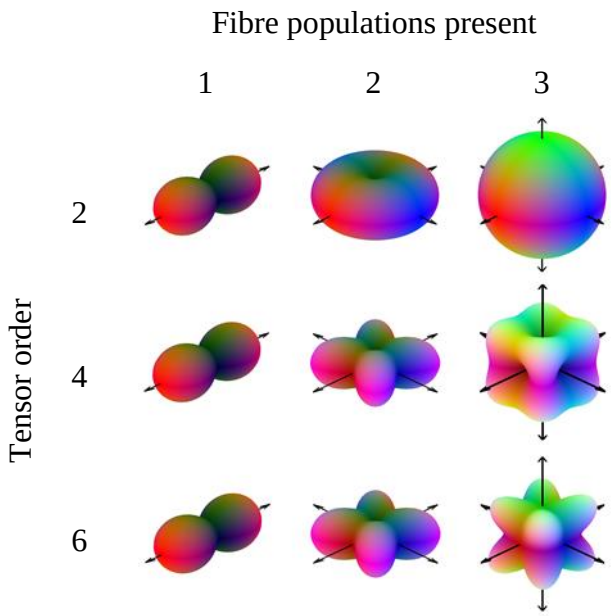

Figure 65: Diffusivity isosurfaces of overlapping fibre populations constructed using diffusion tensors of different orders. The orientation of each fibre population is indicated with double-headed arrows. As the number of overlapping fibre populations increases, tensors of a lower rank become less effective in describing the more complicated diffusion patterns. However, the diffusivity isosurfaces do not necessarily indicate the correct orientation of these fibre populations.

The minimum order of $\mathbf{D}^{(l)}$ required to characterise a restricted system can be defined as the point at which increasing the order of the diffusion tensor no longer significantly changes the shape of the apparent diffusivity profile. For example, for a voxel containing a single fibre population, the apparent diffusivity profile is identical for a second, fourth or sixth order tensor (Figure 65, left column). Therefore a second order diffusion tensor is sufficient to characterise this system. If two fibre populations are present, using a tensor of an order greater than four results in no further changes to the appearance of the apparent diffusivity profile (Figure 65, middle column). Therefore a fourth order diffusion tensor is sufficient to characterise this system. This pattern is repeated for increasing numbers of intravoxel fibre populations. In general, a tensor with an order of $2n$ is required to characterise diffusion within voxels containing n fibre populations.

Similarly to the second order diffusion tensor, scalar features can also be extracted from higher order diffusion tensors. For example, a generalised FA (GFA) index can be calculated by expanding Eq. (48) in accordance with the definition of the FA

index: the deviation of the eigenvalues/diagonal elements of $\mathbf{D}^{(l)}$ from the root mean square of $\mathbf{D}^{(l)}$ [151], i.e.,

$$\mathrm{GFA} = \frac{\mathrm{std}(\mathbf{D})}{\mathrm{rms}(\mathbf{D})} = \sqrt{\frac{n}{n-1}\frac{\sum_{i=1}^{n}\left(D(\hat{\mathbf{u}}_i) - \left\langle \mathbf{D}^{(l)} \right\rangle\right)^2}{\sum_{i=1}^{n} D(\hat{\mathbf{u}}_i)^2}} \quad . \tag{85}$$

where n equal to the number of ADCs extracted from $\mathbf{D}^{(l)}$ (see Eq. (78)) and $\langle \mathbf{D}^{(l)} \rangle$ is the mean diffusivity of the higher order diffusion tensor, i.e.

$$\left\langle \mathbf{D}^{(l)} \right\rangle = \frac{1}{n}\sum_{i=1}^{n} D(\hat{\mathbf{u}}_i). \tag{86}$$

The accuracy of the GFA can be improved by increasing the number of ADCs included in Eq. (85). As the GFA index is an extension of the FA index, the value will range between zero and one.

The greatest drawback of HODTI is that the local maxima of higher-order tensor apparent diffusivity profiles do not correspond to the orientations of overlapping fibre populations (Figure 65). This discrepancy can be explained using the following example; consider a voxel which contains $n \geq 2$ distinct fibre populations. The probability of a single water molecule displacing $\mathbf{R}$ in time t is given by

$$P(\mathbf{R}, t) = \sum_{i=1}^{n} f_i P_i(\mathbf{R}, t) \tag{87}$$

where f_i and $P_i(\mathbf{D},t)$ are the respective volume fraction and diffusion propagator associated with i-th fibre population. Likewise, if it is assumed that the contribution of each fibre population to the measured diffusion-weighted signal add independently,

$$E(\hat{\mathbf{u}}) = \sum_{i=1}^{n} f_i \exp\left(-bD_i(\hat{\mathbf{u}})\right) \tag{88}$$

where $D_i(\mathbf{u})$ is the ADC associated with the i-th fibre population when diffusion is measured along $\mathbf{u}$. Thus, the observed ADC is

$$D(\hat{\mathbf{u}}) = -\frac{1}{b}\ln\left[\sum_{i=1}^{n} f_i \exp\left(-bD_i(\hat{\mathbf{u}})\right)\right] . \tag{89}$$

Thus from Eq. (89) it can be seen that the ADCs corresponding to each fibre population do not add linearly. Consequently, the ADCs of directions which are super-positions of the fibre orientations are larger than the ADCs of directions parallel to the fibres. Consequently the local maxima of the apparent diffusivity profile do not correspond to the orientations of the overlapping fibre populations. However Eq. (87) demonstrates that the diffusion propagators of different fibre populations do add linearly; therefore, the local maxima of a diffusion propagator (i.e., probability) isosurface will match the orientation for any number of overlapping fibre populations. This concept is discussed further in following section.

Generalised diffusion tensor imaging

Generalised diffusion tensor imaging (GDTI) is a natural extension of DTI and HODTI. Instead of characterising diffusion with a single diffusion tensor, GDTI employs a series of tensors with an infinitely increasing order [229, 230]. For example, generalising Eq. (13) in this manner yields

$$\mathrm{J}_P(\mathbf{r}_0,\mathbf{r}_1,t) = -\mathrm{D}^{(2)}\nabla^{(1)}P(\mathbf{r}_0,\mathbf{r}_1,t) - \mathrm{D}^{(3)}\nabla^{(2)}P(\mathbf{r}_0,\mathbf{r}_1,t) - \mathrm{D}^{(4)}\nabla^{(3)}P(\mathbf{r}_0,\mathbf{r}_1,t)\ldots \tag{90}$$

where

$$\nabla^{(l)} = \frac{\partial}{\partial u_{i_1}\partial u_{i_2}\ldots\partial u_{i_l}} . \tag{91}$$

The advantage of using a series of tensors is that each array contains non-redundant information regarding diffusion (i.e., information is not shared between the tensors). Each tensor describes a different aspect of diffusion, such as variance, skewness or kurtosis (the diffusion, skewness and kurtosis tensors, respectively) [229, 230]. It also means that unlike DTI and HODTI, GDTI does not require the assumption that diffusion is free. Replacing the ADC in the Bloch-Torrey equation (see Eq. (28)) by the tensor series featured in Eq. (90) gives

$$\frac{\partial \mathbf{M}}{\partial t} = \gamma \mathbf{M} \times \mathbf{B} - \frac{M_x \hat{\mathbf{i}} + M_y \hat{\mathbf{j}}}{T_2} - \frac{\left(M_z - M_0\right)\hat{\mathbf{k}}}{T_1} + \nabla\left(-\mathbf{D}^{(2)}\nabla^{(1)}\mathbf{M} - \mathbf{D}^{(3)}\nabla^{(2)}\mathbf{M} - \mathbf{D}^{(4)}\nabla^{(3)}\mathbf{M}\ldots\right). \quad (92)$$

Rewriting Eq. (92) in the rotating frame and in terms of its transverse magnetisation therefore yields

$$\frac{\partial m_{xy}}{\partial t} = -i\gamma\left(\mathbf{g}\cdot\mathbf{r}\right)m_{xy} - \frac{m_{xy}}{T_2} + \nabla\left(-\mathbf{D}^{(2)}\nabla^{(1)}m_{xy} - \mathbf{D}^{(3)}\nabla^{(2)}m_{xy} - \mathbf{D}^{(4)}\nabla^{(3)}m_{xy}\ldots\right). \quad (93)$$

As m_{xy} relaxes exponentially with time, when Eq. (93) is integrated,

$$m_{xy} = m_D \exp\left(-i\gamma\left(\mathbf{g}\cdot\mathbf{r}\right)t - t/T_2\right) \quad (94)$$

where m_D is the component of the transverse magnetisation affected by diffusion. Substituting Eq. (94) in Eq. (93) yields,

$$\frac{\partial m_D}{\partial t} = \left(-i\right)^2 \gamma^2 g_{i_1} g_{i_2} \mathbf{D}^{(2)} m_D + \left(-i\right)^3 \gamma^3 g_{i_1} g_{i_2} g_{i_3} \mathbf{D}^{(3)} m_D + \left(-i\right)^4 \gamma^4 g_{i_1} g_{i_2} g_{i_3} g_{i_4} \mathbf{D}^{(4)} m_D \ldots \quad (95)$$

Using an approach similar to Bloch-Torrey (see Section 4.1 The Bloch-Torrey equation), Eq. (95) can be solved leading to the expression [109, 229],

$$\ln E\left(\mathbf{u}\right) = \sum_{l=2}^{\infty}\left(i\right)^l \sum_{i_1=1}^{3}\sum_{i_2=1}^{3}\ldots\sum_{i_l=1}^{3} \mathfrak{B}_{i_1 i_2 \ldots i_l} D_{i_1 i_2 \ldots i_l} = \sum_{l=2}^{\infty}\left(i\right)^l \mathfrak{B}^{(l)} : \mathbf{D}^{(l)}, \quad (96)$$

where $\mathfrak{B}_{i_1 i_2 \cdots i_l} = \gamma^l \delta^l g_{i_1} g_{i_2} \ldots g_{i_l}\left(\Delta - \left(l-1\right)/\left(l+1\right)\delta\right)$ are the components of the l-th order magnetic gradient tensor $\mathfrak{B}^{(l)}$.

The physical meaning of each tensor in the series depends upon the order of the tensor. For example, $\mathbf{D}^{(2)} = \mathbf{D}$, and thus describes the variance in diffusion displacement. $\mathbf{D}^{(3)}$, on the other hand, reflects diffusion skewness while $\mathbf{D}^{(4)}$ depicts the extent of diffusion kurtosis. Diffusion tensors with an order higher than four do not have a physical analogy; they are best thought of as increasingly higher dimensional descriptors of the diffusion profile. In the case of free diffusion, the diffusion propagator exhibits no skew or kurtosis; thus the elements of the diffusion tensors of an order greater than two are equal to zero. From Eq. (96) it can also be inferred that the magnitude (i.e., real component) of the diffusion-weighted MR

signal relates to the tensors of the series with an even order while the phase (i.e., imaginary component) of the MR signal relates to tensors with an odd order. Unfortunately, MR signal phase is easily corrupted; for example, by eddy currents [231] or subject motion. Since accounting for or correcting these phase errors is a very difficult task, diffusion MRI data sets typically only contain the signal magnitude values. As a result, the odd order tensors (e.g. the skewness tensor) are excluded from the tensor series. This is unfortunate because only the odd ordered tensors are able to account for asymmetric diffusion (e.g. when a single fibre population diverges within a voxel).

When the diffusion tensor series in Eq. (96) is truncated to a specific order, it can be rewritten as a linear equation. For example, truncating Eq. (96) to the fourth order, and excluding the odd order tensor from the series, yields

$$\begin{aligned}
\ln E(\hat{\mathrm{u}}) = & -\mathfrak{B}(\hat{\mathrm{u}})_{xx} D_{xx} - \mathfrak{B}(\hat{\mathrm{u}})_{yy} D_{yy} - \mathfrak{B}(\hat{\mathrm{u}})_{zz} D_{zz} \\
& -2\mathfrak{B}(\hat{\mathrm{u}})_{xy} D_{xy} - 2\mathfrak{B}(\hat{\mathrm{u}})_{xz} D_{xz} - 2\mathfrak{B}(\hat{\mathrm{u}})_{yz} D_{yz} \\
& +\mathfrak{B}(\hat{\mathrm{u}})_{xxxx} D_{xxxx} + \mathfrak{B}(\hat{\mathrm{u}})_{yyyy} D_{yyyy} + \mathfrak{B}(\hat{\mathrm{u}})_{zzzz} D_{zzzz} \\
& +4\mathfrak{B}(\hat{\mathrm{u}})_{xxxy} 4D_{xxxy} + 4\mathfrak{B}(\hat{\mathrm{u}})_{xxxz} D_{xxxz} + 4\mathfrak{B}(\hat{\mathrm{u}})_{xyyy} D_{xyyy} \; . \\
& +4\mathfrak{B}(\hat{\mathrm{u}})_{yyyz} D_{yyyz} + 4\mathfrak{B}(\hat{\mathrm{u}})_{xzzz} D_{xzzz} + 4\mathfrak{B}(\hat{\mathrm{u}})_{yzzz} D_{yzzz} \\
& +6B(\hat{\mathrm{u}})^{(4)}_{xxyy} D^{(4)}_{xxyy} + 6B(\hat{\mathrm{u}})^{(4)}_{xxzz} D^{(4)}_{xxzz} + 6B(\hat{\mathrm{u}})^{(4)}_{yyzz} D^{(4)}_{yyzz} \\
& +12B(\hat{\mathrm{u}})^{(4)}_{xxyz} D^{(4)}_{xxyz} + 12B(\hat{\mathrm{u}})^{(4)}_{xyyz} D^{(4)}_{xyyz} + 12B(\hat{\mathrm{u}})^{(4)}_{xyzz} D^{(4)}_{xyzz}
\end{aligned} \tag{97}$$

Similarly to Eq. (84), this equation can be used as the basis of a system of linear equations. In order to calculate the independent elements of each diffusion tensor in the linear equation, this system must contain a number of linear equations equal to or greater than the total number of independent elements present (e.g. a minimum of twenty-one linear equations are required to solve Eq. (97)). Since GDTI provides information regarding the radial component of the apparent diffusion processes, *q*-space must be sampled on multiple *q*-shells (i.e., one *q*-shell per tensor in the series). The number of points sampled on each *q*-shell must also equal or exceed the number of independent elements contained within the highest order diffusion tensor present in the series. For example, to determine the independent elements of $\mathbf{D}^{(2)}$ and $\mathbf{D}^{(4)}$ using the system of questions constructed from Eq. (97) would require sampling *q*-space on a minimum of two different *q*-shells with fifteen points on each shell in

addition to the q-space origin. The independent elements of each diffusion tensor in the series can be determined using an iterative or direct diffusion tensor reconstruction method, similarly to DTI and HODTI (see Appendix B). Although this method requires a greater number of points of q-space to be sampled relative to DTI and HODTI, GDTI can still be performed in a time period acceptable for a clinical setting with fast diffusion MRI sequences.

Once the independent elements of Eq. (97) have been calculated, the higher order diffusion tensors can be visualised. As previously discussed (see Appendix A Higher order diffusion tensor imaging), it is advantageous to visualise the diffusion propagator profile rather than the apparent diffusivity profile. Since the diffusion propagator is described in terms of its cumulants, and the higher order diffusion tensors that have been calculated must be converted into their corresponding cumulant tensors. Fortunately this conversion process can exploit the fact that the natural logarithm of characteristic functions (e.g. $E(\mathbf{q})$) can be expanded as a series of cumulants using the cumulant generating function,

$$\ln E(\mathbf{q}) = \sum_{l=2}^{\infty} \frac{(-i)^l}{l!} \sum_{i_1=1}^{3} \sum_{i_2=1}^{3} \cdots \sum_{i_l=1}^{3} q_{i_1} q_{i_2} \cdots q_{i_l} \kappa_{i_1 i_2 \ldots i_l} \tag{98}$$

where $\kappa_{i_1 i_2 \ldots i_l}$ is a component of the l-th order cumulant tensor, $\boldsymbol{\kappa}^{(l)}$. Therefore, comparing Eqs. (98) and (96),

$$\boldsymbol{\kappa}^{(l)} = (-1)^l \, l! \left(\Delta - \frac{l-1}{l+1} \delta \right) \mathbf{D}^{(l)} . \tag{99}$$

Once the cumulant tensors have been calculated, $P(\mathbf{r})$ can then be reconstructed using the Gram-Charlier A series (i.e., the Fourier expansion of $P(\mathbf{r})$ in terms of Hermite polynomials [232] allowing the approximation of a probability distribution as a series of its cumulants) for a large number of $\mathbf{r}$ [230, 233],

$$P(\mathbf{R}) = \frac{1}{\sqrt{2\pi \boldsymbol{\kappa}^{(2)}}} \exp\left(-\frac{1}{2} \mathbf{R}^{\mathrm{T}} \left(\boldsymbol{\kappa}^{(2)} \right)^{-1} \mathbf{R} \right) \left(1 + \sum_{l=3}^{\infty} \frac{1}{l!} \boldsymbol{\kappa}^{(l)} : \mathbf{H}^{(l)}(\mathbf{R}) \right) \tag{100}$$

where $\mathbf{H}^{(l)}(\mathbf{R})$ is the symmetric l-th order Hermite tensor, which is comprised of the components

$$H_{i_1 i_2 \ldots i_l}(\mathbf{R}) = (-1)^l \exp\left(\frac{\mathbf{R}\cdot\mathbf{R}}{2}\right)\left(\frac{\partial}{\partial R_{i_1}}\frac{\partial}{\partial R_{i_2}}\cdots\frac{\partial}{\partial R_{i_l}}\right)\exp\left(\frac{\mathbf{R}\cdot\mathbf{R}}{2}\right). \tag{101}$$

For example, the elements of the first to fourth order Hermite tensor are given by

$$\begin{aligned}
H_i(\mathbf{R}) &= R_i \\
H_{ij}(\mathbf{R}) &= \begin{cases} R_i^2 - 1 & i = j \\ R_i R_j & i \neq j \end{cases} \\
H_{ijk}(\mathbf{R}) &= \begin{cases} R_i^3 - 3R_i & i = j = k \\ R_k\left(R_i^2 - 1\right) & i = j \neq k \\ R_i R_j R_k & i \neq j \neq k \end{cases} \\
H_{ijkl}(\mathbf{R}) &= \begin{cases} R_i^4 - 6R_i + 3 & i = j = k = l \\ R_l\left(R_i^3 - 3R_i\right) & i = j = k \neq l \\ R_k R_l\left(R_i^2 - 1\right) & i = j \neq k \neq l \\ \left(R_k^2 - 1\right)\left(R_i^2 - 1\right) & i = j \neq k = l \end{cases}
\end{aligned} \quad . \tag{102}$$

Upon reconstructing the diffusion propagator profile using Eq. (100), the profile can then be converted into a probability isosurface similarly to how a large collection of ADCs can be used to construct an apparent diffusivity profile (see Section 4.2 Diffusion tensor imaging). The maxima of this probability isosurface will correspond to the orientation of the present fibre populations. This allows the orientations of complicated restricting microstructures to be examined without *a priori* knowledge of the system.

Anomalous diffusion tensor imaging

Recalling Eq. (31), it can be inferred that the relationship between $\ln E(b)$ and b will remain linear for all values of b. However, this relationship hinges on the condition that diffusion is free. For diffusion within restricted system the relationship between $\ln E(b)$ and b may be non-linear (Figure 66) [45, 95]. The gradient of a linear fit is therefore dependent on the distribution of b-values with which $E(b)$ was sampled, potentially leading to significant variations in calculated ADCs or elements of diffusion tensors. This problem affects any diffusion MRI measurement of a system involving restricted diffusion where it is simplistically assumed that the decay of the

diffusion-weighted MR signal is a monoexponential function (e.g., Eq. **(30)**) or that the diffusion propagator can be modelled as a Gaussian function (e.g. Eq. (15)).

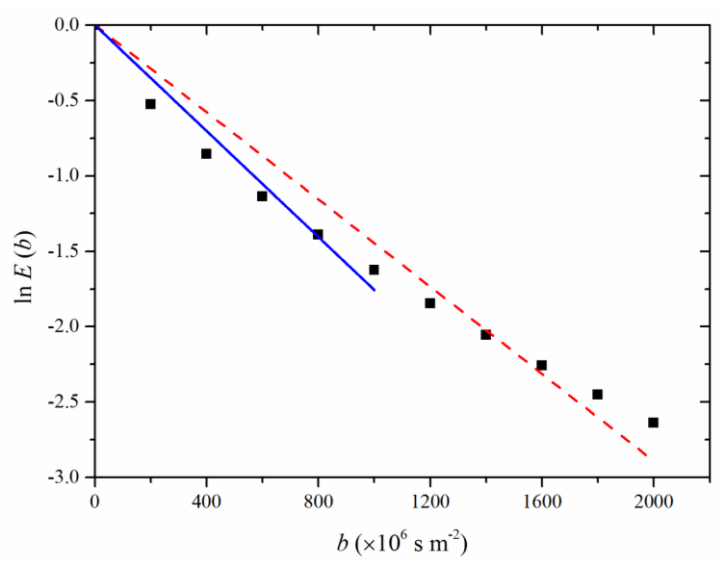

Figure 66: The non-linear relationship between $\ln E(b)$ and b for restricted diffusion. Here the attenuation of the diffusion-weighted MR signal has been recorded for a number of different b-values (●). By attempting a linear fit to non-linear diffusion data, the gradient of the fitted curve will depend on the distribution of b-values the diffusion-weighted MR signal was sampled. For example, if the diffusion-weighted MR signal was only sampled using values of $b \leq 1000 \times 10^6$ s m^{-2}, the gradient of the curve (i.e., the ADC) is 1.76×10^6 m^2 s^{-1} (blue unbroken line). Sampling the MR signal up to $b = 2000 \times 10^6$ s m^{-2}, on the other hand, results in an ADC of 1.45×10^6 m^2 s^{-1} (red dashed line).

The non-linear relationship between $\ln E(b)$ and b for the case of restricted diffusion arises due to the presence of two or more diffusion compartments within the voxel which restrict diffusion to different degrees [234, 235]. The superposition of the resultant diffusion-weighted MR signal profiles results in the observed non-linear relationship between $\ln E(b)$ and b. One method for resolving this problem for simple tissue samples (i.e., tissues consisting of a single type of cells) involves fitting a bi-exponential model (see Eq. (88), where $n = 2$) to the diffusion-weighted MR signal decay curve [234, 236].

The slower apparent diffusivity component is generally attributed to diffusion in the intracellular space and the faster apparent diffusion component to diffusion in the

extracellular space. However, the volume fractions of these two cellular compartments do not necessarily match their physiological volume fractions [161, 234]. An alternative to the bi-exponential model is to treat diffusion as a heterogeneous process [237]. In other words, when the diffusion process is modelled as a random walk, the step size (i.e., the displacement per iteration of the simulation) is not fixed. This form of the random walk model is known as a Lévy flight [238, 239]: a series of small, localised movements interspaced by larger, periodic displacements (Figure 67). The small displacements can be attributed to diffusion within highly restricted regions while the larger displacements correspond to diffusion within regions which are less restricted. Aspects of the local environment can therefore be inferred without the need to model any part of the restricting microstructure.

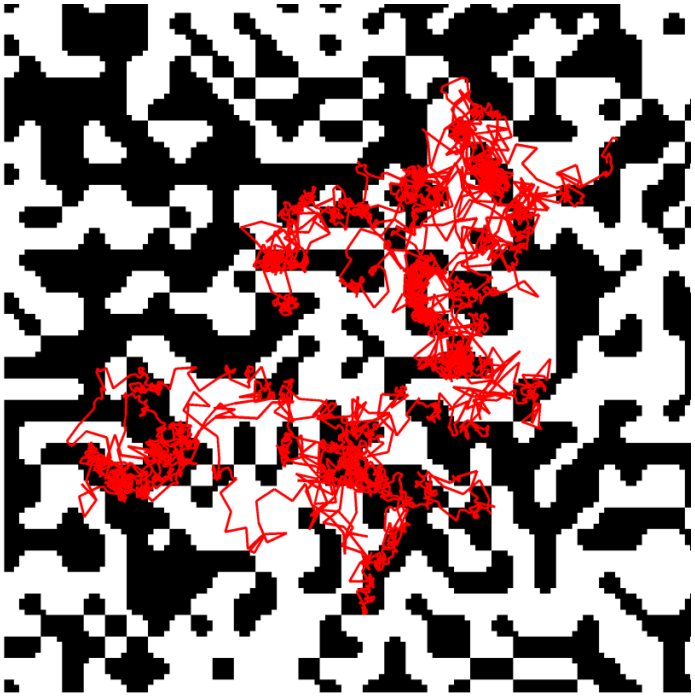

Figure 67: Representing anomalous diffusion of a single particle in a restricted system as a Lévy flight. The displacement of the particle at each time point (as indicated by changes in the direction of the red path) is dependent upon the degree of diffusion restriction. The particle can diffuse through both white and black regions, although the white regions restrict diffusion less than the black.

Since in a Lévy flight the displacement of a particle is treated as a function of position, it is possible that the mean square displacement of the diffusing ensemble no longer has a linear relationship with time. The one dimensional MSD equation (see Eq. (20)) must therefore be generalised to account for this change [240, 241], i.e.,

$$\left\langle \mathbf{R}^2 \right\rangle = 2Dt^{\varsigma} \tag{103}$$

where ς is a unitless stretching exponent. The stretching exponent indicates the complexity of the diffusion path within the restricted system. For example, when $\varsigma = 1$, the diffusion process is free and Eq. (103) equates to Eq. (20). However, when $\varsigma \neq 1$ the diffusion process is *anomalous*. ς is related to the fractal dimension, d_w, of the local microstructures restricting diffusive motion via the relation,

$$\varsigma = 2/d_w \,. \tag{104}$$

The fractal dimension is a useful scalar index which characterises how the detail of restricting microstructure changes with the scale of the measurement. It can thus be used to describe the heterogeneity of the restricting microstructure within a voxel.

The EAP of an ensemble of anomalously diffusing particles (i.e., the anomalous EAP) is a Lévy distribution. The Fourier transform of the anomalous diffusion propagator, $\bar{P}_A(\mathbf{R})$, in the one dimensional case is a stretched exponential [241-243]

$$E = \int \bar{P}_A(R)\exp(i\gamma\delta gR)\,dR = \exp\left(-(bD_A)^{\varsigma}\right) \tag{105}$$

where D_A is the anomalous ADC, also known as the distributed diffusion coefficient. While D_A is analogous to D (cf. Eq. (31)), the two values are only equal when $\varsigma = 1$. The values of D_A and ς can be calculated by fitting a power law model to the diffusion data, i.e.,

$$E = \exp\left(-Ab^{\varsigma}\right) \tag{106}$$

where $A = D_A^{\varsigma}$. This model of heterogeneous diffusion can be easily fitted to the diffusion data. Thus a complicated restricted system can be potentially characterised

using a small number of scalar values, without *a priori* knowledge of the number or size of the diffusion compartments present.

This one-dimensional anomalous MRI technique can be modified to account for anomalous diffusion anisotropy by replacing A and ς with their respective second-order tensors, $\mathbf{A}$ and $\boldsymbol{\zeta}$, similarly to how DTI replaces D with $\mathbf{D}$ [244]. This diffusion imaging technique is known as anomalous diffusion tensor imaging (ADTI). Analogously to Eqs. (31) and (39), Eq. (106) becomes

$$\ln E(\mathbf{u}) = -\left(\mathbf{u}^{\mathrm{T}}\mathbf{A}\mathbf{u}\right)b^{\left(\mathbf{u}^{\mathrm{T}}\boldsymbol{\zeta}\mathbf{u}\right)} = \left(-u_{xx}A_{xx}\cdots - 2u_{yz}A_{yz}\right)b^{\left(u_{xx}\zeta_{xx}\cdots + 2u_{yz}\zeta_{yz}\right)}. \qquad (107)$$

This expression can thus be used as the basis for a system of non-linear equations. Since Eq. (107) possesses two second-order symmetric tensors, q-space must be sampled on a minimum of two q-shells with six unique points on each shell. Additionally, since Eq. (107) is non-linear, an iterative approach is required in order to determine the independent elements of the two tensors (see Appendix B). As $\mathbf{A}$ and $\boldsymbol{\zeta}$ are second-order tensors, the information contained within them (e.g. eigenvalues, eigenvectors) can be extracted and visualised in the manner previously described for DTI. However, as $\mathbf{A}$ and $\boldsymbol{\zeta}$ also possess the same tensor properties of $\mathbf{D}$, ADTI suffers from poor angular contrast when multiple intravoxel fibre populations are present.

Describing diffusion with the diffusion propagator

Thus far a number of three-dimensional diffusion MRI techniques have been described that determine the effect of diffusion on net spin magnetisation by solving the Bloch-Torrey equation. However, these methods tend to require certain assumptions be made about the diffusion process (e.g. DTI and HODTI both require the assumption that the diffusion process is free) or require extensive modelling (e.g. GDTI and ADTI).

The inverse Fourier transform of Eq. (26), on the other hand, allows the direct reconstruction of the one-dimensional EAP from the diffusion weighted signal attenuation

$$\bar{P}(\mathbf{R}) = \int E(\mathbf{q}) \exp\left(-2\pi i \mathbf{q} \cdot \mathbf{R}\right) d\mathbf{q}. \tag{108}$$

Since the reciprocal space of the Fourier transform is described in terms of **q**, diffusion MRI techniques that make use of this formalism are commonly referred to as *q*-space imaging techniques. While no assumptions regarding the EAP are required to solve Eq. (108), three key conditions need to be met. Firstly, it must be assumed that the SGP condition has been met. If this condition is violated, quantitative measures of the size and density of restricting microstructures are likely to be underestimated [245, 246]. Secondly, the diffusion measurement must be taken in the long time limit to ensure that the diffusing spin ensemble has adequate time to probe the system microstructure [247]. Thirdly, the maximum *q*-value, *q*', used must be large enough to achieve near complete MR signal attenuation. Using *q*-values of this magnitude is necessary to avoid truncation artefacts when taking the inverse Fourier transform of the MR signal data [248]. Truncation artefacts, also known as Gibbs artefacts, result in spurious, relatively high signal intensities appearing near sharp transitions in the image (i.e., at the boundaries between regions with very different signal intensities); this creates the distinct, ring shaped appearance of this image artefact. Due to these three conditions, *q*-space diffusion MRI techniques are best suited to a spectrometer capable of producing powerful diffusion-sensing magnetic gradient pulses with fast gradient ramp up times.

Diffusion spectrum imaging

Diffusion spectrum imaging (DSI) [101] has perhaps the great potential of all three-dimensional diffusion MRI techniques. This technique samples *q*-space using a Cartesian lattice sampling scheme (see Section 3.4 *q-space* imaging); thus Eq. (108) can be used to directly reconstruct the EAP from the measured diffusion-weighted MR signal. This reconstruction is achieved without a model of diffusion or prior assumptions of the angular or radial characteristics of the diffusion-weighted MR signal profile. The EAP should therefore possess all of its angular and radial features, including the orientations of overlaying fibre populations and distributions of fibre diameter, length and density.

As previously discussed, a Cartesian sampling scheme must be quite dense so as to prevent aliasing the EAP. Sampling q-space in this manner requires vast amounts of diffusion data, leading to lengthy acquisition times. Fortunately, by employing a diffusion-weighted echo-planar MRI pulse sequence (a fast diffusion MRI protocol), it is possible to reduce the total acquisition time of DSI to a clinically acceptable timeframe while maintaining an acceptable spatial resolution [249]. However, even with these fast diffusion MRI sequences, there is still not enough time to sample the entirety of q-space. As a consequence, only the region of q-space around the origin (i.e., lower q-values) is typically sampled.

The lack of diffusion data sampled at high q-values can result in the appearance of truncation artefacts. To reduce the appearance of these artefacts, the diffusion data can be multiplied with a Hann window function [250], $\varpi(q)$, i.e.,

$$\varpi\left(q\right)=\frac{1}{2}\left(1-\cos\left(\frac{2\pi q}{\mathrm{FWHM}}\right)\right) \tag{109}$$

where the FWHM is the full-width at half-maximum of the window. Window functions have a value of zero outside of a chosen interval and thus help ensure a smooth decay of the diffusion-weighted MR signal at high q-values.

Due to the limitations of the diffusion gradient coils of clinical NMR spectrometers, the length of the diffusion gradient are often similar to that of the diffusion period. This unfortunately violates the SGP condition. Thus the current use of DSI in clinical studies is primarily useful for providing qualitative contrast rather than quantitative measurements of restricting microstructures [251]. Consequently, many diffusion MRI techniques solely reconstruct the angular component of the EAP using the aforementioned HARDI sampling scheme with a large number of points sampled on a small number of q-shells. This allows the orientation of restricting microstructure to be determined while also reducing the total length of the MR acquisition. The size of the q-values can also be kept small in order to minimise the length of the diffusion gradient.

q-ball imaging

As discussed previously, HARDI *q*-space sampling schemes are more time efficient than sampling on a Cartesian lattice. However, the Fourier transform featured in Eq. (108) requires that the diffusion data be sampled at each point of a Cartesian lattice. Therefore, Eq. (108) will need to be suitably modified in order to reconstruct the EAP from diffusion data acquired over the surface of a sphere. This can be achieved using a number of different approaches. One example is the *q*-space MRI technique known as *q*-ball imaging (QBI), which estimates the angular component of the EAP from diffusion data acquired on a single shell of *q*-space [151, 168, 252]. Diffusion anisotropy can be observed by calculating the radial projection of the EAP, more commonly known as the orientation distribution function (ODF), i.e.,

$$\psi\left(\mathbf{R}'\right)=\int_0^\infty \bar{P}\left(\mathbf{R}\right)R^2 d\mathbf{R} \tag{110}$$

where $\psi(\mathbf{R}')$ is the ODF. The definition of the ODF given here differs from the original, which did not include the R^2 term in Eq. (110) [151]. The R^2 factor prevents the artificial weighting of the EAP at large and small values of R, and also eliminates the need for a normalisation constant [101, 103].

In the original implementation of QBI, the ODF was calculated from the diffusion-weighted MR signal using an operation known as the Funk-Radon transform (FRT). The FRT integrates a spherical function over its own equator, resulting in a new spherical function. Thus, the FRT of $E(\mathbf{q})$ involves the integration of $E(\mathbf{q})$ over a set of points perpendicular to $\mathbf{q}$, [151],

$$\mathfrak{G}\left[E\left(\mathbf{q}\right)\right]=\int E\left(\mathbf{q}\right)\delta\left(\mathbf{q}\cdot\mathbf{w}\right)d\mathbf{q} \tag{111}$$

where $\mathbf{w}$ is a unit vector perpendicular to $\mathbf{q}$ (i.e., $\mathbf{q}\cdot\mathbf{w}=0$). Using the relationship between the diffusion-weighted MR signal and the EAP in Eq. (26),

$$\mathfrak{G}\left[E\left(\mathbf{q}\right)\right]=\int \bar{P}(\mathbf{R})\exp\left(2\pi i\mathbf{q}\cdot\mathbf{R}\right)\delta\left(\mathbf{q}\cdot\mathbf{w}\right)d\mathbf{q} \tag{112}$$

Eq. (112) can be expanded as a series of cylindrical waves [151]. Rewriting this expression in the form of a Hankel (i.e., Fourier-Bessel) transform yields

$$E\left(\mathbf{q}\right)=2\pi q\int \bar{P}\left(\mathbf{R}\right)J_0\left(2\pi qR\right)d\mathbf{R} \tag{113}$$

where J_0 is the zeroth order Bessel function of the first kind. Substituting Eq. (113) into Eq. (111) yields

$$\mathfrak{G}\left[E(\mathbf{q})\right] = 2\pi q \int \bar{P}(\mathbf{R}) J_0(2\pi q R)\,\delta(1-\mathbf{R}\cdot\mathbf{w})\,d\mathbf{R}\,. \tag{114}$$

Comparing Eqs. (110) and (114), it becomes apparent that

$$\psi(\mathbf{R}') \approx \mathfrak{G}\left[E(\mathbf{q})\right], \tag{115}$$

allowing the estimation of the ODF using Eq. (114).

The sharpness of the ODF profile is dependent on the width of the Bessel function (i.e., $1/q$) [151, 253]. Thus when low q-values are employed, the ODF profile will exhibit a low angular contrast and it is difficult to separate overlapping fibre populations. An alternative approach to performing QBI which allows good angular contrast at low q-values is one that utilises a basis constructed from spherical harmonic functions in the place of Bessel functions [168, 252].

Using this real symmetrical spherical harmonic basis, the number of coefficients required to describe diffusion anisotropy reduces to

$$\sum_{x=0}^{l}(2x+1) = 1+5+9+\ldots+(2l+1) = \frac{(l+1)(l+2)}{2}\,. \tag{116}$$

Since the spherical harmonic functions are independent of the radial component of $E(\mathbf{q}')$, the diffusion-weighted MR images can be acquired on a single shell of q-space; thus the total acquisition time required for QBI is similar to HODTI and is achievable in a clinically acceptable time frame.

In order to determine the ODF from the spherical harmonic coefficients of $E(\mathbf{q}')$, $E(\mathbf{q}')$ is redefined in terms of infinite series of spherical harmonic functions (Appendix C, see Eq. (208)) and then substituted into Eq. (111). Using the relationship in Eq. (115), the ODF can therefore be expressed as

$$\psi(\mathbf{w}) = \sum_{l}^{\infty}\sum_{m=-l}^{l} \alpha_l^m \int Y_l^m(\mathbf{q}')\,\delta(\mathbf{q}'\cdot\mathbf{w})\,d\mathbf{q}'\,. \tag{117}$$

Since spherical harmonic functions are analytical with respect to the equator of the FRT [168, 252],

$$\int Y_l^m(\mathbf{q}')\delta(\mathbf{q}'\cdot\mathbf{w})d\mathbf{q}' = 2\pi\mathcal{P}_l^m(0)Y_l^m(\mathbf{w}). \tag{118}$$

Therefore, using the relationship featured in Eq. (118), Eq. (117) can thus be rewritten as

$$\psi(\mathbf{w}) = \sum_{l}^{\infty}\sum_{m=-l}^{l} 2\pi\mathcal{P}_l^m(0)\alpha_l^m Y_l^m(\mathbf{w}). \tag{119}$$

Using the same process for creating apparent diffusivity and probability isosurfaces, a profile of the ODF can be created. This can be done by extrapolating ODF values from the spherical harmonic coefficients using Eq. (119) in conjunction with a large number of **w** vectors spaced evenly over the unit sphere. This profile can then be readily converted into an isosurface (Figure 68). Additionally, certain invariant scalar features can be extracted from the ODF in much the same way values are extracted from a higher order diffusion tensor. For example, the GFA index of the ODF profile can be calculated by modifying Eq. (85) [151], i.e.

$$\mathrm{GFA} = \frac{\mathrm{std}(\psi(\mathbf{w}))}{\mathrm{rms}(\psi(\mathbf{w}))} = \sqrt{\frac{\int(\psi(\mathbf{w})-\langle\psi\rangle)^2 d\mathbf{w}}{\int\psi(\mathbf{w}_i)^2 d\mathbf{w}}} = \sqrt{\frac{n}{n-1}\frac{\sum_{i=1}^{n}(\psi(\mathbf{w}_i)-\langle\psi\rangle)^2}{\sum_{i=1}^{n}\psi(\mathbf{w}_i)^2}} \tag{120}$$

where n is equal to the number of values in the ODF profile (see Eq. (119)) and $\langle\psi\rangle$ is the mean of the values in the ODF profile.

Since the ODF is an estimation of the angular component of the EAP, it will indicate the orientations of the intravoxel fibre populations. However, the number of different fibre orientations that can be resolved is dependent on the maximum spherical harmonic order that the spherical harmonic series is truncated (see Appendix C, Eq. (209)). In order to resolve n distinct fibre populations, the maximum spherical harmonic order of the spherical harmonic series must be equal to or greater than $2n$. Unlike HODTI, increasing the maximum spherical harmonic order of the spherical harmonic series beyond the minimum value required will continue to improve the angular contrast of the ODF, although this requires an increase in the density of

points sampled on the q-shell (see Eq. (116)). Other methods of improving angular contrast include sampling q-space at a larger q-value and the use of ad hoc post-processing methods to exaggerate the shape of the ODF isosurface, such as min-max normalisation [151], i.e.

$$\psi'(\mathbf{w}) = \frac{\psi(\mathbf{w}) - \min\psi(\mathbf{w})}{\max\psi(\mathbf{w}) - \min\psi(\mathbf{w})} \tag{121}$$

where $\psi'(\mathbf{w})$ is the normalised ODF. Unfortunately, ODF profiles still tend to have low angular contrast when the orientations of two or more fibre population are separated by a shallow angle. This problem will be demonstrated in the following section (see Appendix A Diffusion orientation transform imaging).

Diffusion orientation transform imaging

Diffusion orientation transform (DOT) imaging is an analytical method for computing the Gaussian EAP from apparent diffusivity profiles or diffusion tensors. To perform a DOT [137, 254], the plane wave featured in Eq. (108) is first rewritten in terms of spherical wave functions, i.e.

$$\mathfrak{W} = \exp(-2\pi i\mathbf{q}\cdot\mathbf{R}) = 4\pi\sum_{l=0}^{\infty}\sum_{m=-1}^{l}(-i)^l J_l(2\pi qR)Y_l^m(\mathbf{q}')Y_l^m(\mathbf{R}')^* . \tag{122}$$

Substituting Eq. (122) into Eq. (108) yields

$$\bar{P}(R_0\mathbf{R}') = \sum_{l=0}^{\infty}\sum_{m=-1}^{l}(-i)^l Y_l^m(\mathbf{R}')\int Y_l^m(\mathbf{q}')^* I_l(\mathbf{q}')d\mathbf{q}' \tag{123}$$

where

$$I_l(\mathbf{q}') = 4\pi\int_0^{\infty} q^2 J_l(2\pi qR_0)E(\mathbf{q}')dq . \tag{124}$$

$E(\mathbf{q}')$ is given by solving Eq. (28) for free diffusion under the SGP condition, i.e.,

$$E(\mathbf{q}') = \exp\left(-4\pi^2 q^2 \Delta D(\mathbf{q}')\right) \tag{125}$$

where $D(\mathbf{q}')$ has been calculated from a higher order tensor for each diffusion gradient direction (see Eq. (78)).

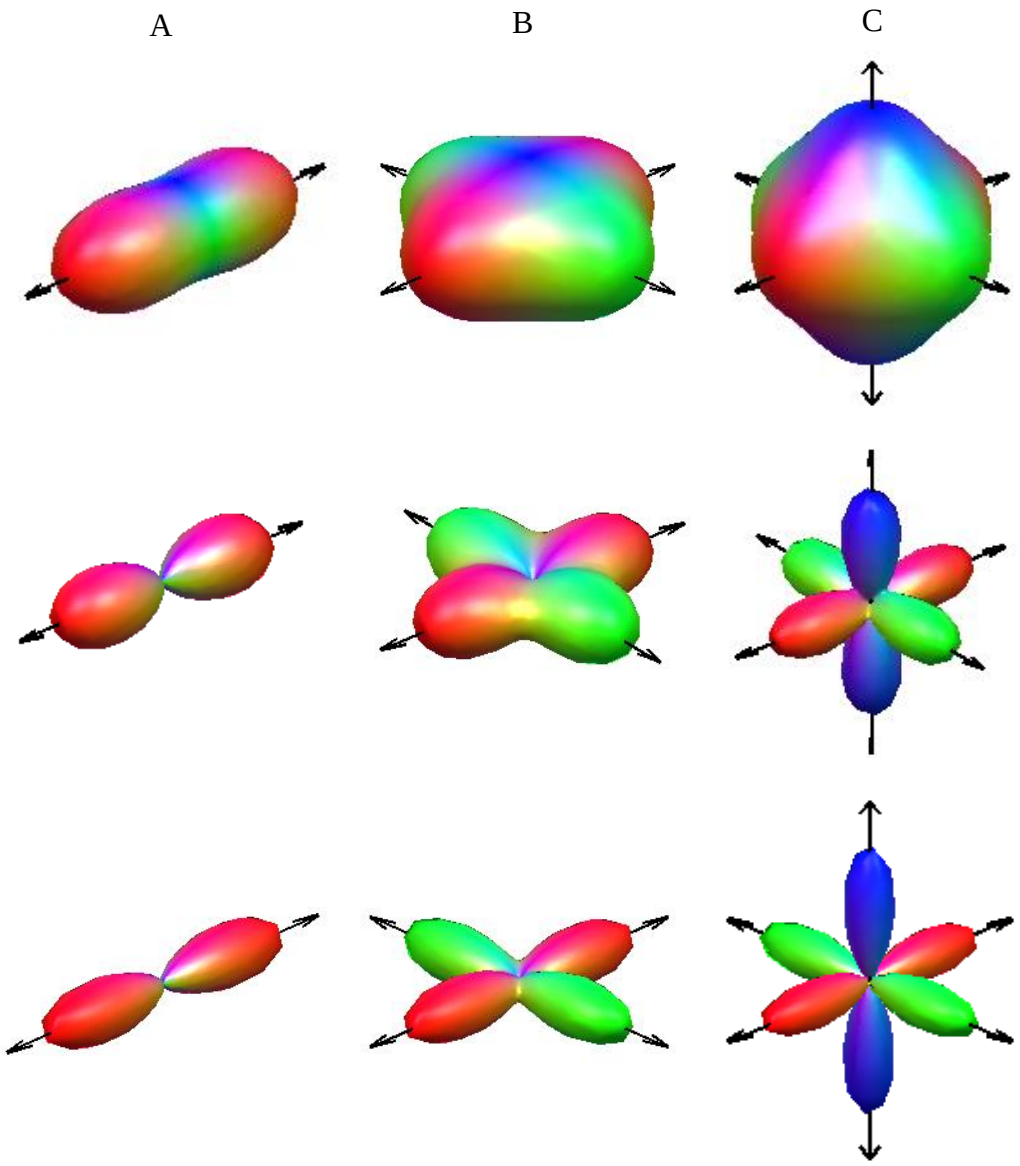

Figure 68: ODF isosurfaces which correspond to one (column A), two (column B) and three (column C) intravoxel fibre populations. The orientation of each fibre population is indicated with a double headed arrow. The first row of ODF isosurfaces were generated from simulated diffusion data where $b = 1500 \times 10^6$ s m^{-2} and a spherical harmonic series truncated at $L = 6$ with no additional isosurface post-processing. The isosurfaces in the second row are the same as the first but with min-max ODF normalisation. The third row of ODF isosurfaces were generated from simulated diffusion data where $b = 4000 \times 10^6$ s m^{-2} and a spherical harmonic series truncated at $L = 12$ with min-max ODF normalisation.

Solving Eq. (124) using the standard integral (6.631 (1) [85]) yields

$$I_l\left(\mathbf{q}'\right)=\frac{R_0^l\Gamma\left(\frac{l+3}{2}\right)}{2^{(l+3)}\pi^{3/2}\Gamma\left(l+3/2\right)\left(D\left(\mathbf{q}'\right)t\right)^{(l+3)/2}}\times{}_1F_1\left(\frac{l+3}{2};l+\frac{3}{2};-\frac{R_0^2}{4D\left(\mathbf{q}'\right)t}\right) \quad (126)$$

where ${}_1F_1(\cdot,\cdot,\cdot)$ is the confluent hypergeometric function of the first-order and $\Gamma(\cdot)$ is the gamma function. Since $I_l(\mathbf{q}')$ is a distribution of orientation, Eq. (126) can be written as a series of spherical harmonics, i.e.,

$$I_l\left(\mathbf{q}'\right)=\sum_{l'=0}^{\infty}\sum_{m'=-1}^{l'}\alpha_{ll'}^{m'}Y_{l'}^{m'}\left(\mathbf{q}'\right) \quad (127)$$

where $\alpha_{ll'}^{m'}$ are coefficients of the series. Eq. (127) can be rewritten as

$$\alpha_{ll'}^{m'}=\int Y_{l'}^{m'}\left(\mathbf{q}'\right)^{*}I_l\left(\mathbf{q}'\right)d\mathbf{q}'. \quad (128)$$

Thus, substituting Eq. (128) into Eq. (123) allows the diffusion propagator to be expanded as a Laplace series,

$$\bar{P}\left(R_0\mathbf{R}'\right)=\sum_{l=0}^{\infty}\sum_{m=-1}^{l}\left(-i\right)^l\alpha_{ll}^{m}Y_l^m\left(\mathbf{R}'\right). \quad (129)$$

The series coefficients for Eq. (129) can be calculated by solving Eq. (128) using a direct or iterative reconstruction method. For the direct method, Eq. (127) can be written as the matrix multiplication,

$$\mathbf{I}_l=\mathbf{Y}\boldsymbol{\alpha}_l. \quad (130)$$

Y is a matrix constructed from the spherical harmonic basis,

$$\mathbf{Y}=\begin{bmatrix} Y_0^0\left(\mathbf{q}_1'\right) & \cdots & Y_l^{-l}\left(\mathbf{q}_1'\right) & \cdots & Y_l^{l}\left(\mathbf{q}_1'\right) \\ \vdots & & \ddots & & \vdots \\ Y_0^0\left(\mathbf{q}_n'\right) & \cdots & Y_l^{-l}\left(\mathbf{q}_n'\right) & \cdots & Y_l^{l}\left(\mathbf{q}_n'\right) \end{bmatrix}; \quad (131)$$

while $\boldsymbol{\alpha}_l$ is a vector containing the spherical harmonic coefficients associated with $\mathbf{I}_l$, a vector containing $I_l(\mathbf{q}')$ for the harmonic order l. Thus,

$$\begin{bmatrix} I_l(\mathbf{q}_1') \\ \vdots \\ I_l(\mathbf{q}_n') \end{bmatrix} = \begin{bmatrix} Y_0^0(\mathbf{q}_1') & \cdots & Y_{l'}^{-l'}(\mathbf{q}_1') & \cdots & Y_{l'}^{l'}(\mathbf{q}_1') \\ \vdots & & \vdots & & \vdots \\ Y_0^0(\mathbf{q}_n') & \cdots & Y_{l'}^{-l'}(\mathbf{q}_n') & \cdots & Y_{l'}^{l'}(\mathbf{q}_n') \end{bmatrix} \begin{bmatrix} \alpha_{l0}^{0} \\ \vdots \\ \alpha_{ll'}^{-l'} \\ \vdots \\ \alpha_{ll'}^{l'} \end{bmatrix} \tag{132}$$

Eq. (132) can be solved using matrix inversion to determine the series coefficients for each harmonic order *l*. These coefficients can then be substituted into Eq. (129) to yield the EAP. The EAP can be visualised using the standard approach for visualising probability isosurfaces (see Section 4.2 Diffusion tensor imaging). Alternatively the EAP can be converted into an ODF profile by multiplying the series coefficients by $2\pi\mathcal{Y}_l^m(0)$ (see Eq. (119)). Using Eq. (120), the GFA index can be calculated for either the probability profile or the ODF profile.

The advantages of DOT imaging relate to its analytical nature; for example, *q*-space can be treated as continuous space rather than a discrete one and it can extend to infinity. The calculations are also fast and robust. Unfortunately, the ODF isosurfaces reconstructed using DOT (and QBI) often have low angular contrast [255]. When two or more intravoxel fibre populations are present and their orientations differ by a small angle, the maxima of the ODF isosurface merge making it difficult to discern the orientations of these intravoxel fibres (Figure 69).

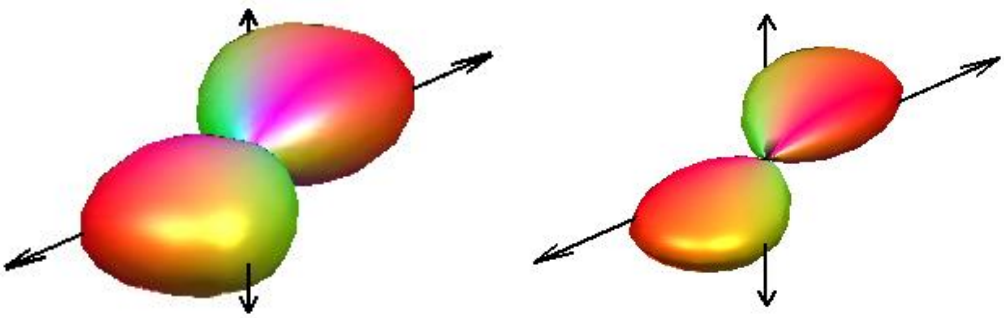

Figure 69: Simulated ODF profiles of the diffusion of water in two overlapping fibres separated by 45° (orientation indicated by double headed arrows), reconstructed using (A) QBI and (B) DOT MRI. The parameters used for the simulations included 200 diffusion gradient directions, $b = 2000 \times 10^6$ s m^{-1}, $\delta = 2.5$ ms and $\Delta = 30$ ms. The maximum spherical harmonic order of the reconstructions was four. The fibres were simulated as cylinders with a 5 μm radius and 100 μm length.

Additionally, the calculated EAP will be a Gaussian function due to the inclusion of Eq. (125) in the reconstruction. As a result, DOT MRI only reconstructs the angular component of the EAP.

Persistent angular structure MRI

An alternative to the ODF calculated by QBI and DOT, which has better angular contrast, is the radially persistent angular structure (PAS) of the EAP [256]. Similarly to the ODF, the PAS of the EAP indicates the relative mobility of particles along different directions by projecting $\bar{P}(\mathbf{R})$ onto a sphere (see Eq. (108)), i.e.,

$$\bar{P}(\mathbf{R}) = p(\mathbf{R})\frac{\delta(R-R_0)}{R_0^{\,2}} \tag{133}$$

where $p(\mathbf{R})$ is the PAS. The choice of R_0 will determine the smoothness of $p(\mathbf{R})$, and it can be arbitrarily adjusted to increase structure sensitivity at the expense of increased noise. The relationship between the diffusion-weighted MR signal and the PAS can be demonstrated by substituting Eq. (135) into Eq. (26). The resultant expression, when rewritten using Euler's formula (i.e., $\exp(i\,x) = \cos x + i \sin x$), is given by

$$E(\mathbf{q}) = R_0^{-2}\int p(\mathbf{R})\cos(2\pi\mathbf{q}\cdot\mathbf{R})\,d\mathbf{R}\,. \tag{134}$$

Since it can be reasonably assumed that $\bar{P}(\mathbf{R}) = \bar{P}(-\mathbf{R})$ when no bulk motion is present, the imaginary component can be omitted from this equation.

PAS MRI is able to extract the PAS from $E(\mathbf{q})$ by using the principle of maximum entropy. This principle states that for precisely stated prior data (e.g. a set of conserved quantities that describe a probability distribution), the probability distribution which best represents this data will also possess the greatest information entropy. The information entropy, I_s, of a probability distribution is given by

$$I_s = \int P(\mathbf{R})\ln P(\mathbf{R})\,d\mathbf{R}\,. \tag{135}$$

By applying an equality constraint to the information entropy, the maxima of I_s, can be found using the method of Lagrange multipliers [257], i.e.

$$\Lambda = \int P(\mathbf{R}) \ln P(\mathbf{R}) - P(\mathbf{R}) \sum_{i=1}^{n} \lambda_i x_i - P(\mathbf{R}) \mu \, d\mathbf{R} \tag{136}$$

where Λ is known as the Lagrangian function (or Lagrangian), λ_i represents the Lagrange multipliers, x_i represents the constraint functions and μ is a constant that controls the normalisation of $P(\mathbf{R})$. Using Eq. (133), and the plane wave function featured in Eq. (26) as the constraint function, the Lagrangian function becomes

$$\Lambda = \int p(\mathbf{R}) \ln p(\mathbf{R}) - p(\mathbf{R}) \sum_{i=1}^{n_q} \lambda_i \exp(2\pi i q_i R) - p(\mathbf{R}) \mu \, d\mathbf{R} \tag{137}$$

where n_q is the number of diffusion measurements made on a single q-shell. The maxima of I_s, occur when the variational derivative of the Lagrangian is equal to zero, i.e.

$$\frac{\partial \Lambda}{\partial p(\mathbf{R})} = -\ln p(\mathbf{R}) - 1 + \sum_{i=1}^{N} \lambda_i \exp(2\pi i q_i R) + \mu = 0 \,. \tag{138}$$

Therefore, information entropy is maximised when

$$p(\mathbf{R}) = \exp\left(\lambda_0 + \sum_{i=1}^{N} \lambda_i \exp(2\pi i \mathbf{q}_i \cdot r\mathbf{x}) \right) \tag{139}$$

where $\lambda_0 = \mu - 1$. To assist in the stabilisation of fitting algorithms, Eq. (139) can be rewritten using Euler's formula, yielding

$$p(\mathbf{R}) = \exp\left(\lambda_0 + \sum_{i=1}^{N} \lambda_i \cos(2\pi q_i R) \right). \tag{140}$$

By combining Eqs. (134) and (140), non-linear regression can be used to determine the values of the Lagrange multipliers. Suggested initial values for the iterative minimisation algorithm include $\lambda_0 = -\ln(4\pi)$, that all other Lagrange multipliers are equal to zero, and $R_0 = 1.4$ [256]. Once the Lagrange multipliers have been calculated, they can be substituted into Eq. (140) to determine $p(\mathbf{R})$. The PAS profile can then be visualised using the same approach employed for visualising apparent diffusivity, probability and ODF isosurfaces (see Section 4.2 Diffusion tensor imaging). Similarly to the ODF profile and the probability profile, the PAS profile

can be used to calculate invariant scalar features of diffusion, such as the GFA index using Eq. (120).

Simulations suggest that PAS MRI has a lower sensitivity to diffusion-weighted MR signal noise than spherical deconvolution imaging [258]. These simulations also suggest that PAS profiles exhibit better angular contrast than ODF profiles. However, the computation times associated with PAS MRI are very long, relative to previously described diffusion MRI methods. This is because the number of Lagrange multipliers that must be calculated is equal to the number of points sampled on the *q*-shell. While the computation time could be decreased by reducing the number of points sampled in *q*-space, the angular contrast of the PAS isosurface would likewise be reduced. Also, since the fitting algorithm can never be over determined, the PAS isosurface is potentially less stable than its ODF counterpart.

Spherical deconvolution imaging

While the ODF and PAS can give a good approximation of the orientation of multiple intravoxel restricting microstructures, the relationship between these functions and the true orientations of intravoxel fibre populations is not explicit. It would therefore be advantageous if the true fibre ODF (fODF) could be directly reconstructed from $E(\mathbf{q})$, for example by using the *q*-space diffusion MRI technique known as spherical deconvolution imaging.

Convolution is a mathematical operation performed on a pair of functions, yielding a modified version of one of the original functions. For example, spherical deconvolution imaging treats the measured diffusion-weighted MR signal as though it is the rotation of a response function, $\Omega(\varphi)$, by the fODF, $\mathfrak{F}(\theta,\varphi)$, i.e.

$$E(\theta,\varphi) = \Omega(\varphi) \otimes \mathfrak{F}(\theta,\varphi) \tag{141}$$

where $\otimes$ is the convolution operator. In spherical deconvolution imaging it is generally assumed that the fODF is the sum of *n* Dirac delta functions, where each delta function is aligned with one of the intravoxel fibre populations present. The response function, on the other hand, is assumed to be equivalent to the attenuated

diffusion-weighted MR signal profile of a single intravoxel fibre population aligned along the *z*-axis (Figure 70).

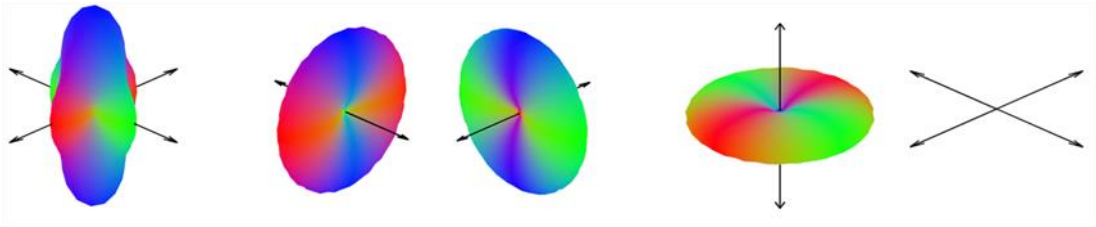

$$E(\mathbf{q}) \quad = \quad f_1E_1(\mathbf{q}) \quad + \quad f_2E_2(\mathbf{q}) \quad = \quad \Omega(\varphi) \quad \otimes \quad \mathfrak{F}(\theta,\varphi)$$

Figure 70: The convolution of the attenuated MR signal originating from a voxel containing two distinct fibre populations. The attenuated MR signal can be considered the linear combination of the attenuated signal from the two fibre populations, or the convolution of a response function $\Omega(\mathbf{q},\mathbf{x})$ with the true fibre ODF.

The fODF can be extracted from $E(\mathbf{q})$ by the process of spherical deconvolution. To perform the deconvolution, $E(\mathbf{q})$, and $\mathfrak{F}(\mathbf{x})$ are first decomposed into a series of spherical harmonics, i.e.

$$E(\mathbf{q}) = \sum_{l=0}^{\infty} \sum_{m=-1}^{l} s_l^m Y_l^m(\mathbf{q}'), \tag{142}$$

and

$$\mathfrak{F}(\mathbf{q}) = \sum_{l=0}^{\infty} \sum_{m=-1}^{l} f_l^m Y_l^m(\mathbf{q}') \tag{143}$$

where s_l^m and f_l^m are the respective spherical harmonic coefficients of $E(\mathbf{q})$ and $\mathfrak{F}(\mathbf{x})$. By truncating Eqs. (142) and (143) to L, and excluding the spherical harmonics with odd orders (due to their lack of symmetry), the coefficients of the two series can be calculated (see Appendix A *q*-ball imaging). These coefficients are then grouped to create a set of vectors $\mathbf{s}_l$ and $\mathbf{f}_l$, i.e.

$$\mathbf{s}_l = \begin{bmatrix} s_l^{-2l} & s_l^{-2l+1} & \dots & s_l^{2l} \end{bmatrix} \tag{144}$$

and

$$\mathbf{f}_i = \begin{bmatrix} f_l^{-2l} & f_l^{-2l+1} & \dots & f_l^{2l} \end{bmatrix} \tag{145}$$

for l = 0,2,…L. The convolution operation in Eq. (141) then becomes a matrix multiplication for each harmonic order [259], i.e.

$$\mathbf{s}_l = \mathfrak{R}_l \mathbf{f}_l \tag{146}$$

where $\mathfrak{R}_l$ is a $(2l+1)\times(2l+1)$ rotational harmonic matrix. The elements of $\mathfrak{R}_l$ are the coefficients of the rotational harmonic decomposition of $\Omega(q)$. Unfortunately, the rotational harmonic decomposition is not straightforward [259]. However, since $\Omega(q)$ is assumed to be aligned along the z-axis, the attenuated diffusion-weighted MR signal profile will be axially symmetric. Consequently, only the diagonal elements of $\mathfrak{R}_l$ will be non-zero, i.e.,

$$\mathfrak{R}_l = r_l \mathcal{I}_l \tag{147}$$

where $\mathcal{I}_l$ is an identity matrix of rank l. $\mathfrak{R}_l$ can thus be reduced to a single scalar per harmonic order, r_l, and Eq. (146) can be rewritten as

$$\mathbf{s}_l = r_l \mathbf{f}_l \,. \tag{148}$$

To progress further, a model for $\Omega(q)$ is required. If a voxel containing a single fibre population (e.g. a voxel which has a very high FA index) can be identified, the $\mathfrak{F}(\mathbf{x})$ associated with this voxel will collapse to form a single Dirac delta function. By adjusting the image reference frame so that the fibre population in this voxel is also aligned with the z-axis, the response function will become equivalent to the attenuated diffusion-weighted MR signal profile of the fibre population [260, 261]. Additionally, since $\mathbf{s}_l$ and $\mathbf{f}_l$, are aligned along the z-axis, they are axially symmetric, and spherical harmonic coefficients where m ≠ 0 will equal zero. This allows r_l to be calculated on a per element basis, i.e.,

$$r_l = \frac{s_l^0}{f_l^0} \,. \tag{149}$$

With the calculated r_l values and Eq. (147), the rotational harmonic matrix can be reconstructed. If it is assumed that the response function is consistent across the whole sample, this matrix needs to be calculated only once. Once $\mathfrak{R}_l$ has been reconstructed, Eq. (146) can be rewritten to yield $\mathbf{f}_l$, by using matrix inversion, i.e.,

$$\mathbf{f}_l = \mathfrak{R}_l^{-1}\mathbf{s}_l \,. \tag{150}$$

Substituting the calculated coefficients of $\mathbf{f}_l$, into Eq. (143) will therefore yield the fODF. The fODF profile can be visualised using the same approach for visualising profiles of apparent diffusivity, ODF or probability, and will yield an isosurface with high angular contrast (Figure 71) [262]. To find the *n* Dirac delta functions that correspond to the orientations of the intravoxel fibre populations present, a peak finding algorithm can be used to find the directions associated with the local maxima of the isosurface. However, it is often beneficial to leave the reconstructed fODF as a profile, as its shape will indicate the fibre orientation probability.

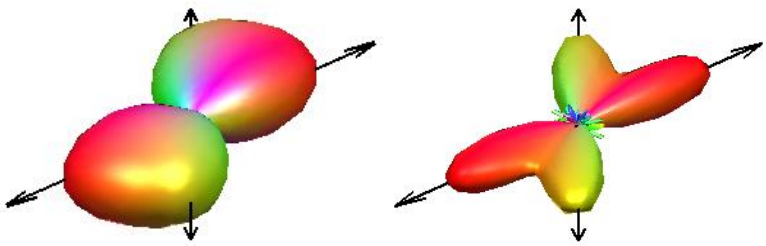

Figure 71: Simulated ODF profiles of the diffusion of water in two overlapping fibres separated by 45° (orientation indicated by double headed arrows), reconstructed using (A) QBI and (B) and non-negative constrained spherical deconvolution imaging. The parameters used for the simulations included 200 diffusion gradient directions, b = 2000 × 10^6 s m^{-1}, δ = 2.5 ms and Δ = 30 ms. The maximum spherical harmonic order of the reconstructions was ten. The fibres were simulated as cylinders with a 5 μm radius and 100 μm length.

Unfortunately spherical deconvolution is highly susceptible to signal noise. This susceptibility can result in spurious and/or negative local maxima in the fODF. To improve robustness of the algorithm, and smooth the fODF, regularisation terms can be incorporated into the reconstruction algorithm. For example, non-negativity constraints can be included in the algorithm to prevent the calculation of a non-

physical fODF [261]; and confidence bands can be calculated for the fODF to determine the uncertainty in the estimation [263]. Another limitation of spherical deconvolution imaging is that it requires the assumption that the response function will be the same for all intravoxel fibre populations. In a real system, it is likely that different fibre populations will have a different density, permeability and packing configuration, and will thus have a different response function. If the true response function differs significantly from the estimated response function, the reconstruction of the fODF can be adversely affected [264].

Diffusion propagator imaging

As the spherical harmonic basis employed by QBI and DOT MRI does not model the radial component of the EAP, it would be advantageous to combine the spherical harmonic basis with a radial function. Diffusion propagator imaging (DPI) is a diffusion MRI technique that employs one such combined basis [138].

From the earlier derivation of the spherical harmonic functions (see Appendix A *q*-ball imaging), a solution for the Laplace equation in spherical coordinates was calculated which contained only the radial component of the harmonic function (i.e., $R(r)$). If spin displacement is measured in terms of q (i.e., $r = q$), and it is assumed that $\lambda = l(l + 1)$, Eq. (195) can be solved for $R(q)$.

Using the ansatz that $R_k(r) \propto r^k$, two solutions for $R_k(q)$ can be found; $R_l(q) = q^l$ and $R_l(q) = q^{-(l+1)}$. Multiplying these radial functions with the spherical harmonic functions featured in Eq. (194) will yield two sets of solutions; these are the regular solid harmonic functions,

$$R_l^m(\mathbf{q}) = \underbrace{\sqrt{\frac{4\pi}{2l+1}}}_{N} q^l Y_l^m(\mathbf{q}'), \tag{151}$$

and the irregular solid harmonic functions,

$$I_l^m(\mathbf{q}) = \underbrace{\sqrt{\frac{4\pi}{2l+1}}}_{N} \frac{1}{q^{l+1}} Y_l^m(\mathbf{q}') \ . \tag{152}$$

Combining Eqs. (151) and (152) results in the orthonormal solid harmonic basis. Expanding $E(\mathbf{q})$ in this basis (see Eq. (208)) yields

$$E(\mathbf{q}) = \sum_{l=0}^{L} \sum_{m=-l}^{l} \left[\frac{c_l^m}{q^{l+1}} + d_l^m q^l \right] Y_l^m(\mathbf{q}') \tag{153}$$

where c_l^m and d_l^m are the respective irregular and regular solid harmonic coefficients of the series. Similarly to QBI and DOT, only even values of l are included in the expansion. To calculate c_l^m and d_l^m, these coefficients are written in the form of a pair of vectors, $\mathbf{X}_c$ and $\mathbf{X}_d$. Eq. (153) is then rewritten as a system of linear equations, i.e.,

$$\mathbf{E}(\mathbf{q}) = \mathbf{Y}(\mathbf{q}')\mathbf{G}(q)\mathbf{X}_c + \mathbf{Y}(\mathbf{q}')\mathbf{F}(q)\mathbf{X}_d \tag{154}$$

where $\mathbf{E}(\mathbf{q})$ is a vector containing the diffusion-weighted signal attenuation values for $\mathbf{q}$. $\mathbf{G}$ and $\mathbf{F}$ are square, diagonal matrices which respectively contain the regular and irregular solid harmonic coefficients of the series, i.e.

$$\mathbf{G}(q) = \begin{bmatrix} q^0 & & & \\ & q^2 & & \\ & & \ddots & \\ & & & q^l \end{bmatrix} \qquad \mathbf{F}(q) = \begin{bmatrix} q^{-1} & & & \\ & q^{-3} & & \\ & & \ddots & \\ & & & q^{-(l+1)} \end{bmatrix}.$$

Rewriting Eq. (154) in the general linear form, $\mathbf{E} = \mathbf{AX}$, yields

$$\underbrace{\begin{bmatrix} E_1 \\ E_2 \\ \vdots \\ E_n \end{bmatrix}}_{\mathbf{E}} = \underbrace{\begin{bmatrix} \mathbf{YG}_1 & \mathbf{YF}_1 \\ \mathbf{YG}_2 & \mathbf{YF}_2 \\ \vdots & \vdots \\ \mathbf{YG}_n & \mathbf{YF}_n \end{bmatrix}}_{\mathbf{A}} \underbrace{\begin{bmatrix} \mathbf{X}_c \\ \mathbf{X}_d \end{bmatrix}}_{\mathbf{X}}. \tag{155}$$

The series coefficients can be reconstructed using matrix pseudo-inversion (Appendix B). In order to perform this reconstruction, q-space must have been sampled on two or more q-shells as the radial component of the diffusion-weighted MR signal is described in terms of both its regular and irregular solid harmonics. The minimum number of non-antipodal points that must be sampled on each q-shell can

be calculated using Eq. (116), as the angular component of the EAP is described using spherical harmonic functions.

If **A** is an ill-conditioned matrix, the Laplace-Beltrami operator can be used to regularise the matrix [148, 149]. This matrix regularisation helps smooth spherical functions by penalising higher order tensor terms which do not significantly improve the accuracy of the reconstruction. This in turn improves the robustness of the matrix pseudo-inversion of **A**.

When employing Laplace-Beltrami regularisation in DPI, **X** can be determined using the expression

$$\mathbf{X} = \left(\mathbf{A}^{\mathrm{T}}\mathbf{A} + \lambda\mathbf{L}\right)^{-1}\mathbf{A}^{\mathrm{T}}\mathbf{E} \tag{156}$$

where **L** is the Laplace-Beltrami regulation matrix and λ_L is the angular regularisation constant. The Laplace-Beltrami regulation matrix is a diagonal matrix, the entries of which are $l^2(l+1)^2$.

However, this method requires an appropriate value for λ so that the higher order terms are not over smoothed. A good value for this regularisation constant can be found using the *L*-curve numerical method [150].

Upon calculating the solid harmonic coefficients of $E(\mathbf{q})$, the EAP can be calculated. Substituting Eq. (153) into Eq. (124) gives,

$$I_l(\mathbf{q}') = 4\pi\int_0^\infty q^2 J_l(2\pi qR)\sum_{l'=0}^{\infty}\sum_{m'=-l'}^{l'}\left[\frac{c_{l'}^{m'}}{q^{l'+1}} + d_{l'}^{m'}q^{l'}\right]Y_{l'}^{m'}(\mathbf{q}')\,dq\,. \tag{157}$$

Solving Eq. (123) using Eq. (157) will then yield [138]

$$\bar{P}(\mathbf{R}) = 2\sum_{l=0}^{\infty}\sum_{m=-l}^{l}\frac{(-1)^{l/2}\,2\pi^{l-1}R^l}{(2l-1)!!}c_l^m Y_l^m(\mathbf{R}') \tag{158}$$

where $(i-1)!! = (i-1)\times(i-1)\times\ldots\times 3\times 1$. The regular solid harmonic functions are not present in the final equation because, unlike the irregular solid harmonic functions, they are not antipodally symmetric. The EAP can then be visualised using the previously discussed approach for visualising probability isosurfaces (see Section 4.2 Diffusion tensor imaging). The shape of the probability isosurface will be

dependent on the choice of R_0; as R_0 increases, so does the angular contrast of the isosurface. However, high values of R_0 can result in spurious peaks appearing in the probability isosurface.

In addition to the previously discussed GFA index, another scalar index known as the zero displacement probability, $\bar{P}(0)$, can be calculated. $\bar{P}(0)$ describes the likelihood of individual particles having no net displacement during the diffusion period. This probability will increase as the restricting microstructure becomes narrower. Thus this value can be used as a measure of diffusion anisotropy. An analytical expression for the zero displacement probability can be calculated by substituting Eq. (153) into Eq. (108), and solving the resultant expression where **R** = 0 [138], i.e.,

$$\bar{P}(0) = q'^2 \sqrt{\pi} \left(c_0^0 + d_0^0 \frac{2q'}{3} \right) . \tag{159}$$

The advantage of using DPI is chiefly due to the analytical relationship between the diffusion-weighted signal approximation in the solid harmonic basis and the diffusion propagator. As such, the angular and radial components of the diffusion propagator can be estimated without assumptions regarding the angular or radial profile of the diffusion-weighted signal. Since the number of points in *q*-space required is moderate, the total length of the acquisition is comparable to that of GDTI and is acceptable for a clinical setting. However, it is unclear as to how the Laplacian is able to model the measured diffusion-weighted MR signal functions. The inclusion of irregular solid harmonic functions in the radial model also requires the unrealistic assumption that $E(0)$ does not exist (see Eq. (153)). Consequently this model results in the nonsensical prediction that the second order cumulant of the EAP will be zero [140]. The inclusion of the Laplace equation also results in the intrinsic smoothing of the diffusion propagator. While this smoothing is useful in removing spurious peaks from the diffusion propagator profile, the degree of smoothing cannot be controlled. This could lead to the over smoothing of the EAP, thus removing the fine details of the profile.

Spherical polar Fourier imaging

An alternative to DPI is the diffusion MRI technique known as spherical polar Fourier imaging (SPFI) [139, 265]. SPFI was designed with the intention to process noisy diffusion-weighted MR images with few radial samples of q-space. It was also designed to provide a generic framework for the reconstruction of many different features of the EAP.

SPFI expands $E(\mathbf{q})$ in the spherical polar Fourier (SPF) basis,

$$E(\mathbf{q}) = \sum_{k}^{\infty}\sum_{l}^{\infty}\sum_{m=-l}^{l} \alpha_{kl}^{m} R_k(q) Y_l^m(\mathbf{q}') \tag{160}$$

where α_{kl}^{m} denotes the coefficients of the expansion, k indicates the radial order and $R_k(q)$ represents the spherical polar Fourier radial basis functions of the expansion. The radial basis functions consists of orthonormal Gaussian–Laguerre polynomials,

$$R_k(q) = \left[\frac{2}{\zeta^{3/2}}\frac{k!}{\Gamma(k+3/2)}\right]^{1/2} \exp\left(-\frac{q^2}{2\zeta}\right) L_k^{1/2}\left(\frac{q^2}{\zeta}\right) \tag{161}$$

where ζ is the scaling factor for the function (found by fitting the Gaussian-Laguerre polynomials to the diffusion-weighted MR signal profile) and $L_k^{(y)}(x)$ is the generalised Laguerre polynomial,

$$L_k^{(y)}(x) = \left((y+1)_k / k!\right) {}_1F_1(-k, y+1, x) \tag{162}$$

with $(x)_n = \Gamma(x + n)/\Gamma(x)$. Gaussian-Laguerre polynomials are well suited to describing the radial component of $E(\mathbf{q})$ even when little radial information is available [139, 265]. For example, if diffusion is sampled on a single q-shell, the radial component of $E(\mathbf{q})$ will be modelled as a Gaussian profile. However, as the number of q-shells sampled is increased, the radial functions will be able to model the oscillation of the diffusion-weighted MR signal that occurs at high q-values.

To determine the series coefficients in Eq. (160), the equation can be used as the basis of a system of linear equations and rewritten as the matrix operation

$$\mathbf{E}(\mathbf{q}) = \mathbf{\Psi}(\mathbf{q})\mathfrak{A} \tag{163}$$

where $\mathfrak{A}$ is a vector containing the coefficients of Eq. (160) and $\mathbf{\Psi}(\mathbf{q})$ is the SPF basis matrix,

$$\mathbf{\Psi}(\mathbf{q}) = \begin{bmatrix} R_0(q)Y_0^0(\mathbf{q}_1') & \cdots & R_k(q)Y_l^{-l}(\mathbf{q}_1') & \cdots & R_k(q)Y_l^l(\mathbf{q}_1') \\ \vdots & & \ddots & & \vdots \\ R_0(q)Y_0^0(\mathbf{q}_N') & \cdots & R_k(q)Y_l^{-l}(\mathbf{q}_N') & \cdots & R_k(q)Y_l^l(\mathbf{q}_N') \end{bmatrix}. \quad (164)$$

The series coefficients can therefore be calculated by matrix inversion. Since this method also uses spherical harmonic functions to model the angular component of the EAP, the number of points that must be sampled on each q-shell can be determined using Eq. (116). The number of q-shells that must be sampled, on the other hand, is equal to the radial order by which Eq. (160) was truncated. However, unlike many other diffusion MRI techniques, SPFI is well suited to processing diffusion data with either few or many radial samples of q-space.

Once the a_{nlm} coefficients of Eq. (160) have been calculated a number of different descriptors of diffusion can be reconstructed. These include the EAP, ODF and return to zero probability. In the original implementation of SPFI, these diffusion features were reconstructed using the generic mathematical framework [139]

$$\mathfrak{G}(\mathbf{k}) = \int \bar{P}(\mathbf{R}) H_{\mathbf{k}}(\mathbf{R}) d\mathbf{R} \quad (165)$$

where $\mathfrak{G}(\mathbf{k})$ is a particular feature of the EAP and $H_{\mathbf{k}}(\mathbf{R})$ is the corresponding projection (i.e., kernel) function. For example, if $H_{\mathbf{k}}(\mathbf{R}) = R^2$ Eq. (165) will be equivalent to Eq. (110); thus $\mathfrak{G}(\mathbf{k})$ corresponds to the ODF. As the SPF functions form an orthonormal basis, the following relationship is implied

$$\mathfrak{G}(\mathbf{k}) = \int P(\mathbf{r}) H_{\mathbf{k}}(\mathbf{r}) d\mathbf{r} = \int E(\mathbf{q}) h_{\mathbf{k}}(\mathbf{q}) d\mathbf{q} = \sum_{n=1}^{\infty} \sum_{l}^{\infty} \sum_{m=-l}^{l} a_{nlm} h_{nlm}^{\mathbf{k}} \quad (166)$$

where $h_{\mathbf{k}}(\mathbf{q})$ is the inverse Fourier transform of $H_{\mathbf{k}}(\mathbf{R})$ and $h_{nlm}^{\mathbf{k}}$ are the SPF expansion coefficients of $h_{\mathbf{k}}(\mathbf{q})$. Thus the problem can be reduced to a straightforward dot product between the a_{nlm} coefficients and the $h_{nlm}^{\mathbf{k}}$ coefficients.

To calculate the $h_{nlm}^{\mathbf{k}}$ coefficients, $H_{\mathbf{k}}(\mathbf{R})$ is transformed into $h_{\mathbf{k}}(\mathbf{q})$ using the inverse fast Fourier transform. This transform must be performed along a large number of

directions in q-space, evenly spaced over the unit sphere. Unfortunately, these calculations are highly computationally intensive. However, the process can be accelerated when calculating the angular features of the EAP (e.g. the ODF) by exploiting the rotational properties of spherical harmonics [259]. Upon calculating the $h_{nlm}^{\mathbf{k}}$ coefficients of $h_{\mathbf{k}}(\mathbf{q})$ along one direction in q-space (e.g. parallel to the z-axis), the remaining $h_{nlm}^{\mathbf{k}}$ coefficients corresponding to other directions in q-space can be determined by using matrix rotation, i.e.,

$$h_{nlm}^{\prime\mathbf{k}} = \mathbf{W}^{(l)}(\varphi,\theta,0)\, h_{nlm}^{\mathbf{k}} = \sum_{m=-l}^{l} W_{m',m}^{(l)}(\varphi,\theta,0)\, h_{nlm}^{\mathbf{k}} \,, \tag{167}$$

where $h_{nlm}^{\prime\mathbf{k}}$ signifies the rotated coefficients and $\mathbf{W}(\varphi,\theta,0)$ is the real Wigner rotation matrix in terms of Euler angles [266-268]. The real Wigner rotation matrix is given by,

$$\mathbf{W}(\alpha,\beta,\gamma) = \sum_{m'=-l}^{l} \exp(-im'\alpha)\, d_{m'm}^{(l)}(\beta) \exp(-im'\gamma) \tag{168}$$

where $d_{m'm}^{(l)}(\beta)$ is the Wigner (small) d-matrix,

$$d_{m'm}^{(l)}(\beta) = \sqrt{\frac{(l+m')!(l-m')!}{(l+m)!(l-m)!}} \times \sum_{k=\max(0,m-m')}^{\min(l-m',l+m)} \frac{(-1)^{k+m'-m}(\cos\beta/2)^{2l+m-m'-2k}(\sin\beta/2)^{2k+m'-m}}{(l+m-k)!k!(k+m'-m)!(l-m'-k)} \,. \tag{169}$$

Once the $h_{nlm}^{\mathbf{k}}$ coefficients have been calculated, these coefficients can be substituted into Eq. (166), along with the a_{nlm} coefficients to create the profile of $\mathfrak{G}(\mathbf{k})$. This feature of the EAP can then be visualised using the same method for visualising probability isosurfaces.

A list of example kernel functions is given in Table 9 [139, 265]. The modular nature of the generic framework is one of the advantages of SPFI. It allows the extraction of useful information from diffusion data sets covering different regions of q-space and can also make use of new kernel functions when they are derived.

Table 9: Kernel functions for SPFI

$\mathfrak{G}(\mathbf{k})$	$H_{\mathbf{K}}(\mathbf{R})$
FRT	$2\pi q J_0(2\pi q R)\delta(1-\mathbf{R}\cdot\mathbf{k})$
ODF	$\delta\left(1-(\mathbf{R}\cdot\mathbf{k})/(\lvert\mathbf{R}\rvert\lvert\mathbf{k}\rvert)\right)$
EAP	$\delta(\mathbf{R}-\mathbf{k})$
Zero displacement probability	$\delta(\mathbf{R})$

An alternative approach to SPFI, similar to DOT MRI and DPI [265], uses derived analytical expressions for the $h_{nlm}^{\mathbf{k}}$ coefficients corresponding to a number of different $\mathfrak{G}(\mathbf{k})$ (see Eq. (166), Table 10). By replacing $E(\mathbf{q})$ in Eq. (124) with Eq. (160), the expression becomes

$$I_l(\mathbf{q}') = 4\pi\int_0^\infty q^2 J_l(2\pi q R_0)\sum_{k=0}^{\infty}\sum_{l'=0}^{\infty}\sum_{m'=-l'}^{l'}\alpha_{kl}^{\ m}R_k(q)Y_l^m(\mathbf{q}')dq\,. \tag{170}$$

Table 10: The kernel function coefficients for SPFI.

$\mathfrak{G}(\mathbf{k})$	$h_{nlm}^{\mathbf{k}}$
FRT	$2\pi q^2 R_n(q)P_l(0)Y_l^m(\mathbf{k})$
ODF	$4\pi(-1)^n\gamma^{3/4}\sqrt{\dfrac{\Gamma(n+3/2)}{n!}}\mathfrak{P}_l(0)Y_l^m(\mathbf{k})$
EAP	$4(-1)^{l/2}\dfrac{\zeta^{(l+3)/2}\pi^{l+3/2}k^l}{\Gamma(l+3/2)}\sum_{n=0}^{N}f_{nlm}(\zeta,R_0)a_{nlm}\times$ $\kappa_n(\zeta)\sum_{i=0}^{n}\left(\begin{array}{l}\dfrac{(-1)^i}{i!}\begin{pmatrix}n+1/2\\ n-i\end{pmatrix}2^{(l+2i-1)/2}\Gamma\left(\dfrac{l+2i+3}{2}\right)\times\\ {}_1F_1\left(\dfrac{2i+l+3}{2},\dfrac{2l+3}{2},-2\pi^2R_0^{\ 2}\zeta\right)Y_l^m(k)\end{array}\right)$
Zero displacement probability	$4\sqrt{\pi}\xi^{3/4}(-1)^n\sqrt{\dfrac{\Gamma(n+3/2)}{n!}}a_{n,0,0}$

When Eq. (170) is substituted into Eq. (123), it can be shown that [265]

$$\bar{P}(\mathbf{R}) = \sum_{l}^{\infty} \sum_{m=-l}^{l} c_l^m Y_l^m(\mathbf{q}'), \tag{171}$$

where c_l^m are the coefficients of the expansion (see Eq. (161)), which are given by

$$c_l^m = 4(-1)^{l/2} \frac{\zeta^{(l+3)/2} \pi^{l+3/2} k^l}{\Gamma(l+3/2)} \sum_{k=0}^{n} f_{kl}^{\ m}(\zeta, R_0) a_{kl}^{\ m} \tag{172}$$

with

$$f_{nlm}(\zeta, R_0) = \kappa_n(\zeta) \sum_{i=0}^{n} \left(\begin{array}{l} \frac{(-1)^i}{i!} \binom{n+1/2}{n-i} 2^{(l+2i-1)/2} \Gamma\left(\frac{l+2i+3}{2}\right) \times \\ {}_1F_1\left(\frac{2i+l+3}{2}, \frac{2l+3}{2}, -2\pi^2 R_0^{\ 2} \zeta\right) \end{array} \right). \tag{173}$$

This process thus avoids the need for Fourier transformation (and rotation) of the kernel functions, allowing the analytical calculation of the full EAP and its features.

SPFI is a robust, noise insensitive diffusion MRI technique. It requires no prior assumptions regarding the radial or angular components of the diffusion-weighted signal attenuation profile and requires fewer samples of *q*-space. The use of the SPF basis also allows $E(\mathbf{q})$ to be described using a single set of SPFI coefficients. Unlike DPI, no information is discarded when the EAP is reconstructed. The different kernel functions provide a number of analytical solutions for many diffusion features of the EAP. As many of the reconstruction kernels are based on spherical harmonic functions, the number of points on each also benefits from increased computational stability. Additionally, the MSD of the EAP can be calculated as $E(\mathbf{q} = 0)$ exists. However, it has been found that SPFI has a tendency to severely underestimate the true MSD of the EAP; it has been speculated that the reason for this is because the SPFI basis is not an eigenfunction of the Laplacian operator [140].

Appendix B

In the case of the iterative reconstruction, S_0 and the elements of **D** can be estimated by substituting estimates of S_0 and the elements of **D** into Eq. (39) and minimising the difference between the resultant values of S and the measured values of S. In order to perform iterative diffusion tensor reconstruction, Eq. (39) is first rewritten as a system of non-linear equations,

$$\begin{aligned} S_1 &= S_0 \exp\left(-b_{1_{xx}} D_{xx} - b_{1_{yy}} D_{yy} - b_{1_{zz}} D_{zz} - 2b_{1_{xy}} D_{xy} - 2b_{1_{xz}} D_{xz} - 2b_{1_{yz}} D_{yz}\right) \\ S_2 &= S_0 \exp\left(-b_{2_{xx}} D_{xx} - b_{2_{yy}} D_{yy} - b_{2_{zz}} D_{zz} - 2b_{2_{xy}} D_{xy} - 2b_{2_{xz}} D_{xz} - 2b_{2_{yz}} D_{yz}\right) \\ &\vdots \\ S_n &= S_0 \exp\left(-b_{n_{xx}} D_{xx} - b_{n_{yy}} D_{yy} - b_{n_{zz}} D_{zz} - 2b_{n_{xy}} D_{xy} - 2b_{n_{xz}} D_{xz} - 2b_{n_{yz}} D_{yz}\right) \end{aligned} . \quad (174)$$

Then using a multivariate least-squares regression method, such as the Levenberg-Marquardt method [269, 270], S_0 and the independent elements of **D** can be estimated from Eq. (174). The elements of **D** can then be arranged to create **D**. The iterative diffusion tensor reconstruction method can be applied to any tensor-based diffusion MRI technique by replacing the system of equations in Eq. (174) with the appropriate model. Direct diffusion tensor reconstruction methods, on the other hand, rely on matrix operations to calculate the unknown elements directly. For the direct reconstruction of the second-order diffusion tensor there are several variations of the method. Two of these variations will be described here.

The first direct method of diffusion tensor reconstruction requires a minimum of six S images and one S_0 image. The S_0 image is required to normalise the S images. To begin the reconstruction, $\mathbf{B}_i$ and **D** are both rewritten as vectors,

$$\mathbf{b}_i = \begin{bmatrix} B_{xxi} & B_{yyi} & B_{zzi} & 2B_{xyi} & 2B_{xzi} & 2B_{yzi} \end{bmatrix} \quad (175)$$

$$\mathbf{d}_a = \begin{bmatrix} D_{xx} & D_{yy} & D_{zz} & D_{xy} & D_{xz} & D_{yz} \end{bmatrix}^{\mathrm{T}} . \quad (176)$$

Upon substituting Eqs. (175) and (176) into Eq. (39),

$$S_i = S_0 \exp\left(-\mathbf{b}_i \, \mathbf{d}_a\right). \quad (177)$$

Eq. (177) can then be rewritten as

$$\ln\left(E_i\right) = \ln\left(\frac{S_i}{S_0}\right) = -\mathbf{b}_i\mathbf{d}_a \tag{178}$$

Working on a per voxel basis, the diffusion weighted signal data for the selected voxel for each image is combined into a single vector, $\mathbf{Y}_a$,

$$\mathbf{Y}_a = \begin{bmatrix} \ln\left(E_1\right) & \ln\left(E_1\right) & \cdots & \ln\left(E_n\right) \end{bmatrix}^{\mathrm{T}} \tag{179}$$

and the **b**-vectors are combined into a single matrix, $\mathbf{B}_a$,

$$\mathbf{B}_a = \begin{bmatrix} \mathbf{b}_1 & \mathbf{b}_2 & \ldots & \mathbf{b}_n \end{bmatrix}^{\mathrm{T}} \tag{180}$$

$$\mathbf{B}_a = \begin{pmatrix} b_{1_{xx}} & b_{1_{yy}} & b_{1_{zz}} & 2b_{1_{xy}} & 2b_{1_{xz}} & 2b_{1_{yz}} \\ b_{2_{xx}} & b_{2_{yy}} & b_{2_{zz}} & 2b_{2_{xy}} & 2b_{2_{xz}} & 2b_{2_{yz}} \\ \vdots & \vdots & \vdots & \vdots & \vdots & \vdots \\ b_{n_{xx}} & b_{n_{yy}} & b_{n_{zz}} & 2b_{n_{xy}} & 2b_{n_{xz}} & 2b_{n_{yz}} \end{pmatrix}.$$

Upon substituting Eqs. (179) and (180) into Eq. (178),

$$\mathbf{Y}_a = -\mathbf{B}_a\mathbf{d}_a \tag{181}$$

$$\begin{pmatrix} \ln\left(E_1\right) \\ \ln\left(E_2\right) \\ \vdots \\ \ln\left(E_n\right) \end{pmatrix} = -\begin{pmatrix} b_{1_{xx}} & b_{1_{yy}} & b_{1_{zz}} & 2b_{1_{xy}} & 2b_{1_{xz}} & 2b_{1_{yz}} \\ b_{2_{xx}} & b_{2_{yy}} & b_{2_{zz}} & 2b_{2_{xy}} & 2b_{2_{xz}} & 2b_{2_{yz}} \\ \vdots & \vdots & \vdots & \vdots & \vdots & \vdots \\ b_{n_{xx}} & b_{n_{yy}} & b_{n_{zz}} & 2b_{n_{xy}} & 2b_{n_{xz}} & 2b_{n_{yz}} \end{pmatrix} \begin{pmatrix} D_{xx} \\ D_{yy} \\ D_{zz} \\ D_{xy} \\ D_{xz} \\ D_{yz} \end{pmatrix}.$$

The second method of diffusion tensor reconstruction, on the other hand, requires a minimum of seven S images. Rather than using an S_0 image to normalise the S images, it estimates S_0 based on the supplied S values.

Similar to the first method of direct diffusion tensor reconstruction, **B** and **D** are both rewritten as vectors. However, a notable difference between the two methods is that **B** and **D** are rewritten to include –1 and ln (S_0), respectively,

$$\boldsymbol{\beta}_i = \begin{bmatrix} B_{xxi} & B_{yyi} & B_{zzi} & 2B_{xyi} & 2B_{xzi} & 2B_{yzi} & -1 \end{bmatrix} \tag{182}$$

$$\mathbf{d}_b = \begin{bmatrix} D_{xx} & D_{yy} & D_{zz} & D_{xy} & D_{xz} & D_{yz} & \ln(S_0) \end{bmatrix}^{\mathrm{T}}. \tag{183}$$

Upon substituting Eqs. (182) and (183) into Eq. (39),

$$\ln(S_i) = -\boldsymbol{\beta}_i \mathbf{d}_b . \tag{184}$$

Working on a per voxel basis, the diffusion weighted signal data for the selected voxel for each image is combined into a single vector, **Y**,

$$\mathbf{Y}_b = \begin{bmatrix} \ln(S_1) & \ln(S_1) & \cdots & \ln(S_n) \end{bmatrix}^{\mathrm{T}} \tag{185}$$

and the **b**-vectors are combined into a single matrix, $\mathbf{B}_b$,

$$\mathbf{B}_b = \begin{bmatrix} \mathbf{b}_1 & \mathbf{b}_2 & \ldots & \mathbf{b}_n \end{bmatrix}^{\mathrm{T}} \tag{186}$$

$$\mathbf{B}_b = \begin{pmatrix} b_{1_{xx}} & b_{1_{yy}} & b_{1_{zz}} & 2b_{1_{xy}} & 2b_{1_{xz}} & 2b_{1_{yz}} & -1 \\ b_{2_{xx}} & b_{2_{yy}} & b_{2_{zz}} & 2b_{2_{xy}} & 2b_{2_{xz}} & 2b_{2_{yz}} & -1 \\ \vdots & \vdots & \vdots & \vdots & \vdots & \vdots & \vdots \\ b_{n_{xx}} & b_{n_{yy}} & b_{n_{zz}} & 2b_{n_{xy}} & 2b_{n_{xz}} & 2b_{n_{yz}} & -1 \end{pmatrix}.$$

Upon substituting Eqs. (179) and (180) into Eq. (178),

$$\mathbf{Y}_b = -\mathbf{B}_b \mathbf{d}_b \tag{187}$$

$$\begin{pmatrix} \ln(S_1) \\ \ln(S_2) \\ \vdots \\ \ln(S_n) \end{pmatrix} = -\begin{pmatrix} b_{1_{xx}} & b_{1_{yy}} & b_{1_{zz}} & 2b_{1_{xy}} & 2b_{1_{xz}} & 2b_{1_{yz}} & -1 \\ b_{2_{xx}} & b_{2_{yy}} & b_{2_{zz}} & 2b_{2_{xy}} & 2b_{2_{xz}} & 2b_{2_{yz}} & -1 \\ \vdots & \vdots & \vdots & \vdots & \vdots & \vdots & \vdots \\ b_{n_{xx}} & b_{n_{yy}} & b_{n_{zz}} & 2b_{n_{xy}} & 2b_{n_{xz}} & 2b_{n_{yz}} & -1 \end{pmatrix} \begin{pmatrix} D_{xx} \\ D_{yy} \\ D_{zz} \\ D_{xy} \\ D_{xz} \\ D_{yz} \\ \ln(S_0) \end{pmatrix}.$$

Due to the notable similarities in Eqs. (181) and (187), the computation for both methods from this point is much the same. If the *b*-matrix used is a square, invertible matrix, Eqs. (181) and (187) can be rearranged as

$$\mathbf{d}_k = -\mathbf{B}_k^{-1} \mathbf{Y}_k \tag{188}$$

Where $\mathbf{B}_k^{-1}$ is the inverted **B**-matrix. If $\mathbf{B}_k$ is not a square, invertible matrix, it can be pseudo-invertible instead. Pseudo-inversion of the $\mathbf{B}_k$ can be achieved by either using the relation

$$\mathbf{B}_k^{\psi} = \left(\mathbf{B}_k^T \mathbf{B}_k\right)^{-1} \mathbf{B}_k^T , \tag{189}$$

where $\mathbf{B}_k^{\psi}$ is pseudo-inverted $\mathbf{B}_k$, or by the singular value decomposition of $\mathbf{B}_k$ [271]. Upon substituting $\mathbf{B}_k^{-1}$ in Eq. (188) with $\mathbf{B}_k^{\psi}$,

$$\mathbf{d}_k = -\mathbf{B}_k^{\psi} \mathbf{Y}_k . \tag{190}$$

Once $\mathbf{d}_k$ has been calculated, the components of this vector can be rearranged to produce **D**. In order to directly reconstruct the diffusion tensor, it must have the form of Eq. (190). This limits this reconstruction method to imaging techniques which have a single tensor (i.e., DTI and GDTI). However, direct diffusion tensor reconstruction does have some advantages over iterative methods. Firstly, it is more robust. It does not require a starting point for the calculations, and is unaffected by local minima errors. Direct diffusion tensor reconstruction is also quicker to perform as it is a single calculation rather than many. It should be noted that calculations involving very large **B** and/or **D** tensors place high demands on computer system memory.

For example, the relation between the calculated α values and **A** is given by

$$\begin{pmatrix} \alpha_1 \\ \alpha_2 \\ \vdots \\ \alpha_n \end{pmatrix} = \begin{pmatrix} u_{1_{xx}} & u_{1_{yy}} & u_{1_{zz}} & 2u_{1_{xy}} & 2u_{1_{xz}} & 2u_{1_{yz}} \\ u_{2_{xx}} & u_{2_{yy}} & u_{2_{zz}} & 2u_{2_{xy}} & 2u_{2_{xz}} & 2u_{2_{yz}} \\ \vdots & \vdots & \vdots & \vdots & \vdots & \vdots \\ u_{n_{xx}} & u_{n_{yy}} & u_{n_{zz}} & 2u_{n_{xy}} & 2u_{n_{xz}} & 2u_{n_{yz}} \end{pmatrix} \begin{pmatrix} A_{xx} \\ A_{yy} \\ A_{zz} \\ A_{xy} \\ A_{xz} \\ A_{yz} \end{pmatrix} . \tag{191}$$

Appendix C

Due to the popularity of the spherical harmonic basis for the analysis of diffusion data acquired using HARDI sampling schemes, the derivation of the spherical harmonic functions is provided here.

A harmonic function, F, is a function that satisfies the Laplace equation,

$$\nabla^2 F(x,y,z) = \left[\frac{\partial^2}{\partial x^2} + \frac{\partial^2}{\partial y^2} + \frac{\partial^2}{\partial z^2}\right] F(x,y,z) = 0\,. \tag{192}$$

When rewritten in spherical coordinates, Eq. (192) becomes

$$\begin{aligned}\nabla^2 F(r,\theta,\varphi) &= \left[\frac{1}{r^2}\frac{\partial}{\partial r}\left(r^2\frac{\partial}{\partial r}\right) + \frac{1}{r^2\sin\theta}\frac{\partial}{\partial\theta}\left(\sin\theta\frac{\partial}{\partial\theta}\right) + \frac{1}{r^2\sin^2\theta}\frac{\partial^2}{\partial\varphi^2}\right] F(r,\theta,\varphi) \\ &= 0\end{aligned} \tag{193}$$

where r is the characteristic radial length of the function, φ is the azimuth angle ($0 \le \varphi \le 2\pi$) and θ is the colatitude angle ($0 \le \theta \le 2\pi$). Assuming that the angular component, $Y(\theta,\varphi)$, of the harmonic function is independent of its radial component, $R(r)$, i.e.

$$F(r,\theta,\varphi) = R(r)Y(\theta,\varphi)\,, \tag{194}$$

these two components can be separated. Substituting Eq. (194) into Eq. (193) will yield two solutions,

$$\frac{r^2}{R(r)}\frac{d^2R(r)}{dr^2} + \frac{2r}{R(r)}\frac{dR(r)}{dr} = \lambda \tag{195}$$

and

$$\frac{1}{Y(\theta,\varphi)\sin\theta}\frac{\partial}{\partial\theta}\left(\sin\theta\frac{\partial Y(\theta,\varphi)}{\partial\theta}\right) + \frac{1}{Y(\theta,\varphi)\sin^2\theta}\frac{\partial^2 Y(\theta,\varphi)}{\partial\varphi^2} = -\lambda\,, \tag{196}$$

where λ is a constant. Assuming that $Y(\theta,\varphi)$ can be further separated (i.e., $Y(\theta,\varphi) = \Theta(\theta,)\,\Phi(\varphi)$) , Eq. (196) will yield the solutions

$$\frac{1}{\Phi(\varphi)}\frac{d^2\Phi(\varphi)}{d\varphi^2}=-m^2 \tag{197}$$

and

$$\lambda\sin^2\theta+\frac{\sin\theta}{\Theta(\theta)}\frac{d}{d\theta}\left(\sin\theta\frac{d\Theta(\theta)}{d\theta}\right)=m^2 \tag{198}$$

where m is a constant. Integrating Eq. (197) gives the result,

$$\Phi=\exp(\pm im\varphi); \tag{199}$$

Eq. (198) on the other hand, assuming that $\lambda = l(l + 1)$ and that $|m| \leq l$, can be rewritten as

$$\frac{d^2\Theta(\theta)}{d\theta^2}+\frac{\cos\theta}{\sin\theta}\frac{d\Theta(\theta)}{d\theta}+\left[l(l+1)-\frac{m^2}{\sin^2\theta}\right]\Theta(\theta)=0. \tag{200}$$

Eq. (200) has the same form as an associated Legendre differential equation (a generalisation of the Legendre differential equation). Therefore Eq. (200) has the solution

$$\Theta(\theta)=c_1\mathfrak{P}_l^m(\cos\theta)+c_2\mathfrak{Q}_l^m(\cos\theta) \tag{201}$$

where c_1 and c_2 are constants, $\mathfrak{P}_l^m(x)$ are the associated Legendre polynomials of the first kind (i.e., when l is an integer) and $\mathfrak{Q}_l^m(x)$ are the associated Legendre polynomials of the second kind (i.e., when l is not an integer). l denotes the harmonic order of the polynomial while m indicates its phase. To ensure that $Y(\theta,\varphi)$ is regular at the poles of the function (i.e., $\theta = 0,\pi$), l must be a non-negative integer. Thus,

$$\Theta(\theta)=c_1\mathfrak{P}_l^m(\cos\theta). \tag{202}$$

where

$$\mathfrak{P}_l^m(x)=\frac{(-1)^m}{2^l l!}\left(1-x^2\right)^{m/2}\frac{d^{l+m}}{dx^{l+m}}\left(x^2-1\right)^l. \tag{203}$$

Multiplying Eqs. (200) and (199) therefore yields

$$Y_l^m(\theta,\varphi) = \underbrace{\sqrt{\frac{2l+1}{4\pi}\frac{(l-m)!}{(l+m)!}}}_{N} \exp(im\varphi)\mathfrak{P}_l^m(\cos\theta)\,. \tag{204}$$

The solutions of Eq. (204) are termed spherical harmonic functions (Figure 72). These functions form a complete orthonormal basis, i.e.

$$\begin{aligned}
&\int_0^{2\pi}\int_0^{\pi} Y_l^m(\theta,\phi) Y_{l'}^{m'}(\theta,\varphi)^* \sin\theta\, d\theta\, d\varphi \\
&= \int_0^{2\pi}\int_{-1}^{1} Y_l^m(\theta,\phi) Y_{l'}^{m'}(\theta,\varphi)^* d(\cos\theta)\, d\varphi \\
&= \delta_{ll'}\delta_{mm'}
\end{aligned} \tag{205}$$

where δ_{ij} is the Kronecker delta,

$$\delta_{ij} = \begin{cases} 0 & i \neq j \\ 1 & i = j \end{cases}, \tag{206}$$

and * denotes the function complex conjugate. The complex conjugate of a spherical harmonic function is given by

$$Y_l^m(\theta,\phi)^* = (-1)^m Y_l^{-m}(\theta,\phi)\ . \tag{207}$$

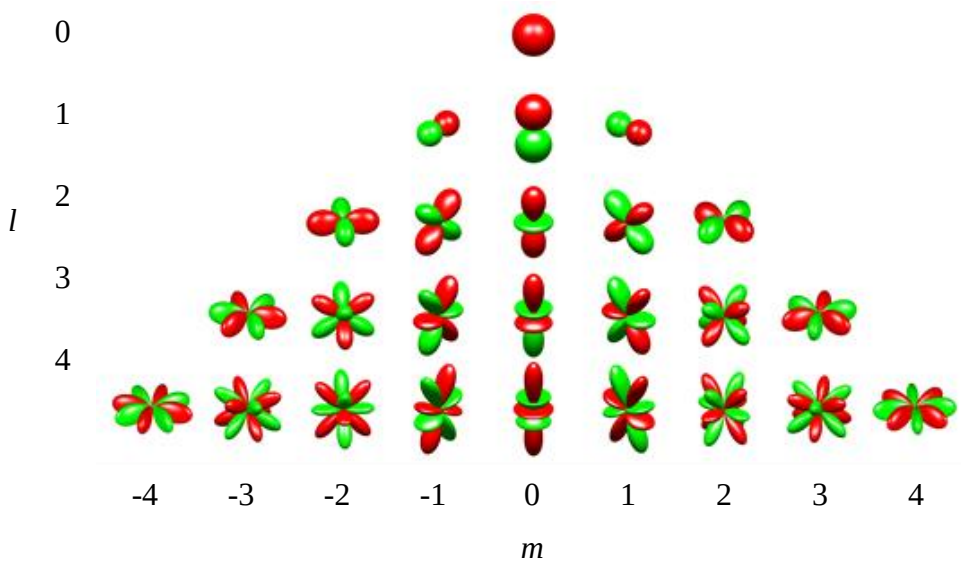

Figure 72: Representations of spherical harmonic function for the first few harmonic orders. The red component of each surface is the positive component of the spherical harmonic while the green indicates the negative component.

Using the spherical harmonic functions as a basis, a harmonic function can be approximated on the surface of a sphere; for example, expanding $E(\mathbf{q}')$ using an infinite series of spherical harmonic functions as a linear basis yields

$$E(\mathbf{q}') = \sum_{l}^{\infty} \sum_{m=-l}^{l} \alpha_l^m Y_l^m(\mathbf{q}') \tag{208}$$

where α_l^m are the spherical harmonic coefficients of the series. These coefficients are a continuous representation of the diffusion-weighted signal. The coefficients of Eq. (208) can be found by truncating the expansion to a finite harmonic order, L, yielding the linear equation,

$$\begin{aligned} E(\mathbf{q}') = {} & \alpha_0^0 Y_0^0(\mathbf{q}') \\ & + \alpha_1^{-1} Y_1^{-1}(\mathbf{q}') + \alpha_1^0 Y_1^0(\mathbf{q}') + \alpha_1^1 Y_1^1(\mathbf{q}') \\ & + \alpha_2^{-2} Y_2^{-2}(\mathbf{q}') + \alpha_2^{-1} Y_2^{-1}(\mathbf{q}') + \alpha_2^0 Y_2^0(\mathbf{q}') + \alpha_2^1 Y_2^1(\mathbf{q}') + \alpha_2^2 Y_2^2(\mathbf{q}') . \\ & + \ldots \\ & + \alpha_L^{-L} Y_L^{-L}(\mathbf{q}') + \ldots + \alpha_L^L Y_L^L(\mathbf{q}') \end{aligned} \tag{209}$$

Similar to Eq. (39), Eq. (209) can be used to construct a system of linear equations which can be solved to determine the coefficients of the spherical harmonic functions. Since it can be assumed that $E(\mathbf{q}')$ is real, positive and antipodally symmetric, diffusive motion can be described using a subset of spherical harmonic functions which are both real and symmetric [168], i.e.

$$Y_l^m = \begin{cases} \sqrt{2}\,\mathrm{Re}\left(Y_l^m\right) & 0 < m \le l \\ Y_l^0 & m = 0 \\ \sqrt{2}\,\mathrm{Im}\left(Y_l^{|m|}\right) & -l \le m < 0 \end{cases} \tag{210}$$

where l is also an even integer.

Appendix D

```
%== BFOR image reconstruction (v 1.0)
%== By Ryan J. Dean
%== May 2015

%=====================================================================
% SYNTAX: [P, basis] = BFOR_image_recon(images, n_factor, diff_grads, q_values, tau, Lmax_input, Nmax_input,
% reg_factors)
%
% INPUTS:
%
% images        - The diffusion-weighted (S) image stack (including the diffusion-weighted (S0) image) [ n x m x 3 ]
%                 I.e., [ S0; S(q(1), diff_grad(1)); S(q(2), diff_grad(1)); ...; S(q(n), diff_grad(1)); ...; S(q(n),
diff_grad(n)) ];
% n_factor      - Threshold for image noise (voxel with an S0 value < n_factor will not be reconstructed)
% diff_grads    - Diffusion gradient directions (normalised) [ n x 3 ]
% q_values      - List of q-values used in mm^-1
% tau           - q-value that the MR signal should attenuated to 0 in mm^-1
% Lmax_input    - Maximum spherical harmonic order of the reocnstruction (must be an even number > 0)
% Nmax_input    - Maximum radial order of the reconstruction (must be > 0)
% reg_factors   - [Ll, Ln, t, p, t]
%                    - Ll is the angular Laplace-Beltrami regularisation coefficient (e.g. 0.1)
%                    - Ln is the radial Laplace-Beltrami regularisation coefficient (e.g. 0.1)
%                    - t is time (e.g. 0)
%                    - p is the particle displacement distance in mm (e.g. 25 x 10^-3 mm)
%
```

```
% OUTPUTS:
%
% P              - Probability values [ n x 1 ]
% H              - Reconstruction basis [ n x 3 ]
%
%=====================================================================

function [P, H] = BFOR_image_recon(images, n_factor, diff_grads, q_values, tau, Lmax_input, Nmax_input, reg_factors)

%== Begin timer
tic

%== Start MATLAB pool for parallel processing (if the pool is not open)
if matlabpool('size') == 0
    matlabpool(4)
end

%== Extract the S0 image
S0 = images(:,:,1);

%== Extract the S images
S = zeros([size(S0) size(images,3)-1]);

for i = 2:size(images,3)
    S(:,:,(i-1)) = images(:,:,i);
end

```

```
%== Create a stack of attenutated MR images
E_stack = zeros(size(S));
for y = 1:size(S0,1)
    for x = 1:size(S0,2)
        if (S0(y,x) > nfactor)
            E_stack(y,x,:) = S(y,x,:)/S0(y,x);
        end
    end
end

%== Extract the regularisation coefficients
Ll = reg_factors(1);
Ln = reg_factors(2);
t = reg_factors(3);
p = reg_factors(4);

%====== Image processing ==================================================

%== Create figure
figure
hold on

%== Renaming Lmax_input
Lmax = Lmax_input;

%== Reconstruction scheme (vertices and facets)
V = load('/sampling_and_reconstruction_schemes/On_the_sphere/514_shell.txt');
```

```
F = load('/sampling_and_reconstruction_schemes/On_the_sphere/514_sphere_facets.txt');

% The sampling and reconstruction schemes loaded here are a part of
% the 'Suite of functions to perform uniform sampling of a sphere' package
% created by Anton Semechko (a.semechko@gmail.com).
% This package is available from the MATLAB Central File Exchange.

%== Divide the reconstruction scheme further for a smoother reconstructed isosurface
TQ = TriQuad({V,F});

% 'TriQuad' was written by Anton Semechko (a.semechko@gmail.com)
% It is a function from the 'Suite of functions to perform uniform sampling of a sphere' package.
% This package is available from the MATLAB Central File Exchange.

V = cell2mat(TQ(1));
F = cell2mat(TQ(2));

%== Principal code loop
for im_y = 1:size(E_stack,1)
    for im_x = 1:size(E_stack,1)

        %== Do not reconstruct voxels below the S0 threshold
        if S0(im_y, im_x) > n_factor

            %== Loop for each radial order
            for N_index = 1:Nmax_input

```

```
%== Current radial order
Nmax = N_index;

%== Attenuated MR signal for the current voxel
E = squeeze(E_stack(im_y, im_x,:));

%== Local variables
n_E = length(E);
n_LM = (Lmax+1)*(Lmax+2)*0.5;
n_NLM = Nmax*n_LM;

%== Create the spherical harmonic (SH) matrix
Y = construct_SH_basis(Lmax, diff_grads, 2, 'real');

% 'construct_SH_basis' was written by bjian
% It is a function from the 'High Angular Resolution Diffusion Imaging (HARDI) Tools' package,
% compiled by Canales-Rodríguez, Melie-García, Iturria-Medina, Alemán-Gómez
% This package is available from the MATLAB Central File Exchange.

%== Local variables for finding the roots of the spherical Bessel function
bessel_x_axis = (0.0001:0.0001:5);
SqrtLambda = zeros(Lmax+1, Nmax);

%== Loop for each SH order
for l = 0:Lmax

    %== Generate the values of the Bessel functions
```

```
J = zeros(length(bessel_x_axis),1);
for i = 1:length(bessel_x_axis)
    J(i) = sphericalbesselj(l, bessel_x_axis(i)*tau);
end

%== Estimate the zero crossing points
X = [];
for i = 2:length(bessel_x_axis)
    if J(i-1) >= 0 && J(i) <= 0
        X = [X; bessel_x_axis (i-1) bessel_x_axis (i)];
    end

    if J(i-1) <= 0 && J(i) >= 0
        X = [X; bessel_x_axis (i-1) bessel_x_axis (i)];
    end

    if size(X,1) >= Nmax
        break
    end
end

%== Check to ensure there are enough roots.
%== If not, increase the max value of bessel_x_axis
if size(X,1) < Nmax, error('There are not enough Bessel function roots!'); end

%== Find the nth root for each spherical bessel function
for n = 1:Nmax
```

```
        x0 = X(n,1);
        z = fzero(@(sqrtlambda) sphericalbesselj(l, tau*sqrtlambda), x0);
        SqrtLambda(l+1,n) = z;
    end
end

%== Convert square root lambda to lambda
Lambda = SqrtLambda.^2;

%== List of SH orders in j notation
l_list = [];
for l = 0:2:Lmax
    for m = -l:l
        l_list = [l_list; l];
    end
end

%== Create the expanded SH basis (to account for different q-values)
YQ = [];
for j = 1:size(Y,1)
    for q = 1:length(q_values)
        YQ = [YQ; Y(j,:)];
    end
end

%== Create the BFOR reconstruction matrix
Z = [];
```

```
            for n = 1:Nmax

                U = [];

                for j = 1:n_E

                    %== Select a q-value
                    v = mod(j, length(q_values));
                    if v == 0, v = length(q_values); end
                    q = q_values(v);

                    U_vector = [];

                    for i = 1:n_LM

                        %== Select the SH order
                        l = l_list(i);

                        %== Select the root value
                        a = SqrtLambda(l+1,n);

                        %== Spherical Bessel value
                        J = sphericalbesselj(l, q*a);

                        if J == 0
                            error('The Bessel function returned zero.')
```

```
                end

                %== Complete the basis
                U_vector = [U_vector, YQ(j,i)*J];
            end

            U = [U; U_vector];
        end

        Z = [Z, U];
    end

    %== Laplace-Beltrami regularisation
    Lreg = [];
    Nreg = [];

    for n = 1:Nmax
       Nreg = [Nreg; (n^2)*((n + 1)^2)*ones(n_LM,1)];
       Lreg = [Lreg; l_list.*l_list.*(l_list + 1).^2];
    end

    Nreg = diag(Nreg);
    Lreg = diag(Lreg);

    C = ((Z'*Z + Ll*Lreg + Ln*Nreg)^-1)*Z'*E;
```

```
%== Reshape the regularisation coefficient vectors for later use
C0 = C;
C = reshape(C, n_LM, Nmax);

%== SSE value (indicates the goodness of fit)
SSE_E = Z*C0;
SSE = sum((SSE_E-E).^2);

%== Calculate the Legendre polynomials for diffusion propagator reconstruction
K = [];
for L = 0:2:Lmax
    for m = -L:L
        Pnm = legendre(L,0);
        K = [K; Pnm(1)];
    end
end

%== Multiply the expansion coefficents by the Legendre polynomials
LPM = [];
for n = 1:Nmax
    LPM = [LPM, C(:,n).*K];
end
C = LPM;

%== Create the SH matrix for the BFOR reconstruction
H = construct_SH_basis (Lmax, V, 2, 'real');
```

```
% 'construct_SH_basis' was written by bjian
% It is a function from the 'High Angular Resolution Diffusion Imaging (HARDI) Tools' package,
% compiled by Canales-Rodríguez, Melie-García, Iturria-Medina and Alemán-Gómez
% This package is available from the MATLAB Central File Exchange.

%== Reconstruct the diffusion propagator
P = zeros(size(H,1),1);
parfor h = 1:size(H,1)
    for n = 1:Nmax
        for j = 1:n_LM

            l = l_list(j);

            part1 = ((-1)^(l*0.5));
            part2 = exp(-(Lambda(l+1,n)^2)*t);
            part3 = sqrt(SqrtLambda(l+1,n)*tau)
            part4 = besselj(l-0.5,SqrtLambda(l+1,n)*tau)*sphericalbesselj(l,2*pi*tau*p);
            part5 = 4*pi*pi*p*p-Lambda(l+1,n)*t;

            P(h) = P(h) + part1*C(j,n)*part2*H(h,j)*(part3*part4)/part5;

        end
    end
end

%== The diffusion propagator
P = 2*tau*sqrt(2*pi*pi*pi)*P;
```

```
                %== Negative probability values are non-physical
                for i = 1:size(P,1)
                    if P(i) < 0
                        P(i) = 0;
                    end
                end

                %== Normalise P
                norm_P = P./max(P);

                %== Local variables for visulisation
                Origin = [im_y*2 im_x*2 0];

                %== Plot the diffusion propagator
                plot_ODF(norm_P, V, F, Origin);

                % 'plot_ODF' was written by Pedro Valdez Hernandez
                % It is a function from the 'High Angular Resolution Diffusion Imaging (HARDI) Tools' package,
                % compiled by Canales-Rodríguez, Melie-García, Iturria-Medina and Alemán-Gómez
                % This package is available from the MATLAB Central File Exchange.
            end
        end
    end
end
```

```
%====== Complete visualisation
axis equal;
axis off;
view(0,90)

camlight left
camlight right
lighting phong
set(gcf,'color','w');

%== BFOR image reconstruction complete
toc
end


%== Function for calculating spherical Bessel functions
% (this code snippet should be saved in a separate function file)
function [J] = sphericalbesselj(l, x)
    J = sqrt(pi/(2*x))*besselj(0.5+l,x);
end
```

References

1. Pater J: **Wine Australia 2012-2013 annual report** Adelaide: Wine Australia Corporation; 2013.

2. Australian Bureau of Statistics: **Australian wine and grape industry, 2012-13** Canberra: Australian Government; 2013.

3. Department of Environment and Primary Industries: **Grape industry profile**. Melbourne: Department of Environment and Primary Industries; 2014.

4. Pratt C: **Reproductive anatomy in cultivated grapes - A review**. *Am J Enol Viticult* 1971, **22**:92-109.

5. Hardie WJ, O'Brien TP, Jaudzems VG: **Morphology, anatomy and development of the pericarp after anthesis in grape, *Vitis vinifera* L.** *Aust J Grape Wine R* 1996, **2**:97-142.

6. Patrick JW: **Phloem unloading: Sieve element unloading and post-sieve element transport**. *Annu Rev Plant Physiol* 1997, **48**:191-222.

7. Wang Z-P, Deloire A, Carbonneau A, Federspiel B, Lopez F: **An *in vivo* experimental system to study sugar phloem unloading in ripening grape berries during water deficiency stress**. *Ann Bot* 2003, **92**:523-528.

8. Zhang X-Y, Wang X-L, Wang X-F, Xia G-H, Pan Q-H, Fan R-C, Wu F-Q, Yu X-C, Zhang D-P: **A shift of phloem unloading from symplasmic to apoplasmic pathway is involved in developmental onset of ripening in grape berry**. *Plant Physiol* 2006, **142**:220-232.

9. Thomas T, Matthews M, Shackel K: **Direct *in situ* measurement of cell turgor in grape (*Vitis vinifera* L.) berries during development and in response to plant water deficits**. *Plant, Cell Environ* 2006, **29**:993-1001.

10. Husken D, Steudle E, Zimmermann U: **Pressure probe technique for measuring water relations of cells in higher plants**. *Plant Physiol* 1978, **61**:158-163.

11. Maurel C: **Aquaporins and water permeability of plant membranes**. *Annu Rev Plant Physiol* 1997, **48**:399-429.

12. Tyerman SD, Tilbrook J, Pardo C, Kotula L, Sullivan W, Steudle E: **Direct measurement of hydraulic properties in developing berries of *Vitis vinifera* L. cv Shiraz and Chardonnay**. *Aust J Grape Wine R* 2004, **10**:170-181.

13. Kriedemann PE: **Sugar uptake by the grape berry: A note on the absorption pathway**. *Planta* 1969, **85**:111-117.

14. Findlay N, Oliver KJ, Nil N, Coombe BG: **Solute accumulation by grape pericarp cells: IV. Perfusion of pericarp apoplast via the pedicel and evidence for xylem malfunction in ripening berries**. *J Exp Bot* 1987, **38**:668-679.

15. Levitt MH: **Spin dynamics: Basics of nuclear magnetic resonance**, 2nd edn. New York: Wiley; 2001.

16. Bloch F: **Nuclear induction**. *Phys Rev* 1946, **70**:460-474.

17. Kumar A, Welti D, Ernst RR: **NMR Fourier zeugmatography**. *J Magn Reson* 1975, **18**:69-83.

18. Van Der Weerd L, Claessens MMAE, Efdé C, Van As H: **Nuclear magnetic resonance imaging of membrane permeability changes in plants during osmotic stress**. *Plant, Cell Environ* 2002, **25**:1539-1549.

19. Van As H, Scheenen T, Vergeldt FJ: **MRI of intact plants**. *Photosynth Res* 2009, **102**:213-222.

20. Sibgatullin T, Vergeldt F, Gerkema E, Van As H: **Quantitative permeability imaging of plant tissues**. *Eur Biophys J* 2009, **39**:699-710.

21. Kuchenbrod E, Haase A, Benkert R, Schneider H, Zimmermann U: **Quantitative NMR microscopy on intact plants**. *Magn Reson Imaging* 1995, **13**:447-455.

22. Neeman M, Freyer JP, Sillerud LO: **A simple method for obtaining cross-term-free images for diffusion anisotropy studies in NMR microimaging**. *Magn Reson Med* 1991, **21**:138-143.

23. Trudeau JD, Dixon WT, Hawkins J: **The effect of inhomogeneous sample susceptibility on measured diffusion anisotropy using NMR imaging**. *J Magn Reson B* 1995, **108**:22-30.

24. Boujraf S, Luypaert R, Eisendrath H, Osteaux M: **Echo planar magnetic resonance imaging of anisotropic diffusion in asparagus stems**. *Magn Reson Mater Phys, Biol Med* 2001, **13**:82-90.

25. Lätt J, Nilsson M, Rydhög A, Wirestam R, Ståhlberg F, Brockstedt S: **Effects of restricted diffusion in a biological phantom: A *q*-space diffusion MRI study of asparagus stems at a 3T clinical scanner**. *Magn Reson Mater Phys, Biol Med* 2007, **20**:213-222.

26. Goodman B, Williamson B, Chudek J: **Identification of the distribution of sugars in grapes using chemical shift selective NMR microscopy**. *Magn Reson Imaging* 1993, **11**:1039-1041.

27. Glidewell SM, Williamson B, Goodman BA, Chudek JA, Hunter G: **An NMR microscopic study of grape (*Vitis vinifera* L.)**. *Protoplasma* 1997, **198**:27-35.

28. Rogiers SY, Hatfield JM, Jaudzems VG, White RG, Keller M: **Grape berry cv. Shiraz epicuticular wax and transpiration during ripening and preharvest weight loss**. *Am J Enol Viticult* 2004, **55**:121-127.

29. Ortega-Regules A, Ros-García JM, Bautista-Ortín AB, López-Roca JM, Gómez-Plaza E: **Differences in morphology and composition of skin and pulp cell walls from grapes (*Vitis vinifera* L.): technological implications**. *Eur Food Res Technol* 2008, **227**:223-231.

30. Casanova L, Casanova R, Moret A, Agustí M: **The application of gibberellic acid increases berry size of "Emperatriz" seedless grape**. *Span J Agric Res* 2009, **7**:919-927.

31. Coombe BG: **Research on development and ripening of the grape berry**. *Am J Enol Viticult* 1992, **43**:101-110.

32. Coombe BG: **Growth stages of the grapevine: Adoption of a system for identifying grapevine growth stages**. *Aust J Grape Wine R* 1995, **1**:104 -110.

33. Conde C, Silva P, Fontes N, Dias ACP, Tavares RM, Sousa MJ, Agasse A, Delrot S, Gerós H: **Biochemical changes throughout grape berry development and fruit and wine quality**. *Food* 2007, **1**:1-22.

34. Considine JA: **A statistical study of rain damage of grapes grown for drying in Victoria**. *Anim Prod Sci* 1973, **13**:604-611.

35. Gallander JF: **Effect of grape maturity on the composition and quality of Ohio Vidal Blanc wines**. *Am J Enol Viticult* 1983, **34**:139-141.

36. Flaherty DL: **Grape pest management** 2nd edn. California: ANR; 1992.

37. Bethe HA, Bacher RF: **Nuclear physics A. Stationary states of nuclei**. *Rev Mod Phys* 1936, **8**:82.

38. Neubert T, Mandea M, Hulot G, von Frese R, Primdahl F, Jørgensen JL, Friis-Christensen E, Stauning P, Olsen N, Risbo T: **Ørsted satellite captures high-precision geomagnetic field data**. *EOS Trans Am Geophys Union* 2001, **82**:81-88.

39. Bernstein MA, King KE, Zhou XJ, Fong W: **Handbook of MRI pulse sequences**. *Med Phys* 2005, **32**:1452.

40. Brateman L: **Chemical shift imaging: a review**. *Am J Roentgenol* 1986, **146**:971-980.

41. Hoult DI: **NMR imaging. Rotating frame selective pulses**. *J Magn Reson* 1980, **38**:369-374.

42. Gupta A, Stait-Gardner T, Ghadirian B, Price WS, Dada MO: **Fundamental concept for the theory, dynamics and applications of MRI**. In: *Theory, dynamics and applications of magnetic resonance imaging.* Edited by Awojoyogbe OB, vol. 1. New York: Science Publishing Group; 2014: 1-38.

43. Traficante DD: **Time averaging. Does the noise really average toward zero?** *Concept Magnetic Res* 1991, **3**:83-87.

44. McKeehan LW: **Combinations of circular currents for producing uniform magnetic field gradients**. *Rev Sci Instrum* 1936, **7**:178-179.

45. Price WS: **NMR studies of translational motion**. Cambridge: Cambridge University Press; 2009.

46. Hahn EL: **Spin Echoes**. *Phys Rev* 1950, **80**:580-594.

47. Twieg DB: **The *k*-trajectory formulation of the NMR imaging process with applications in analysis and synthesis of imaging methods**. *Med Phys* 1983, **10**:610-621.

48. Bochner S, Chandrasekharan K: **Fourier transforms**. New Jersey: Princeton University Press; 1949.

49. Fourier J-BJ: **The analytical theory of heat**. Cambridge: Cambridge University Press; 1878.

50. Bracewell RN: **The Fourier transform and its applications**. New Delhi: Tata McGraw-Hill; 2003.

51. Doyle FH, Pennock JM, Banks LM, McDonnell MJ, Bydder GM, Steiner RE, Young IR, Clarke GJ, Pasmore T, Gilderdale DJ: **Nuclear magnetic resonance imaging of the liver: initial experience**. *Am J Roentgenol* 1982, **138**:193-200.

52. McRobbie DW, Moore EA, Graves MJ, Prince MR: **MRI from picture to proton**. Cambridge: Cambridge University Press; 2006.

53. Bloembergen N, Purcell EM, Pound RV: **Relaxation effects in nuclear magnetic resonance absorption**. *Phys Rev* 1948, **73**:679-712.

54. Meiboom S, Gill D: **Modified spin-echo method for measuring nuclear relaxation times**. *Rev Sci Instrum* 1958, **29**:688-691.

55. Carr HY, Purcell EM: **Effects of diffusion on free precession in nuclear magnetic resonance experiments**. *Phys Rev* 1954, **94**:630-638.

56. Pykett IL, Mansfield P: **A line scan image study of a tumorous rat leg by NMR**. *Phys Med Biol* 1978, **23**:961.

57. Lauterbur P, Mendonca-Dias M, Rudin A: **Augmentation of tissue water proton spin-lattice relaxation rates by *in vivo* addition of paramagnetic ions**. *Frontiers of biological energetics* 1978, **1**:752-759.

58. Merbach A, Helm L, Tóth É: **The chemistry of contrast agents in medical magnetic resonance imaging**. Chichester: John Wiley & Sons, Ltd; 2013.

59. Mendonça-Dias MH, Gaggelli E, Lauterbur PC: **Paramagnetic contrast agents in nuclear magnetic resonance medical imaging**. *Semin Nucl Med* 1983, **13**:364-376.

60. Watts LT, Shen Q, Deng S, Chemello J, Duong TQ: **Manganese-enhanced magnetic resonance imaging of traumatic brain injury**. *J Neurotrauma* 2014, **32**:1-10.

61. Bouilleret V, Cardamone L, Liu YR, Fang K, Myers DE, O'Brien TJ: **Progressive brain changes on serial manganese-enhanced MRI following traumatic brain injury in the rat**. *J Neurotrauma* 2009, **26**:1999-2013.

62. Yu X, Wadghiri YZ, Sanes DH, Turnbull DH: ***In vivo* auditory brain mapping in mice with Mn-enhanced MRI**. *Nat Neurosci* 2005, **8**:961-968.

63. Lee J-W, Park J-A, Lee J-J, Bae S-J, Lee S-H, Jung J-C, Kim M-N, Lee J, Woo S, Chang Y: **Manganese-enhanced auditory tract-tracing MRI with cochlear injection**. *Magn Reson Imaging* 2007, **25**:652-656.

64. Carr DH, Brown J, Bydder GM, Steiner RE, Weinmann HJ, Speck U, Hall AS, Young IR: **Gadolinium-DTPA as a contrast agent in MRI: initial clinical experience in 20 patients**. *Am J Roentgenol* 1984, **143**:215-224.

65. Kim KS, Park W, Hu J, Bae YH, Na K: **A cancer-recognizable MRI contrast agents using pH-responsive polymeric micelle**. *Biomaterials* 2014, **35**:337-343.

66. Fick A: **On liquid diffusion**. *Lond Edinb Dubl Phil Mag* 1855, **10**:30-39.

67. Crank J: **The mathematics of diffusion**. Oxford: Oxford University Press; 1979.

68. Northrop JH: **The kinetics of osmosis**. *J Gen Physiol* 1927, **10**:883-892.

69. Lauffer MA: **Motion in biological systems**. New York: Alan R. Liss, Inc.; 1989.

70. Truskey GA, Yuan F, Katz DF: **Transport phenomena in biological systems**. New York: Prentice Hall; 2003.

71. Balcom BJ, Fischer AE, Carpenter TA, Hall LD: **Diffusion in aqueous gels. Mutual diffusion coefficients measured by one-dimensional nuclear magnetic resonance imaging**. *J Am Chem Soc* 1993, **115**:3300-3305.

72. Heink W, Kärger J, Pfeifer H: **Application of zeugmatography to study kinetics of physical adsorption**. *Chem Eng Sci* 1978, **33**:1019-1023.

73. Matsunaga N, Hori M, Nagashima A: **Measurement of mutual diffusion coefficients of gases by the Taylor method: Measurements on H_2–Air, H_2–N_2, and H_2–O_2 systems**. *Heat Transfer Asian Res* 2002, **31**:182-193.

74. Ribeiro ACF, Ortona O, Simões SMN, Santos CIAV, Prazeres PMRA, Valente AJM, Lobo VMM, Burrows HD: **Binary mutual diffusion coefficients of aqueous solutions of sucrose, lactose, glucose, and fructose in the temperature range from (298.15 to 328.15) K**. *J Chem Eng Data* 2006, **51**:1836-1840.

75. Lehner FK: **On the validity of Fick's law for transient diffusion through a porous medium**. *Chem Eng Sci* 1979, **34**:821-825.

76. Brown R: **XXVII. A brief account of microscopical observations made in the months of June, July and August 1827, on the particles contained in the pollen of plants; and on the general existence of active molecules in organic and inorganic bodies**. *Phil Mag Series 2* 1828, **4**:161-173.

77. Einstein A: **Investigations on the theory of the Brownian movement**. New York: Dover Publications; 1956.

78. Kärger J, Heink W: **The propagator representation of molecular transport in microporous crystallites**. *J Magn Reson* 1983, **51**:1-7.

79. Callaghan P: **Principles of nuclear magnetic resonance microscopy**. Oxford: Oxford University Press; 1993.

80. Van Kampen NG: **Stochastic processes in physics and chemistry**, 3rd edn. Amsterdam: Elsevier; 2007.

81. Dill K, Bromberg S: **Molecular driving forces: Statistical thermodynamics in biology, chemistry, physics, and nanoscience**. New York: Garland Science; 2003.

82. Mills R: **Self-diffusion in normal and heavy water in the range 1-45°**. *J Phys Chem* 1973, **77**:685-688.

83. Mahawanich T, Schmidt SJ: **Molecular mobility and the perceived sweetness of sucrose, fructose, and glucose solutions**. *Food Chem* 2004, **84**:169-179.

84. Lenk R: **Fluctuations, diffusion and spin relaxation**. Amsterdam: Elsevier; 1986.

85. Jeffrey A, Zwillinger D: **Table of integrals, series, and products**. USA: Academic Press; 2007.

86. Moseley ME, Cohen Y, Kucharczyk J, Mintorovitch J, Asgari HS, Wendland MF, Tsuruda J, Norman D: **Diffusion-weighted MR imaging of anisotropic water diffusion in cat central nervous system**. *Radiology* 1990, **176**:439-445.

87. Cleveland GG, Chang DC, Hazlewood CF, Rorschach HE: **Nuclear magnetic resonance measurement of skeletal muscle: Anisotropy of the diffusion coefficient of the intracellular water**. *Biophys J* 1976, **16**:1043-1053.

88. Family F, Landau DP: **Kinetics of aggregation and gelation**. New York: Elsevier; 1984.

89. Kimmich R, Klammler F, Skirda VD, Serebrennikova IA, Maklakov AI, Fatkullin N: **Geometrical restrictions of water diffusion in aqueous protein**

systems. A study using NMR field-gradient techniques. *Appl Magn Reson* 1993, **4**:425-440.

90. Stejskal EO: **Spin-echo measurement of self-diffusion in colloidal systems**. *Adv Mol Relax Pr* 1972, **3**:27-42.

91. Woessner DE: **N.M.R. spin-echo self-diffusion measurements on fluids undergoing restricted diffusion**. *J Phys Chem* 1963, **67**:1365-1367.

92. Hajnal JV, Doran M, Hall AS, Collins AG, Oatridge A, Pennock JM, Bydder GM: **MR imaging of anisotropically restricted diffusion of water in the nervous system: technical, anatomic, and pathologic considerations**. *J Comput Assisted Tomogr* 1991, **15**:1-18.

93. Douek P, Turner R, Pekar J, Patronas N, Le Bihan D: **MR color mapping of myelin fiber orientation**. *J Comput Assisted Tomogr* 1991, **15**:923-929.

94. Chenevert TL, Brunberg JA, Pipe JG: **Anisotropic diffusion in human white matter: demonstration with MR techniques *in vivo***. *Radiology* 1990, **177**:401-405.

95. Stejskal EO, Tanner JE: **Spin diffusion measurements: Spin echoes in the presence of a time-dependent field gradient**. *J Chem Phys* 1965, **42**:288-292.

96. Stejskal EO: **Use of spin echoes in a pulsed magnetic-field gradient to study anisotropic, restricted diffusion and flow**. *J Chem Phys* 1965, **43**:3597-3603.

97. Codd SL, Callaghan PT: **Spin echo analysis of restricted diffusion under generalized gradient waveforms: planar, cylindrical, and spherical pores with wall relaxivity**. *J Magn Reson* 1999, **137**:358-372.

98. Tanner JE: **Use of the stimulated echo in NMR diffusion studies**. *J Chem Phys* 1970, **52**:2523-2526.

99. Altieri AS, Hinton DP, Byrd RA: **Association of biomolecular systems via pulsed field gradient NMR self-diffusion measurements**. *J Am Chem Soc* 1995, **117**:7566-7567.

100. Callaghan PT: **Susceptibility-limited resolution in nuclear magnetic resonance microscopy**. *J Magn Reson* 1990, **87**:304-318.

101. Wedeen VJ, Hagmann P, Tseng WYI, Reese TG, Weisskoff RM: **Mapping complex tissue architecture with diffusion spectrum magnetic resonance imaging**. *Magn Reson Med* 2005, **54**:1377-1386.

102. Tuch DS, Reese TG, Wiegell MR, Makris N, Belliveau JW, Wedeen VJ: **High angular resolution diffusion imaging reveals intravoxel white matter fiber heterogeneity**. *Magn Reson Med* 2002, **48**:577-582.

103. Aganj I, Lenglet C, Sapiro G, Yacoub E, Ugurbil K, Harel N: **Reconstruction of the orientation distribution function in single- and multiple-shell *q*-ball imaging within constant solid angle**. *Magn Reson Med* 2010, **64**:554-566.

104. Kingsley PB: **Introduction to diffusion tensor imaging mathematics: Part II. Anisotropy, diffusion-weighting factors, and gradient encoding schemes**. *Concept Magn Reson A* 2006, **28A**:123-154.

105. Cornish EA, Fisher RA: **Moments and cumulants in the specification of distributions**. *Rev Inst Int Stat* 1938, **5**:307-320.

106. Kurtz AK, Edgerton HA: **Statistical dictionary of terms and symbols**. New York: J. Wiley & Sons; 1939.

107. Pearson K: **"Das Fehlergesetz und Seine Verallgemeinerungen Durch Fechner und Pearson." A Rejoinder**. *Biometrika* 1905, **4**:169-212.

108. Minati L, Bruzzone MG, Grisoli G, Maccagnano C, Rampoldi S, Banasik T, Mandelli ML, Farina L: **Preliminary findings with diffusional kurtosis imaging (DKI) of brain tumours**. In: *23rd Meeting of the European Society for Magnetic Resonance in Medicine and Biology: 2006; Warsaw*.

109. Torrey HC: **Bloch Equations with Diffusion Terms**. *Phys Rev* 1956, **104**:563-565.

110. Motulsky HJ, Ransnas LA: **Fitting curves to data using nonlinear regression: a practical and nonmathematical review**. *FASEB J* 1987, **1**:365-374.

111. Le Bihan D: **Molecular diffusion, tissue microdynamics and microstructure**. *NMR Biomed* 1995, **8**:375-386.

112. Tanner JE, Stejskal EO: **Restricted self-diffusion of protons in colloidal systems by the pulsed-gradient, spin-echo method**. *J Chem Phys* 1968, **49**:1768-1777.

113. Le Bihan D, Mangin J, Poupon C, Clark C, Pappata S, Molko N, Chabriat H: **Diffusion tensor imaging: concepts and applications**. *J Magn Reson Imaging* 2001, **13**:534-546.

114. Basser PJ, Mattiello J, LeBihan D: **Estimation of the effective self-diffusion tensor from the NMR spin echo**. *J Magn Reson B* 1994, **103**:247-254.

115. Synge JL: **Tensor calculus**, vol. 5. New York: Dover Publications; 1978.

116. Jeevanjee N: **An introduction to tensors and group theory for physicists**. New York: Springer Science & Business Media; 2015.

117. Basser PJ, Mattiello J, LeBihan D: **MR diffusion tensor spectroscopy and imaging**. *Biophys J* 1994, **66**:259-267.

118. Özcan A: **(Mathematical) Necessary conditions for the selection of gradient vectors in DTI**. *J Magn Reson* 2005, **172**:238-241.

119. Frank LR: **Anisotropy in high angular resolution diffusion-weighted MRI**. *Magn Reson Med* 2001, **45**:935-939.

120. Riley KF, Hobson MP, Bence SJ: **Mathematical methods for physics and engineering: A comprehensive guide**. New York: Cambridge University Press; 2006.

121. Van Doom A, Bovendeerd PHM, Nicolay K, Drost MR, Janssen JD: **Determination of muscle fibre orientation using diffusion-weighted MRI**. *Eur J Morphol* 1996, **34**:5-10.

122. Pajevic S, Pierpaoli C: **Color schemes to represent the orientation of anisotropic tissues from diffusion tensor data: application to white matter fiber tract mapping in the human brain**. *Magn Reson Med* 1999, **42**:526-540.

123. Basser PJ: **New histological and physiological stains derived from diffusion-tensor MR images**. *Ann N Y Acad Sci* 1997, **820**:123-138.

124. Baird AE, Warach S: **Magnetic resonance imaging of acute stroke**. *J Cerebr Blood F Met* 1998, **18**:583-609.

125. Moseley ME, Cohen Y, Mintorovitch J, Chileuitt L, Shimizu H, Kucharczyk J, Wendland MF, Weinstein PR: **Early detection of regional cerebral ischemia in cats: Comparison of diffusion and T_2-weighted MRI and spectroscopy**. *Magn Reson Med* 1990, **14**:330-346.

126. Papadakis NG, Xing D, Houston GC, Smith JM, Smith MI, James MF, Parsons AA, Huang CLH, Hall LD, Carpenter TA: **A study of rotationally invariant and symmetric indices of diffusion anisotropy**. *Magn Reson Imaging* 1999, **17**:881-892.

127. Hasan KM, Alexander AL, Narayana PA: **Does fractional anisotropy have better noise immunity characteristics than relative anisotropy in diffusion tensor MRI? An analytical approach**. *Magn Reson Med* 2004, **51**:413-417.

128. Basser PJ, Pierpaoli C: **Microstructural and physiological features of tissues elucidated by quantitative-diffusion-tensor MRI**. *J Magn Reson B* 1996, **111**:209-219.

129. Lo C, Shifteh K, Gold T, Bello JA, Lipton ML: **Diffusion tensor imaging abnormalities in patients with mild traumatic brain injury and neurocognitive impairment**. *J Comput Assisted Tomogr* 2009, **33**:293-297.

130. Huisman TAGM, Schwamm LH, Schaefer PW, Koroshetz WJ, Shetty-Alva N, Ozsunar Y, Wu O, Sorensen AG: **Diffusion tensor imaging as potential biomarker of white matter injury in diffuse axonal injury**. *Am J Neuroradiol* 2004, **25**:370-376.

131. Mansfield P: **Multi-planar image formation using NMR spin echoes**. *J Phys C* 1977, **10**:L55.

132. Zaraiskaya T, Kumbhare D, Noseworthy MD: **Diffusion tensor imaging in evaluation of human skeletal muscle injury**. *J Magn Reson Imaging* 2006, **24**:402-408.

133. Gulani V, Iwamoto GA, Jiang H, Shimony JS, Webb AG, Lauterbur PC: **A multiple echo pulse sequence for diffusion tensor imaging and its application in excised rat spinal cords**. *Magn Reson Med* 1997, **38**:868-873.

134. Ellingson B, Schmit B, Ulmer J, Kurpad S: **Diffusion tensor magnetic resonance imaging in spinal cord injury**. *Concept Magn Reson A* 2008, **32A**:219-237.

135. Mori S, Van Zijl PCM: **Diffusion weighting by the trace of the diffusion tensor within a single scan**. *Magn Reson Med* 1995, **33**:41-52.

136. Lu S, Ahn D, Johnson G, Cha S: **Peritumoral diffusion tensor imaging of high-grade gliomas and metastatic brain tumors**. *Am J Neuroradiol* 2003, **24**:937-941.

137. Özarslan E, Shepherd TM, Vemuri BC, Blackband SJ, Mareci TH: **Resolution of complex tissue microarchitecture using the diffusion orientation transform (DOT)**. *NeuroImage* 2006, **31**:1086-1103.

138. Descoteaux M, Deriche R, Bihan D, Mangin J-F, Poupon C: **Diffusion propagator imaging: Using Laplace's equation and multiple shell acquisitions to reconstruct the diffusion propagator**. In: *Information processing in medical imaging.* Edited by Prince JL, Pham DL, Myers KJ, vol. 5636. Berlin: Springer; 2009: 1-13.

139. Assemlal H-E, Tschumperlé D, Brun L: **Efficient computation of PDF-based characteristics from diffusion MR signal**. In: *Medical image computing and computer-assisted intervention – MICCAI 2008.* Edited by Metaxas D, Axel L, Fichtinger G, Székely G, vol. 5242. Berlin: Springer; 2008: 70-78.

140. Hosseinbor AP, Chung MK, Wu Y-C, Alexander AL: **Bessel Fourier orientation reconstruction (BFOR): An analytical diffusion propagator reconstruction for hybrid diffusion imaging and computation of *q*-space indices**. *NeuroImage* 2013, **64**:650-670.

141. Hosseinbor AP, Chung MK, Wu Y-C, Alexander AL: **Bessel Fourier orientation reconstruction: An analytical EAP reconstruction using multiple shell acquisitions in diffusion MRI**. In: *Medical image computing and computer-assisted intervention – MICCAI 2011*. Edited by Fichtinger G, Martel A, Peters T, vol. 6892. Berlin: Springer; 2011: 217-225.

142. Dautray R, Lions J-L: **Mathematical analysis and numerical methods for science and technology**, vol. 5. Heidelberg: Springer Science & Business Media; 2000.

143. Chung MK, Dalton KM, Li S, Evans AC, Davidson RJ: **Weighted Fourier series representation and its application to quantifying the amount of gray matter**. *IEEE Trans Med Imaging* 2007, **26**:566-581.

144. Andrews GE, Askey R, Roy R: **Special functions**. Cambridge: Cambridge University Press; 2001.

145. Atkinson K, Han W: **Spherical harmonics and approximations on the unit sphere: an introduction**. Berlin: Springer; 2012.

146. Tenenbaum M, Pollard H: **Ordinary differential equations: an elementary textbook for students of mathematics, engineering, and the sciences**. New York: Dover Publications; 1985.

147. Abramowitz M, Stegun IA: **Handbook of mathematical functions**. New York: Dover; 1972.

148. Descoteaux M, Angelino E, Fitzgibbons S, Deriche R: **Apparent diffusion coefficients from high angular resolution diffusion imaging: Estimation and applications**. *Magn Reson Med* 2006, **56**:395-410.

149. Descoteaux M, Deriche R, Le Bihan D, Mangin J-F, Poupon C: **Multiple *q*-shell diffusion propagator imaging**. *Med Image Anal* 2011, **15**:603-621.

150. Hansen PC: **The *L*-curve and its use in the numerical treatment of inverse problems**. In: *Computational inverse problems in electrocardiology*. Edited by Johnston P. Southampton: WIT Press; 2001.

151. Tuch DS: **Q-ball imaging**. *Magn Reson Med* 2004, **52**:1358-1372.

152. Haase A, Frahm J, Matthaei D, Hanicke W, Merboldt KD: **FLASH imaging. Rapid NMR imaging using low flip-angle pulses**. *J Magn Reson* 1986, **67**:258-266.

153. Duyn JH: **High-speed interlaced spin-echo magnetic resonance imaging**. *Magn Reson Med* 2000, **43**:905-908.

154. Hennig J, Nauerth A, Friedburg H: **RARE imaging: A fast imaging method for clinical MR**. *Magn Reson Med* 1986, **3**:823-833.

155. Rossi C, Capuani S, Fasano F, Alesiani M, Maraviglia B: **DTI of trabecular bone marrow**. *Magn Reson Imaging* 2005, **23**:245-248.

156. Gruwel MLH, Latta P, Sboto-Frankenstein U, Gervai P: **Visualization of water transport pathways in plants using diffusion tensor imaging**. *Prog Electromagn Res C* 2013, **35**:73-82.

157. Sigmund EE, Song Y-Q: **Multiple echo diffusion tensor acquisition technique**. *Magn Reson Imaging* 2006, **24**:7-18.

158. Tang Y, Nyengaard JR, Pakkenberg B, Gundersen HJG: **Age-induced white matter changes in the human brain: A stereological investigation**. *Neurobiol Aging* 1997, **18**:609-615.

159. Hildebrand C: **Ultrastructural and light-microscopic studies of the nodal region in large myelinated fibres of the adult feline spinal cord white matter**. *Acta Physiol Scand* 1971, **82**:43-79.

160. Jones DK, Knösche TR, Turner R: **White matter integrity, fiber count, and other fallacies: The do's and don'ts of diffusion MRI**. *NeuroImage* 2013, **73**:239-254.

161. Clark CA, Le Bihan D: **Water diffusion compartmentation and anisotropy at high *b* values in the human brain**. *Magn Reson Med* 2000, **44**:852-859.

162. Grebenkov DS: **NMR survey of reflected Brownian motion**. *Rev Mod Phys* 2007, **79**:1077-1137.

163. Brownstein KR, Tarr CE: **Importance of classical diffusion in NMR studies of water in biological cells**. *Phys Rev A* 1979, **19**:2446-2453.

164. Callaghan PT: **Pulsed-gradient spin-echo NMR for planar, cylindrical, and spherical pores under conditions of wall relaxation**. *J Magn Reson A* 1995, **113**:53-59.

165. Söderman O, Jönsson B: **Restricted diffusion in cylindrical geometry**. *J Magn Reson A* 1995, **117**:94-97.

166. Gudbjartsson H, Patz S: **The Rician distribution of noisy MRI data**. *Magn Reson Med* 1995, **34**:910-914.

167. Rice SO: **Mathematical analysis of random noise**. *Bell Syst Tech J* 1944, **23**:282-332.

168. Descoteaux M, Angelino E, Fitzgibbons S, Deriche R: **Regularized, fast, and robust analytical *q*-ball imaging**. *Magn Reson Med* 2007, **58**:497-510.

169. Hodgson RW: **Horticultural varieties of citrus**. California: Division of Agricultural Sciences; 1967.

170. Dyer JM, Stymne S, Green AG, Carlsson AS: **High-value oils from plants**. *Plant J* 2008, **54**:640-655.

171. Rangel B, Platt KA, Thomson WW: **Ultrastructural aspects of the cytoplasmic origin and accumulation of oil in olive fruit (*Olea europaea*)**. *Physiol Plant* 1997, **101**:109-114.

172. King JR: **Morphological development of the fruit of the olive**. *Hilgardia* 1938, **11**:437-458.

173. Rapoport HF, Manrique T, Gucci R: **Cell division and expansion in the olive fruit**. *Acta Hort* 2004, **636**:461-465.

174. Tukey JW: **The problem of multiple comparisons**. In: *The Collected Works of John W Tukey*. Edited by Braun HL, vol. 3. USA: Chapman & Hall; 1994.

175. Kramer CY: **Extension of multiple range tests to group means with unequal numbers of replications**. *Biometrics* 1956, **12**:307-310.

176. Pope J, Jonas D, Walker R: **Applications of NMR micro-imaging to the study of water, lipid, and carbohydrate distribution in grape berries**. *Protoplasma* 1993, **173**:177-186.

177. Harris JM, Kriedemann PE, Possingham JV: **Anatomical aspects of grape berry development**. *Vitis* 1968, **7**:106-119.

178. Edzes HT, van Dusschoten D, Van As H: **Quantitative T_2 imaging of plant tissues by means of multi-echo MRI microscopy**. *Magn Reson Imaging* 1998, **16**:185-196.

179. Tilbrook J, Tyerman S: **Cell death in grape berries: varietal differences linked to xylem pressure and berry weight loss**. *Funct Plant Biol* 2008, **35**:173.

180. Krasnow M, Matthews M, Shackel K: **Evidence for substantial maintenance of membrane integrity and cell viability in normally developing grape (*Vitis vinifera* L.) berries throughout development**. *J Exp Bot* 2008, **59**:849-859.

181. Hortelano S, García-Martín ML, Cerdan S, Castrillo A, Alvarez A, Bosca L: **Intracellular water motion decreases in apoptotic macrophages after caspase activation**. *Cell Death Differ* 2001, **8**:1022-1028.

182. Coombe BG: **The development of fleshy fruits**. *Annu Rev Plant Physiol* 1976, **27**:207-228.

183. Neuhaus HE: **Transport of primary metabolites across the plant vacuolar membrane**. *FEBS Lett* 2007, **581**:2223-2226.

184. Cadot Y, Miñana-Castelló MT, Chevalier M: **Anatomical, histological, and histochemical changes in grape seeds from *Vitis vinifera* L. cv. Cabernet Franc during fruit development**. *J Agric Food Chem* 2006, **54**:9206-9215.

185. Mullins M, Bouquet A, Williams L: **Biology of the grapevine**. Cambridge: Cambridge University Press; 1992.

186. Ebadi A, Sedgley M, May P, Coombe BG: **Seed development and abortion in *Vitis vinifera* L., cv. Chardonnay**. *Int J Plant Sci* 1996, **157**:703-712.

187. Hammami SB, Rapoport HF: **Quantitative analysis of cell organization in the external region of the olive fruit**. *Int J Plant Sci* 2012, **173**:993-1004.

188. Srichamnong W, Price WS, Stait-Gardner T, Dean RJ, Plougonven E, Léonard A, Srzednicki G: **Studies of microstructure of kernels of macadamia integrifolia and its hybrids through MRI, x-ray tomography and confocal microscopy**. *J Food Sci Eng* 2013, **3**:503-516.

189. Lang A, Thorpe M: **Why do grape berries split?** In: *Second International Cool Climate Viticulture and Oenology Symposium Auckland, New Zealand: 1988*.

190. Nair NG, Emmett RW, Parker FE: **Some factors predisposing grape berries to infection by *Botrytis cinerea***. *New Zeal J Exp Agr* 1988, **16**:257-263.

191. Lang A, Düring H: **Grape berry splitting and some mechanical properties of the skin**. *Vitis* 1990, **29**:61-70.

192. Considine J, Kriedemann P: **Fruit splitting in grapes: determination of the critical turgor pressure**. *Aust J Agric Res* 1972, **23**:17-24.

193. Brown K, Considine J: **Physical aspects of fruit growth: stress distribution around lenticels**. *Plant Physiol* 1982, **69**:585-590.

194. Considine J, Brown K: **Physical aspects of fruit growth: theoretical analysis of distribution of surface growth forces in fruit in relation to cracking and spliting**. *Plant Physiol* 1981, **68**:371-376.

195. Becker T, Knoche M: **Deposition, strain, and microcracking of the cuticle in developing 'Riesling' grape berries**. *Vitis* 2012, **51**:1-6.

196. Clarke SJ, Hardie WJ, Rogiers SY: **Changes in susceptibility of grape berries to splitting are related to impaired osmotic water uptake associated with losses in cell vitality**. *Aust J Grape Wine R* 2010, **16**:469-476.

197. Bernstein Z, Lustig I: **Hydrostatic methods of measurement of firmness and turgor pressure of grape berries (*Vitis vinifera* L.)**. *Sci Hort* 1985, **25**:129-136.

198. Lustig I, Bernstein Z: **Determination of the mechanical properties of the grape berry skin by hydraulic measurements**. *Sci Hort* 1985, **25**:279-285.

199. Becker T, Knoche M: **Water induces microcracks in the grape berry cuticle**. *Vitis* 2012, **51**:141-142.

200. Majno G, Joris I: **Apoptosis, oncosis, and necrosis. An overview of cell death**. *Am J Pathol* 1995, **146**:3-15.

201. Becker T, Grimm E, Knoche M: **Substantial water uptake into detached grape berries occurs through the stem surface**. *Aust J Grape Wine R* 2012, **18**:109-114.

202. Becker T, Knoche M: **Water movement through the surfaces of the grape berry and its stem**. *Am J Enol Viticult* 2011, **62**:340-350.

203. Cacho J, Castells JE, Esteban A, Laguna B, Sagristá N: **Iron, copper, and manganese influence on wine oxidation**. *Am J Enol Viticult* 1995, **46**:380-384.

204. Pohl P: **What do metals tell us about wine?** *TrAC, Trends Anal Chem* 2007, **26**:941-949.

205. Mckinnon AJ, Cattrall RW, Scollary GR: **Aluminum in wine - Its measurement and identification of major sources**. *Am J Enol Viticult* 1992, **43**:166-170.

206. Rogiers SY, Greer D, Hatfield J, Orchard B, Keller M: **Mineral sinks within ripening grape berries (*Vitis vinifera* L.)**. *Vitis* 2006, **45**:115.

207. Jackson RS: **Wine science: Principles, practice, perception** 2nd edn. USA: Academic Press; 2000.

208. Patrick J, Zhang W, Tyerman S, Offler C, Walker N: **Role of membrane transport in phloem translocation of assimilates and water**. *Aust J Plant Physiol* 2001, **28**:697-710.

209. de Boer AH, Volkov V: **Logistics of water and salt transport through the plant: structure and functioning of the xylem**. *Plant, Cell Environ* 2003, **26**:87-101.

210. Zhang H-P, Wu J-Y, Tao S-T, Wu T, Qi K-J, Zhang S-J, Wang J-Z, Huang W-J, Wu J, Zhang S-L: **Evidence for apoplasmic phloem unloading in pear fruit**. *Plant Mol Biol Rep* 2014, **32**:931-939.

211. Gould N, Morrison DR, Clearwater MJ, Ong S, Boldingh HL, Minchin PEH: **Elucidating the sugar import pathway into developing kiwifruit berries (Actinidia deliciosa)**. *N Z J Crop Hortic Sci* 2013, **41**:189-206.

212. Almeida DPF, Huber DJ: **Apoplastic pH and inorganic ion levels in tomato fruit: A potential means for regulation of cell wall metabolism during ripening**. *Physiol Plant* 1999, **105**:506-512.

213. Kessissoglou DP: **Manganese-proteins and enzymes and relevant trinuclear synthetic complexes**. In: *Bioinorganic chemistry: An inorganic perspective of life.* Edited by Kessissoglou DP. Greece: Springer; 1995: 299-320.

214. Tarbouriech N, Charnock SJ, Davies GJ: **Three-dimensional structures of the Mn and Mg dTDP complexes of the family GT-2 glycosyltransferase SpsA: a comparison with related NDP-sugar glycosyltransferases1**. *J Mol Biol* 2001, **314**:655-661.

215. Slunjski S, Coga L, Custic MH, Petek M, Spoljar A: **Phosphorus, manganese and iron ratios in grapevine (*Vitis vinifera* L.) leaves on acid and calcareous soils**. *Acta Hort* 2012.

216. Hirschi KD, Korenkov VD, Wilganowski NL, Wagner GJ: **Expression of *Arabidopsis* CAX2 in tobacco. Altered metal accumulation and increased manganese tolerance**. *Plant Physiol* 2000, **124**:125-134.

217. Mills RF, Doherty ML, López-Marqués RL, Weimar T, Dupree P, Palmgren MG, Pittman JK, Williams LE: **ECA3, a Golgi-localized P2A-type ATPase, plays a crucial role in manganese nutrition in *Arabidopsis***. *Plant Physiol* 2008, **146**:116-128.

218. Shigaki T, Pittman JK, Hirschi KD: **Manganese specificity determinants in the *Arabidopsis* metal/H+ antiporter CAX2**. *J Biol Chem* 2003, **278**:6610-6617.

219. Simon EW: **The symptoms of calcium defficiency in plants**. *New Phytol* 1978, **80**:1-15.

220. Sekse L: **Fruit cracking mechanisms in sweet cherries (*Prunus avium* L.) - a review**. *Acta Hort* 1998, **468**:637-648.

221. Aoki I, Wu Y-JL, Silva AC, Lynch RM, Koretsky AP: ***In vivo* detection of neuroarchitecture in the rodent brain using manganese-enhanced MRI**. *NeuroImage* 2004, **22**:1046-1059.

222. Buckley DL, Parker GJM: **Measuring contrast agent concentration in T_1-weighted dynamic contrast-enhanced MRI**. In: *Dynamic contrast-enhanced magnetic resonance imaging in oncology.* Edited by Jackson A, Buckley DL, Parker GJM. Berlin: Springer; 2005: 69-79.

223. Bondada BR, Matthews MA, Shackel KA: **Functional xylem in the post-veraison grape berry**. *J Exp Bot* 2005, **56**:2949-2957.

224. Keller M, Smith JP, Bondada BR: **Ripening grape berries remain hydraulically connected to the shoot**. *J Exp Bot* 2006, **57**:2577-2587.

225. Rogiers SY, Smith JA, White R, Keller M, Holzapfel BP, Virgona JM: **Vascular function in berries of *Vitis vinifera* (L) cv. Shiraz**. *Aust J Grape Wine R* 2001, **7**:47-51.

226. Özarslan E, Mareci TH: **Generalized diffusion tensor imaging and analytical relationships between diffusion tensor imaging and high angular resolution diffusion imaging**. *Magn Reson Med* 2003, **50**:955-965.

227. Qi L, Wang Y, Wu EX: ***D*-eigenvalues of diffusion kurtosis tensors**. *J Comput Appl Math* 2008, **221**:150-157.

228. Yang Y, Yang Q: **Further results for Perron-Frobenius theorum for nonnegative tensors**. *SIAM J Matrix Anal Appl* 2010, **31**:2517-2530.

229. Liu C, Bammer R, Acar B, Moseley ME: **Characterizing non-Gaussian diffusion by using generalized diffusion tensors**. *Magn Reson Med* 2004, **51**:924-937.

230. Liu C, Bammer R, Moseley ME: **Generalized diffusion tensor imaging (GDTI): A method for characterizing and imaging diffusion anisotropy caused by non-Gaussian diffusion**. *Isr J Chem* 2003, **43**:145-154.

231. Le Bihan D, Poupon C, Amadon A, Lethimonnier F: **Artifacts and pitfalls in diffusion MRI**. *J Magn Reson Imaging* 2006, **24**:478-488.

232. Blinnikov S, Moessner R: **Expansions for nearly Gaussian distributions**. *Astron Astrophys Sup* 1998, **130**:193-205.

233. Zucker UH, Schulz H: **Statistical approaches for the treatment of anharmonic motion in crystals. I. A comparison of the most frequently used formalisms of anharmonic thermal vibrations**. *Acta Crystallogr A* 1982, **38**:563-568.

234. Niendorf T, Dijkhuizen RM, Norris DG, van Lookeren Campagne M, Nicolay K: **Biexponential diffusion attenuation in various states of brain tissue: Implications for diffusion weighted imaging**. *Magn Reson Med* 1996, **36**:847-857.

235. Assaf Y, Cohen Y: **Detection of different water populations in brain tissue using ^{2}H single- and double-quantum-filtered diffusion NMR spectroscopy**. *J Magn Reson B* 1996, **112**:151-159.

236. Bourne RM, Kurniawan N, Cowin G, Stait-Gardner T, Sved P, Watson G, Price WS: **Microscopic diffusivity compartmentation in formalin-fixed prostate tissue: Preliminary findings**. *Magn Reson Med* 2012, **68**:614-620.

237. Bennett KM, Schmainda KM, Bennett R, Rowe DB, Lu H, Hyde JS: **Characterization of continuously distributed cortical water diffusion rates with a stretched-exponential model**. *Magn Reson Med* 2003, **50**:727-734.

238. Köpf M, Corinth C, Haferkamp O, Nonnenmacher TF: **Anomalous diffusion of water in biological tissues**. *Biophys J* 1996, **70**:2950-2958.

239. Mandelbrot BB: **The fractal geometry of nature**, vol. 173. New York: W. H. Freeman; 1983.

240. Webman I: **Effective-medium approximation for diffusion on a random lattice**. *Phys Rev Lett* 1981, **47**:1496.

241. ben-Avraham D, Havlin S: **Diffusion and reactions in fractals and disordered systems**. Cambridge: Cambridge University Press; 2000.

242. Özarslan E, Basser PJ, Shepherd TM, Thelwall PE, Vemuri BC, Blackband SJ: **Observation of anomalous diffusion in excised tissue by characterizing the diffusion-time dependence of the MR signal**. *J Magn Reson* 2006, **183**:315-323.

243. Hall MG, Barrick TR: **From diffusion-weighted MRI to anomalous diffusion imaging**. *Magn Reson Med* 2008, **59**:447-455.

244. Hall MG, Barrick TR: **Two-step anomalous diffusion tensor imaging**. *NMR Biomed* 2012, **25**:286-294.

245. Mitra PP, Halperin BI: **Effects of finite gradient-pulse widths in pulsed-field-gradient diffusion measurements**. *J Magn Reson A* 1995, **113**:94-101.

246. Malmborg C, Topgaard D, Söderman O: **NMR diffusometry and the short gradient pulse limit approximation**. *J Magn Reson* 2004, **169**:85-91.

247. Callaghan PT, MacGowan D, Packer KJ, Zelaya FO: **High-resolution *q*-space imaging in porous structures**. *J Magn Reson* 1990, **90**:177-182.

248. Callaghan PT, Xia Y: **Velocity and diffusion imaging in dynamic NMR microscopy**. *J Magn Reson* 1991, **91**:326-352.

249. Nezamzadeh M, Wedeen VJ, Wang R, Zhang Y, Zhan W, Young K, Meyerhoff DJ, Weiner MW, Schuff N: **In-vivo investigation of the human cingulum bundle using the optimization of MR diffusion spectrum imaging**. *Eur J Radiol* 2010, **75**:e29-e36.

250. Ming X, Kang D: **Corrections for frequency, amplitude and phase in a fast Fourier transform of a harmonic signal**. *Mech Syst Signal Pr* 1996, **10**:211-221.

251. Lätt J, Nilsson M, Malmborg C, Rosquist H, Wirestam R, Sthlberg F, Topgaard D, Brockstedt S: **Accuracy of *q*-space related parameters in MRI: Simulations and phantom measurements**. *IEEE Trans Med Imaging* 2007, **26**:1437-1447.

252. Hess CP, Mukherjee P, Han ET, Xu D, Vigneron DB: **Q-ball reconstruction of multimodal fiber orientations using the spherical harmonic basis**. *Magn Reson Med* 2006, **56**:104-117.

253. Tristán-Vega A, Aja-Fernández S, Westin C-F: **On the blurring of the Funk–Radon transform in *q*–ball imaging**. In: *Medical Image Computing and Computer-Assisted Intervention–MICCAI 2009.* Springer; 2009: 415-422.

254. Canales-Rodríguez EJ, Lin C-P, Iturria-Medina Y, Yeh C-H, Cho K-H, Melie-García L: **Diffusion orientation transform revisited**. *NeuroImage* 2010, **49**:1326-1339.

255. Tristán-Vega A, Westin C-F, Aja-Fernández S: **Estimation of fiber orientation probability density functions in high angular resolution diffusion imaging**. *NeuroImage* 2009, **47**:638-650.

256. Jansons KM, Alexander DC: **Persistent angular structure: new insights from diffusion magnetic resonance imaging data**. *Inverse Probl* 2003, **19**:1031.

257. Guiasu S, Shenitzer A: **The principle of maximum entropy**. *Math Intell* 1985, **7**:42-48.

258. Alexander D, Christensen G, Sonka M: **Maximum entropy spherical deconvolution for diffusion MRI**. In: *Information processing in medical imaging.* vol. 3565. Berlin: Springer; 2005: 27-57.

259. Healy DM, Hendriks H, Kim PT: **Spherical deconvolution**. *J Multivariate Anal* 1998, **67**:1-22.

260. Tournier JD, Calamante F, Gadian DG, Connelly A: **Direct estimation of the fiber orientation density function from diffusion-weighted MRI data using spherical deconvolution**. *NeuroImage* 2004, **23**:1176-1185.

261. Tournier JD, Calamante F, Connelly A: **Robust determination of the fibre orientation distribution in diffusion MRI: Non-negativity constrained super-resolved spherical deconvolution**. *NeuroImage* 2007, **35**:1459-1472.

262. Tournier JD, Yeh C-H, Calamante F, Cho K-H, Connelly A, Lin C-P: **Resolving crossing fibres using constrained spherical deconvolution: Validation using diffusion-weighted imaging phantom data**. *NeuroImage* 2008, **42**:617-625.

263. Kaden E, Anwander A, Knösche TR: **Variational inference of the fiber orientation density using diffusion MR imaging**. *NeuroImage* 2008, **42**:1366-1380.

264. Parker GD, Marshall D, Rosin PL, Drage N, Richmond S, Jones DK: **A pitfall in the reconstruction of fibre ODFs using spherical deconvolution of diffusion MRI data**. *NeuroImage* 2013, **65**:433-448.

265. Cheng J, Ghosh A, Jiang T, Deriche R: **Model-free and analytical EAP reconstruction via spherical polar fourier diffusion MRI**. In: *Medical image computing and computer-assisted intervention – MICCAI 2010.* Edited by Jiang T, Navab N, Pluim JW, Viergever M, vol. 6361. Berlin Springer; 2010: 590-597.

266. Zare RN: **Angular Momentum: Understanding spatial aspects in chemisty and physics**. New York: Wiley; 1988.

267. Varshalovich D, Moskalev A, Khersonskii V: **Quantum theory of angular momentum**. New York: World Scientific; 1988.

268. Wigner E: **Group theory and its application to the quantum mechanics of atomic spectra**. New York: Academic Press; 1959.

269. Levenberg K: **A method for the solution of certain problems in least squares**. *Q Appl Math* 1944, **2**:164-168.

270. Marquardt DW: **An algorithm for least-squares estimation of nonlinear parameters**. *J Soc Ind Appl Math* 1963, **11**:431-441.

271. Kingsley PB: **Introduction to diffusion tensor imaging mathematics: Part III. Tensor calculation, noise, simulations, and optimization**. *Concept Magn Reson A* 2006, **28A**:155-179.